



HAL
open science

Conception et évaluation de systèmes robotiques de ponction d'aiguilles percutanées sous contrôle d'imagerie médicale

Nikolai Hungr

► **To cite this version:**

Nikolai Hungr. Conception et évaluation de systèmes robotiques de ponction d'aiguilles percutanées sous contrôle d'imagerie médicale. Médecine humaine et pathologie. Université de Grenoble, 2014. Français. NNT : 2014GRENS003 . tel-00997017

HAL Id: tel-00997017

<https://theses.hal.science/tel-00997017>

Submitted on 27 May 2014

HAL is a multi-disciplinary open access archive for the deposit and dissemination of scientific research documents, whether they are published or not. The documents may come from teaching and research institutions in France or abroad, or from public or private research centers.

L'archive ouverte pluridisciplinaire **HAL**, est destinée au dépôt et à la diffusion de documents scientifiques de niveau recherche, publiés ou non, émanant des établissements d'enseignement et de recherche français ou étrangers, des laboratoires publics ou privés.

THÈSE

Pour obtenir le grade de

DOCTEUR DE L'UNIVERSITÉ DE GRENOBLE

Spécialité : **Biotechnologie, Instrumentation, Signal et Imagerie pour la Médecine, la Biologie et l'Environnement**

Arrêté ministériel : 7 août 2006

Présentée par

Nikolai HUNGR

Thèse dirigée par **Jocelyne TROCCAZ** et **Philippe CINQUIN**

préparée au sein du **Laboratoire TIMC-IMAG**
dans l'**École Doctorale EDISCE**

Conception et évaluation de systèmes robotiques de ponction d'aiguilles percutanées sous contrôle d'imagerie médicale

Design and evaluation of robotic systems for medical image guided percutaneous needle interventions

Thèse soutenue publiquement le **30 janvier, 2014**,
devant le jury composé de :

Dr. Jocelyne TROCCAZ

Directrice de Recherche au CNRS, Grenoble, Directrice

Dr. Philippe CINQUIN

Professeur à l'Université Joseph Fourier et Praticien Hospitalier au CHU de
Grenoble, Co-directeur

Dr. Bernard BAYLE

Professeur à Télécom Physique Strasbourg, Rapporteur

Dr. Gabor FICHTINGER

Professeur à Queen's University, Ontario, Canada, Rapporteur

Dr. Philippe POIGNET

Professeur au LIRMM, Montpellier, Membre

Dr. Ivan BRICAULT

Professeur à l'Université Joseph Fourier et Praticien Hospitalier au CHU de
Grenoble, Président



To my family: Pilar, Simón and little Pierre.

Abstract

This thesis describes the design and evaluation of robotic systems for medical image guided percutaneous needle interventions. Percutaneous needle interventions have become increasingly more common in the diagnosis and treatment of a variety of illnesses in the human population. Examples include biopsies, radiofrequency ablation, cryotherapy, abscess drainage, and brachytherapy, amongst others.

The coupling of medical imaging to the insertion of a needle raises a number of difficulties for the physician, such as accurately aligning the needle to the planned trajectory in the image, realizing complex out-of-plane trajectories that are difficult to visualize and compensating for soft tissue motion. Robotics can be used to assist these procedures and simplify these challenges, potentially resulting in more accurate procedures, better clinical outcomes and greater patient eligibility.

This thesis outlines the technical and clinical challenges typically faced during the design and evaluation of such needle insertion robots. Focus is given primarily to the aspects which differentiate needle insertion robots from other medical robots. A review of the state of the art is used to describe these challenges and to present some of the solutions that have been proposed to face them. On this basis, two such robotic systems, developed during this thesis, are described in detail, providing concrete examples of the variety of design constraints imposed in a medical image guided needle insertion setting.

The first system, called PROSPER, is for ultrasound(US)-guided transperineal prostate interventions, in particular brachytherapy. It is mounted to the surgical table and a 3D transrectal US probe is rigidly connected to it, allowing one-time pre-operative calibration between the image and the robot coordinate spaces. The protocol developed for this system includes intra-operative US-US registration in order to compensate for prostate motion and deformation during insertion. This chapter exposes the challenges of a system that is not physically present in the imaging space and that takes into account the various constraints inherent to a soft tissue environment.

The second system, called the LPR, is for thoracic and abdominopelvic interventional radiology procedures under CT and MRI guidance. It is mounted on the patient's body and positions and inserts the needle according to the trajectory and target chosen by the radiologist in the image. The robot is calibrated to the image intra-operatively using multi-modal fiducials embedded in the robot's structure. It is fully compatible with both imaging modalities in terms of image quality and space constraints. As opposed to the PROSPER robot, this chapter shows how the presence of the robot in the imaging space brings about a number of additional challenges that must be faced for its clinical acceptability.

In the descriptions of both systems, emphasis is placed on the novel solutions put into place with the goal of providing a real clinical benefit to both patients and clinicians. Prototypes of each system were developed and evaluated on synthetic phantoms in terms of their pre-clinical compatibility and accuracy.

Résumé

Cette thèse décrit la conception et l'évaluation de systèmes robotiques de ponctions percutanées d'aiguilles guidées par imagerie médicale. Les ponctions percutanées d'aiguilles sont devenues de plus en plus communes dans le diagnostic et le traitement de diverses maladies humaines. Des exemples d'interventions fréquentes sont les biopsies, les ablations de tumeurs par radiofréquence, la cryothérapie, le drainage et la curiethérapie, entre autres.

Le couplage de l'imagerie médicale avec l'insertion d'une aiguille amène un nombre de difficultés pour le clinicien, tels que l'alignement précis de l'aiguille à la trajectoire planifiée dans l'image, la réalisation de trajectoires complexes et hors-plans difficiles à visualiser, et la compensation du mouvement et de la déformation des tissus mous. La robotique peut être utilisée pour assister ces procédures pour simplifier les défis et potentiellement améliorer leur précision, leur bénéfices cliniques et d'étendre leurs critères d'éligibilité des patients.

Cette thèse expose les défis techniques et cliniques auxquels il faut faire typiquement face pendant la conception et l'évaluation de tels robots de ponction, tout en restant sur les aspects qui les différencient d'autres robots médicaux. Une revue de l'état de l'art est utilisée pour décrire ces défis et pour présenter les diverses solutions déjà proposées pour leur faire face. Sur cette base, deux tels systèmes robotiques, développés pendant cette thèse, sont décrits en détail, donnant ainsi des exemples concrets des nombreuses contraintes imposées dans le cadre de ponctions d'aiguilles guidées par imagerie médicale.

Le premier système, s'appelant PROSPER, est dédié aux interventions prostatiques transpérinéales guidées par imagerie ultrasonique, en particulier la curiethérapie. Le robot est fixé à la table chirurgicale et une sonde échographique 3D transrectale lui est rigidement relié, permettant ainsi un calibrage préopératoire entre l'espace du robot et l'espace image. Le protocole développé pour ce système inclut un recalage écho-écho peropératoire pour compenser le mouvement et la déformation de la prostate pendant l'insertion des aiguilles. Ce chapitre expose les défis d'un système qui n'est pas physiquement présent dans l'espace de l'image et qui tient compte des diverses contraintes intrinsèques à l'environnement des tissus mous.

Le deuxième système s'appelle LPR et est destiné à la radiologie interventionnelle des régions thoraciques et abdominopelviennes, sous guidage TDM ou IRM. Il est fixé sur le corps du patient et positionne et insère une aiguille selon une trajectoire et visant une cible choisies par le radiologue dans l'image. Le robot est calibré à l'image en peropératoire par moyens de mires multimodales incorporées dans la structure du robot. Il est entièrement compatible avec les deux modalités d'imagerie en terme de qualité d'image et de contraintes de taille. Par rapport au robot PROSPER, ce système montre comment la présence du robot dans l'espace de l'image conduit à nombre d'autres défis qui doivent être relevés pour permettre son acceptabilité clinique.

Dans les descriptions des deux systèmes, l'accent est mis sur les solutions innovantes mises en place dans le but de fournir des vrais bénéfices cliniques aux patients ainsi qu'aux cliniciens. Des prototypes de chaque système ont été développés et évalués sur des fantômes synthétiques en termes de leur précision et compatibilité préclinique.

Acknowledgments

This thesis is the cumulative result of over three years of very rewarding work in an extremely stimulating and enriching multi-disciplined environment. I was very fortunate to be a part of the TIMC-IMAG laboratory, and in particular the GMCAO (CAMI) team and the countless individuals and collaborators who have all played a vital role in advancing my work and sharing with me their expert knowledge.

I must first acknowledge and sincerely thank my two supervisors, Joce and Philippe, without whom I never would have discovered such an inspiring field. Their technical experience in so many aspects of this extremely multi-faceted field is surpassed only by their incredible ability in creating outstanding human and working relationships with the people around them. Through them I have learnt how to channel my work in a pertinent direction, how to look at the big picture and how to ask the right questions. For Joce and Philippe, the finality of all their very creative work is always the wellbeing of the patient, which, in my opinion, is why they have had so much success. I could not have asked for better bosses and colleagues. Merci!

The GMCAO team being such a tight-knit family, I have been very fortunate to work closely with a number of other extremely competent and highly knowledgeable people who have become not just colleagues but friends as well. In particular Michael Baumann, who guided my first steps into the field of soft-tissue needle interventions. Indeed, a large part of the PROSPER work described here stemmed from the numerous discussions we had together in the lab, on the bike and on the skis. Also Céline Fouard, who has been my co-supervisor on the LPR project, and without whose energy, drive, ideas and chocolate cakes, the LPR project would not be where it is at. I would also never have learnt so much about C++ programming without her guidance.

One of the biggest professional benefits of working with the TIMC-IMAG laboratory is its very close relationship with the clinicians and staff of the Grenoble University Hospital (CHU de Grenoble) located a few dozen steps away. Radiologists, urologists, radiation therapists, radio-physicists, interns, all have participated with enthusiasm, willingness, and faith in the solutions we have proposed to them. Indeed, both the LPR and PROSPER projects are the fruit of their direct discussions with Joce and Philippe. Thank you Ivan (Bricault) for your constant availability, the late night scanner sessions and for not only the medical knowledge added to my work, but also your incredible technical understanding. Thank you Jean-Alex (Long) for the fun we had building and poking PVC prostates together, for your availability and for your enthusiasm. Thank you Jean-Luc (Descotes), Mr. Bolla and Jean-Yves (Giraud) for your wide-open arms in the many brachytherapies I was able to watch and for your ability to put things into a clinical perspective with always the patient at the end of the line. A robot could never replace your experience and contributions. Thank you Gaelle (Fiard) for also participating in the PROSPER experiments with such enthusiasm.

I would also like to gratefully acknowledge the staff at the CHUG who helped me, sometimes even in their off-hours, during my countless experiments at the hospital: the technicians and nurses in the urology and radiology departments, and in particular in the MRI of the Hôpital Couple-Enfant. In addition, the help and advice from the CHU's sterilization and hygiene unit was vital.

A very big thank you to Axe Systems (Bruno Mouzon, Bruno Schaefer and more recently David Santos) for their very strong mechanical engineering knowledge and machining professionalism in the development of the PROSPER prototype. The same thanks to Ralph Gros of the Laboratoire Interdisciplinaire de Physique mechanical workshop for the same level of professionalism and unfailing availability for the numerous little machining projects I needed done.

Along with the hospital, the GMCAO team is very fortunate to be closely linked to our neighbouring start-up companies, in particular Koelis SAS, headed by Antoine Leroy, who's

industrial approach and interest in the PROSPER project was key and which gave me a hint of the other world into which any robotic project will eventually have to tip. And thank you for the opportunity to share a patent with you. Thanks also to IMACTIS for simplifying my life in the CT and MRI scanners.

Thank you to all the engineering students I was fortunate to supervise: Adeline Robert who worked with me on the sterilization aspects of the LPR robot, Vincent Beix and Sébastien Briot who worked with me on the PROSPER needle rotation study, Giulia Toti for the work on the development of the clinical protocol for PROSPER and Mouloud Ourak and William Ranou for the help with the electronics and programming of the LPR robot.

Thank you Jean-Pierre (Alcaraz) of the SyNaBi team who helped us with Adeline in the bacterial analysis for the sterilization of the LPR and for the many “bricolage” sessions we had together. Thank you to Agnès Ciapa of Act Pathologie for the help with the needle rotation histology study that we began with Sébastien. Thank you Françoise Giroud, Marie-Paule Montmasson and Flavien Caraguel of the DyCTIM team, and Naceur Belgacem and Bertrand Quesne of the Laboratoire Génie des Procédés Papetiers (LGP2) also for their help with the needle rotation study.

Thank you to Claudio Lobos for the generation of the beautiful fiducial meshes used in the LPR calibration routine and to Nicolas Saubat and Mahnu Promayon for all their programming wizardry and unfailing help with CamiTK.

A particular acknowledgement to Nabil Zemiti and Nathanael Tripodi for being the brains behind the initial parallel manipulator architecture of both projects. It is a pleasure to be working with Nabil again now on the continuation of the LPR/ROBACUS project.

Thanks Margaux (Janier) of the CICIT, for helping me haul the material to and from the hospital during my tests and for being a key part in the risk analysis for both upcoming clinical prototypes, along with Christophe Nennig of Surgiquial Institute.

I was also very fortunate to have access to the Laboratoire d'Anatomie Des Alpes Françaises (LADAF) for my cadaver experiments, where Pr. Palombi, Nathalie Cau, Philippe Masson and Catherine Roulet were instrumental in setting up our experiments and giving us ideas.

And of course, I would like to thank the Agence Nationale de la Recherche (ANR) for providing the funding for my work through the PROSPER and ROBACUS “Technologies pour la Santé” programs, and my Masters supervisor, Tony Hodgson of UBC, who got me into this PhD mess in the first place.

Finally, and most importantly, I would like to thank my family to whom I dedicate this work. First and foremost, Pilar for her huge personal sacrifices to give me the time I needed when it was needed, to give me back my confidence when things got rough, and to take care of all the concerns of daily family life that I didn't have the time to look after during the writing of this manuscript. My beautiful sons Simón and Pierre who changed our lives half way through this PhD, and especially little P who had it hardest of us all and who could not possibly have made the pertinence of my work and all others doing medical research any more real! And thanks of course to my parents, brother Pierre and sister Clara for the motivation and for always being there, even when 8000 km apart.

It's been a wild ride! Merci à tous.

Table of Contents

Abstract	ii
Résumé	ii
Acknowledgments	iii
Table of Contents	v
Chapter 1 : Introduction to percutaneous image guided interventions	1
1.1 Interventional radiology in the thorax, abdomen and pelvis.....	3
1.1.1 Imaging technology used in interventional radiology.....	3
<i>Ultrasound</i>	3
<i>Fluoroscopy</i>	5
<i>CT</i>	5
<i>MRI</i>	7
1.1.2 Common interventional radiology acts.....	8
<i>Biopsies</i>	8
<i>Tumour ablation</i>	9
<i>Abscess drainage</i>	10
<i>Spinal Injection</i>	11
1.1.3 Difficulties of conventional IR acts.....	11
1.2 Prostate cancer interventions.....	12
1.2.1 Prostate anatomy.....	12
1.2.2 Common percutaneous prostate interventions.....	13
<i>Prostate Biopsy</i>	13
<i>Prostate LDR Brachytherapy</i>	14
<i>Focal therapy</i>	17
1.2.3 Difficulties of conventional prostate interventions.....	17
1.3 Summary.....	18
Chapter 2 : Needle insertion robots	19
2.1 Thesis Context.....	20
2.2 Existing needle insertion robots.....	20
2.3 Particularities of needle insertion robots.....	24
<i>Medical imaging constraints</i>	24
<i>Needle constraints</i>	26
<i>Soft tissue constraints</i>	27
2.4 Robot-Image Calibration.....	28
2.5 Sources of Error.....	29
2.6 Validation and Testing.....	31
<i>Sterilization</i>	31
<i>Regulatory issues</i>	32
<i>Preclinical validation</i>	33
<i>Clinical validation</i>	33
2.7 Summary.....	34
Chapter 3 : PROSPER – US-guided prostate transperineal puncture robot	35

3.1 System description.....	36
3.1.1 Clinical incentive	36
3.1.2 General layout.....	36
3.1.3 Clinical workflow	37
3.2 Technical description.....	39
3.2.1 Technical constraints	39
3.2.2 Robot description	40
<i>Mechanical description</i>	40
<i>Robot workspace</i>	42
<i>Electronics description</i>	42
<i>Sterilization and safety</i>	43
3.2.3 Robot kinematics and calibration	44
<i>Forward kinematics</i>	44
<i>Inverse kinematics</i>	48
<i>Kinematics calibration</i>	51
<i>Needle Tip calibration</i>	53
3.2.4 Imaging hardware	53
3.2.5 Image processing	54
3.2.6 User interface.....	54
3.2.7 Robot-image calibration	55
3.3 Pre-clinical evaluation	58
3.3.1 Mobile prostate phantom design.....	58
<i>Prior art</i>	59
<i>Phantom description</i>	59
<i>Imaging characteristics</i>	59
<i>Phantom speed of sound</i>	60
<i>Phantom motion</i>	62
<i>Other phantom characteristics</i>	63
3.3.2 Needle rotation study.....	64
<i>PVC tests</i>	65
<i>Animal tissue tests</i>	65
<i>Cadaver tests</i>	66
<i>Tissue damage</i>	66
<i>Discussion</i>	67
3.3.3 Phantom study	68
<i>Materials and methods</i>	68
<i>Results</i>	69
<i>Sources of error</i>	70
<i>Analysis</i>	71
3.4 Discussion.....	72
Chapter 4 : LPR - CT and MRI-guided abdominal and thoracic puncture robot.....	75
4.1 System description.....	77
4.1.1 Clinical incentive	77
4.1.2 General layout.....	77

4.1.3	Clinical workflow	78
4.2	Technical design.....	80
4.2.1	Technical constraints	80
4.2.2	Robot description	81
	<i>Mechanical description</i>	81
	<i>Robot workspace</i>	84
	<i>Electronics description</i>	85
	<i>Robot fixation</i>	85
	<i>Sterilization</i>	86
4.2.3	Robot Kinematics	87
	<i>Forward kinematics</i>	87
	<i>Inverse kinematics</i>	90
4.2.4	Cable stretch.....	91
	<i>Material choice</i>	92
	<i>Cable tension</i>	92
	<i>Housing curvature</i>	93
	<i>Cable stretch calibration</i>	94
4.2.5	Robot-image calibration	96
	<i>Fiducial design</i>	96
	<i>Image processing</i>	97
	<i>Coordinate frames</i>	102
4.2.6	User interface.....	103
4.3	Pre-clinical evaluation	105
4.3.1	MRI and CT compatibility.....	106
	<i>CT compatibility</i>	106
	<i>MRI compatibility</i>	106
4.3.2	CT and MRI phantom study.....	109
	<i>Materials and methods</i>	109
	<i>Results</i>	112
	<i>Sources of error</i>	114
	<i>Analysis</i>	115
4.4	Discussion.....	116
Chapter 5	: Conclusion	118
5.1	Thesis summary	118
5.2	Contributions.....	119
5.3	Perspectives	120
5.4	Publications	122
References	123
Appendix 1: PROSPER workspace	144
Appendix 2: Prostate phantom article	145
Appendix 3: LPR workspace	165
Appendix 4: LPR GUI protocol	166
Appendix 5: Synthèse (Français)	173

Chapter 1: Introduction to percutaneous image guided interventions

1.1 Interventional radiology in the thorax, abdomen and pelvis	3
1.1.1 Imaging technology used in interventional radiology	3
<i>Ultrasound</i>	3
<i>Fluoroscopy</i>	5
<i>CT</i>	5
<i>MRI</i>	7
1.1.2 Common interventional radiology acts	8
<i>Biopsies</i>	8
<i>Tumour ablation</i>	9
<i>Abscess drainage</i>	10
<i>Spinal Injection</i>	11
1.1.3 Difficulties of conventional IR acts	11
1.2 Prostate cancer interventions	12
1.2.1 Prostate anatomy	12
1.2.2 Common percutaneous prostate interventions	13
<i>Prostate Biopsy</i>	13
<i>Prostate LDR Brachytherapy</i>	14
<i>Focal therapy</i>	17
1.2.3 Difficulties of conventional prostate interventions	17
1.3 Summary	18

Percutaneous interventions are minimally-invasive clinical procedures that involve the insertion of needles through a patient's skin for diagnostic or therapeutic purposes. Compared to surgical interventions, their particularity is that they rely on medical imaging for the planning and execution of the needle trajectory. The clinical protocol can in many cases be generalized to the steps shown in Figure 1-1.

The procedure usually begins with a pre-operative planning stage in which the physician closely examines pre-operative images of the patient prior to the intervention. This allows the physician to compare images from various modalities and to make a preliminary diagnosis upon which the intervention is based. On the day of the intervention, the patient is installed and anaesthetized either generally or locally, depending on the severity of the intervention and contra-indications. In the local anaesthesia case, the anaesthetic is applied initially at the surface of the skin and then progressively deeper as the needle is inserted.

Once the patient is installed, an intra-operative planning stage is done in which an image is taken of the patient and the diagnosis or treatment plan is determined. The needle is then inserted, either progressively or in a single shot, depending on the imaging modality (live or static), the degree of difficulty or risk of the insertion, and the experience of the physician. The needle progression is controlled either using live imaging or with a static control image at the end of each needle insertion. The needle insertion stages can be repeated for a number of needles, depending on the type of intervention.

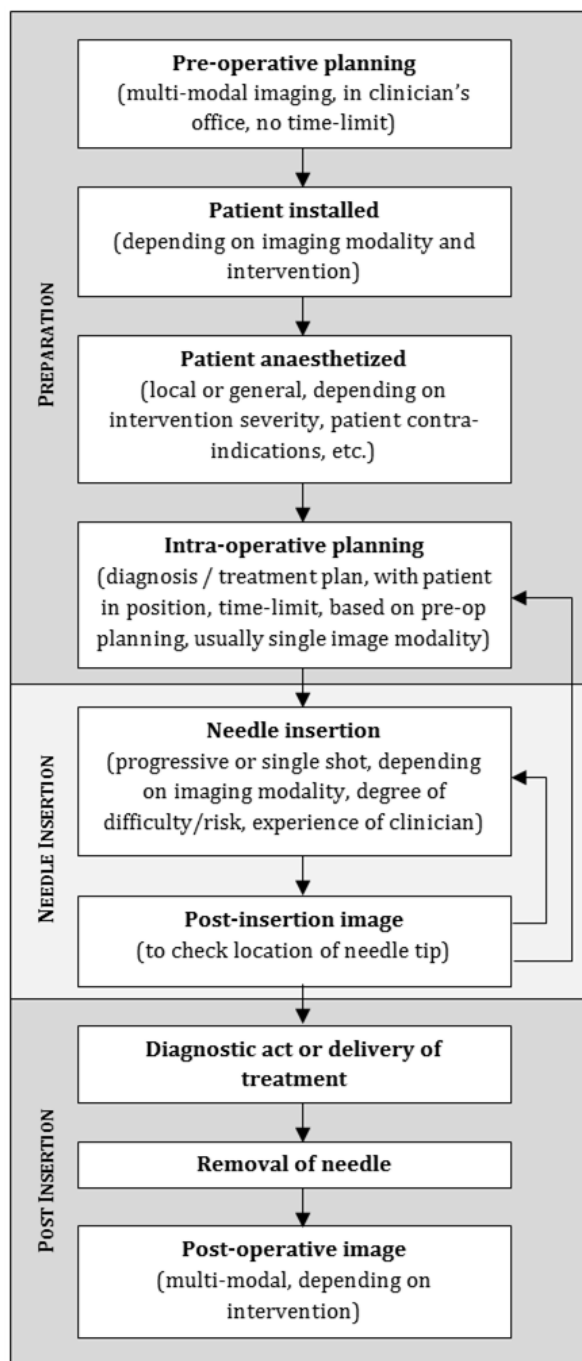


Figure 1-1: Generalized clinical protocol for percutaneous needle interventions.

Once the needle(s) is/are in place, the physician can perform the diagnostic act or deliver the treatment through the needle's hollow shaft. The needle is then removed and a post-operative image is taken to verify the result of the intervention.

Because the patient is not surgically opened, the procedure relies heavily upon the study and analysis of medical images, not only before, but also during the operation. Many percutaneous interventions are therefore performed by radiologists or physicians specifically trained to read and interpret medical images. This has led to the fairly recent introduction of the specialized field of interventional radiology (IR), under which many needle-based interventions can be classified.

The following two sub-sections will describe in more detail the various types of interventions that are based on percutaneous needle access. The first section focuses on the numerous procedures done by interventional radiologists primarily in the thoracic, abdominal and pelvic regions. The second section focuses specifically on prostate interventions which are an entire domain of their own, both clinically and in research. The clinical objectives will be described along with the difficulties that physicians encounter in order to meet these objectives using the conventional techniques.

1.1 Interventional radiology in the thorax, abdomen and pelvis

Interventional radiology is a constantly evolving field that includes a vast number of procedures encompassing a large number of organs in the human body. IR can be categorized into vascular, percutaneous and natural orifice acts [1]. In this thesis we focus on percutaneous acts, in which a needle is used to access an organ through the patient's skin. Because interventional radiology is only a very recently accredited medical subspecialty in many countries, information on the existing IR procedures and statistics on the number of these procedures performed per year is scattered throughout different, not-so-recent sources.

According to a document published by the French National Institute of Cancer (INCa) in 2009, nearly 330 000 diagnostic and 132 000 therapeutic non-vascular cancer-related IR acts were registered in France in 2006 [2]. The Royal College of Radiologists reported an increase of 31% in general IR acts between 2008 and 2011 in the UK [3]. In the USA, IR has only recently, in 2012, been recognized as a certified specialty [4], while in Canada specialization is currently under evaluation. Concrete numbers on the IR acts being performed in North America are hard to come by, however publications exist describing the IR workforce in the USA. Bluth et al. report that interventional radiologists made up the third largest subcategory (8% of the total workforce) of practicing radiologists in the USA in 2011 with increases expected in the years to come [5]. In 2008, Baerlocher et al. provided estimates of the IR treatments performed per capita for each of the G7 nations in 2005 along with seemingly conservative but increasing predictions for 2010 [6].

From this patchwork of information, it is evident that interventional radiology is an important field with growing recognition and increasing activity worldwide. This increase can not only be attributed to the ever-growing importance placed on minimally invasive approaches in medicine, but also on the increase in availability and use of medical imaging technologies worldwide [7] [8] [3]. The following section describes how these imaging technologies are used in the context of interventional radiology.

1.1.1 Imaging technology used in interventional radiology

An important difference between interventional radiology and "standard" surgical interventions is its reliance on medical imaging technology to visualize diseases in the body and to guide minimally invasive tools to these diseased targets. The four primary imaging technologies used in IR are ultrasound (US), fluoroscopy, CT and MRI. The advantages and limitations of these four modalities in terms of percutaneous needle guidance are summarized in Table 1-1 and will be discussed in detail in this section.

Ultrasound

Ultrasound imaging in IR is primarily used to guide biopsy needles to thoracic and abdominopelvic organs. Many different types of transducers, or probes, exist, depending on the application (see Figure 1-2a). Convex, microconvex and linear probes are used for surface interventions while biplanar and end-fire endocavitary probes are used for imaging within body

Table 1-1: Overview of the four primary imaging techniques used for percutaneous needle guidance.

Imaging modality	Primary dependent tissue characteristics	Advantages	Disadvantages
US	Density Acoustic properties	<ul style="list-style-type: none"> - Non-invasive imaging - Real-time - 3D - Mobile - Relatively inexpensive 	<ul style="list-style-type: none"> - Depth-dependent resolution - Requires good skin contact - Acoustic shadows - Few contrast agents - Depends on patient echogenicity - Prone to noise - Very operator dependent
Fluoroscopy	Density Attenuation properties	<ul style="list-style-type: none"> - Real-time - Contrast agents - Bone visualization 	<ul style="list-style-type: none"> - X-ray radiation exposure - Mostly only 2D projection images - Size - Poor soft-tissue definition
CT	Density Attenuation properties	<ul style="list-style-type: none"> - High precision - High spatial resolution - Good tissue differentiation - 3D - CT fluoroscopy - Contrast agents 	<ul style="list-style-type: none"> - X-ray radiation exposure - Expensive - Size
MRI	Magnetic resonance	<ul style="list-style-type: none"> - Non-irradiating - 3D - High contrast resolution - Any orientation plane - Real-time MRI - Contrast agents 	<ul style="list-style-type: none"> - Expensive - Availability - Constrained tunnel size - Magnetic compatibility - Poor bone visualization - Requires receiving antennas - Noise - Size - Long 3D imaging times

cavities (rectal and vaginal imaging). Most transducers provide real-time two-dimensional (2D) images. Three dimensional (3D) probes are however recently becoming more common, allowing the construction of three-dimensional volume images by sweeping a 2D transducer either manually across a region or mechanically within the probe head. Some very recent 3D probes use a static planar matrix of piezo elements. These are mostly used in cardiac imaging.

Ultrasound-guided needle insertion is done either freehand or using a needle guide mounted to the probe (see Figure 1-2b-d). These guides align the needle in the image plane and constrain motion along the needle's axis. A technology recently introduced to industrial US machines is the use of magnetic tracking sensors mounted on the needle head or in the needle's tip to track its position in the image.

According to the French National Institute of Cancer (INCa), 78% of diagnostic interventions in 2006 were US-guided [2]. This popularity is in part because US is non-invasive and real-time, but also because US equipment is relatively inexpensive, easy to operate and mobile. No specially-built imaging rooms are required and the technical and maintenance costs are significantly lower than other imaging technologies. Because the probes are placed by the physician on the patient's body, very little setup and patient preparation are necessary making straight-forward interventions very rapid.

An example of such a procedure, performed on a regular basis in the Grenoble University Hospital (CHUG), is US-guided insertion of gold markers for prostate radiotherapy. The gold markers, inserted using transrectal US guidance, are used to track prostate motion during external beam radiotherapy. The intervention is done in a standard US examination room on an out-patient basis. Preparation of the patient takes about half an hour, including patient installation in the lithotomic position and equipment setup. The patient is anaesthetized locally and the markers are inserted through a hollow needle using a transrectal needle-guide mounted on the US probe. The intervention itself takes only about 5 minutes and the patient walks out on his own immediately afterward, the entire procedure taking less than an hour. Complications can include minor bleeding, prostatic oedema, and infection due to the transrectal approach. It

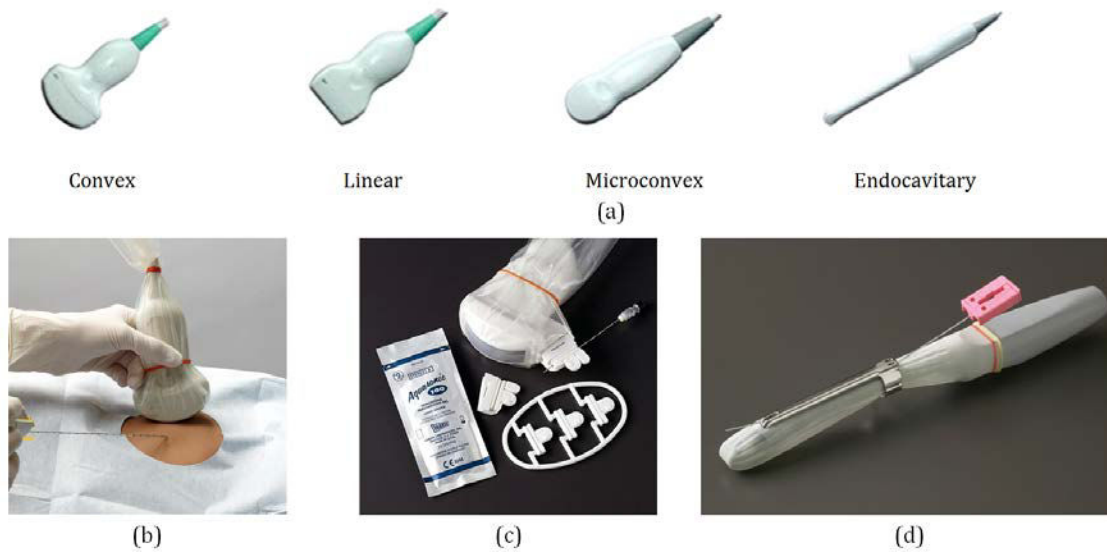


Figure 1-2: a) Typical ultrasound transducers. b) Freehand US-guided biopsy. c) Surface probe US needle guide. (d) Transrectal probe US needle guide (courtesy CIVCO).

is evident that the compactness, simplicity and real-time imaging capability of the US equipment make this intervention almost anodyne in the list of procedures typically done by urologists.

Ultrasound does, of course, have certain disadvantages. One drawback is its depth-dependent lateral resolution, as at greater depths the US beam gets progressively more scattered. It is also fairly susceptible to image artifacts, such as reverberation artifacts around the needles, and is unable to cross hard surfaces, such as bone, resulting in acoustic shadows. Beamwidth distortion can also have significant effects on needle tip localization during interventions [9].

Fluoroscopy

Fluoroscopy is a valuable imaging modality in IR because it allows for real-time imaging of moving organs, instruments or contrast agents. It provides a 2D projection of the tissues it images. Soft-tissues are difficult to distinguish and therefore contrast agents usually need to be used. It is primarily used for vascular procedures. Fluoroscopy-guided percutaneous interventions include intra-articular infiltrations and vertebroplasty, amongst others.

The INCa report states that 16% of diagnostic interventions are done using fluoroscopy-guidance. Likely reasons are the relative abundance of available equipment and its real-time capabilities. However, the method must evidently be used with caution because of the x-ray exposure not only present for the patient [10] [11] but also for the radiologist who has to hold the needle during imaging and is thus exposed on a more frequent basis [12].

CT

CT has become a standard imaging modality for interventional radiologists. Machines have become faster and more efficient, with decreased radiation doses. The ability to acquire 3D volumes of any part of the body, with excellent resolution and soft tissue differentiation gives radiologists the ability to target regions with high accuracy. Although volume acquisition and reconstruction requires far from real-time intervals, 2D CT fluoroscopy can be used to help guide interventions in certain cases.

Percutaneous needle interventions under CT-guidance are done primarily freehand (see Figure 1-3). In other words, the radiologist plans the trajectory on the screen in the control room and then tries to reproduce it on the patient in the imaging room. Tools or tricks exist to



Figure 1-3: CT-guided kidney biopsy.

simplify this procedure. When no evident externally-visible anatomical landmark is present, the radiologist can choose the needle insertion point relative to a CT-visible marker placed on the patient's skin. The trajectory of the needle can also be simplified by choosing a vertical orientation or by orienting the needle only in the imaging plane of the CT scanner and then aligning the needle using the laser line markers built into the tunnel of the scanner.

To help radiologists with this challenging task, a new method of navigated CT-guided needle insertion is currently being developed and marketed by a Grenoble company, IMACTIS (<http://www.imactis.com/>) [13]. Their product is similar to the above-mentioned US magnetically tracked needles. A magnetic tracking sensor is mounted to the needle head, allowing the radiologist to follow the needle's position directly within the 3D volume displayed on a screen in the imaging room.

A large number of interventions are done under CT-guidance. Amongst the most common are biopsies, tumor ablations and abscess drainage. Regardless of the intervention, the initial insertion of the needle to the desired target generally follows the same procedure of recursively inserting the needle and verifying the trajectory with control images, as described in the beginning of this chapter. Because of the high spatial resolution of CT images, radiologists are able to reach their targets with high accuracy. The needles are perfectly visible in the images, although they do cause artifacts that can affect the clarity of the images (see Figure 1-4). Standard scanner bores have a large diameter of 70 cm and are shallow, giving radiologists ample room for placing the needles and allowing for larger patients with minimal risk of claustrophobia.

Because of the many benefits that they provide, the availability of CT scanners has increased steadily over the years, as reported in the OECD data plotted in Figure 1-5a. With this increased availability and therefore increased use, the concern over radiation doses administered to patients has also risen [14] [15] [16] [17]. Compared to standard diagnostic imaging, which typically require only a few images, interventional procedures require multiple image acquisitions during a single procedure, making them of greater concern in terms of radiation exposure.

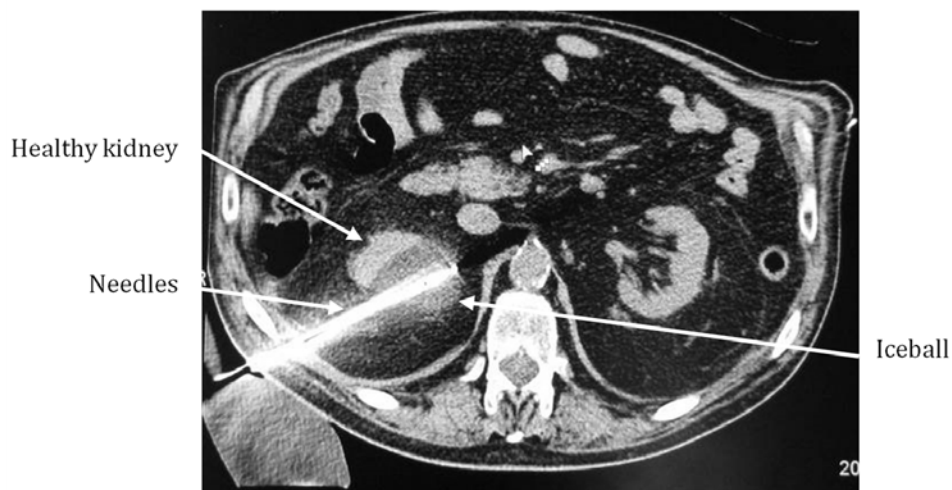


Figure 1-4: CT image showing two 17G cryotherapy needles inserted into a kidney tumour. Note that the needles are difficult to distinguish from each other.

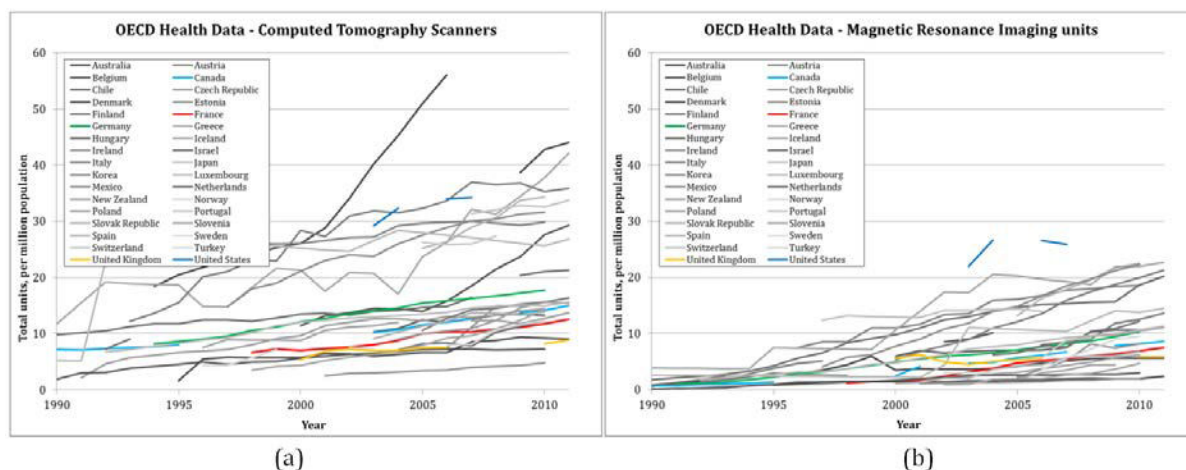


Figure 1-5: Organisation for Economic Co-operation and Development data showing the number of a) CT scanner and b) MRI units per million population in partner countries from 1990 to 2011.

MRI

Of the four imaging modalities described in this section, MRI is by far the least used for interventional guidance. The advantages of MRI are significant, however, high cost and compatibility issues make it a difficult modality to use for interventional radiology procedures.

Like CT imaging, MRI provides 3D imaging of the body, with the difference of being able to image in any given orientation plane. This characteristic is valuable to interventional procedures as it can allow precise imaging directly in the needle plane [18]. Soft tissue contrast resolution is excellent in MR imaging, a property which is commonly used for cancer detection. Organs in which tumour detection is noticeably higher than in CT include the liver, pancreas, kidneys and spine [19]. For prostate cancer detection, conventional T2-weighted MRI is known to have high specificity (i.e. the ability to detect negative results) [20]. In addition, multiparametric MRI can be used to achieve fairly high sensitivity (the detection of positive results), by combining endorectal receiver coils, MR spectroscopy, dynamic contrast-enhanced MRI or diffusion-weighted MRI [21] [22] [23] [24] [25]. This improved ability to detect lesions

is very attractive for interventional procedures in order to provide a more targeted approach. Another major advantage over CT is, of course, that MRI is non-irradiating; a characteristic especially important for real-time imaging.

The benefits of MRI are evident, however a number of important issues have impeded the development of MRI-guided interventional procedures. One of the primary issues is in terms of material compatibility. Typical IR equipment is not compatible with the high magnetic environment of the MRI, not only in terms of the safety of the patient, operators and imaging equipment, but also for maintaining the imaging quality [26] [18]. Another important issue is physician access to the patient, which is very limited in conventional 60 cm diameter closed-bore MRI machines [18]. The recent emergence of 70 cm wide-bore machines has improved access, but the depth of the tunnel still makes it difficult to do interventions within the bore. Open MRI's have been used extensively for interventions, but their field-strength and therefore image quality is lower than closed-bore machines [27].

Examples of MRI-guided percutaneous needle interventions include biopsies, cryoablation and prostate brachytherapy [26] [18]. Although their expansion is slowed due to the limited availability of MRI machines and due to the elevated cost of such interventions, interest in MRI's non-irradiating nature and soft tissue resolution capabilities is growing [28]. In consequence, like with CT machines, the number of MR machines worldwide is progressively increasing, as shown in Figure 1-5b.

1.1.2 Common interventional radiology acts

The human pelvic, abdominal and thoracic cavities, shown in Figure 1-6, are the most common regions of percutaneous needle intervention because of the high concentration of organs and soft tissues. Numerous diagnostic and therapeutic interventions exist including, in particular, biopsies, tumor ablations, abscess drainage, and spinal injection, amongst others. This section will describe the conventional methods of performing these interventions.

Biopsies

Biopsies are some of the most common types of non-vascular image-guided interventions. A biopsy consists of extracting a sample of tissue from an organ suspected of having a disease. This suspicion can stem from various signs, such as an abnormal concentration of specific blood markers (proteins), abnormal lesions seen in medical images, patient symptoms, such as pain,

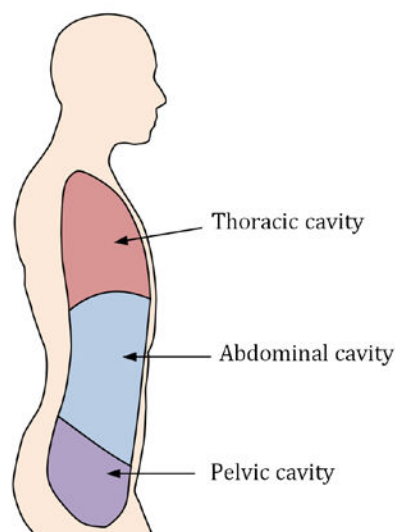


Figure 1-6: The three main regions of the human body in which percutaneous needle interventions are performed.

loss of organ function, swelling, and many other signs. The sample is analyzed under a microscope by a histopathologist in order to determine the level of disease of the extracted cells. Biopsies are usually the only fully reliable method of determining the health status of a tissue.

The needle types used for biopsies depend on the organ being punctured and the type of biopsy being performed. A standard soft-tissue biopsy needle consists of a cutting cannula, inner stylet and firing mechanism, as shown in Figure 1-7a. The inner stylet has a notch at its end that fills with the specimen tissue when the cutting cannula is fired rapidly over it. A coaxial needle is sometimes inserted first in order to provide a channel through which to take multiple biopsies. Another type of biopsy needle is shown in Figure 1-7b and is used in aspiration biopsies and injections. Aspiration biopsies use a syringe connected to the needle's head to draw up tissue or liquid for analysis. The method is typically used during drainage, as explained below. Needle tips are usually surface-treated to improve echogenicity for US-guided biopsies. Non-ferromagnetic needles (titanium, etc.) also exist for MRI-guided biopsies. Needle sizes typically used at the Grenoble University Hospital vary between 14G and 22G, with lengths depending on the depth of the lesion.

Biopsies can either be targeted or "exploratory." Targeted biopsies are biopsies that target a specific region in an organ, based on suspicious lesions found during image diagnosis. If no lesions are apparent in the images, a number of systematic or random biopsies can be taken to explore which regions of the organ are affected by disease, as is commonly done in the prostate.

Tumour ablation

In cancer treatment, needle-based tumour ablations are becoming increasingly more frequent, particularly for treating relatively small, localized tumours [29] [30] [31]. The goal of tumour ablations is to destroy a focalized cancer by applying either energy or a chemical agent to a defined volume containing the malignant cells. Amongst the many types of ablations, the most common are radiofrequency (RF) ablation and cryoablation.

In RF ablation, an electrical current is applied between electrodes, oscillating typically between 200 and 1200 kHz [30], causing ionic agitation across the tissue and consequently frictional heating. The heat conducts across neighbouring tissue creating a zone of irreversible

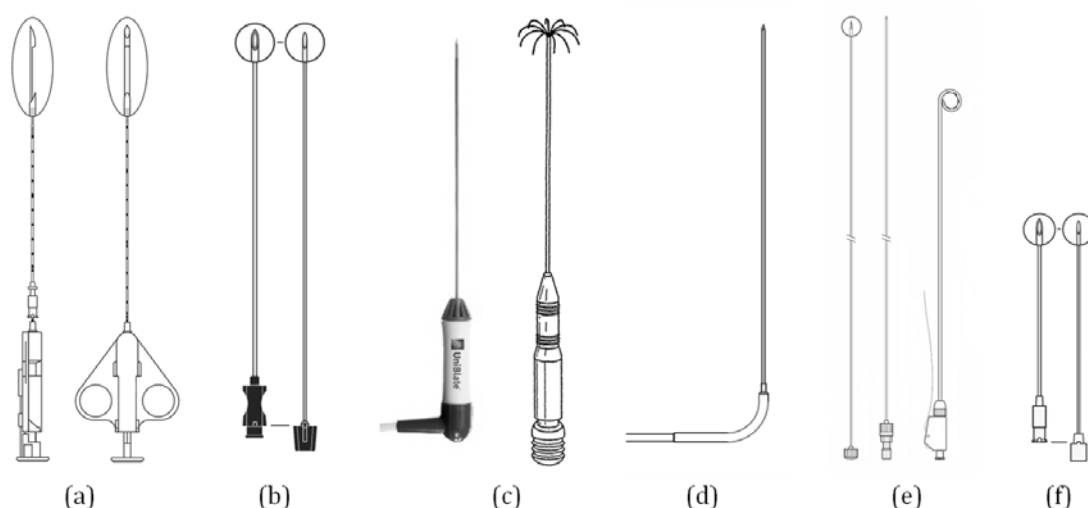


Figure 1-7: Different types of interventional needles. a) Biopsy needle (courtesy Cook Medical). b) Aspiration biopsy needle (courtesy Cook Medical). c) Straight and multitined RF ablation electrodes (courtesy Angiodynamics). d) 17G cryoablation probe (courtesy Galil Medical). e) Typical drainage catheter set (courtesy Cook Medical). f) Quincke needle for spinal injections or spinal fluid sampling (courtesy Cook Medical).

coagulation necrosis of the cells. The technique is typically used in the liver, kidneys and lungs under CT, US or sometimes MRI guidance. Intra-operative US images are prone to deterioration due to the vaporization of intracellular water. CT-guidance, on the other hand, has the benefit of providing lesion discrimination and improved lesion targeting [32] [33].

Monopolar or bipolar RF ablation systems can be used. The former consists of a single percutaneous “interstitial electrode” for delivering the energy and a dispersive “ground pad” electrode mounted on the skin surface to close the electrical current. The latter consists of two percutaneous interstitial electrodes acting as energy source and sink between which the current runs. Two primary types of electrodes exist for RF ablation, as shown in Figure 1-7c. Single straight electrodes are insulated needle-like electrodes with an exposed metallic tip to concentrate heating around the end of the needle. These needles are typically of 17G diameter and can be internally cooled to further improve heat concentration [31]. Multitined expandable electrodes consist of a single hollow needle that can range between 13-14G in diameter and 10-25 cm in length [30] [31]. Once the needle has been inserted into the tissue, multiple tines are deployed in order to distribute energy over a larger area. Electrodes can be CT or MRI-compatible.

Cryoablation uses freeze-thaw cycles to inhibit cell necrosis. The controlled freezing and subsequent thawing of tissue, results in cellular dehydration and ischemia due to the coagulation of the local vascular system [34] [35]. Needle-like cryoprobes are inserted percutaneously into the tumour. Argon gas is expanded in the probe tip to achieve the freezing which conducts through neighbouring tissue to create a localized ice ball. Although passive thawing is used primarily, rapid active thawing can be induced using helium gas to release the probes from the ice ball [36]. The procedure is most often used on renal tumours [35], but also on pulmonary tumours [36] and in the focal treatment of prostate cancer [37]. CT and US imaging allows for monitoring of the ice ball formation, as can be seen in Figure 1-4 (page 7). In the prostate, transrectal ultrasound guidance is used. The number of probes used depends on the size of the tumour, the main guideline being that treatment must include an approximate margin of 1 cm of healthy tissue around the tumour [30]. Modern probes are 16-17G in diameter (see Figure 1-7d) depending on the manufacturer, and can be US, CT and MRI-compatible.

Other types of percutaneous ablations include microwave ablation [38], laser ablation [39], photodynamic therapy [40] and ethanol ablation [41].

Abscess drainage

Another common type of image-guided percutaneous intervention is abscess drainage. Drainage uses a catheter inserted through the patient’s skin to drain fluid buildup due to inflammation, disease or hematoma [42]. Abscesses can occur in most areas of the human body, either within an organ (such as intra-hepatic or intra-pancreatic abscesses) or in extravisceral spaces (such as peritoneal, retroperitoneal or pleural abscesses). US and CT imaging are the most commonly used guidance modalities, the latter being used for deep abscesses with difficult access [43].

Catheters come in many sizes, typically varying between 8 F and 16 F [42], with different tip configurations for locking the catheter in the abscess. Figure 1-7e shows an example catheter set including a hollow stiffening cannula, cutting trocar and flexible catheter with a pigtail locking tip and multiple drainage holes. Numerous techniques exist to insert a catheter for abscess drainage, but the majority rely on the initial insertion of a straight needle. The hollow needle can be used to place a guidewire into the abscess, along which the catheter is then pushed, as described by Seldinger [44]. In the tandem-trocar technique, the catheter, armed with the stiffening cannula and cutting trocar, can be inserted directly into the skin parallel to the previously inserted needle, using the latter as a visual depth and orientation guide [42]. Regardless of the technique, the initial needle is used because it is easier to insert than a thick catheter, allowing for careful placement under image-guidance. The needle can also be used to draw up a sample of the liquid for analysis, called aspiration.

Spinal Injection

Spinal injections include interventions in which medication is injected into spinal tissue to reduce pain or inflammation. Typical medication includes anti-inflammatory drugs and steroid-based anaesthetics. Such injections are done in particular in the lumbar area, including facet joint and nerve root blocks, and sacroiliac joint injections [45]. The typical imaging modality used for needle guidance is fluoroscopy or CT, although US and MR imaging have been reported as well [46] [47] [48]. One of the particularities of these needle insertions which make them challenging are the tight spaces between vertebrae, nerves, ligaments and articular structures. The spine is, however, easily accessible from the posterior side of the patient and requires relatively small needle lengths compared to the other procedures described above. The typical needles used for spinal procedures are 18-25G diameter Quincke tip needles, as shown in Figure 1-7f.

1.1.3 Difficulties of conventional IR acts

Percutaneous interventional radiology procedures have introduced huge benefits over open surgery solutions, in particular with respect to their minimal invasiveness, shortened procedure time, lower cost and even clinical efficacy in certain cases. They are, however, prone to numerous difficulties which can increase the risks of the interventions and even sometimes limit patient eligibility or limit the procedures to specialized expert physicians.

The primary challenge for percutaneous IR procedures comes from the use of medical imaging to guide the procedure. Firstly, the quality of the image can play a large role in the difficulty of the procedure. Ultrasound imaging, for example, can be difficult to interpret, requiring very specific training or experience to be able to correctly identify the viewed anatomy and to choose the appropriate interventional approach to be used [46] [47]. Often multiple imaging modalities must be used to complement each other and provide a more accurate plan of the intervention.

The coupling between what is planned in the image and what is done in reality on the patient is another challenge. For example, in CT-guided procedures, the needle's insertion point on the patient's skin and the final target within the body is planned in the imaging room, requiring the physician to mentally reproduce this plan on the patient. This limits out-of-plane insertions due to the complexity of reproducing orientations in multiple directions by hand. As a result, CT and MRI-guided needle interventions tend to be iterative with multiple image acquisitions required for accurate targeting. This affects patient comfort, since each image acquisition and needle insertion step requires a breath-hold that is usually fairly disquieting. In the case of CT-guidance, these repeated imaging steps also increase radiation exposure.

A third challenge directly related to the use of image guidance is compatibility. All materials and methods used must be compatible with the imaging modality. In US, the needle must be visible in the image with the least amount of artifacts possible. The same is true for CT and MRI. In the latter two, and in particular in MRI, the interventional method and material must be adapted to fit within the tight size constraints of the imaging tunnel. An important point is also that the material used must not affect the clinical image acquired by the machine. Streaking and beam hardening artifacts must be kept to a minimum in CT images, while in MRI, the signal-to-noise ratio must not be affected [49] [50] [51]. In MRI, a particular issue is safety around the high magnetic field of the machine. The magnetic forces and torques induced on the material must be reduced to a minimum, or ideally avoided by using non-ferromagnetic materials. In addition, induced currents that could cause dangerous heating of materials must be controlled [51].

Another difficulty that is often encountered during IR procedures is the choice of needle trajectory. The complex anatomy of the human torso makes many targets difficult to access, with only small trajectory windows through which a needle can safely pass. Maher et al. list a number of organs that must not be punctured during abdominopelvic deep abscess drainage

procedures, including the gallbladder, pancreas, spleen, small and large bowels, urinary bladder, uterus, ovaries and prostate [43]. In addition, major blood vessels, bile ducts and nerve bundles must be avoided to prevent or reduce internal hemorrhage, infection and pain. Of course bone, such as ribs, vertebrae and pelvis, must also be avoided. The liver, for example, although it can be punctured, is highly irrigated, requiring accurate trajectories to avoid bleeding [52]. During hepatic RF ablation, blood vessels must also be avoided to prevent incomplete tissue necrosis due to their heat dissipative nature [33]. Other examples are deep pelvic and spinal punctures which are delicate due to surrounding bone, organs and tissues including the bowel and nerves [43] [42] [53].

1.2 Prostate cancer interventions

An organ of particular interest for percutaneous needle interventions, located in the male pelvic region, is the prostate. This non-essential gland is highly prone to cancer particularly in men over the age of 50 [54]. Prostate cancer is, in fact, one of the most common causes of cancer-related death in men in western developed countries, making it a large public health problem. In the US, 238 590 new cases and 29 720 deaths were estimated for the year 2013 [55], while in France, 71 000 new cases and 8 700 deaths were estimated in 2011 [54].

The prostate can be distinguished from the other organs typically described in the field of interventional radiology for a few reasons. The organ is traditionally dealt with by urologists, specialized in the urinary and reproductive systems rather than by interventional radiologists. More importantly, the transperineal or transrectal needle accesses to the organ are particular compared to other organs accessible from the patient's abdomen.

1.2.1 Prostate anatomy

The prostate is a gland, approximately 20 to 50 cc in volume that surrounds the urethra between the bladder and the rectum, as shown in Figure 1-8. It secretes a small amount of fluid that is mixed with the seminal fluid and it also helps contain urine flow during ejaculation. Anatomically, it can be split into base, apex, anterior, posterior and lateral sides as shown in Figure 1-9. Structurally, it consists of peripheral, central and transition zones, the first being the most common location of cancerous lesions. It consists of glandular and muscular tissue, with a fibrous capsule surrounding its exterior. Nearby organs include the urethra that passes through the center of the gland from base to apex, the bladder against which it is abutted at its base, the rectum passing directly below its posterior side, and the seminal vesicles located on the postero-lateral sides. The perineal space separating the prostate and the perineum consists of skin, fat and muscle tissue.

The prostate is very adapted to needle-based interventions. It is easily accessible by transperineal or transrectal approaches with needle depths generally less than 10 cm in order to access its entire volume. Needle insertion is also not particularly hindered by any critical anatomy, although attention, of course, must be paid to avoiding surrounding nerve bundles, seminal vesicles, and other structures. In addition, the gland is not highly vascularized like the liver for example, reducing the risk of severe internal hemorrhage. The prostate capsule makes it easy for a physician to "feel" when they have pierced into the prostate body with a needle. The prostate is also very visible in US and MR images, making image-guidance feasible.

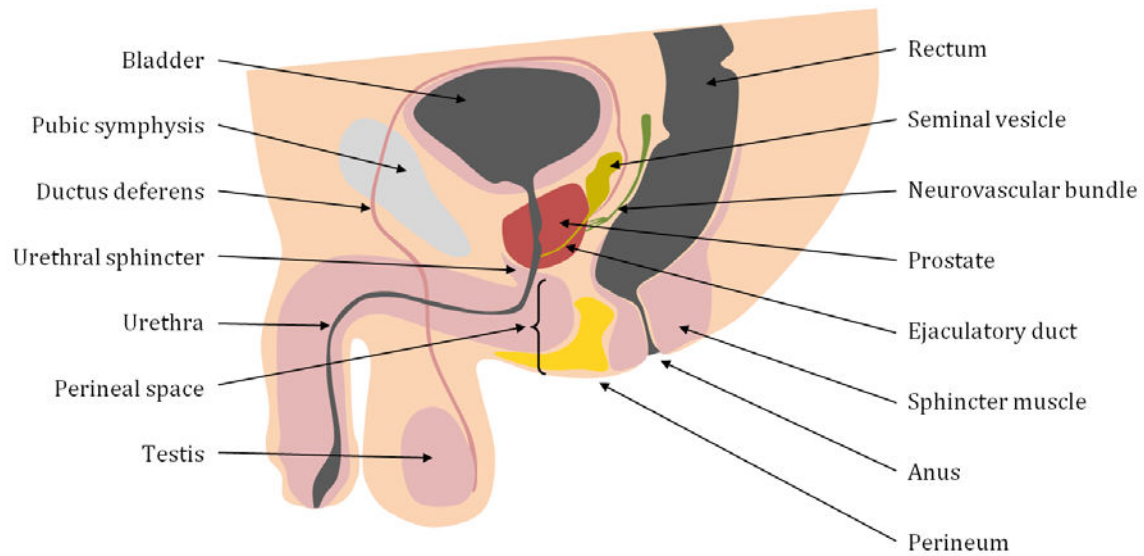


Figure 1-8: Male pelvic anatomy, sagittal section.

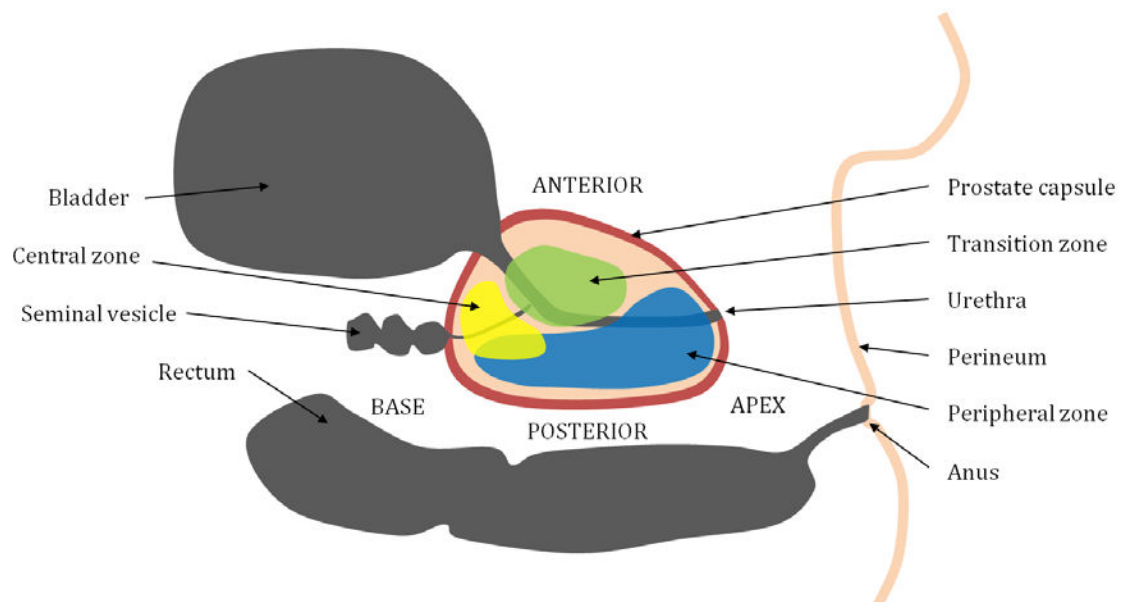


Figure 1-9: Prostate anatomy, sagittal view in dorsal decubitus position.

1.2.2 Common percutaneous prostate interventions

A number of needle-based image guided interventions have been developed to deal with prostate cancer. Of these, the two primary percutaneous interventions practiced today are biopsies for diagnosing the cancer and low dose rate (LDR) brachytherapy for treating the gland.

Prostate Biopsy

Prostate biopsies are used as the gold standard for diagnosing prostate cancer in men. Because prostatic tumours are very difficult to distinguish from healthy tissue in US, and MRI is

an expensive and less available resource, exploratory biopsies need to be done to properly diagnose a patient. A number of protocols exist but their comparative efficacy and reliability is still under debate and standards have changed numerous times over the past 10 years [56].

Two needle insertion approaches can be used: transrectal or transperineal, both typically guided by transrectal ultrasound (TRUS). Transrectal biopsies are by far the most common. They use a needle guide mounted on the transrectal end-fire probe, as shown in Figure 1-2d (page 5), to align the needle to the image plane. The biopsy is taken through the rectal wall at an oblique angle to the posterior surface of the prostate. A number of systematic cores are taken, targeting the various regions of the prostate. The exact number of samples to take and where to take them remains controversial [57], but the current worldwide standard is a 12-core extended sextant biopsy [56]. Because access to the prostate is fairly direct through the rectum, this technique requires minimal anaesthesia.

Transperineal biopsies are less common and involve the insertion of needles through the perineum using a template, as will be described in the brachytherapy section below. This approach is used when a transrectal approach is contra-indicated, or for saturation biopsies in which more than 20 cores are sampled. Saturation biopsies are used for patients with persistent cancer signs even after negative standard biopsy results [58] [56], or when considering a focal treatment in which the exact location and volume of the tumour is vital [59] [60].

Advantages of the transperineal approach compared to the transrectal approach are the reduced risk of infection and rectal bleeding, and potentially improved correlation with pathology results compared to the obliquely placed transrectal approach [61] [62]. In addition, the transperineal approach allows for better access to the entire prostate, while the transrectal approach is more accurate for the peripheral zone. However, these advantages are counterbalanced by practicality problems, such as longer time and material setup as well as increased pain and therefore more complex anaesthesia.

Regardless of the technique used, an accurate mapping of the biopsy cores within the prostate volume is vital for determining the stage of the cancer, for comparing to other imaging modalities (MRI in particular) and for choosing an appropriate treatment [63]. Accurate needle placement is therefore very important.

Prostate LDR Brachytherapy

Permanent LDR prostate brachytherapy is a prostate cancer treatment that involves the localized irradiation of the prostate by the insertion of about 100 tiny radioactive seeds. The conventional procedure introduces the seeds into the prostate according to a pre-operative dose distribution plan, by means of hollow needles inserted through the perineum of the patient in the lithotomy position. The number and distribution of seeds is determined to satisfy standardized dose constraints. A template is used to insert the needles along a grid of horizontal holes, the depth of each needle being adjusted visually using 2D TRUS guidance. Its primary benefits over other popular techniques, such as radical prostatectomy and external beam radiation therapy, are its short hospitalization period (1 to 2 days) as well as its potential for providing intense localized therapy within the prostate, with limited morbidity and side-effects.

Recent discussions, motivated by the appearance of new studies showing a minimal death rate for untreated early-stage prostate cancer patients [64] [65], have been provoked on whether treatments, including LDR prostate brachytherapy, are sufficiently beneficial to outweigh the side-effects and cost of the procedures. An important argument is that reported side-effects, such as urinary incontinence and erectile dysfunction, can be directly related to the quality and precision of the treatment delivered. The success of a brachytherapy procedure (i.e. the complete destruction of the cancer, with minimal side-effects) is reliant on dose conformity, that is, the uniform distribution of the radioactive dose throughout the entire volume of the prostate (or the precise focalized application of the dose in the case of focal therapy), without over-dosage and without affecting adjoining organs. The procedure is therefore heavily reliant

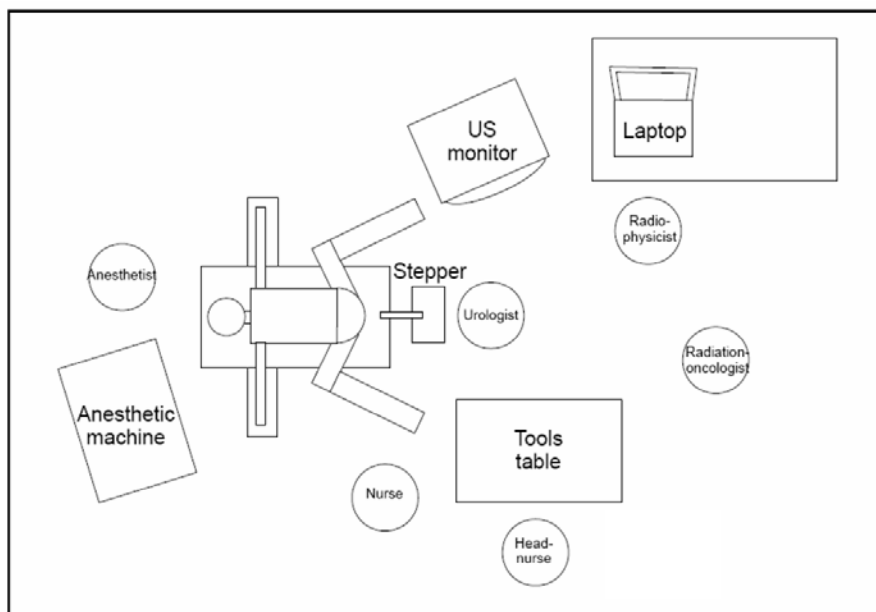


Figure 1-10: General distribution of equipment and personnel in the brachytherapy OR (courtesy G. Toti).

on the ability of the clinicians and physicists in reproducing the pre-planned dosimetry within the prostate.

A number of variations exist to the clinical procedure. The two main approaches are based on the dose distribution plan being done either pre-operatively and assuming the patient is in the same position once in the OR, or doing the planning intra-operatively with the patient already in position. The second approach is used at the CHUG, with single, un-stranded iodine-125 sources and Variseed treatment planning software (Varian Medical Systems, Palo Alto, CA). The distribution of equipment and personnel in the operating room (OR) is shown in Figure 1-10 and Figure 1-11. The staff required for the procedure includes a urologist for doing all the surgical acts, a radiophysicist for calculating the dosimetry, a radiation oncologist for inserting the seeds, an anesthetist and nurses. The TRUS probe is mounted to a device called the stepper, which provides the coupling between the probe and the template used to align the needles. The stepper (CIVCO, Kalona, Iowa) allows the probe to be translated and rotated axially in order to acquire accurately placed images. The TRUS probe has two 2D transducers: one transverse transducer for taking images perpendicular to the needle axes, and one sagittal transducer for taking images parallel to the needles. The radioactive seeds are held in shielded capsules and are inserted through the needles using a Mick Applicator (Mick Radio-Nuclear Instruments, Mount Vernon, NY), as shown in Figure 1-11.

In the CHUG, the technique takes between two and four hours under full anesthesia, depending on the complexity of each case. The procedure follows the general workflow illustrated in Figure 1-1 (page 2). The patient is anaesthetized and installed in a surgical operating room. The TRUS probe is installed on the stepper and inserted into the patient's rectum. An image sequence is acquired by taking a set of 2D transverse images from base to apex of the prostate, every 2.5 mm. The essential anatomy in all the images is segmented by manually clicking around the prostate, rectum, seminal vesicles and urethra. This is vital for analysing the dose applied to the prostate and surrounding tissues. A dose plan is then calculated by the radiophysicist using the Variseed software. The contouring and planning steps can easily take over an hour, in which nothing is done on the patient.

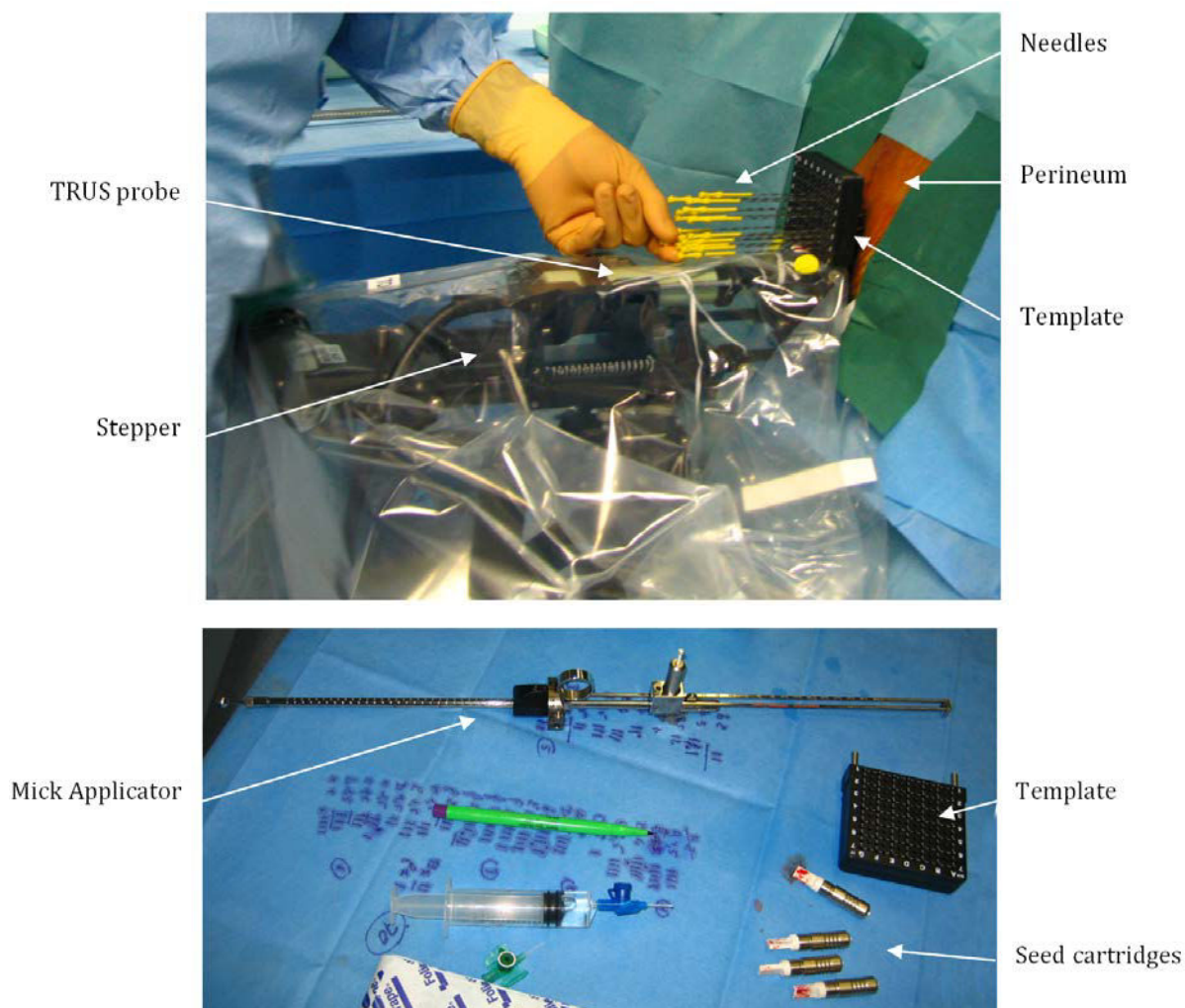


Figure 1-11: Conventional brachytherapy setup and tools in the OR.

Once the dose plan is defined, the peripheral needles are inserted. They are inserted using the template and a grid of points in the transverse US image. All peripheral needles are inserted until they are visible in the transverse image. Then each needle depth is adjusted using the sagittal image. To adjust for any cranio-caudal (apex-to-base) prostate motion due to needle insertion, the segmented contours in the Variseed software can be aligned manually to the live sagittal image, although prostate deformation is not accounted for. The radiation oncologist then inserts the seeds using the Mick Applicator tool and by retracting each needle from base towards apex to drop each line of seeds. Once all the peripheral seeds are inserted, the same procedure is repeated for the internal needles. The advantage of doing the procedure in two steps, peripheral then internal is that the dose plan can be adapted between the steps, depending on the true position of the peripheral seeds after deposition.

Two other seed insertion techniques exist: preloaded seed lines and stranded seeds. In the latter, a line of seeds is prepared for each needle with inert and absorbable spacers between each seed. The seed line is then deposited in one shot. Similarly, the other technique uses a seed line stranded together with an absorbable braided suture (RAPID Strand, Oncura, Inc., Plymouth Meeting, PA). The idea behind these methods is to be able to deposit the seeds in a straighter line than individual seeds and to help reduce the risk of individual seed migration [66]. They, however, give less flexibility for progressively adapting the dose plan throughout the procedure and require handling of the exposed seeds by the clinical personnel.

Focal therapy

With the advent of more precise biopsy protocols and new imaging techniques, such as multiparametric MRI, focal therapy of the prostate has become an important topic of clinical research and development. The goal of focal therapy is to locally treat the cancerous tissue while reducing the risk of side-effects caused by unnecessary damage to surrounding healthy tissue.

Until recently, treatments, including the LDR brachytherapy technique described above, have focused on treating the entire gland because of the difficulty in precisely locating the cancerous cells in the prostate. Proponents of focal therapy are now arguing that certain low risk patients can be treated with less invasive treatments [67]. Among these treatments can be included a number of the thermal ablation treatments described above for general IR procedures (section 1.1.2, page 8). In particular, cryotherapy has been shown to have good results with low morbidity, short hospitalization and relatively few side-effects [68] [69]. Focal LDR brachytherapy has also shown promise with guidelines being published recently on patient selection and the clinical protocol to follow [70].

Two types of focal treatments are used in the prostate. The hemi-gland approach involves the treatment of one half of the prostate in the case of unilateral disease. The ultra-focal approach involves localized treatment directly around a unifocal lesion. These treatments have typically been proposed either to young patients who have a greater likelihood of their localized cancer spreading into a higher risk case, or to patients who are unwilling to face the higher risks of quality-of-life side-effects attributed to more radical treatments [69].

1.2.3 Difficulties of conventional prostate interventions

Needle-based prostate interventions are challenging procedures because of the relatively small size of the gland and the numerous nearby essential structures that need to remain intact to conserve a patient's quality of life. Needles must be placed very accurately to properly target the desired region and nothing else. The urethral sphincter at the base of the prostate and the urethra passing through the center of the gland must be spared to prevent urinary incontinence. The rectum must be preserved to avoid bowel problems. The seminal vesicles must not be affected in order to retain the patient's fertility. The neurovascular bundles must be spared to preserve erectile function. In addition, prostate cancer can be either unifocal or multifocal, making it difficult to precisely target, especially during biopsies, making false negatives an important issue [61].

In prostate brachytherapy, as described in section 1.2.2, dose conformity is an important aspect to the success of the treatment, since even small seed misplacement could significantly affect the dose received by the gland [71]. Multiple limitations to the conventional manual technique make this a difficult task. The primary challenge lies in the mobility of the prostate and surrounding soft tissues during the intervention. Both the insertion of the needles and the movement of the TRUS probe cause significant motion and deformation of the prostate [72] [73] [74] [75]. This motion is often easily noticeable in the intra-operative TRUS images and, from the experience of our partner clinicians at the CHUG, varies significantly depending on the patient. Since the dosimetry plan is typically based on the manual segmentation of only two sets of ultrasound images taken before the insertion of the needles (i.e. non-adaptive planning), the resultant accuracy of the seed placement is difficult to verify in real-time.

This accuracy is additionally affected by a number of other factors, including the random migration of the seeds upon their release within the prostate, the flexion of the needles upon insertion into the tissue and prostatic oedema during the intervention. Another important limitation to the technique is that needle insertion is restricted to the horizontal axes defined by the needle template.

Not only is needle placement limited to a grid of 5mm spacing, but perhaps more importantly, this parallel grid system does not allow access behind the pubic arch in the

relatively frequent case of the latter eclipsing parts of the prostate [76]. The maximum recommended prostate volume for brachytherapies is limited to 60 cc in part to reduce the risk of pubic arch interference as well as to reduce the chances of urinary toxicity [77] [78]. Larger prostates can be reduced in volume through pre-adjuvant hormone therapy. The stepper, probe and template unit can also be set up at an angle, in order to allow the needles to pass under and behind the pubic arch [79]. If pubic arch interference remains unavoidable or is only discovered after some seeds have already been inserted, then the needles can either be curved manually to reach behind the bone or the dose plan has to be adapted [76]. Severe pubic arch interference could potentially lead to the impossibility of applying a complete dose, requiring subsequent external radiation therapy.

These issues, among others, result in a lengthy and unavoidably repetitive procedure that relies heavily on the experience of the clinicians and physicists and that limits patient eligibility. They become even more important when considering the growing interest in focal diagnosis and therapy, where accurate needle placement is vital.

1.3 Summary

As we have seen in this chapter, percutaneous needle interventions are of great interest in both the diagnosis and the treatment of a variety of illnesses. A large number of techniques exist based on the organ or illness concerned as well as on the imaging modality used for guidance. Although often less challenging than open surgical approaches, their effectiveness usually relies highly on the accuracy, rapidity and ease in reaching a desired target along a predefined insertion path.

In percutaneous needle interventions, inaccurate targeting could result in inaccurate diagnosis or incomplete treatment, while inaccurately following the planned path could result in incidental damage on neighbouring vital structures. Both could lead to serious consequences, such as misdiagnosis, recurrence of the illness and the appearance of secondary effects.

Because of the minimally invasive nature of needle interventions, their rapidity is often an expected criteria of success as well. In IR procedures, for example, many images are usually required: a certain number to first align the needle with the desired trajectory, and subsequently, another set of repeat images to accurately reach the desired depth without over or under shooting the target. Reducing the number of images required would reduce the comings-and-goings of the radiologist between the patient and the control room, the number of breath-holds required by the patient, and consequentially would reduce the procedure time. In CT interventions, it would also decrease the radiation dose obtained by the patient.

The procedure time is often directly related to the ease of the operation. The easier it is to align the needle to the desired insertion path, the less time it takes. This is why, in both general IR and prostate procedures, needle insertions are most often done in the imaging plane. More complex trajectories that are out of the imaging plane or that require needle inclinations that are not adapted to the techniques and materials used, provide added challenges to clinicians. It is also difficult in conventional techniques to take into account the mobility of the tissues, requiring visual estimation of the motion (in particular for prostate interventions) and significant clinical experience.

In summary, to obtain accurate targeting requires the application of more challenging techniques that often increase the length of the procedure and can increase the uncertainty in obtaining the desired result. Robotic assistance could provide an effective solution for improving these aspects compared to the conventional techniques described in this first chapter. The next chapter describes more specifically how robotic systems can help improve percutaneous needle interventions and outlines the primary aspects governing their design and evaluation.

Chapter 2: Needle insertion robots

2.1 Thesis Context	20
2.2 Existing needle insertion robots	20
2.3 Particularities of needle insertion robots	24
<i>Medical imaging constraints</i>	24
<i>Needle constraints</i>	26
<i>Soft tissue constraints</i>	27
2.4 Robot-Image Calibration	28
2.5 Sources of Error	29
2.6 Validation and Testing	31
<i>Sterilization</i>	31
<i>Regulatory issues</i>	32
<i>Preclinical validation</i>	33
<i>Clinical validation</i>	33
2.7 Summary	34

The previous chapter introduced the different types of percutaneous needle procedures done on the thorax, abdomen and pelvis. Their clinical and technical benefits were presented along with the number of challenges they introduce for the physician primarily due to their reliance on medical images rather than direct visual guidance as is the case in open surgeries. This chapter describes how robotics and computer assistance can help improve the simplicity, efficacy, and ultimately the clinical benefit of these procedures.

Compared to conventional manual techniques, robotic assistance can help improve needle targeting accuracy and in consequence, potentially improve the quality of the treatment or diagnosis. If, in addition to the high accuracy attributed to robots, the manipulator were calibrated to the image space, it could eliminate the uncertainty of visually aligning the needle to the desired insertion path and depth. Targets could potentially be reached accurately with fewer re-introductions of the needle, in less time and much easier, hence improving patient and physician comfort and safety.

A calibrated robot could also provide more varied needle orientations with greater ease, giving the physician increased options for choosing more clinically viable but sometimes more complex insertion paths. Examples include needle directions that are out of the imaging plane in CT-guided IR procedures or angled needle insertions during prostate brachytherapy in order to avoid pubic arch interference.

Although robotic procedures may seem more complex than standard manual techniques, they can provide improved safety and working conditions for both the patient and the clinical staff. An example is replacing the radiologist's hand when holding the needle during real-time fluoroscopic imaging, reducing work-related exposure to radiation. Radiation exposure can also be reduced to the patient during CT-guided IR procedures by requiring fewer image acquisitions in order to reach a target compared to an equivalent manual insertion. In addition, because a robotic tool can be calibrated to the patient's medical image, more accurate needle control can be obtained especially in constrained, high risk insertions. In the case of MRI-guided interventions, robotics may be the only possible solution because of the difficult access to the patient's body within the deep imaging tunnel as well as the highly restrictive material constraints.

Although robotics can provide evident technical advantages over conventional manual needle insertions, the ultimate goal is to improve patient treatment or diagnosis as well as to increase patient eligibility, making these minimally invasive procedures available and efficient for a greater variety of patients and in an increased number of situations.

This chapter reviews the existing thoracic and abdomino-pelvic needle insertion robots found in the current literature, and describes the particularities of such robots and the distinct aspects that need to be considered in their design. Throughout this chapter, the work done in this thesis is placed into context of these design aspects.

2.1 Thesis Context

The TIMC-IMAG laboratory has been involved in image-guided needle insertion robots since 2004, with the development of two systems: the 3D US-guided PROSPER brachytherapy robot and the CT and MRI-guided Light Puncture Robot (LPR).

The PROSPER robot comes from work that has been done in the laboratory since 2006 on the development of a non-rigid 3D ultrasound prostate registration algorithm in the context of prostate biopsies [80] [81] [82] [83]. The method is a fully automatic intensity-based approach and has been successfully incorporated into a prostate biopsy workstation (the Urostation, developed and marketed by Koelis SAS, <http://www.koelis.com/>), currently used worldwide for the computation of 3-D maps of prostate biopsies in presence of organ motion and deformation.

It was identified with the incentive of the cooperating clinical team at the CHUG, that this method of organ motion tracking, combined with a needle insertion robot, could provide significant benefit during prostate brachytherapy procedures. It could improve the accuracy of dose distribution inside the prostate by taking into account the gland's deformations during needle insertion. The project was called PROSPER, for PROState transPERineal interventions.

Work on the LPR robot was begun a few years earlier [84] [85] [86]. Its purpose was to simplify and improve the accuracy of CT and MRI-guided interventional radiology procedures. The initial LPR design consisted of a patient-mounted needle insertion module stretched from a bed-mounted frame between four straps. The straps were pulled individually by special pneumatically activated sprocket wheel actuators to control the needle position.

The primary goal of the LPR was to increase the scope of percutaneous interventions available to clinicians by 1) increasing needle insertion accuracy by allowing accurate location of needle position and inclination in the images, combined with progressive needle insertion, 2) allowing more complex 3DOF approach angles (between the ribs or deep insertions, for example), 3) reducing the number of image acquisitions required (and hence decreasing radiation doses in CT), 4) improving intervention efficiency, and 5) offering the possibility of MR-guided interventions (for example for patients with certain contraindications to CT contrast agents, or for better visualization of equal-density tumors, etc.).

Animal testing, reported in [86], showed the feasibility and accuracy of the LPR in a CT-guided environment. However, a number of limitations were revealed to the design that jeopardized its potential clinical value. It was decided, therefore, that a new pre-clinical prototype iteration was necessary to improve on these issues.

The work described in this thesis involved the development, testing and initial pre-clinical validation of these two systems.

2.2 Existing needle insertion robots

Over the last two decades, a large number of image-guided robotic needle insertion systems have been described in the literature. Table 2-1 presents an extensive list of these

systems, focusing primarily on US, CT and MRI-guided robots with clinical applications limited to thoracic and abdomino-pelvic regions.

Looking at the table, a number of observations can be made. Firstly, from a purely technical point of view, a huge diversity of manipulator designs exists, with degrees of freedom (DOF) ranging from 2 all the way to 16 for the most complex systems. Only recently have a few of these systems reached the clinical testing stage; the majority are still in the phantom validation stages. This is likely because regulations for medical devices have become progressively more and more stringent worldwide. Many research institutions are likely not prepared for the rigorous, time consuming and potentially expensive organization required in the design and validation stages in order to pass certification standards [87] [88].

Since medical robotics implies the automation of manual gestures, their level of risk towards patient safety is obviously an important issue. For this reason, many systems listed in the table position a manual needle guide instead of inserting the needle robotically. This way they bypass the inherent risk of automated needle insertion and potentially simplify the certification of the robot. Some other reasons for using manual needle insertion include design simplification and preserving the clinician's haptic feedback during the needle insertion.

Looking at the thoracic and abdominal robots, the majority are mounted to the imaging table rather than to the patient's body. Again, this could be attributed to design simplification, however, table-mounted robots are exposed to a higher risk of being affected by patient motion and need to rely either on full anaesthesia of the patient or on some sort of navigation solution in order to track patient motion.

Looking now at the prostate robots, we can see that the majority are intended for MRI-guidance. This can likely be explained by the modality's attractive potential to improve prostate cancer detection, but all the while imposing technical constraints (notably space and material compatibility constraints) that make it difficult to operate manually.

Regardless of the clinical application, it is evident, simply from the amount of research being done, that robotic needle insertion systems are of considerable interest to the medical community. It is interesting therefore to describe the distinguishing features that differentiate them from typical robotic manipulators, including what are considered as "standard" medical robots (i.e. laparoscopic robots, such as the da Vinci).

As mentioned above, existing needle manipulator designs vary enormously. A large variety of DOFs exists; designs are based on varying combinations of prismatic or revolute joints; a number of designs use remote centre of motion (RCM) architectures; some use haptic feedback during needle insertion; actuators vary from common micro-motors to custom designed pneumatic motors to specialized ultrasonic (piezo) motors; and of course the clinical applications are widespread.

Notwithstanding, in the diverse field of robotics, needle insertion robots could very well be classified in their own category. Despite the assortment of manipulator designs, all these systems have a number of key aspects in common that impose certain specific design constraints that are not necessarily present in other robotic applications.

Table 2-1: List of percutaneous needle insertion robots published in the literature, classified under either prostate or thoracic and abdominal interventions. The imaging modalities used to guide the robots are colour-coded for easier visualization. The project status is either clinical patient tests (C), live animal tests (A) or phantom tests (P). The precision and needle depth values in parentheses are values that are not specifically stated in the publications but are rather estimates taken from images or textual hints. US motor stands for ultrasonic motor.

Institution	Project Name	Status	Imaging Modality	Actuation Technology	Robot Position	DOF	Reported Accuracy				References
							Accuracy (mm)	Needle Depth (cm)	Test Medium	Insertion Type	
PROSTATE INTERVENTIONS:											
Johns Hopkins University	APT	C	MRI	US motor	Transrectal	2	1.3	(10-50)	Patient	Manual	[89] [90] [91] [92] [93] [94] [95]
Radboud University	-	C	MRI	Pneumatic	Transrectal	5	3	-	Agar phantom	Manual	[96] [97] [98]
Imperial College	-	P	MRI	US motor	Transrectal	5	2.3	(10-40)	PVC phantom	Robotic	[99] [100]
Johns Hopkins University	-	A	MRI	Motor	Transrectal	3	-	-	-	-	[101]
AIST Tsukuba	-	P	MRI	US motor	Transperineal	5	1.2	90	PVC phantom	Manual	[102] [103] [104]
UMC Utrecht	UMCU Robot	C	MRI	Pneumatic	Transperineal	5	-	-	-	Robotic	[105]
Johns Hopkins University / Queens University	-	P	MRI	Pneumatic	Transperineal	6	2.5	(30-80)	PVC phantom	Manual	[106] [107] [108] [109] [110] [111] [112] [113]
University of Toronto	MRI-P	P	MRI	US motor	Transperineal	6	< 2	-	Gelatin phantom	Robotic	[114]
Robarts Research Institute	-	C	MRI	Manual	Transperineal	5	2.1	85	Alginate phantom	Manual	[115] [116]
Worcester Polytechnic Institute	-	P	MRI	US motor	Transperineal	6	1.25	-	Gelatin phantom	Robotic	[117] [118] [119] [120]
LSHT (ICUBE)	MRGuide	P	MRI	Cable-driven	Transperineal	-	-	-	-	Manual	[121] [122]
Harvard Medical School	Smart Template	P	MRI	US motor	Transperineal	2	-	-	-	-	[123]
Johns Hopkins University	MRBot	A	MRI / CT	Pneumatic	Transperineal	5	< 3	-	Gelatin phantom	Robotic	[124] [125] [126] [127]
Singapore General Hospital	BioXBot	C	US	Micro motor	Transperineal	5	< 1	(40-70)	Gelatin phantom	Robotic	[128] [129]
Singapore General Hospital	-	C	US	Manual	Transperineal	9	< 2.5	-	Patient	Manual	[130]

Robarts Research Institute	-	P	US	Manual / Micro motor	Transperineal	2	< 1.6	60-100	Agar phantom	Manual	[131]
University of Western Ontario	-	P	US	Micro motor	Transperineal	5	1.45	76	Agar phantom	Robotic	[132]
Imperial College	-	P	US	Micro motor	Transperineal	4	-	-	-	Robotic	[133]
Thomas Jefferson University	Euclidean	P	US	Micro motor	Transperineal	16	0.69	-	PVC phantom	Robotic	[134] [135] [136] [137]
Thomas Jefferson University	-	P	US	Micro motor	Transperineal	-	-	-	-	Robotic	[138]
University of British Columbia	Brachyguide	P	US	Micro motor	Transperineal	4	1.2	(30-80)	CIRS phantom	Manual	[139]

THORACIC & ABDOMINAL INTERVENTIONS:

Johns Hopkins University	B-ROB / iSYS	C	US / CT	Motor	Table-mounted	4	1.1	85	Foam phantom	Manual	[140] [141] [142] [143] [144] [145]
Johns Hopkins University	PAKY / RCM / AcuBot	C	CT / US / Fluor.	Motor	Table-mounted	6	1.2	-	Agar phantom	Robotic	[146] [147] [148] [149] [150] [151] [152] [153] [154]
University of Freiburg	-	P	CT	Motor	Table-mounted	2	1.6	75	In vitro pig organs	Manual	[155]
Innomedic	Innomotion	C	MRI / CT	Pneumatic	Table-mounted	5	1	(40-70)	In vivo pig	Manual	[156] [157] [158] [159] [160]
KIOS Research Center	-	P	MRI	Manual	Table-mounted	6	< 5	-40	Butter phantom	Manual	[161]
Washington University	-	P	MRI	US motor	Table-mounted	7	-	-	-	Manual	[162] [163] [164] [165]
Worcester Polytechnic Institute	-	P	MRI	US motor	Table-mounted	6	-	-	-	Manual	[166] [167] [168]
LSIIT (ICUBE)	CT-Bot	A	CT	US motor	Patient-mounted	5	< 5	65	Artificial phantom	Manual	[169] [170] [171] [172] [173]
MIT	Robopsy	A	CT / MRI	Motor / US Motor	Patient-mounted	3	(< 20)	-80	In vivo pig	Robotic	[174] [175] [176]
TIMC Laboratory	LPR	A	CT / MRI	Pneumatic	Patient-mounted	5	< 2mm	100	Foam phantom	Robotic	[177] [86] [85]

2.3 Particularities of needle insertion robots

The design of needle insertion robots is constrained by the medical imagers that they rely on for guidance, the needles that they insert, and the soft tissues with which they interact. The following sub-sections describe these constraints in further detail.

Medical imaging constraints

Needle insertion robots are necessarily controlled by medical-image-based feedback. Since needles are used to target internal organs and lesions, direct visual-based control cannot be used. This creates specific constraints on a number of design aspects.

One of the more crucial constraints is the compatibility of the system with the imaging modality. Since the manipulator holds the needle, it is more than likely to be within range of the images being taken. This, of course, means that no part of the robot must affect the clinical validity of the image upon which the success of the procedure is based. In other words, the robot must not create any undesirable image artifacts that could distort, hide or blur the image.

Table 2-2: List of common artifacts seen in US, CT and MR images [246] [9] [248] [239], focusing primarily on artifacts that could be caused by the presence of a medical device in the image.

Modality	Artifact	Design Constraints
US	Acoustic shadow artifacts <ul style="list-style-type: none"> - Highly attenuating materials cause loss of signal distally. 	- Avoid placing any hard objects in the image.
	Far field spatial resolution deterioration <ul style="list-style-type: none"> - Progressive scattering of signal with increasing depth. 	- Place robot workspace as close to the US transducer as possible. - Use shallower imaging depths.
	Non-uniform beam width <ul style="list-style-type: none"> - Objects assumed to be located along the central beam line are in fact offset. 	- Use low gain. - Take care interpreting needle tips in images.
	Speed of sound distortion <ul style="list-style-type: none"> - Distortion caused by differences in speed of sound. 	- Use materials close to the standard speed of sound of tissue (1540 m/s), during calibration for example.
	Reverberation artifacts <ul style="list-style-type: none"> - Repeated echoes between two reflective surfaces. 	- Take care interpreting images of hollow needles (during calibration in water bath for example).
CT	Streaking artifacts <ul style="list-style-type: none"> - Beam hardening variations in highly heterogeneous cross-sections. 	- Avoid high-density (metallic) materials.
	Aliasing artifacts <ul style="list-style-type: none"> - Under-sampling of sharp structures when imaging with large projection intervals. 	- Avoid sharp corners.
MRI	Magnetic susceptibility artifacts <ul style="list-style-type: none"> - Magnetic structures contribute to and distort the main field. 	- Avoid using ferromagnetic (metallic) materials.
	Eddy current artifacts <ul style="list-style-type: none"> - Changes in the magnetic field during imaging create electrical currents in conductive materials. 	- Avoid using conductive materials. - Avoid creating closed loops with conductive materials.
	Chemical shift artifacts <ul style="list-style-type: none"> - Protons with different resonant frequencies cause spatial misregistration in the frequency encoding direction. 	- Take care choosing calibration fiducials
General	Motion artifacts <ul style="list-style-type: none"> - Movement of the patient can cause blurring, smearing and ghosting artifacts. 	- Use gating or breath hold techniques during acquisition. - Appropriate patient fixation. - Reduce image acquisition time.

Table 2-2 lists some of the most common artifacts seen in US, CT and MR imaging, along with the design constraints that they impose.

In US imaging, the only critical device design constraint is not to place any hard object in the field of view that would cause an ultrasound barrier. Otherwise, the various other artifacts primarily result in potential misinterpretation of the images which could cause accuracy issues during calibration or during actual use of the device. In CT and MR imaging, constraints can be summarized essentially into material and shape constraints, with high density, ferromagnetic and conductive materials being typically incompatible.

For MRI-guided robots, the constraints are much greater than in the other imaging modalities because they apply not only to objects within the imaging FOV, but also in the surrounding proximity of the imager. The effect of medical devices on the signal-to-noise ratio (SNR) of the MR image must therefore be verified, as described by the NEMA Standards Publication MS 1-2008 [178].

In addition to image compatibility, the MRI environment also requires specific safety precautions to be taken in order not to harm the patient and staff or damage equipment. Non-magnetic materials must not be used to prevent projectile damage, and conductive materials must be carefully studied to prevent radiofrequency-induced heating [179]. A number of ASTM standards exist for measuring the force, torque and heating induced by the MR scanner on a medical device [180].

These imaging and safety constraints make actuator compatibility an important aspect for MRI-guided robots [181]. Actuators must not induce any electromagnetic fields and must not have any ferromagnetic wiring. Standard motors are therefore incompatible and specialized solutions must be considered. These include ultrasonic motors, pneumatic actuators or remote actuation, as shown in Figure 2-1. Ultrasonic motors use vibrating piezoelectric elements to advance a rotor or slider. They have high torque, low speeds and are not backdriveable. They are MRI-compatible when not powered. When powered, however, they have been found to negatively affect the SNR of images [182] and therefore must be used judiciously. Pneumatic actuators use pressurized air to create motion. Solutions range from custom pneumatic rotary motors [127] [86] to controllable pneumatic piston-cylinders [159] [106]. Air pressure can be obtained from either a compressor, a medical gas cylinder or directly from the hospital's compressed air network. Remote actuation requires the use of transmission elements to distance the actuators from the imaging site. Examples include Bowden cable systems [121] and drive shafts [101].

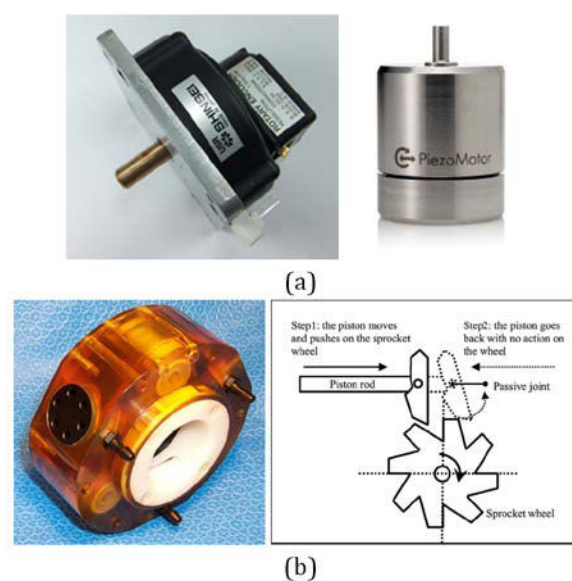


Figure 2-1: Examples of actuators typically used in MRI-guided robots: a) ultrasonic motors (Shinsei [251], Piezomotor [252]), b) pneumatic actuators (PneuStep [250], Pneumatic ratchet [167]).

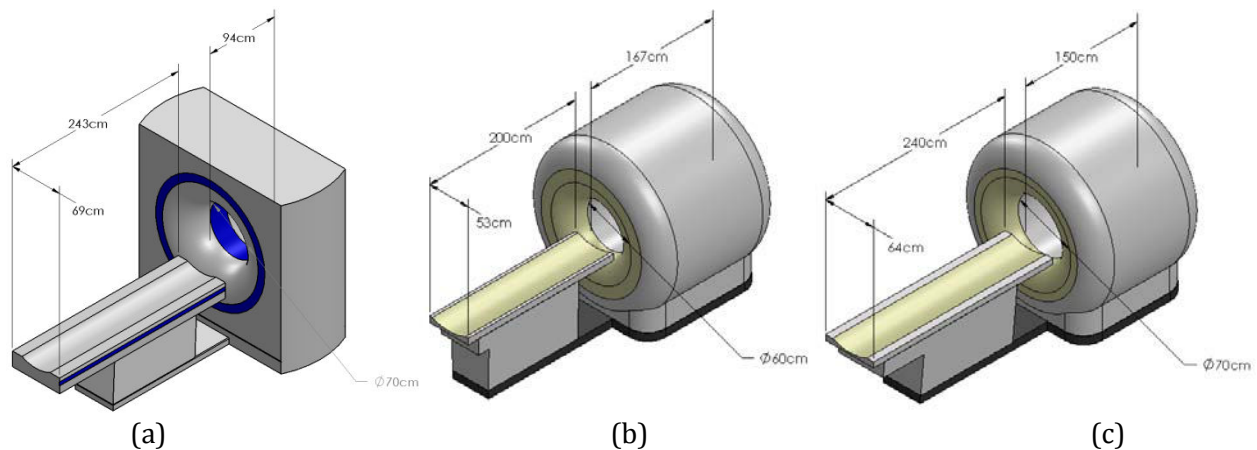


Figure 2-2: a) Siemens Somatom Sensation 16 CT scanner, b) Philips Achieva 3.0T MRI scanner and c) Philips Ingenia 1.5T wide-bore MRI scanner dimensions.

For CT and MRI-guided devices, another design aspect to consider is workspace compatibility. The devices must fit within the constrained space of the scanner bore, the best part of which is already occupied by the patient. Figure 2-2 shows typical CT and MRI scanner bore dimensions. Compact designs that do not take up more vertical space than the needles they manipulate are therefore necessary.

Needle constraints

In addition to their reliance on medical imaging, a number of constraints arise specifically from working with needles. Manipulator workspace can be kept relatively small firstly because needle depths are rarely greater than 15 to 20 cm and secondly because needle approach angles and paths for the many procedures tend to be well defined or at least well planned in advance. This allows the physician to place the robot very near the insertion point before activating it. Needle insertions are also relatively low force procedures, with puncture forces typically remaining well below 20N [183], meaning that architectures can be kept fairly minimalistic. Furthermore, as needle insertions can be done in close vicinity to bone structures (such as the pubic arch, ribs or the spine), robotic systems must take into account some form of force feedback in order to react in case of bone contact and thus prevent injury to the patient.

All needle insertion procedures can be decomposed into two phases of motion: a positioning phase and an insertion phase. During the positioning phase, the needle is aligned with the planned insertion point and direction outside of the patient. This requires five DOFs: three to position the needle tip at the patient's skin and two to orient the needle shaft towards the internal target. Some of the existing robot solutions automate only the positioning phase (see *Insertion Type* column in Table 2-1, page 22), others only the two orientation DOFs [174] [176].

The insertion phase inserts the needle either in one pass or in several incremental passes until the planned target is reached, requiring only one DOF. A second DOF can be added in the form of rotation about the needle axis in an attempt to decrease needle-tissue interaction forces or to perform needle steering [136] [132] [114]. Other DOFs in the insertion phase include needle gripping/releasing and post-insertion DOFs, such as seed insertion in brachytherapy [133] [136] [132] [125].

The method of holding the needle can vary depending on whether the robot is used as a needle guide or for automated insertion. Needle guides can be disposable or reusable sterile components that can be clipped onto the robot end effector [131] [141] [157]. Their advantages include ease of sterilization, lighter architectures and full clinician control during insertion. In contrast, robots with automated needle insertion have the benefit of being able to precisely control the insertion depth, to apply specific insertion schemes (needle rotation, variable speed,

Table 2-3: List of the four main solutions for reducing tissue deformation, needle insertion force and needle bending as proposed in the literature. Down arrows refer to the solution reducing tissue deformation. Up arrows refer to the solution increasing tissue deformation. A cross means the solution had no effect. The in vitro column lists results on dead human or animal tissue. The artificial column lists results on synthetic phantoms.

Solution	In Vivo	In Vitro	Artificial
Increase insertion speed	-	↓ [244]	↑ [197]
		↓ [240]	↑ [218]
			↑ [217]
			↑ [231]
Increase rotation speed	-	↓ [244]	↓ [218]
			↓ [217]
			↓ [231]
Impulse insertion	-	↓ [239]	↓ [235]
Anchoring the tissue	↑ [74] × [73]	-	↑ [74]

tapping, etc.) and to hold the needle in place without requiring the clinician to move back and forth between the images and the patient. For such systems, automated needle grips are often used. Grips vary from finger-type grips [86], roller-based friction grips [146] [174] and clutch-based grips [172]. Other systems, instead of gripping the needle body, push the needle from behind [135] [105]. This strategy is used when the needles have an inner stylet that needs to be pushed as well, such as in prostate brachytherapy. Regardless of the insertion technique, sterilization aspects are particularly important in these insertion modules, as well as ease of needle installation/release. Automated insertion modules also need to consider unwanted needle bending, accidental needle slip and the consequences of potential bone contact.

Soft tissue constraints

The interaction of needles with the tissue they traverse during the insertion phase gives rise to a number of very challenging constraints. Tissue deformation and needle bending are perhaps the more important of these. As a needle traverses soft tissue, the former tends to bend depending on its tip shape and the tissue's structure while the latter tends to deform and shift in the direction of insertion. This results in inaccuracies between the needle tip and the planned target that are difficult for robotic systems to automatically take into consideration. The prostate is a classic example of this because of its small but compact size that is very prone to needle-induced motion [74] [72] [73] [184] [185] [186].

Two approaches exist to handle tissue deformation. The first involves actually reducing the deformation during insertion. Potential solutions include controlling the insertion speed, rotating the needle, applying impulses to the needle and holding the organ with anchor needles. The first three solutions ultimately aim at reducing the needle insertion force while the last attempts to counteract the insertion force. Table 2-3 lists the references found in the literature that investigate these four solutions. From this table we can see that there is a consensus in artificial tissue that decreasing insertion speed reduces the needle's effect on the tissue. The opposite, however, seems to be the case in in vitro tissue. Although there are not enough results to be conclusive, increasing needle rotation and using high speed impulse insertion seems to be promising in both artificial and in vitro tissues. Controversy remains as to whether the benefits of rotating the needle or anchoring the tissue with extra needles are sufficient to justify the potential added trauma sustained by the tissue. A consensus has not yet been reached mainly because of the difficulty in testing these aspects in vivo.

The second approach to dealing with tissue deformation involves tissue deformation estimation. Proposed solutions involve either pre-insertion modeling to determine the ideal insertion trajectory or post-insertion image registration to evaluate the targeting error. These

are entire research domains of their own and a large amount of work exists in the literature. In general, pre-insertion simulations are based on mass-spring or finite-element models while post-insertion registration is either feature or intensity-based. Very complete reviews of the state of the art in these topics can be found in [187], [188] and [82]. A related topic is needle steering as it involves the modeling of needle behaviour in the tissue. This technique makes use of either the conventional bevel tip of certain needles or some means of bending the needle (such as heat-deformable elements or a steerable tip) in order to steer the needle through the tissue to the target. This subject remains still a conceptual idea as the exact behaviour of a thin needle in heterogeneous real tissue is very difficult to predict [189].

The design of the PROSPER and LPR systems took into consideration the majority of the imaging, needle and soft tissue constraints described in this section. The PROSPER system functions in conjunction with a 3D ultrasound probe. The manipulator's positioning module was therefore designed so as to provide a large workspace within which to place the needle without interfering with the probe. The manipulator uses five motorized DOFs to position the needle in front of the patient's perineum. Two further DOFs are used to insert the needle and rotate it around its axis. Because brachytherapy needles consist of a cannula and stylet, the insertion module pushes the needle instead of grasping it. One of the major contributions of the PROSPER system with respect to the other similar existing systems, is its ability to track prostate motion and deformation using the ultrasound registration technique described in section 2.1 (page 20). The insertion module is also able to control the insertion and needle rotation speeds in an attempt to reduce tissue deformation.

For the LPR robot, material compatibility with both CT and MRI imaging modalities was important, resulting in a non-ferromagnetic robotic manipulator controlled by remote ultrasonic actuators and that consequently does not affect image quality. The manipulator was designed to enter into the imaging tunnel, so workspace constraints were also very important. In addition, it was designed to be mounted directly onto the patient to allow it to follow the patient's movements during the procedure. Four DOFs are used to position and orient the needle above the patient's skin, while a fifth DOF allows the needle to be inserted. It was decided to automate the needle insertion, instead of using a needle guide, in order to allow the patient to remain in the imaging tunnel during the entire procedure. A pneumatic-actuated finger-type grip solution was used so as to grasp and release the needle rapidly, while providing sufficient force to prevent needle slip. Two grips were used to allow incremental insertions, as is conventionally done in CT and MRI-guided procedures.

2.4 Robot-Image Calibration

To be able to reach targets in medical images, robotic systems must be localized within these images. In other words, the robot's reference frame must be calibrated to that of the images being used. This is done by registering a cloud of points in image space with the same cloud of points in robot space. Depending on the imaging modality, this can be done either one-time pre-operatively or intra-operatively.

Pre-operative calibration requires that the imaging modality and the robot be fixed together or tracked with some form of navigation system in order to conserve the calibration until its use in the operating room. This is typically done for US-guided robots, since the US probe is small and near enough to the manipulator to allow for this pairing. The standard technique involves locating a known and tracked calibration phantom (typically wire phantoms) [190] or inserting and segmenting needles inside a water bath. Incidentally, the latter is the same technique as used to calibrate the conventional stepper/template combination to the TRUS image for brachytherapy procedures. Table 2-4 lists some of the advantages and disadvantages of these two calibration methods. A good review of the various publications describing these techniques can be found in [191]. The PROSPER system uses such a pre-operative calibration, the US probe being rigidly fixed to the manipulator.

Table 2-4: Advantages and disadvantages of the main pre-operative image-to-robot calibration techniques.

Calibration Technique	Advantages	Disadvantages
Pre-operative phantom-based calibration	<ul style="list-style-type: none"> - Possible to automate - Easy to segment phantom in image - Fast - Good accuracy 	<ul style="list-style-type: none"> - Requires tracking system - Requires accurate phantom - Speed of sound in water is different from tissue - Requires vertical bench which could affect the robot's kinematics due to gravity
Pre-operative needle-based calibration	<ul style="list-style-type: none"> - Simple - Does not require special material - 3 needles are enough to solve the calibration 	<ul style="list-style-type: none"> - Difficult to automate - Needle tip difficult to segment - Appropriate distribution of needles required - Large number of needles required for high accuracy - Speed of sound of water - Requires vertical bench

Intra-operative calibration is most commonly used in CT and MRI-guided systems. The calibration routine consists in segmenting and registering a special fiducial of known geometry mounted to the robot within the imager's field of view. Similar to the wire phantoms used in US calibrations or to stereotaxic frames used in neurosurgery, numerous fiducial shapes have been proposed. The main geometrical constraint is that the fiducial must be asymmetrical in at least two dimensions to allow spatial and directional registration. Fiducial materials vary, however some examples include metal wire stereotactic frames [150] [169] or the even the needle itself [155] in CT, and gadolinium enhanced liquids in MRI [192] [158] [161]. Some fiducials are mounted to the base of the robot for space and weight reasons [169], however the position and orientation of the needle in the image then relies on the kinematics of the robot and cannot be verified directly from the fiducials. For this reason, most robots include fiducials mounted instead to the end effector such that their reliance on the manipulator's kinematics is minimized, hence reducing the potential for accumulating errors [150] [124] [125] [161]. The LPR system relies on two fiducials embedded into its needle insertion module, allowing the needle position and orientation to be automatically determined in the CT or MRI images.

2.5 Sources of Error

The accuracy of image-guided needle puncture robots is affected by a number of errors, many of which are inherent to their reliance on medical imaging. It is therefore important to identify these sources of error and take measures to minimize them. A list of the primary errors is shown in Table 2-5.

Regardless of the technique used, the image-to-robot calibrations described in the previous section ultimately define a robotic system's accuracy in reaching a target inside the body. The most important source of calibration error comes from the segmentation and localization of the fiducial or needles in the image. The quality of the segmentation is naturally dependent on the resolution of the image and the contrast of the fiducial. The higher the image resolution and of course the higher the fiducial's contrast, the easier and more accurate the segmentation. An example situation in which this may be especially problematic is in US calibration techniques where the image resolution and contrast degrades with depth. Another example is in CT where higher resolution results in an increase in the radiation dose received by the patient. In MRI, this can translate to significantly increased acquisition times. Another important segmentation error when using needle-based calibration can come from needle tip blurring in US and CT images making it difficult to find the true needle tip.

Table 2-5: List of the main sources of error during image-to-robot calibration.

Error type	Sources	Solutions
CALIBRATION ERRORS:		
Segmentation errors	<ul style="list-style-type: none"> - Image resolution - Fiducial resolution and contrast - Fiducial distribution 	<ul style="list-style-type: none"> → Use high resolution → Use high contrast fiducial → Distribute fiducials over large area
Registration errors	<ul style="list-style-type: none"> - Linear vs. numerical least-squares 	<ul style="list-style-type: none"> → Choose appropriate mathematical approach
Image artifact errors	<ul style="list-style-type: none"> - Speed of sound in US - Shift artifact in MRI 	<ul style="list-style-type: none"> → Calibrate speed of sound → Choose appropriate fiducial material
Robot kinematic errors	<ul style="list-style-type: none"> - Motor accuracy and resolution - Link geometry - Joint parallelism 	<ul style="list-style-type: none"> → Calibrate robot kinematics
Other calibration errors	<ul style="list-style-type: none"> - Gravitational effects - Needle bending - Tracker error 	<ul style="list-style-type: none"> → Calibrate in same configuration as during use → Use stiff needle and low resistance phantom → Use a tracker-less solution
INSERTION ERRORS:		
Target selection error	<ul style="list-style-type: none"> - Image resolution - Target contrast 	<ul style="list-style-type: none"> → Use high resolution → Use appropriate imaging modality or contrast agent
Needle bending error	<ul style="list-style-type: none"> - Needle tip - Needle diameter - Insertion depth - Tissue type 	<ul style="list-style-type: none"> → Use appropriate needle type for given tissue
Target motion error	<ul style="list-style-type: none"> - Tissue deformation 	<ul style="list-style-type: none"> → Compensate with biomechanics or registration

Another set of calibration errors comes from image artifacts. These are related to segmentation errors since they cause inaccuracies in the point cloud constructed in image space. An important example of this is in the commonly used water-based US calibration, where the speed of sound of water does not match the speed assumed by the US machine, causing distortion of the segmented point cloud [193]. This can also be the case in MRI if a fiducial is used that is affected by the chemical shift artifact [194].

Robot kinematic errors affect the accurate positioning of the robot in Cartesian space. During calibration this affects the distribution of the point cloud in robot space. These errors can come from inaccuracies in the motor and/or position sensors (i.e. resolution or linearity errors), inaccuracies in the geometric representation of the linkages (due to mismatching of the desired CAD model of the robot and the true machined parts), and inaccuracies in the joint bearings (bearing play, parallelism). Other related errors include manipulator deformation due to gravity when calibrating vertically in a water bath, or needle bending in US needle-based calibrations.

A final source of calibration error is registration error, which has two aspects: one is the imperfect matching of the source (robot kinematics) and target (image segmentation) point clouds, resulting from the above-mentioned segmentation inaccuracies. The other comes from the numerical least-squares method used to solve the registration problem and depends on 1) the initial guess used to start the process, 2) the number of iterations used and 3) the step size used between each iteration.

In addition to calibration errors, a number of other errors are present during the intervention. A target segmentation error naturally exists since the selection of the exact centre of the desired target depends on image resolution and target segmentation accuracy. As described in section 1.2.3 (page 17), during insertion, needle bending and target motion due to tissue deformation are also major sources of error.

Concrete examples of most of these sources of error will be seen in Chapter 3 and Chapter 4 in the context of the two systems developed during this thesis.

2.6 Validation and Testing

Needle insertion robots can be classified as Class IIb (according to the European Council Directive) or Class II (according to the US Food and Drug Administration (FDA) regulations) medical devices. They are invasive devices of medium risk that are used for a short duration only (typically less than 60 minutes). They are normally used in an open, non-sterile environment, such as a CT or MRI scanner room, or an US examination room. Brachytherapy robots are an exception and must be used in a sterile, controlled operating room environment because of the large number of needle insertions required, the increased risk of bleeding and therefore infection, and the dangerous nature of the radioactive seeds being handled. All such robots, however, whether used inside or outside of the OR, necessarily contain at least a limited sterile zone around the needle and therefore need to be handled by a sterile user.

Sterilization

Although not at all specific to needle insertion robots, sterilization is a vital design issue that could make or break the clinical viability of a design. It is therefore an essential aspect to incorporate into any medical robot design right from the onset. The general concept behind sterilization is to prevent transferring unwanted external contamination into the patient's body, in particular through the operating site. For percutaneous needle insertions, this translates to preventing any sort of external contamination of the needle. This means that any device or person directly in contact with the needle, must also be sterile.

Regulation-wise, there are no specific sterilization rules depending on the type of intervention. It is generally up to the manufacturer of a device or interventional technique to define the required steps and procedures to follow in order to minimize the risk of contamination to a maximum. During any percutaneous procedure, a sterile working zone is typically defined all around the needle insertion zone, including all areas in which the clinician needs to work in, so as to prevent any risk of accidentally touching a non-sterile area. Because the manipulation of a needle requires steady hand motions, the clinician often needs space around the needle in order to lean on the patient or to hold the needle with different arm positions. This means that a needle insertion robot, as it is directly in the working zone of the needle, must be either entirely sterilized or protected in some way or another in order to allow the clinician full freedom of motion with no risk of contamination.

If a robot cannot be sterilized entirely, solutions include partial sterilization of only the parts that are in direct contact with the needle and using replaceable sterile housing and/or draping for the rest of the robot. Some reasons that could lead to the impossibility of entire system sterilization are: size constraints, material fragility, mobile joint vulnerability and the presence of electronic equipment (sensors and actuators) in the sterile zone. It is therefore essential that a sterilization technique be chosen as of the first brainstorming sessions and that the design be adapted to comply with the typically harsh sterilization conditions. Partial sterilization is used in the PROSPER system because of its numerous vulnerable joints. In contrast, the LPR manipulator is completely sterilized because the needle is entirely contained within the robot architecture and the risk of the radiologist brushing against it is high.

The two main sterilization techniques used at the CHUG are autoclave steam sterilization and hydrogen peroxide plasma sterilization. Steam sterilization involves exposing the device to pressure, heat and humidity. The exact autoclave conditions used at the CHUG are 134 °C at 2.05 bars of pressure for 18 minutes. The entire cycle is of course longer, as it requires time for pressurization and depressurization. So the total time of exposure to water and heat is significant. Directly exposed electronics are evidently incompatible with this type of sterilization and seals and mobile joints must be carefully designed or regularly replaced in order to prevent their rapid degradation. The advantages of this sterilization technique, however, are its widespread use in essentially all hospitals worldwide, fairly low cost, its ability to sterilize bulk quantities of devices, and its large chamber size (see Figure 2-3a).

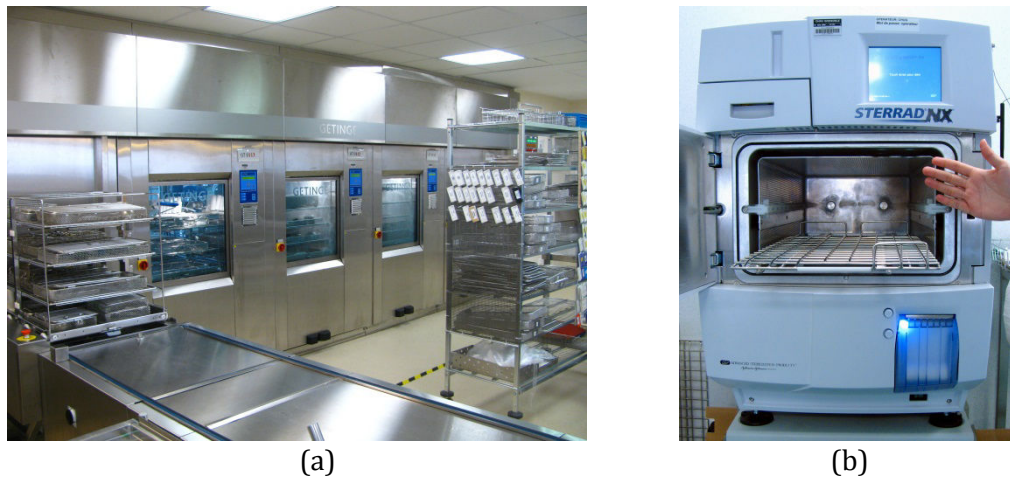


Figure 2-3: (a) Automated steam sterilization line at the CHUG. (b) STERRAD NX hydrogen peroxide plasma sterilization chamber.

The specific hydrogen peroxide plasma sterilization technique used at the CHUG is commercially known as STERRAD (Advanced Sterilization Products, Johnson & Johnson, Irvine, CA) and is a low-temperature, moisture-less method (see Figure 2-3b). It uses hydrogen peroxide condensation and gas plasma oxidation to kill microorganisms. The standard STERRAD NX cycle involves a 38 minute cycle time, with temperatures not exceeding 55°C and pressures ranging from vacuum to atmospheric pressure. It is commonly used for medical electronic equipment, batteries, endoscopes and other fragile equipment requiring low temperatures. Its two primary disadvantages are the fairly small size of the sterilization chamber (312 x 157 x 600 mm) and the difficulty of gas diffusion into tightly constrained spaces, such as long (> 850 mm), fine (< 1 mm Ø) lumens. This technique is used to sterilize the LPR manipulator.

Other important aspects to keep in mind during sterilization design are: 1) the device should fit into a sterilization basket that would be used to transport it throughout the various sterilization steps, 2) the device needs to be simple enough and solid enough to be disassembled and handled by sterilization staff who do not necessarily have expert knowledge of the device, 3) the device needs to be ideally machine or otherwise hand-cleanable and dried before sterilization to get rid of visible contamination, 4) the device needs to be able to withstand disinfection products applied immediately after each intervention. These aspects are not necessarily blocking points and can be looked into in the clinical prototype design stage.

Regulatory issues

The three major risks attributed to needle insertion robots are: 1) infection through the needle, 2) undesired puncture of critical anatomy, such as a blood vessel or a nerve bundle and 3) external injury to the patient or clinical staff due to the automated motion or due to electrocution. Robotic systems must therefore be designed in such a way as to reduce these risks to a minimum, while keeping in mind alternative solutions in case of failure. In Europe, the essential requirements for the clinical use of such devices are outlined in the 2007/47/EC European Directives and numerous technical regulations exist to meet these requirements in the form of harmonized standards, such as the IEC 60601 standards for medical electrical equipment or the EN 556-1 standards for the sterilization of medical devices. These standards can be used as guidelines for developing a robot that is safe for human use.

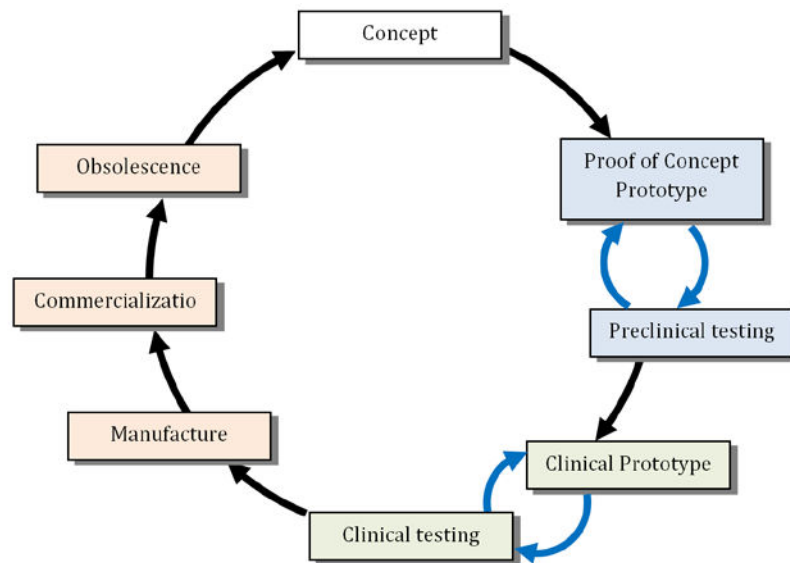


Figure 2-4: Medical device development life cycle (adapted from [187]).

Preclinical validation

An entirely separate aspect in the development of needle robots is validating the potential clinical benefit that they will provide to patients and clinical staff. For this, the common medical device development life cycle described in [195] and [196], and illustrated in Figure 2-4, is essential in order to determine and demonstrate the clinical advantage that they can provide. The two parts of the cycle that allow this to be accomplished are the preclinical and clinical testing stages.

Preclinical tests are used to validate the initial idea using proof-of-concept prototypes and test benches. For needle insertion robots, this typically involves simplified models of the robot, basic user interfaces and a number of laboratory tests. Tests pretty much unanimously first involve phantom testing. Phantoms are artificial models of the working environment, in particular of the targeted soft tissue environment. They are typically used to evaluate the intrinsic accuracy of the system. To include more realistic constraints, such as inhomogeneous tissue properties, needle bending, etc., testing is often also done on meat samples. The next logical testing step is to include live patient constraints, which can be simulated on live animals. In abdomino-thoracic IR applications, this is often done on pigs [86] [174] [197], which have somewhat similar internal organ structure to humans. In prostate applications, dogs have been used in a number of publications [90] [126]. This preclinical stage often brings about numerous redesigns of the robotic architecture, but hopefully matures the idea enough so as to be able to create a complete, detailed and quantified set of technical specifications. Based on these specifications, a first clinical prototype can be built, leading to the clinical testing stage.

Clinical validation

Clinical testing is the critical stage of a medical device, since this testing allows to validate its potential clinical benefit. It involves the testing of the clinical goals ascribed to the device on real patients. Because in this stage the device is not yet certified, these tests are done in a highly controlled manner and often in a reduced fashion compared to the eventual targeted procedure. They must of course be validated by the health authority review board and ethics committee before starting (in France, this is handled by the ANSM: Agence Nationale de Sécurité du Médicament et des Produits de Santé and the CPP: Comité de Protection des Personnes, in the USA, this is done by the FDA). For example, [105] tested a new MRI-guided biopsy and

Table 2-6: Main characteristics of the PROSPER and LPR robotic systems.

Characteristic	PROSPER	LPR
Imaging modality	- US	- CT and MRI
Interventions	- Prostate interventions	- Diverse IR procedures
Anatomical approach	- Transperineal	- Transthoracic and transabdominal
Robotic architecture	- Parallel	- Parallel
Robot mounting	- Table-mounted	- Patient-mounted
Actuation	- Brushless DC motors	- Ultrasonic motors, cables and pneumatics
Robot-image calibration	- Pre-operative needle-based calibration	- Intra-operative fiducial-based calibration

brachytherapy robot on patients in the lower risk procedure of gold marker placement before external radiation therapy. Sometimes, these tests can simply be merged with a standard procedure in order to modify only one selected part of the procedure and extract the required data. An example of such a test can be seen in [63], in which a new prostate biopsy registration technique was tested during a standard 12 core biopsy by acquiring a 3D US volume after each needle insertion. Clinical testing can result in further modification of the robot design, after which a final version can be submitted for CE marking and/or FDA approval and subsequent manufacture and used in regular clinical practice.

2.7 Summary

In the last two chapters, the various commonly done image-guided percutaneous needle insertion procedures were described along with the difficulties encountered in the conventional manual techniques. Robotic systems were proposed as a solution towards resolving these difficulties, and the special characteristics of such systems were described using examples from the literature.

The concepts described in these chapters were used to develop the PROSPER and LPR systems during this thesis. Although the clinical context of these two robots is different, they are both image-guided needle insertion robots and therefore have numerous similarities and common constraints. As summarized in Table 2-6, the two major differences between the two systems lie in 1) the imaging modality used to guide each robot, and 2) the anatomical approach used to insert the needle. These two constraints consequently dictated the type of actuation, the mounting configuration, the manipulator architecture and the type of robot-image calibration chosen for each system. They both allow us to illustrate the majority of the aspects described in this second chapter. Chapter 3 will describe in detail the PROSPER robot and Chapter 4 will describe the LPR robot.

Chapter 3: PROSPER – US-guided prostate transperineal puncture robot

3.1 System description	36
3.1.1 Clinical incentive	36
3.1.2 General layout	36
3.1.3 Clinical workflow	37
3.2 Technical description	39
3.2.1 Technical constraints	39
3.2.2 Robot description	40
<i>Mechanical description</i>	40
<i>Robot workspace</i>	42
<i>Electronics description</i>	42
<i>Sterilization and safety</i>	43
3.2.3 Robot kinematics and calibration	44
<i>Forward kinematics</i>	44
<i>Inverse kinematics</i>	48
<i>Kinematics calibration</i>	51
<i>Needle Tip calibration</i>	53
3.2.4 Imaging hardware	53
3.2.5 Image processing	54
3.2.6 User interface	54
3.2.7 Robot-image calibration	55
3.3 Pre-clinical evaluation	58
3.3.1 Mobile prostate phantom design	58
<i>Prior art</i>	59
<i>Phantom description</i>	59
<i>Imaging characteristics</i>	59
<i>Phantom speed of sound</i>	60
<i>Phantom motion</i>	62
<i>Other phantom characteristics</i>	63
3.3.2 Needle rotation study	64
<i>PVC tests</i>	65
<i>Animal tissue tests</i>	65
<i>Cadaver tests</i>	66
<i>Tissue damage</i>	66
<i>Discussion</i>	67
3.3.3 Phantom study	68
<i>Materials and methods</i>	68
<i>Results</i>	69
<i>Sources of error</i>	70
<i>Analysis</i>	71
3.4 Discussion	72

PROSPER is a robotic transperineal needle insertion system for prostate brachytherapy. It consists of a robotic needle insertion device, a static 3D ultrasound probe and a robust

prostate tracking routine. The robot allows needles to be inserted throughout its workspace, including at oblique angles, and at controlled insertion velocities and rotations. The novelty of the system with respect to existing robots in the literature is its coupling to the 3D TRUS probe and its use of a registration technique to allow for the automatic adjustment of needle depths based on gland motion during the procedure.

The clinical goal of the system is to improve the quality of the conventional brachytherapy procedure by 1) ensuring a better correspondence between seed placement and the initial planned dose distribution, 2) providing a more diverse and flexible choice of seed positions in order to improve dose distribution and 3) potentially making the procedure available to more patients, particularly those with larger prostates or constrained pubic bone anatomies.

This chapter describes the proof-of-concept prototype of the PROSPER system developed during this thesis. The proposed clinical protocol is presented, followed by details of the mechanics and electronics of the prototype manipulator, system calibration and the phantom-based pre-clinical tests done to validate the concept. The section ends with thoughts and comments on the clinical potential of the system given the experience gained with this first prototype.

3.1 System description

3.1.1 Clinical incentive

The original incentive behind this project came from the clinical team at the CHUG which has been doing brachytherapies in standard practice since 2001. The team is highly convinced of the importance of this technique in the arsenal of therapies available against prostate cancer. The accuracy and concentration with which radiation can be applied to the gland, without affecting adjacent anatomy, and the rapid post-operative patient recovery are some of the resounding factors [198] [77]. To the clinicians, however, it was evident from the very first procedures, that it was a technique that was difficult to master because of a number of important challenges. The poor and variable quality of the US images and the considerable mobility of the prostate made it very difficult to know where exactly the needles were being placed. Computer and robotic assistance seemed like a viable option to allow the clinicians to place a seed exactly where it was planned in the image, all the while taking into account the tissue mobility. The uniqueness of this project, compared to existing solutions in the literature, is that it accurately quantifies prostate deformation and hence can take into account target motion during insertion, without which, in our opinion, the high accuracy attributed to any robotic tool would be of little use.

Two other options that seemed worthwhile exploring with this first robotic prototype were 1) to allow oblique needle trajectories in order to bypass the pubic arch and 2) to allow needle rotation during insertion in order to help minimize tissue and needle deformation.

3.1.2 General layout

The general layout of the PROSPER system is shown in Figure 3-1. As in the conventional technique, the patient lies on the surgical bed in the lithotomy position. The robotic needle manipulator is rigidly connected and calibrated pre-operatively to the 3D endfire US probe. At the beginning of the operation, the robot and probe are manipulated in unison by the clinician, by means of an adjustable fixation arm (such as the commercially available CIVCO Multi-Purpose Workstation) attached to the surgical bed, in order to place the probe in the rectum of the patient and obtain an appropriate visualization of the prostate. The whole assembly is then fixed and the 3D probe is able to acquire image volumes of the entire prostate without being displaced. It remains stationary for the entire procedure, unless the rectum-probe contact

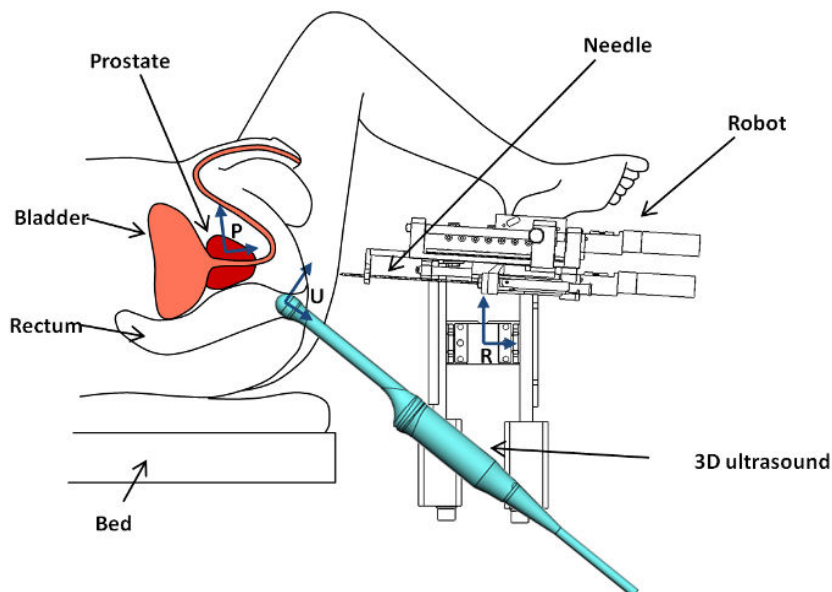


Figure 3-1: General layout of the PROSPER brachytherapy system. Reference frames: P = Prostate, U = Ultrasound probe, R = Robot.

degrades due to patient motion, in which case its position can be re-adjusted by the clinician. The robot adjusts its approach angle based on the orientation of the prostate gland in the US image.

In analogy to the conventional stepper-based technique, the robot replaces the template in front of the perineum and the 3D probe replaces the 2D probe and stepper. As will be described in section 3.2.4, either an end-fire or a lateral-fire 3D probe can be used. The angled orientation of the end-fire probe has certain advantages, but also makes it challenging to display the images to the clinicians in a familiar manner. The prototype system described in this thesis is based on an end-fire probe, since lateral-fire 3D TRUS probes do not exist commercially yet.

3.1.3 Clinical workflow

The clinical workflow designed for the PROSPER system is illustrated in the block diagram of Figure 3-2. It differs from the conventional intra-operative real-time planning workflow described in section 1.2.2, page 13, in that, instead of inserting the needles and seeds in two batches (first the peripheral needles, then the central needles), it inserts a single needle and its respective row of seeds one at a time. Although, the conventional technique may take advantage of the added prostate fixation that results from multiple needle insertions, this added fixation does not eliminate prostate motion.

At the beginning of the robotic procedure, a 3D US reference volume is acquired. The prostate is delineated and an initial dose plan is made. In this initial planning stage, the needle trajectories and seed positions are defined with respect to the reference prostate extracted from the US reference volume.

Next, the following process takes place for each needle. The needle trajectory is computed with respect to the robot coordinates by means of a pre-operative calibration of the US probe with respect to the robot. The robot positions the needle at its insertion point in front of the perineum and inserts the needle. In case of pubic arch interference, the needle is withdrawn and re-inserted at an angle in order to avoid the pubic arch, while still maintaining the seed distribution. Once the needle has been inserted to its planned position, a verification procedure is applied to check for and respond to any prostate motion or deformation caused by the insertion.

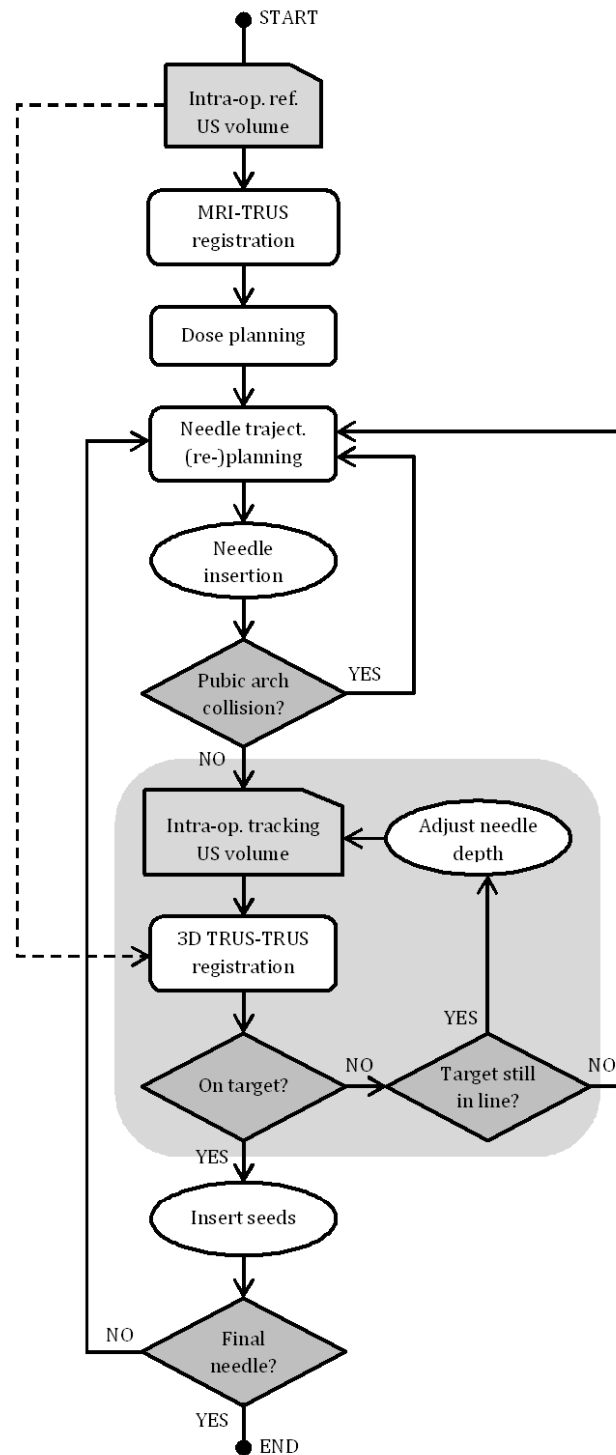


Figure 3-2: Block diagram illustrating the clinical workflow that we propose for our system.

The control loop used to handle prostate motion is highlighted by the gray background in the block diagram. It is important to note that in our control scheme, the dosimetry plan is fixed with respect to the mobile prostate reference frame, rather than to the stationary US probe as is the case in the conventional procedure (see frame P in Figure 3-1). By taking a US volume after the needle insertion, and registering it to the initial reference volume, the original target location can be deformed in conformance to the prostate’s motion and deformation. If the target has moved during insertion, we first check if it can still be reached following the same

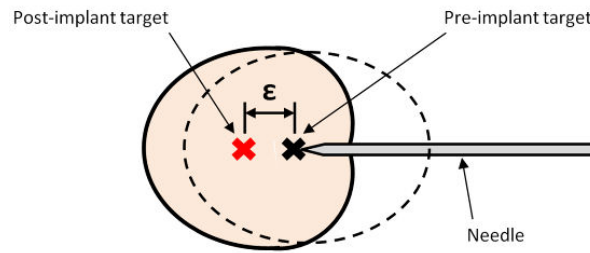


Figure 3-3: Simplified illustration of how the prostate deforms during needle insertion, moving the pre-implant target within the deformed prostate. The pre-implant prostate shape is depicted by the dashed circle. Our system registers the pre-implant image to the post-implant image and determines the amount ϵ by which the target has moved, allowing this to be corrected by advancing the needle further.

needle trajectory. If it can be reached, the needle depth is adjusted iteratively until the clinician is satisfied with the proximity, as shown in Figure 3-3. Otherwise, if the clinician deems the current needle location as unacceptable, the needle is withdrawn and a new insertion trajectory is estimated by the clinician in order to compensate for prostate motion before re-inserting the needle. This re-planning can be done using the clinician's experience to offset the needle's insertion point accordingly, as is done in conventional template-based brachytherapies.

Once the clinician is satisfied with the final needle position, the seeds are inserted using the afterloading technique (using the "Mick Applicator") while progressively removing the needle. A 3D US volume may be acquired for checking the position of each seed separately or globally for all the seeds of a needle. This procedure is repeated until all seeds have been distributed in the prostate.

3.2 Technical description

This section describes the technical aspects of the PROSPER system, beginning with the needle insertion robot, its design constraints, resulting manipulator design, kinematics and calibration, followed by a description of the imaging hardware and software used to guide the robot, and finishing with the robot-image calibration technique used.

3.2.1 Technical constraints

To be able to accomplish the various steps described in the previous section, the following design constraints were established for the robotic manipulator:

- *5 DOF for needle positioning*: three for x-y-z positioning of the needle tip and two for needle orientation in the sagittal and coronal planes.
- *2 DOF for needle insertion*: one for needle insertion and one for needle rotation about its axis during insertion.
- *Workspace*: should be able to cover the 60 x 60 mm grid of the template, along with 30 degree pitch and yaw inclinations in order to contour the pubic arch.
- *Ease of operation*: the robot and the accompanying surgical procedure must be faster and no more complex than the manual technique.
- *Minimal obstruction*: the clinician's access and view of the perineum must not be restricted.
- *Weight*: <5 kg, to ensure ease of installation and handling.
- *Needle compatibility*: compatible with existing needles and seed insertion tools.
- *Safety*: must ensure the safety of the patient and operating room staff.

- *Sterilization*: must meet operating room sterilization constraints.

An additional important constraint to determine was the desired accuracy of the system. From a clinical point of view, the accuracy of needle placement affects the seed and hence the dose distribution in the prostate. The criterion chosen on which to base the system's desired accuracy was therefore the effect of seed placement error on the dose distribution. A number of articles have studied this topic, in particular [199] [200] [201] [202]. Although full consensus has not been reached as to exactly how much inaccuracy should be allowed in order to prevent a clinically meaningful change in dosimetry, they all tend to agree that dose effects become notable as of random average inaccuracies greater than 2 mm. This value was therefore chosen as the system's overall desired accuracy in placing a seed with respect to the original anatomical target location.

To attain this demanding 2 mm cut-off within the highly mobile tissue environment, it was evident that the robotic manipulator accuracy had to be kept as low as possible. A needle placement accuracy of less than 1 mm was therefore chosen for insertions in water. This value is comparable to the 0.97 mm accuracy of the current manual template as measured by [203] in soft gelatin phantoms.

These geometrical accuracies were used during the pre-clinical tests described in this thesis as they gave us a well-defined goal with which to analyse the technical accuracy of the system. To determine the system's clinical accuracy, however, tests will have to be done once the system is complete based on its overall dosimetric accuracy. On eventual patient tests, this would allow us to take into account effects, such as prostatic oedema and inclined seeds which would necessitate dose plan adjustments and that would eventually have a more important effect than the geometrical accuracy on the clinical success of the procedure.

3.2.2 Robot description

This section describes the mechanical architecture of the PROSPER robotic manipulator, its workspace and degrees of freedom, the electronics used to control it, as well as sterilization and patient safety aspects, incorporated into its design

Mechanical description

The prototype robotic manipulator designed to satisfy the constraints listed above is shown in Figure 3-4. The design consists of two primary elements: a 5 DOF needle positioning module and a 2 DOF needle insertion module. The two are independent of each other, allowing each to be modified or replaced separately if necessary. The positioning module positions the needle along the appropriate insertion axis, allowing needle inclinations in the sagittal and coronal planes. The insertion module drives the needle to a given depth and can rotate the needle during insertion if necessary. The clinician inserts the seed manually. The robot is mounted on patient's left of the US probe and thus liberates the entire space directly above and to the opposite lateral side of the operating site.

The positioning module consists of two pairs of linear translation rails mounted in the form of a parallelogram-like manipulator and allows the translation and inclination of the insertion module. For this first pre-clinical prototype, we chose to use off-the-shelf Zaber T-LLS dovetail slides (Zaber Technologies, Inc.) for the rails, which incorporate rail, carriage, motor and controller in an easy to use and precise package.

Translation of the insertion module in the z-axis allows the needle to be prepositioned near the perineal surface and is achieved by a rail and ball screw combination driven by a brushless DC servomotor (Faulhaber 2057) and a 3.71:1 planetary gear reduction (Z-translation motor in Figure 3-4).

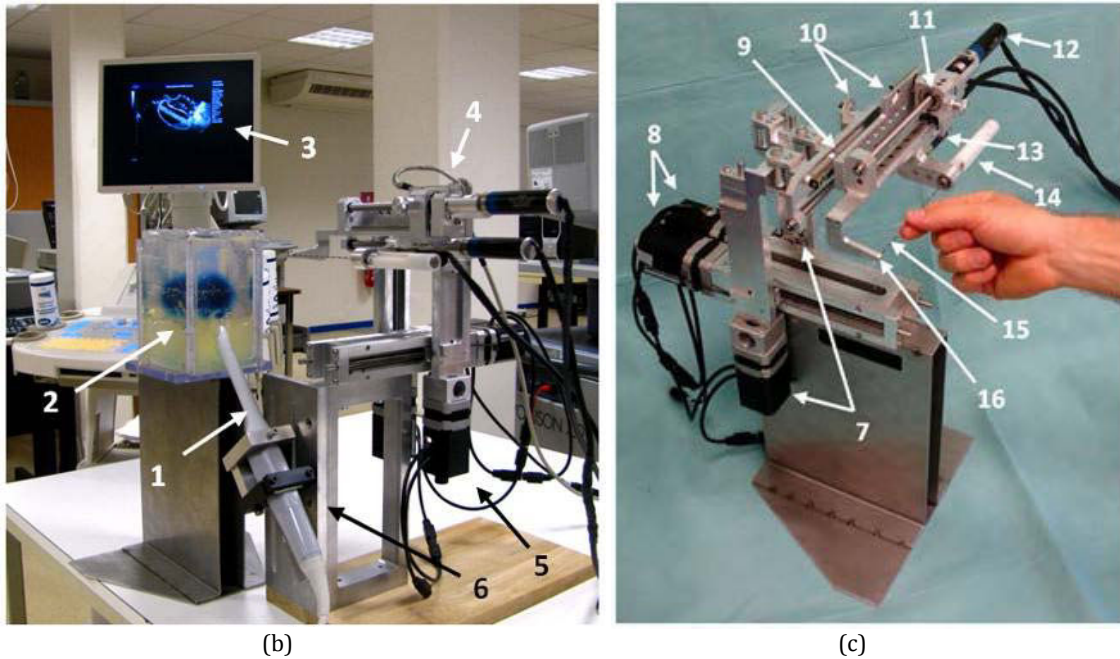
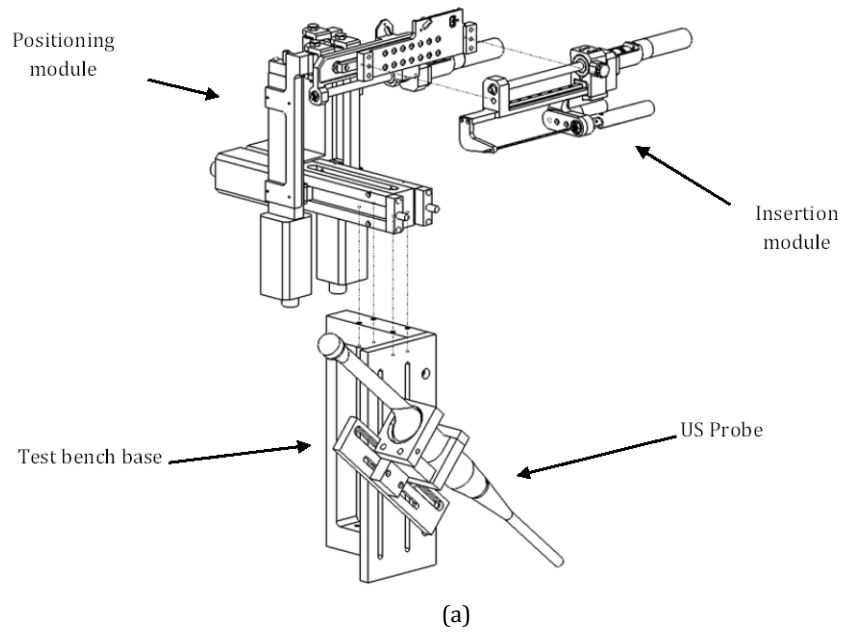


Figure 3-4: (a) CAD drawing of the various components of the PROSPER system. (b) Test-bench setup showing all the components of the PROSPER system (1: 3D endfire US probe, 2: prostate phantom, 3: US machine, 4: needle insertion module, 5: needle positioning module, 6: laboratory robot-probe stand). (c) Photograph of the robot prototype (7: vertical motors, 8: horizontal motors, 9: Z-translation motor, 10: homing Hall sensors, 11: needle disengagement mechanism, 12: needle insertion motor, 13: needle rotation motor, 14: needle grip, 15: needle, 16: needle guide / robot end effector).

The needle insertion module consists of a similar rail, ball screw and servomotor combination that is used to drive the needle during insertion. As shown in Figure 3-5a, the needle is fastened to the robot by a removable, sterilized plastic bushing that provides the interface between the sterile needle and the non-sterile elements of the robot. This bushing is linked through an O-ring belt drive to a third brushless DC servomotor (Faulhaber 1536) which drives the rotation of the needle. The needle can thus be rotated either continuously or by specific amounts in the case of needle-steering.

A needle clamping device was designed to clamp both the needle cannula and stylet for insertion and rotation. Intended specifically for the diamond-tip Mick Ripple-Hub needles (Mick

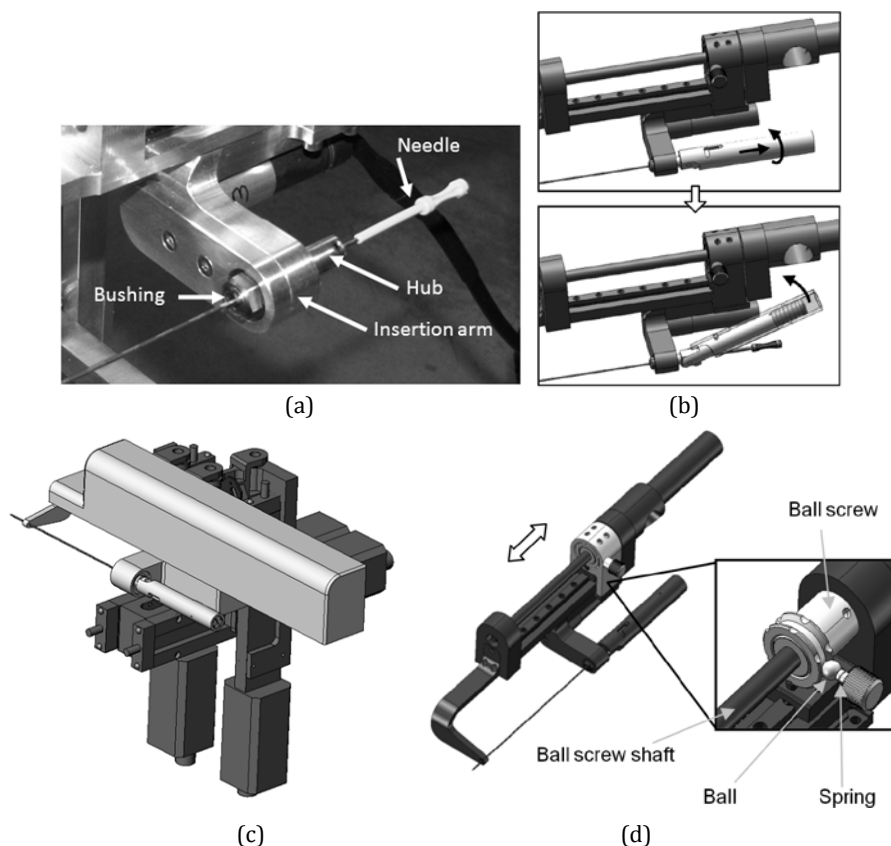


Figure 3-5: Details of the prototype design. (a) Photograph of the needle insertion arm, showing the location of the sterile bushing that separates the sterile needle from the non-sterile rotation hub. (b) Illustration showing how the needle hub and sleeve can be rapidly released in preparation for insertion of seeds. (c) Illustrative CAD model showing how the needle insertion module can be covered by a sterile plastic cap. All white parts are sterile, while all black parts are covered by a sterile drape. (d) Mechanical safety release system that disengages the motorized ball screw from the needle carriage in case of bone contact. The system is based on a ball plunger stop consisting of a ball, spring and adjustment screw.

Radio-Nuclear Instruments, Inc.) used at the CHUG, the needle hub and sleeve are manually releasable by pulling and swinging the auto-locking needle holder, as shown in Figure 3-5b. This allows the clinician to rapidly plug a Mick Applicator or other type of seed dispenser onto the needle. In this first prototype, the needle is held to the rotation hub by a screw for simplicity, however, a clinical version would use a button-clamp that would allow rapid removal of the entire needle from the robot without the need for tools.

Robot workspace

The prototype's seven DOFs are shown Appendix 1. The workspace is defined by 105 mm of horizontal and vertical translation in the transverse plane, 90 mm of translation in the cranial-caudal direction (i.e. in the direction of the needle) and 30° of inclination in the sagittal and coronal planes. In comparison, a conventional brachytherapy needle template has a workspace of 60 by 60 mm in the transverse plane, with needle holes every 5 mm and no possibility of inclination. The needle insertion module allows for a maximum needle insertion depth of 105 mm along with the possibility of rotating the needle at up to a maximum of 12 rotations per second (rps).

Electronics description

The prototype is connected to the control PC through two RS232 connections: one for the Zaber motors and one for the Faulhaber motors. This is because the former have their own

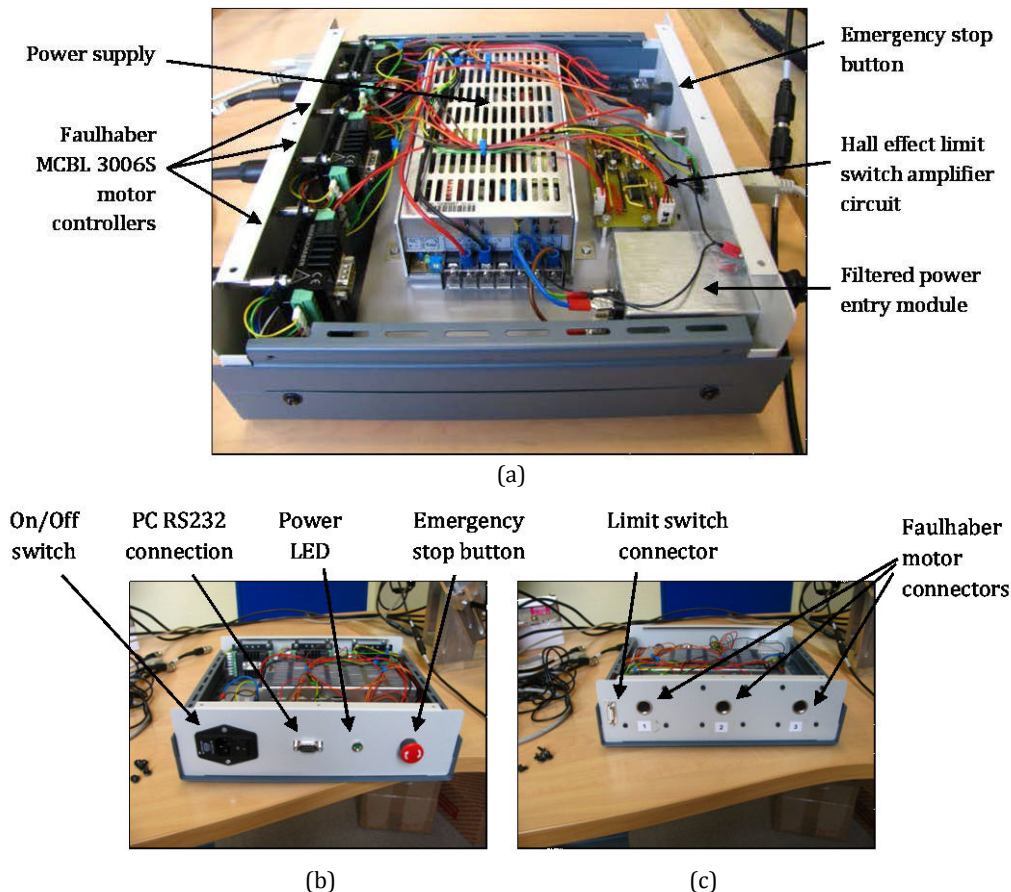


Figure 3-6: The electronics box used to control the PROSPER robot. (a) Inside view. (b) PC-side view. (c) Robot-side view.

integrated controllers and can be daisy-chained together directly to the PC. The rest of the electronics required to control the prototype is contained in a single control box, as shown in Figure 3-6. The box contains the three controllers necessary for controlling the respective Faulhaber motors, daisy-chained together and connected to the second PC RS232 connector. Homing limit switches are used for all six translational DOFs and are all based on standard hall-effect sensors, in which magnets mounted on the moving carriages create a ramp-up signal in proximity to the sensor. A basic signal amplifier circuit had to be constructed in order to make use of these sensor signals.

Sterilization and safety

As described in section 2.6 (page 31), sterilization is a vital issue that needs to be incorporated into the preliminary design process of any new device. In the PROSPER system, the robot and probe are both within the sterile zone required for the intervention. This means that any part of the robot that is either in anticipated contact or in potentially accidental contact with sterile equipment or personnel, must be protected. Normally, the robot is in direct contact with only the sterile needle. The needle bushing mentioned above, along with the clamping device and the needle guide at the front of the needle insertion module are sterilizable and exchangeable to accommodate different diameter needles (ex. 18G or 17G). The rest of the needle guide is cleaned but not sterilized. Instead, it is covered by a sterile plastic casing, as illustrated in Figure 3-5c, that prevents any non-sterile parts from accidentally touching the sterile zone. The positioning module and probe are covered by sterile drapes, as is currently done with the stepper in the conventional technique.

Apart from sterilization, another important safety issue is preventing harm to the patient and equipment in the accidental case of pubic arch contact during needle insertion. With this in mind, and as shown in Figure 3-5d, a mechanical release system was design to disengage the driven ball screw from the needle carriage in case of large axial needle forces. The system functions with an adjustable ball plunger stop whose stiffness is set to release when the axial needle force is greater than the maximum expected tissue-puncture force. It also allows for manual retraction of the needle in case of an electronics malfunction. For this pre-clinical prototype, the disengagement force is adjustable with a screw tensioner in order to easily adjust this limit for testing purposes. A final clinical version would not have this adjustability in order to reduce the risk of accidental misuse.

3.2.3 Robot kinematics and calibration

Forward and inverse kinematics are necessary to control the robot. The former is used to determine the robot's end effector from a set of known joint positions, while the latter is used to determine the joint positions that are necessary in order to place the end-effector in a given location and orientation. The robot's kinematic diagram, excluding needle rotation, is shown in Figure 3-7. It is based on a parallelogram-type manipulator with two kinematic chains that split at the robot's base and reunite at the robot's needle insertion module. The robot's end effector refers to the pin hole at the end of the robot, through which the needle passes, as labeled in Figure 3-4c (page 41).

Forward kinematics

To determine the forward kinematics, the modified Denavit-Hartenberg (DH) convention, as presented by [204], was used in this case. This convention describes where to place and how to orient reference frames on each of the manipulator's links (links being the solid connections between each mobile joint). The frames can be seen in red in Figure 3-7. Based on these

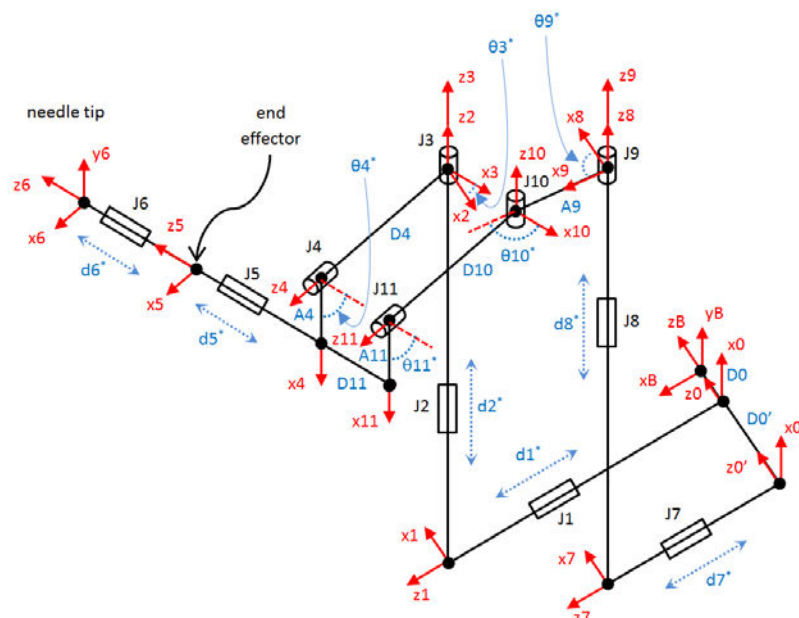


Figure 3-7: Kinematic diagram of the PROSPER prototype manipulator. The letter J represents the robot's various joints. The thetas represent the variable angular positions of the revolute joints. Lowercase d's represent the variable distances attributed to the robot's actuated prismatic joints. Upper case D's and A's represent fixed link lengths. The reference frames attached to each of the manipulator's links are shown in red, with only the x and z axes shown. The robot's end effector is located at reference frame 5 and can be compared to label 16 of Figure 3-4c (page 41). The needle tip is located at reference frame 6.

Table 3-1: PROSPER robot DH parameters. Angles θ and α are written in degrees. Asterisks denote the mobile joint variables. All other values are constant regardless of the robot's pose.

Link (i-1→i)	d_i ($x_{i-1} \rightarrow x_i$ along z_i)	θ_i ($x_{i-1} \rightarrow x_i$ about z_i)	a_{i-1} ($z_{i-1} \rightarrow z_i$ along x_{i-1})	α_{i-1} ($z_{i-1} \rightarrow z_i$ about x_{i-1})
<i>Chain 1</i>				
B→0	-D0	90	0	0
0→1	d1*	90	0	90
1→2	d2*	180	0	90
2→3	0	θ_3^*	0	0
3→4	D4	- θ_4^*	0	90
4→5	d5*	90	A4	90
5→6	d6*	0	0	0
<i>Chain 2</i>				
0→0'	-D0'	0	0	0
0'→7	d7*	90	0	90
7→8	d8*	0	0	90
8→9	0	θ_9^*	0	0
9→10	0	θ_{10}^*	A9	0
10→11	D10	- θ_{11}^*	0	90
11→5	D11 + d5*	90	A11	90

frames, the set of (d, θ, a, α) parameters for each link can be determined in order to fully define the manipulator's kinematic structure. The link parameters are listed in Table 3-1. Using these parameters, the transformation between each set of linked reference frames can be calculated using the following formula:

$$T_{i-1,i} = \begin{bmatrix} \cos \theta_i & -\sin \theta_i & 0 & a_{i-1} \\ \sin \theta_i \cos \alpha_{i-1} & \cos \theta_i \cos \alpha_{i-1} & -\sin \alpha_{i-1} & -\sin \alpha_{i-1} d_i \\ \sin \theta_i \sin \alpha_{i-1} & \cos \theta_i \sin \alpha_{i-1} & \cos \alpha_{i-1} & \cos \alpha_{i-1} d_i \\ 0 & 0 & 0 & 1 \end{bmatrix} \quad 3.1$$

where i is the current frame and $i-1$ is the previous frame in the kinematic chain. The final transformation between the base frame and the needle tip frame is simply the product of these individual link transformations. It defines the pose of the needle tip in space with respect to the robot's base coordinates.

As we can see in Figure 3-7, the robot has 11 mobile joints (6 prismatic and 5 revolute). However, because of the robot's parallel architecture, only the six prismatic joints are actuated with encoders to provide their positions. The remaining five revolute joints are unknown and must be determined from the structural relationship between the links. In the following equations, all the joint variables are denoted with an asterisk, and of these, the d^* represent the actuated prismatic joints while the θ^* represent the unknown revolute joints.

The transformation between the base frame and the needle tip frame can be calculated by following the individual link transformations of either of the two robot's kinematic chains:

Chain 1:

$$T_{B6}^1(d_1^*, d_2^*, \theta_3^*, \theta_4^*, d_5^*, d_6^*) = T_{B0} \cdot T_{01} \cdot T_{12} \cdot T_{23} \cdot T_{34} \cdot T_{45} \cdot T_{56} \quad 3.2$$

Chain 2:

$$T_{B6}^2(d_7^*, d_8^*, \theta_9^*, \theta_{10}^*, \theta_{11}^*, d_5^*, d_6^*) = T_{B0} \cdot T_{00'} \cdot T_{0'7} \cdot T_{78} \cdot T_{89} \cdot T_{910} \cdot T_{1011} \cdot T_{115} \cdot T_{56} \quad 3.3$$

To calculate our forward kinematics, we choose the first chain which has fewer unknowns thetas.

One method of solving for the unknown joint angles θ_3 and θ_4 is described by [205] and involves solving the system of equations defined by the following closed-loop transformation:

$$T^c(\theta_3^*, \theta_4^*, \theta_9^*, \theta_{10}^*, \theta_{11}^*) = I \quad 3.4$$

where I is the identity matrix and:

$$T^c(\theta_3^*, \theta_4^*, \theta_9^*, \theta_{10}^*, \theta_{11}^*) = T_{01} \cdot T_{12} \cdot T_{23} \cdot T_{34} \cdot T_{45} \cdot T_{511} \cdot T_{1110} \cdot T_{109} \cdot T_{98} \cdot T_{87} \cdot T_{70'} \cdot T_{0'0} \quad 3.5$$

This, however, results in a very complex non-linear system of equations. A more intuitive solution can be found by inspection of the manipulator's geometry. The solution consists in determining the positions of frames 3, 9 and 10 from which the unknown angles can then be deduced. The positions of frames 3 and 9 can be found easily by the following known link transformations:

$$T_{B2}(d_1^*, d_2^*) = T_{B0} \cdot T_{01} \cdot T_{12} = \begin{bmatrix} 0 & -1 & 0 & d_1^* \\ 0 & 0 & 1 & d_2^* \\ -1 & 0 & 0 & -D0 \\ 0 & 0 & 0 & 1 \end{bmatrix} \quad 3.6$$

$$T_{B8}(d_7^*, d_8^*) = T_{B0} \cdot T_{00'} \cdot T_{0'7} \cdot T_{78} = \begin{bmatrix} 0 & 1 & 0 & d_7^* \\ 0 & 0 & 1 & d_8^* \\ 1 & 0 & 0 & -(D0 + D0') \\ 0 & 0 & 0 & 1 \end{bmatrix} \quad 3.7$$

To find the position of frame 10, we assume that the (x,y,z) positions of frames 3 and 9 are fixed in space by the joint variables $d_1^* + d_2^*$ and $d_7^* + d_8^*$, respectively. If we split the robot into two parts at frame 10, as shown in Figure 3-8, we can see in the left part that frame 10 can freely move anywhere along the surface of the **sphere** of fixed radius $D11$ centered at frame 3, while in the right part frame 10 can freely move only along the **circle** of fixed radius $A9$ centered at frame 9. The location of frame 10 is therefore at the intersection of this sphere and circle.

To find the intersection of the sphere and the circle, we write their general equations:

$$(x - x_3)^2 + (y - y_3)^2 + (z - z_3)^2 = r_3^2 \quad 3.8$$

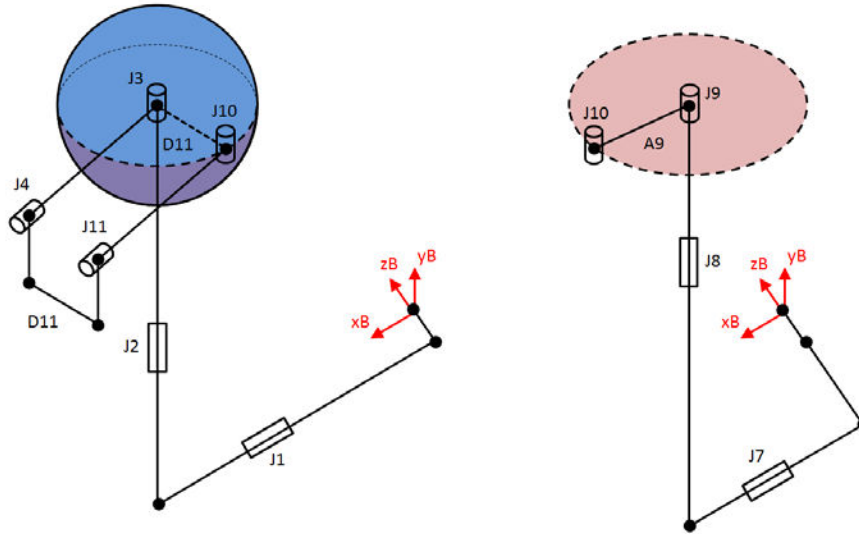


Figure 3-8: The robot kinematic diagram split into two parts at joint 10. Joints 5 and 6 excluded for simplicity.

$$(x - x_9)^2 + (z - z_9)^2 = r_9^2 \quad 3.9$$

where:

$$\begin{aligned} x_3 &= d_1^* \\ y_3 &= d_2^* \\ z_3 &= -D0 \\ r_3 &= D11 \\ x_9 &= d_7^* \\ z_9 &= -(D0 + D0') \\ r_9 &= A9 \end{aligned} \quad 3.10$$

In our case, we can simplify the equation of the sphere by intersecting it with the x-z plane in which the circle lies:

$$y = d_8^* \quad 3.11$$

Therefore, equation 3.8 becomes a circle:

$$(x - x_3)^2 + (z - z_3)^2 = r_3^2 - (d_8^* - y_3)^2 \quad 3.12$$

and the position of frame 10 is therefore the intersection of equations 3.9 and 3.12 which can be found with some simple trigonometry resulting in the x and z coordinates of frame 10 (the y-coordinate is of course defined by equation 3.11):

$$x_{10} = x_3 + \frac{(R^2 - r_9^2 + P^2)(x_9 - x_3)}{2P^2} \pm \sqrt{R^2 - \left(\frac{R^2 - r_9^2 + P^2}{2P}\right)^2} \frac{(z_9 - z_3)}{P} \quad 3.13$$

$$z_{10} = z_3 + \frac{(R^2 - r_9^2 + P^2)(z_9 - z_3)}{2P^2} \mp \sqrt{R^2 - \left(\frac{R^2 - r_9^2 + P^2}{2P}\right)^2} \frac{(x_9 - x_3)}{P} \quad 3.14$$

where:

$$R = \sqrt{r_3^2 - (d_8^* - y_3)^2} \quad 3.15$$

$$P = \sqrt{(x_3 - x_9)^2 + (z_3 - z_9)^2} \quad 3.16$$

P is the distance between the centers of the two circles. Therefore, if $P = (r_9 + R)$, then the robot is at a singularity point, with links A9 and D11 fully stretched out. This and $P > (r_9 + R)$ should never occur if the robot limits are carefully chosen. Hopefully, therefore, in all cases $P < (r_9 + R)$, such that there are two intersection points. The robot is assembled in an “elbow out” configuration (i.e. the elbow created by links A9 and D11 is away from the center of the closed loop), and the singularity position mentioned above is forbidden, allowing us always to choose the largest x and smallest z solution.

In summary:

$$(x_3, y_3, z_3) = (d_1^*, d_2^*, -D0) \quad 3.17$$

$$(x_9, y_9, z_9) = (d_7^*, d_8^*, -D0 - D0')$$

$$(x_{10}, y_{10}, z_{10}) = (\text{Equation 3.13}, d_8^*, \text{Equation 3.14}) \quad 3.18$$

And the subsequent unknown joint angles θ_3^* and θ_4^* , required to solve the forward kinematics equation 3.2, are:

$$\theta_3^* = \text{asin} \left(\frac{x_3 - x_{10}}{\sqrt{D11^2 - (y_3 - y_{10})^2}} \right) \quad 3.19$$

$$\theta_4^* = \frac{\pi}{2} + \text{asin} \left(\frac{y_3 - y_{10}}{D11} \right) \quad 3.20$$

This solution was successfully verified by testing it against the Solidworks (Dassault Systèmes S.A.) CAD model of the robot. The CAD software allows the position of the robot to be simulated based on the position of the six actuated joints. The position of the needle tip with respect to the base frame could therefore be measured in the 3D model with respect to all the extreme motor positions, and then compared to the results calculated by the forward kinematics.

Inverse kinematics

The inverse kinematics can be resolved in a similar, fairly simple geometric fashion as the forward kinematics. In other words, the locations of frames 3, 9 and 10 are found working backwards from the end effector towards the base, and from there the actuated joint variables d^* can be easily calculated. Note that, as opposed to the forward kinematics, the robot's end effector (frame 5) must be used instead of the needle tip (frame 6), since there is a redundancy between the parallel joints J5 and J6.

In general, the procedure involves 1) finding the vector that passes through frame 3 and is parallel to the known needle direction vector, 2) using this vector to find the locations of frames 3 and 10 which both lie on it, and then 3) finding the location of frame 9 from the now known location of frame 10. From these three frame locations we can easily determine the actuated joint variables d_1^* , d_2^* , d_7^* and d_8^* . To find d_5^* , the location of frame 4 is first found by applying forward kinematics and then the normal distance between the known end effector position and the x-z plane of frame 4 determines the joint variable d_5^* .

We are given the homogeneous transformation from the robot's base to the end effector:

$$T_{B5} = \begin{bmatrix} R_{xx} & R_{yx} & R_{zx} & x_5 \\ R_{xy} & R_{yy} & R_{zy} & y_5 \\ R_{xz} & R_{yz} & R_{zz} & z_5 \\ 0 & 0 & 0 & 1 \end{bmatrix} \quad 3.21$$

We begin, therefore, by finding the vector parallel to the known needle insertion vector and that passes through frame 3. To do this, we extend the line joining frames 3 and 10 until it crosses frame 5's x-y plane, as shown in Figure 3-9. This intersection point is labeled with an a. The homogeneous transformation from frame 5 to the parallel frame at point a is known from the robot's geometry:

$$T_{5a} = \begin{bmatrix} 1 & 0 & 0 & -D4 \\ 0 & 1 & 0 & A4 \\ 0 & 0 & 1 & 0 \\ 0 & 0 & 0 & 1 \end{bmatrix} \quad 3.22$$

We can therefore find the transformation from the base frame to frame a:

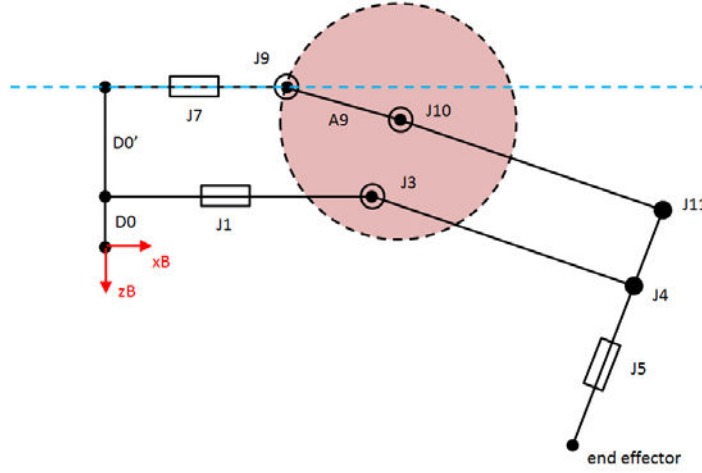


Figure 3-10: The robot manipulator as seen from above. The circle denotes the path swept by the link A9 about joint J10. The dotted line represents the vertical plane along which joint J9 can move.

$$d_1^* = x_3 \quad 3.28$$

$$d_2^* = y_3 \quad 3.29$$

$$d_8^* = y_{10} \quad 3.30$$

To find d_7^* , we need to find the position of frame 9. For this, we can look at the manipulator from above, as shown in Figure 3-10. Frame 9 is at the intersection between the circle described by rotating joint A9 about frame 10 and the vertical x-y plane in which frame 9 is constrained to move:

$$(x_9 - x_{10})^2 + (z_9 - z_{10})^2 = A9^2 \quad 3.31$$

$$z_9 = -(D0 + D0')$$

Therefore:

$$d_7^* = x_9 = \sqrt{A9^2 - (-D0 - D0' - z_{10})^2} + x_{10} \quad 3.32$$

Finally, we must find the joint variable d_5^* . For this we use the transformation between frame 3' (frame centered at joint J3 and parallel to the end effector frame) and new frame b to find point b, whose distance from the end effector represents d_5^* , as seen in Figure 3-11. The transformation from the robot base to frame 3' is:

$$T_{B3'} = \begin{bmatrix} R_{xx} & R_{yx} & R_{zx} & x_3 \\ R_{xy} & R_{yy} & R_{zy} & y_3 \\ R_{xz} & R_{yz} & R_{zz} & z_3 \\ 0 & 0 & 0 & 1 \end{bmatrix} \quad 3.33$$

The transformation from frame 3' to frame b is the inverse of transformation T_{5a} in equation 3.23, therefore, the location of frame b is defined by:

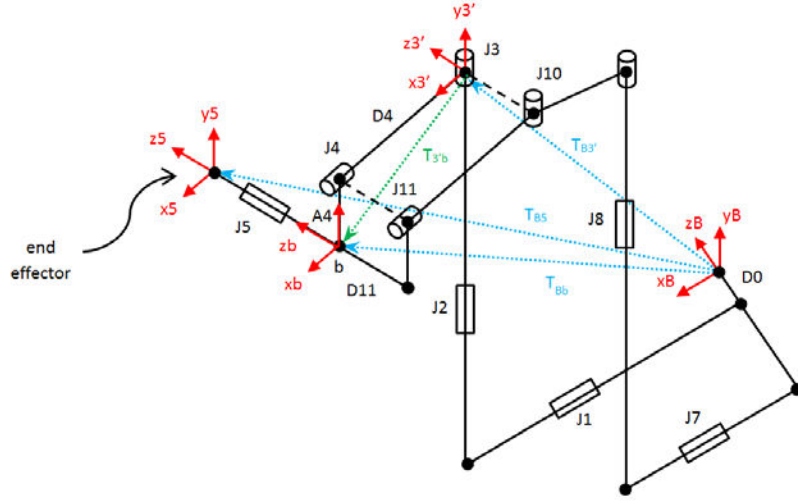


Figure 3-11: The transformations used to find the position of motor 5. Frames 3' and b are parallel to frame 5.

$$T_{Bb} = T_{B3'} \cdot T_{3'b} = \begin{bmatrix} R_{xx} & R_{yx} & R_{zx} & x_b \\ R_{xy} & R_{yy} & R_{zy} & y_b \\ R_{xz} & R_{yz} & R_{zz} & z_b \\ 0 & 0 & 0 & 1 \end{bmatrix} = \begin{bmatrix} R_{xx} & R_{yx} & R_{zx} & x_3 - A4 \cdot R_{yx} + D4 \cdot R_{xx} \\ R_{xy} & R_{yy} & R_{zy} & y_3 - A4 \cdot R_{yy} + D4 \cdot R_{xy} \\ R_{xz} & R_{yz} & R_{zz} & z_3 - A4 \cdot R_{yz} + D4 \cdot R_{xz} \\ 0 & 0 & 0 & 1 \end{bmatrix} \quad 3.34$$

and therefore, d_5^* is:

$$d_5^* = \pm \sqrt{(x_5 - x_b)^2 + (y_5 - y_b)^2 + (z_5 - z_b)^2} \quad 3.35$$

where joint variable is positive when $z_5 > z_b$.

Like for the forward kinematics, this solution was also successfully verified against the CAD model of the robot.

Kinematics calibration

As mentioned in section 2.5 (page 29), kinematic calibration of the manipulator is essential for reducing the error in the forward and inverse kinematics that results from slight differences in dimensions between the CAD and actual machined components of the robot. Our prototype was machined by our manufacturing partner on a high precision 5-axis CNC machine and the dimensions of each piece were verified for their specified tolerances before assembly. We therefore did not expect significant error between the model and the reality. Regardless, kinematic calibration was still necessary in order to take into account effects, such as gravity, bearing play and eventual loose tolerances, for example.

The process involved calibrating the robot's DH parameters based on measurements of the robot's end effector in various poses throughout its workspace. A Polaris optical measurement system (Northern Digital Inc.) was used to measure the poses. Although the reported accuracy of the Polaris system is not ideal (0.25 mm) for the high accuracy required for our application (see section 3.2.1, page 39), it was chosen for availability and simplicity reasons, and deemed sufficient for the pre-clinical use of this first prototype.

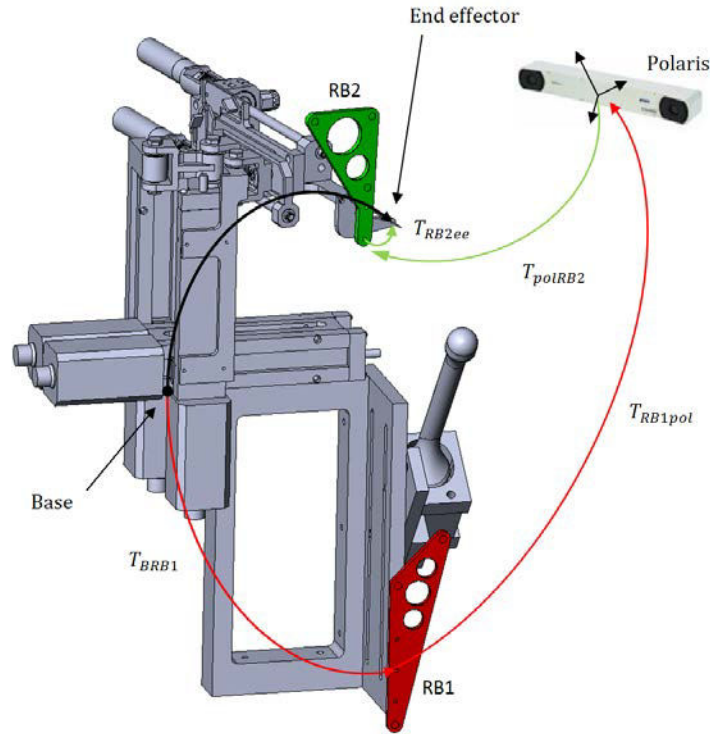


Figure 3-12: Transformations used between the various reference frames during kinematic calibration of the robot. RB = rigid body, B = robot base, ee = robot end effector, pol = Polaris.

The transformations between the various reference frames used in the calibration are shown in Figure 3-12. Two Polaris rigid bodies were used, one attached to the base frame of the robot, and the other to its end effector. The transformations between each rigid body and the true robot base and end effector were measured with a caliper and added to the list of unknown parameters to solve for in the calibration routine. A $100 \times 35 \times 80$ mm grid of 47 different poses were measured throughout the robot's 3D workspace and at random horizontal and vertical inclinations ranging from -12.5° to 11.7° and from -14.3° to 13.4° respectively. This resulted in a system of $k = 47$ equations and 27 unknown robot parameters (22 DH parameters and 6 motor offset parameters) as follows:

$$\varepsilon_k = x_k^{pol} - x_k^{fkin}(P, q_k) \quad 3.36$$

where ε_k is the error between the pose from robot base to end effector measured by the Polaris (x_k^{pol}), and the pose calculated by the robot forward kinematics (x_k^{fkin}). P is the set of DH parameters being solved for, while q_k is the set of robot joint positions at each pose k . The pose measured by the Polaris is derived from the following transformation relationship (see Figure 3-12):

$$T_k^{pol} = T_k^{BRB1} \cdot T_k^{RB1pol} \cdot T_k^{polRB2} \cdot T_k^{RB2ee} \quad 3.37$$

Equation 3.36 was minimized using the least squares Levenberg–Marquardt algorithm. The error between the measured and the calculated end effector locations was reduced from 3.2 ± 0.94 mm to 0.5 ± 0.20 mm. Table 3-2 shows the values of the robot's kinematic parameters before and after the calibration, the main changes being observed in the motor offset values.

Table 3-2: Robot DH parameter values before and after kinematic calibration. The starred values mark the motor offsets at each respective prismatic joint. Dashes represent either variable parameters or values that are not used in the forward kinematics and therefore were not included in the calibration.

Link	d_i	θ_i	a_{i-1}	α_{i-1}
(i-1→i)	($x_{i-1} \rightarrow x_i$ along z_i)	($x_{i-1} \rightarrow x_i$ about z_i)	($z_{i-1} \rightarrow z_i$ along x_{i-1})	($z_{i-1} \rightarrow z_i$ about x_{i-1})
BEFORE CALIBRATION:				
<i>Chain 1</i>				
B→0	-0.9	90	0	0
0→1	*48.205	90	0	90
1→2	*164.42	180	0	90
2→3	0	-	0	0
3→4	109	-	0	90
4→5	*25.75	90	35	90
<i>Chain 2</i>				
0→0'	-42.2	-	-	-
0'→7	*5.015	-	-	-
7→8	*165.5	-	-	-
9→10	-	-	45	-
11→5	38	-	-	-
AFTER CALIBRATION:				
<i>Chain 1</i>				
B→0	-0.9059	90.0363	-0.0187	0.0004
0→1	*48.1860	90.0006	0.0121	90.0004
1→2	*164.4337	179.9888	0.0059	90.0285
2→3	-0.0010	-	-0.0059	0.0016
3→4	108.9995	-	-0.0048	90.0032
4→5	*25.7530	90.0000	34.9972	90.0025
<i>Chain 2</i>				
0→0'	-42.1968	-	-	-
0'→7	*5.0338	-	-	-
7→8	*165.4853	-	-	-
9→10	-	-	45.0191	-
11→5	38.0130	-	-	-

Needle Tip calibration

The above kinematic calibration was based on the measurement of the robot's end-effector pose. Ideally, the needle tip at variable depths should have been used instead, but it would have been technically very challenging to measure the exact needle tip location and orientation without incurring needle bending. Needle insertion could add a few other errors to the system's accuracy. One error is related to the accuracy of the needle insertion motor and mechanism. This was verified using a precision caliper and the error was very minimal. Another error could come from the misalignment of the insertion arm and the end effector that guides the needle. Any misalignment could cause unwanted needle bending without even any needle-tissue interactions. To take this into account, after each new needle installation, the needle was inserted to a maximum (100 mm) and rotated at its highest speed (12rps). The needle tip was observed for any wobble and adjustments were made at the needle's fixation point to decrease this wobble to a minimum.

3.2.4 Imaging hardware

The 3D TRUS probe is a crucial element of the PROSPER system. A 3D probe consists of a 2D array of US transducers mounted to a miniature motor hidden inside the probe head, compared to stepper-based 3D acquisition systems which use a 2D probe mounted on a manual or automatic stepper that moves the entire probe during acquisition. The 3D probe, once

inserted into the patient's rectum, remains stationary for all volume acquisitions, eliminating probe-induced movements of the prostate. It is also faster and allows for more precise volume acquisition.

Two types of probes could be used with PROSPER: an axial side-fire probe or an end-fire probe, each providing certain benefits over the other. A side-fire probe would provide image views similar to those clinicians are accustomed to seeing with conventional bi-plane TRUS probes. In addition to acquiring 3D volumes, it could also allow for real-time 2D viewing of needles axes parallel to the probe axis. An end-fire probe, on the other hand, would have to be inserted at a steep angle, as shown in Figure 3-1 (page 37). This angled approach has the advantage of allowing more space for needle inclination; however the presentation of familiarly oriented 2D slices requires more complex image reconstruction, with, for example, the use of partial scans to view selected needle axes.

At the time of this thesis, no side-fire probe was commercially available, so an Ultrasonix 4DEC9-5 end-fire probe was used and connected to an Ultrasonix RP ultrasound machine. The 10 MHz probe has 128 elements arranged in a convex line, allowing for 145 degrees of coverage between end elements and 106 degrees of sweep. The Ultrasonix RP was chosen for its research interface that allows for full control of low-level probe parameters and image reconstruction directly on the machine.

3.2.5 Image processing

The image processing used to register US images of the prostate together were developed in our laboratory based on the PhD thesis of Michael Baumann [206]. The algorithm was initially developed for the computation of 3D maps of prostate biopsies on a reference volume in the presence of motion and deformation. Since the details of the algorithm have been published extensively [80] [81] [82], and its development is not the work of this thesis, only a brief overview will be given here.

The registration algorithm is fully automated and solely based on the analysis of image-intensity variations, i.e. it does not rely on the explicit identification of prostatic structures. The algorithm uses a multi-step pipeline, where each step refines the registration on increasingly more complex motion models. Rigid registration steps are performed using the correlation coefficient as similarity measure. Deformation estimation is carried out using a variational approach with linear elasticity as motion constraint. Additionally, for two volumes I1 and I2, the forward transformation (mapping I1 to I2) and the backward transformation (mapping I2 to I1) are estimated simultaneously and connected via an inverse consistency constraint to improve the registration behavior in the presence of noise. A novel similarity measure that we call 'shift correlation' is used for very fast yet precise ultrasound to ultrasound registrations. The registration has been validated on 47 biopsy patients and 786 registrations using segmented fiducials inside the prostate as ground truth for accuracy evaluation. The RMS error of the system was evaluated to 0.76 ± 0.52 mm, and the time required for a single registration was about 6-8 seconds on a 2.4 Ghz Intel Core 2 standard PC.

3.2.6 User interface

In this thesis, the image processing described in the previous section was used with a basic custom-developed user interface for imaging 3D volumes with the Ultrasonix probe. The interface is shown in Figure 3-13. It allows the user to acquire 3D volumes and display them in a Cartesian reconstruction. The user can scroll through sagittal, transverse and coronal views (with respect to the probe's long axis). The speed of sound used in the reconstruction can be set, allowing for geometrically correct imaging in different mediums. Points can be specified in the images and used as needle targets for the robot. The interface allows pairs of 3D images to be registered together, allowing the target point locations to be displaced based on the prostate

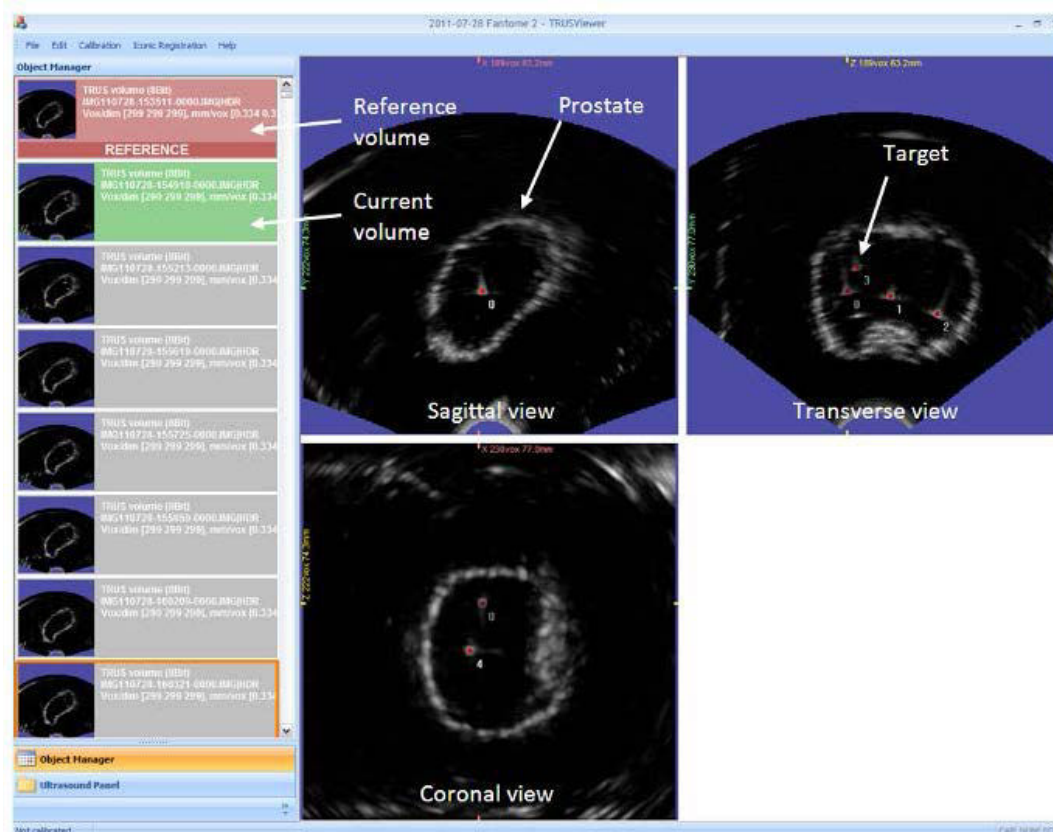


Figure 3-13: User interface for image acquisition, registration and calibration with the Ultrasonix 3D probe.

deformation field and to correct for prostate motion, as shown in Figure 3-3 (page 39). The ultrasound interface is connected to the robot control laptop by a network cable, allowing target points to be sent directly to the robot and the planned insertion trajectory to be executed.

To control the robot, a library was written containing a set of C++ classes that define the robot, as shown in Figure 3-14. A serial port communication class was written to send and receive the RS232 data to and from the motor controllers. An abstract motor class was written that was inherited by two specific low-level motor classes for each motor type: Faulhaber and Zaber. The abstract motor class was instantiated by the robot's seven motors in a high-level robot class. This class contained the robot's high-level control commands (such as move to position, insert to depth, etc.), its kinematics and its workspace. The robot's kinematics and motor parameters are loaded into the robot class from an xml configuration file making it easily modifiable.

3.2.7 Robot-image calibration

The calibration between the robot space and the image space enables the target points chosen in the image to be transformed into robot coordinates in order to send the needle tip carried by the robot to the corresponding point in space. Since the probe and PROSPER robot are fixed together, this calibration is necessary only once, after which the system stays calibrated, provided the probe is kept in place or is installed on the robot before each procedure in a repeatable manner (through the use of a keyed connection, for example). As described in section 2.4 (page 28), this calibration is vital in defining the accuracy of the system.



Figure 3-14: Block diagram describing the software design for controlling the PROSPER prototype. Each block represents an instance of a class. Arrows show the inheritance between classes.

In this pre-clinical prototype, the US probe is rigidly fixed to robot. In a clinical version, however, the interface between the probe and the robot would have to be encoded, allowing the probe's position to be adjusted with respect to each patient's anatomy and position on the surgical table, without having to re-calibrate each time.

We used a water-bath based method to calibrate the robot and the probe together. It involved inserting a needle into a water bath at a number of different poses, segmenting the needle tip in the US image and then registering the two point clouds (one in robot space and one in image space) together to find the best-fit transformation between them. Although the method is simple and commonly used, it was in fact challenging to segment the needle in the water in a reliable and repeatable manner. As can be seen in Figure 3-15a, the US image of the needle was subject to 1) intense reverberation artifacts when the needle was tangent to the probe head surface and 2) a decrease in resolution at larger distances from the probe head (for deep or high needles). This resulted in a needle tip that was very difficult to distinguish, with a segmentation repeatability of greater than 3 mm, even with semi-automated Hough transform

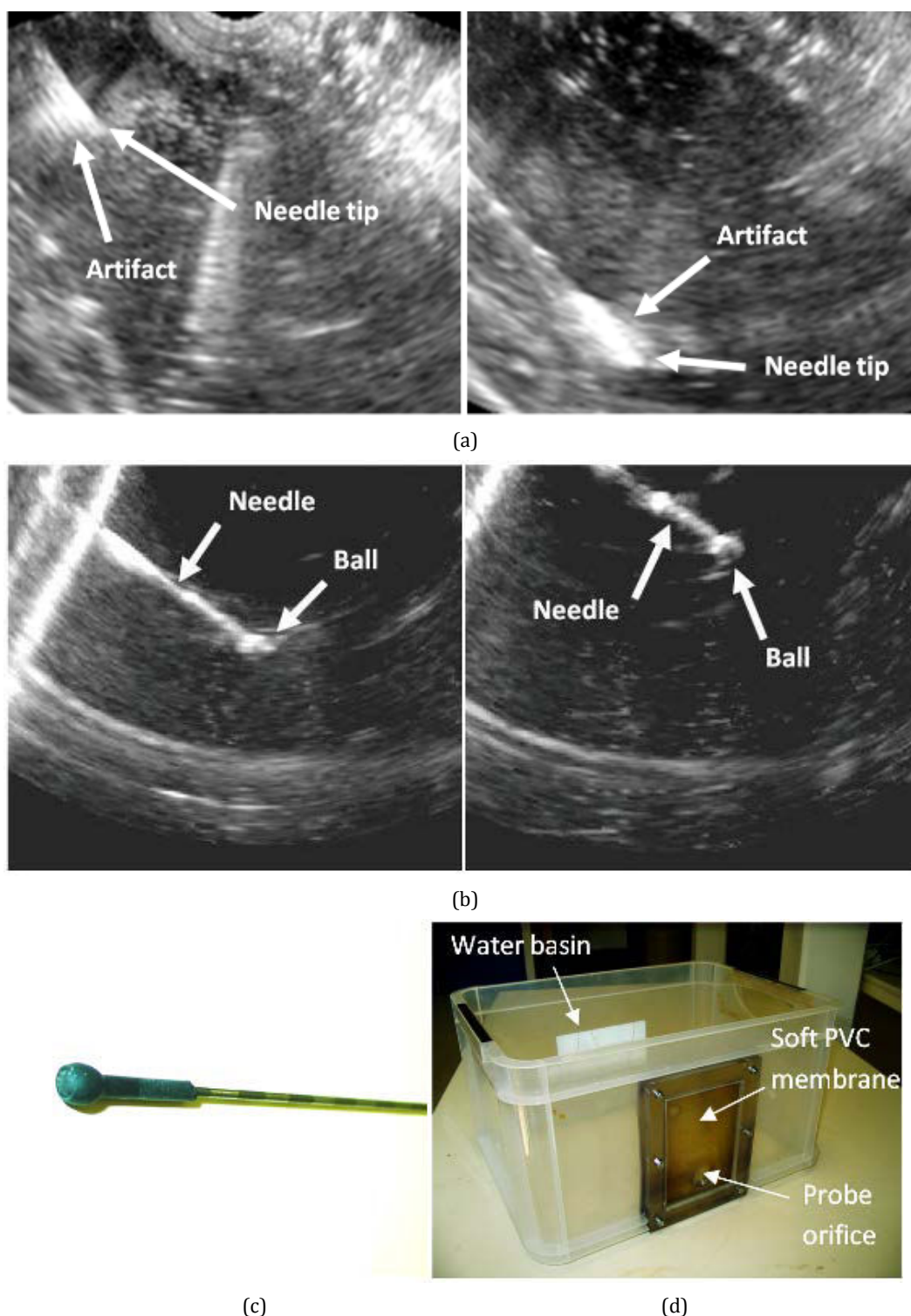


Figure 3-15: (a) Example US images showing the artifacts present with a bare needle in water. (b) Images showing improved visibility by placing a rubber sleeve over the needle tip. (c) Photograph of the rubber sleeve and ball placed over the needle tip. (d) Calibration basin designed to calibrate the PROSPER system in the horizontal position.

segmentation. To improve the localization of the needle tips in the images during calibration, we therefore constructed a small rubber sleeve with a soft ball at one end, as shown in Figure 3-15c. Once placed on the needle tip, the ball was very visible in the image, while the rubber sleeve diminished the reverberation artifacts, improving segmentation quality, as shown in

Table 3-3: Robot-probe calibration results. All values in mm.

Calibration	# of points segmented	All points		Outlier elimination	
		RMS error	Max. error	RMS error	Max. error
1	25	1.04	1.84	0.86	1.32
2	25	1.07	1.78	0.92	1.34

Figure 3-15b. The distance between the needle tip and the center of the ball was measured using a precision caliper.

To prevent any adverse gravitational effects on the kinematics of the robot, we calibrated the robot in its normal horizontal position, instead of tipping it vertically above a water bath, as is typically done in such calibrations [143] [131]. For this, we developed the calibration basin shown in Figure 3-15d, which is placed in front of the robot. A 5mm thick soft PVC membrane was fabricated and placed on the front of the basin, allowing the needle to pierce through into the water behind without bending, and preventing water from leaking out after withdrawal of the needle (note that the rubber sleeve described in the previous paragraph was placed by hand onto the needle tip only once the needle had pierced this membrane and entered into the water). An orifice was made at the base of the membrane, through which the US probe was inserted and sealed to prevent water leakage. The basin was filled with water at room temperature. The water's temperature was measured precisely and used to adjust the speed of sound used in the US image reconstructions, using the Bilaniuk and Wong equation [207].

Two calibrations were done, with 25 robot poses each, covering the entire robot workspace and needle insertion depths. The ball-sleeve was manually segmented in the images at high zoom after each insertion. The cloud of segmented points was then rigidly registered to the corresponding points stored in robot space using Arun least squares fitting [208]. The resulting registration errors are shown in Table 3-3 and are consistent for both calibrations. 10% outlier elimination was used to eliminate major outliers caused by manual segmentation error in points typically very deep and far from the probe head. The calibration errors were less than 1 mm, which was satisfactory given the repeatability of the manual segmentation, the 0.33 mm³ resolution of the images and the kinematic calibration error mentioned in the previous section.

3.3 Pre-clinical evaluation

As described in section 2.6 (page 31), pre-clinical evaluation is compulsory before being able to envision clinical tests. We tested the prototype PROSPER system in a laboratory setting in view of validating the two novel aspects, namely the robotic manipulator itself, but more importantly its ability to compensate prostate motion during needle insertion. To do so, we designed an artificial phantom that mimics the mobility of the prostate and we performed needle targeting experiments to quantitatively evaluate the system's performance.

3.3.1 Mobile prostate phantom design

It was decided to use an artificial phantom in our pre-clinical evaluation, rather than meat or live animals, because it allowed us to test the system in a highly controlled environment, in a simple, repeatable and inexpensive manner, in order to be able to properly quantify the system's accuracy and determine its sources of error. The main goal of the phantom was to allow us to determine the system's capability of accurately depositing a seed in a mobile, deformable environment.

The phantom that we designed, its fabrication process and characteristics, has been published in a peer-reviewed journal [209] that is included in Appendix 2. In this section, these findings will be summarized, and the reader is referred to the publication for further details.

Prior art

A large number of prostate phantoms have been described in the literature over the last decade: everything from very simple uniform blocks [210] [135] [211] [212] [213], to more complex and realistic multi-component phantoms [214] [83], to commercialized tissue-equivalent phantoms [215] [127]. Their main features are (1) to reproduce the anatomy of the prostate environment, (2) to emulate the soft-tissue feel either for applying surface pressure or for needle insertion, and (3) to emulate the imaging characteristics of the prostate, whether it is x-ray, MRI, or US based. The variety of phantoms designed nearly equals the variety of prostate applications being researched.

To our knowledge, however, only two publications exist that describe the use of a phantom specifically for the evaluation of prostate motion due to needle insertion. Both use a harder prostate encapsulated in softer surrounding polyvinyl chloride (PVC) material. In [216] the phantom has a rectum as well as a stiffer inclusion linking the prostate to the base of the phantom in an attempt to reproduce the prostate's rotation about the pubic bone. Needle insertion into the phantom resulted in axial prostate motions of <4 mm. The phantom described by [184] has the added characteristic of including a perineal surface, simulated with a 2 cm layer of stiffer material. The phantom was used in a vertical orientation, with two orthogonal US probes for visualization. Vitamin E capsules were embedded in the phantom to provide specific targets for motion tracking. Target motions up to 11 mm were reported during needle insertion.

These last two mobile phantoms were the closest to our design objectives, and we used them as inspiration for our own design. Our initial building block was therefore the use of a harder prostate embedded in a softer surrounding. Our main goal was then to improve the anatomical realism, adapt the phantom for transrectal ultrasound applications, and ensure its multimodality to generalize its usability. The resulting phantom was found to have very satisfying mechanical and imaging characteristics.

Phantom description

Our phantom can be seen in Figure 3-16. It is made of soft PVC plastic and is composed of a perineum, a rectum, a prostate, and surrounding periprostatic tissue. The different components are made of varying mixtures of PVC polymer solution and the softener diethyl hexyl adipate. The perineum acts as the first “tougher” skin barrier through which the needle must traverse. It also provides a structural frame to maintain the phantom's form and is made of fairly rigid PVC. The rectum accepts an end-fire US probe and is strong enough to resist rough handling during probe placement. The prostate is made of relatively soft PVC and is coated with a capsule, coloured with the biological staining agent toluidine blue, making it visible both to the human eye as well as in ultrasound images. The prostate is hard enough to be mobile but soft enough to be deformable upon needle insertion. It is also embedded with a number of one millimeter diameter glass beads that act as targets for our needle insertions. The periprostatic tissue suspends the prostate in place within the phantom. It is soft enough to allow for sufficient prostatic mobility during ultra- sound probe handling and needle insertion.

Imaging characteristics

A number of phantom characteristics were important for the validation of the PROSPER system. To be used with our system, the phantom, of course, had to be compatible with US imaging. Figure 3-17a shows an image of our phantom acquired with the system's transrectal end-fire probe. The prostate capsule, which is blue to the naked eye, stands out as the white

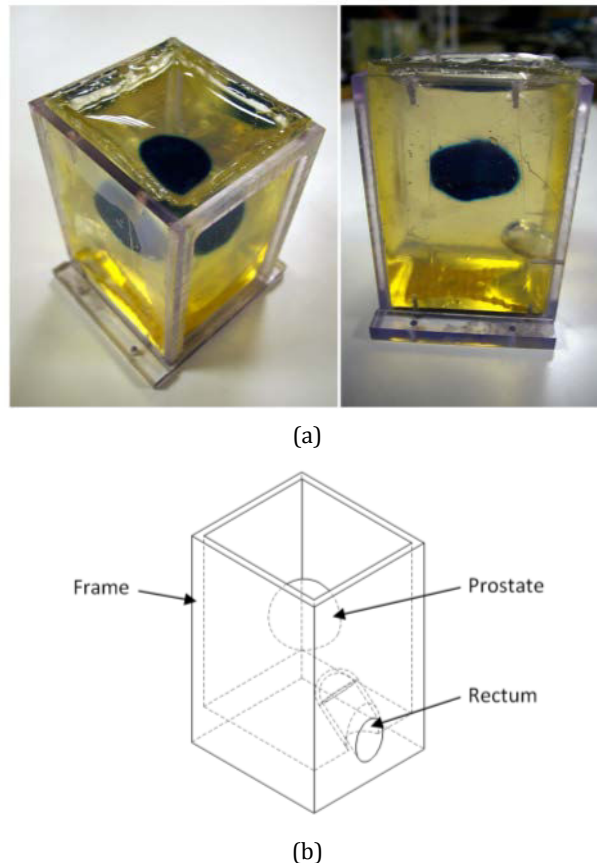


Figure 3-16: (a) Photograph of the phantom with mobile prostate and rectum. (b) CAD drawing of the phantom.

outer boundary of the prostate. The glass targets embedded inside the prostate cast slight white shadows that allow for very easy and accurate segmentation. The system's prostate registration algorithm works flawlessly on these images.

The main disadvantage of the phantom, like with the majority of synthetic phantoms, is that needle insertions leave permanent traces in the US images. In our experience, this limited us to about 15 to 20 insertions per phantom, before the image became too degraded for effective use. At this point, the registration algorithm started showing visible inaccuracies in certain noisier areas of the volumes.

As will be described in section 3.3.3 (page 68), the needle insertions into the phantom were evaluated using CT images. The phantom's compatibility with this modality was therefore also important. Figure 3-17b shows a CT image of the phantom. The PVC mixtures used in the phantom are clearly distinguishable because of their different densities.

To check the segmentation accuracy of the targets in the images, we compared US and CT images of 8 phantoms embedded with 8 to 12 glass targets each. The targets were segmented manually at high zoom in each US and CT image. The clouds of segmented US points were then rigidly registered to the corresponding CT points using Arun least squares fitting [208]. The average registration error for all eight phantoms was 0.66 ± 0.25 mm. This error is very reasonable, as it includes the segmentation errors from both modalities.

Phantom speed of sound

In order to be accurately imaged with US, the speed of sound of the PVC material used in the phantom was essential. The speed of sound of PVC depends on the proportion of hardener and softener used. Values found in the literature were not backed with details on the PVC mixture used [217] [218], so we had to make our own measurements with the help of ultrasound probe manufacturer Vermon (Tours, France). The measurements were done by

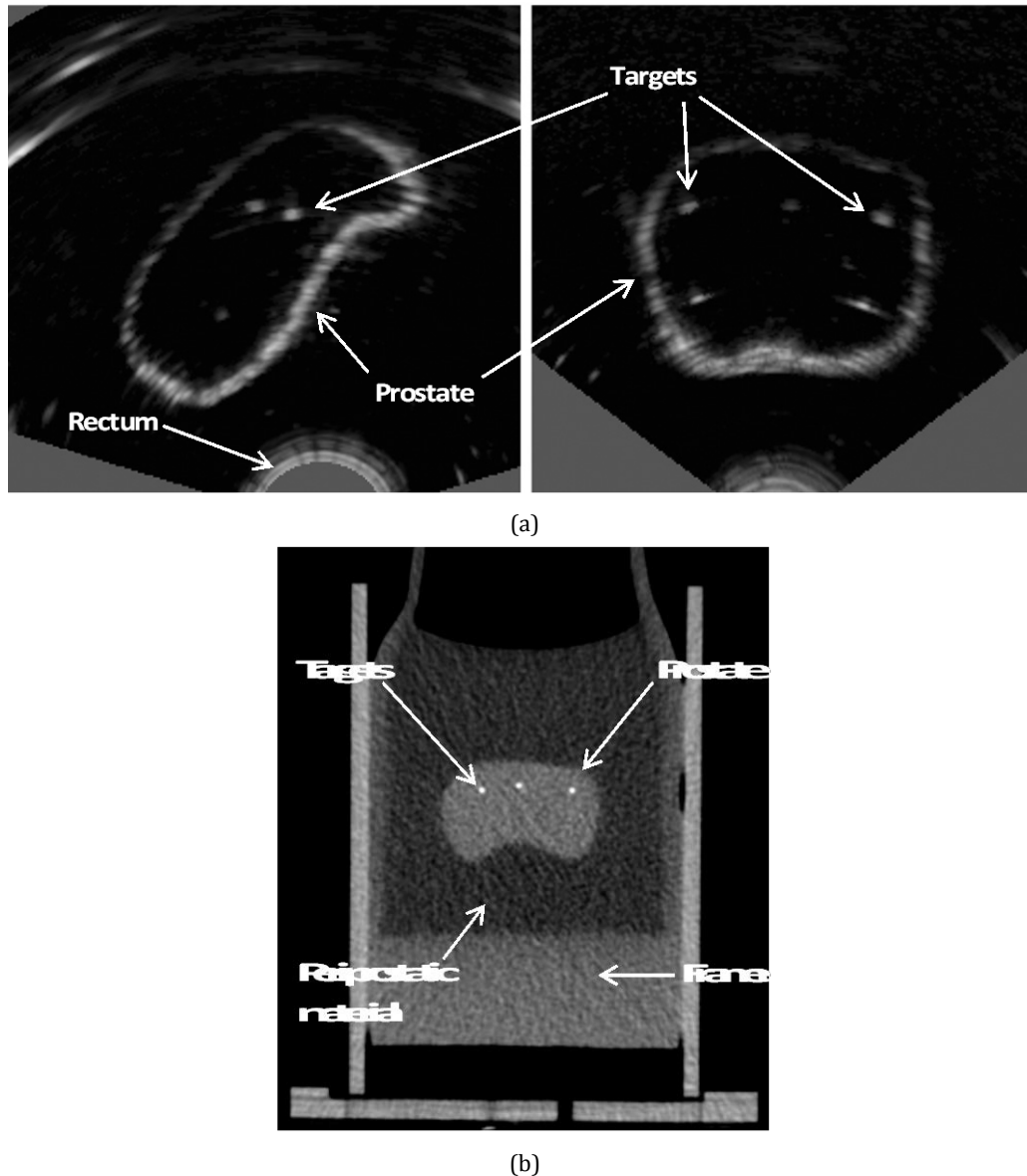


Figure 3-17: (a) Sagittal (left image) and transverse (right image) views of a 3D ultrasound volume taken of our prostate phantom. The images show the 1 mm glass targets embedded in the prostate. Note that the oblique angle of the prostate in the sagittal image is due to the obliquely placed end-fire probe. (b) Transverse CT image of our phantom.

plunging a rectangular PVC sample in a water basin and comparing the distance measured by a US transmitter from the transducer head to the floor of the basin, with and without the presence of the sample. The following geometric formula was then used to calculate the speed of sound of the PVC with respect to the water:

$$c_{PVC} = c_{water} \frac{d_{water}}{d_{PVC}} \quad 3.38$$

where c is speed of sound and d is distance. The resulting speed of sound was different for each PVC hardness, ranging from 1360 to 1580 m/s from the softest to the hardest.

Since the phantom consisted of variable PVC hardnesses, an average value had to be used. To determine this, we calculated the speed of sound at the shallowest and deepest points of the prostate (i.e. at the closest to and farthest from the probe head) as shown in Figure 3-18. The

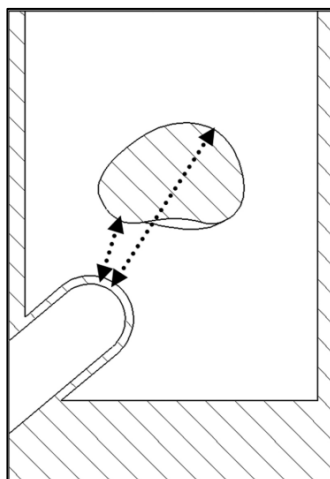


Figure 3-18: The shallowest and deepest trajectories from the probe head, used to calculate the range of sound-speeds in the phantom.

two speeds were calculated based on the depth-weighted average of PVC mixtures that the sound wave must travel through:

$$c_{average} = \frac{c_{PVC1} \cdot d_{PVC1} + c_{PVC2} \cdot d_{PVC2}}{d_{PVC1} + d_{PVC2}} \quad 3.39$$

The resulting maximum and minimum speeds were at the different extremes of the prostate were 1400 m/s and 1360 m/s. The final speed of sound used for the phantom was taken as the average of these: 1380 m/s. The variability in speed of sound due to the varying depths of PVC mixtures would cause an error of 1.5% of the distance from the probe head. For the shallowest areas (~20 mm from the probe head), this would amount to about 0.3 mm, while for the deepest areas of the prostate (~60 mm), the error could be up to 0.9 mm. We consider this variability reasonable, as it is less than the variability due to tissue differences reported in vivo [219] [220].

We verified the speed of sound by manually segmenting the prostate in a 3D US image at the chosen speed of sound and comparing it to the true volume of the prostate. The US volume was $299 \times 299 \times 299$ in size and had a voxel dimension of 0.33 mm^3 . The true volume was determined during construction of the phantom by measuring the volume of water displaced when submerging the prostate. The segmented volume of the prostate was 47.2 cm^3 compared to the true measured volume of 47.0 cm^3 . The proximity of the two results lead us to believe that the chosen speed of sound was suitable.

Phantom motion

Since prostate motion was the primary behavioral aspect that we wished to reproduce in our phantom, we performed measurements to quantify the amount of motion caused by needle insertions in our phantom. We looked at the deformation fields calculated by our registration algorithm for five different insertion locations in the prostate: central, left, right, anterior and posterior, as shown in Figure 3-19. The deformation fields were obtained by registering a reference 3D US image taken before insertion to a second image taken after needle insertion. Insertions were done using the PROSPER robot, with an 18 gauge Mick Ripple-Hub needle, with an insertion speed of 5 mm/s. A grid of 512 points evenly distributed throughout the prostate volume was taken from the resulting 3D deformation field and used to analyze the prostate motion. The center of mass of the points was used to quantify the amount of translation experienced by the prostate. The rotation of the prostate was extracted from the transformation matrix determined by rigidly registering the grid points from the before and

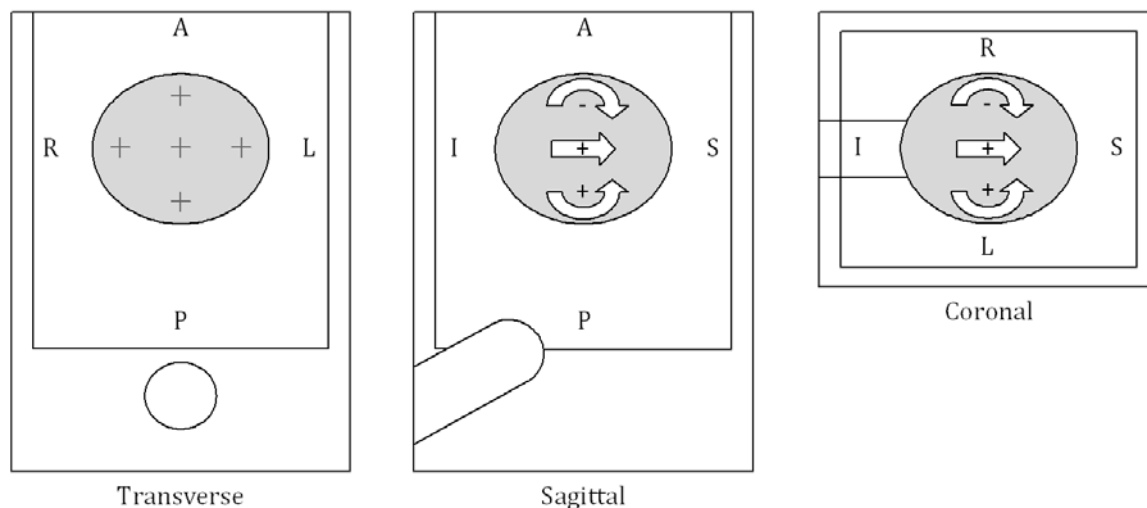


Figure 3-19: Needle insertion locations (crosses in transverse image) and motion directions (arrows in sagittal and coronal images) used for phantom deformation testing. Note that the anatomical locations labeled in the images are all with respect to the patient. A = anterior, P = posterior, R = right, L = left, I = inferior, S = superior.

Table 3-4: Results showing the translation and rotation of the prostate during needle insertion into the phantom, measured at the prostate's centre of mass over 5 insertions.

Needle	Translation (mm)	Rotation (°)	
		Sagittal	Coronal
Central	3.7	-0.2	0.3
Left	2.3	0.3	1.0
Right	2.4	-0.4	-1.2
Anterior	2.7	-2.1	0
Posterior	3.3	1.1	0.3

after US volumes using Arun least squares fitting [208]. The results are shown in Table 3-4 for the five insertions done on a single phantom.

We found, as can be expected, that the prostate motion depended on the direction and location of insertion of the needle and was generally constrained to motion about the fixed US probe head inside the rectum. A needle inserted straight into the center of the prostate resulted in translational motion along the needle axis direction. A needle offset from the center of the prostate resulted in a translation of the prostate along the needle axis direction coupled with a rotation about the probe head. The translation and the coronal-plane rotation of the phantom prostate were realistic, compared to the motions described in the literature. Rotation in the sagittal direction was, however, different, as rotation tended to be downward toward the rectum, rather than upward toward the pubic arch as suggested in the literature. But, as also mentioned in the literature, the sagittal-plane rotation is not as important as other motions and tends to be unpredictable in any case [74]. The measured translations and rotations fall within published results measured in vivo, i.e. on the order of 3–10 mm of translation [72] and between 0° and about 10° of rotation [73], however, they remain illustrative since the published clinical data is not extensive.

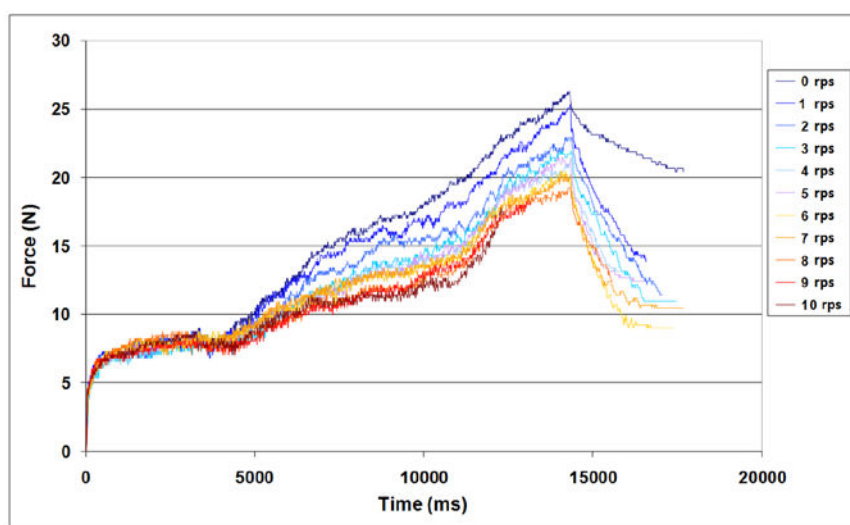
Other phantom characteristics

In addition to imaging, speed of sound, and motion characteristics, two other aspects of our phantom were measured: the elastic properties of the PVC material used and the storage characteristics. The modulus of elasticity of the different PVC mixtures of various stiffnesses used in our phantom were determined using a compression machine resulting in a range from 3

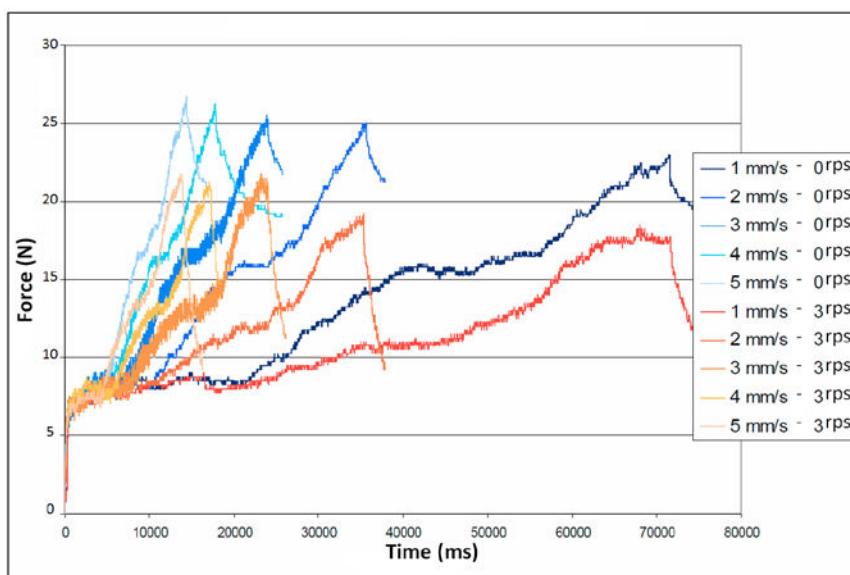
to 200 kPa, which falls within that of real prostatic tissue [221] [222]. The phantom's storage characteristics were verified to see whether the phantom's properties changed over time. Experiments were done on the compression stress-strain relationship and the US image consistency over time. It was found that storage at cold temperatures (such as in a standard freezer) best conserved the phantom's characteristics up to at least a period of one month. Further details of these characteristics can be found in our publication [209].

3.3.2 Needle rotation study

Although our system is designed to track prostate motion during needle insertion, it is logical to think that decreasing this motion and deformation would improve even further its accuracy. For this reason, we decided to explore the option of rotating the needle during insertion, which seemed like the most effective of the motion-reduction methods described in section 2.3 (page 24). As we saw in Table 2-3 (page 27), the effects of needle rotation and



(a)



(b)

Figure 3-20: Force measurements during needle insertion into PVC material at (a) varying rotation speeds and (b) varying insertion speeds. In (a), the insertion speed was kept constant at 5 mm/s for each insertion. In (b), five insertion speeds were tested first with no rotation and then with 3 rps.

insertion speed have been reported a number of times already in the literature with promising results in artificial material.

PVC tests

To verify these published results, we did our own measurements on the PVC material used in our phantom. We mounted a force sensor on the PROSPER robot and inserted a needle into a PVC sample at varying speeds in order to determine the effect of needle insertion and rotation speed on the axial needle-tissue interaction force. The results at varying rotation speeds can be seen in Figure 3-20a. Our results clearly support the published findings that show a decrease in needle insertion force in artificial material with increasing rotation speed. We also examined the effect of varying insertion speed and once again showed the same results as in the literature: a slower insertion speed results in reduced insertion force (see Figure 3-20b).

Animal tissue tests

These experiments were useful for determining the type of insertion to do during our phantom tests and provided promising results in favour of needle rotation. However, it was necessary to verify these results on more realistic tissue. We therefore constructed a simple needle insertion test bench which allowed us to do repeated insertions at insertion speeds up to 400 mm/s and rotation speeds up to 13 rps. We did numerous tests on pig muscle and lamb kidney, but found no significant difference in the insertion force with any speed combinations. This was likely due to the low forces required to puncture these fairly homogenous tissues (< 3.5 N). We also did tests on pork rind and found more notable results, as shown in Figure 3-21. Insertions at rotation speeds ranging from 0 to 13 rps were done for both 5 mm/s and 25 mm/s insertion speeds. Each speed combination was repeated three times and the average of the maximum forces is shown in the figure. There was a clear decrease in force at higher rotation speeds. We therefore took the highest rotation speed and tried a range of insertion speeds from 1 to 400 mm/s and found an increase in force with increasing speed. These results supported our findings in PVC.

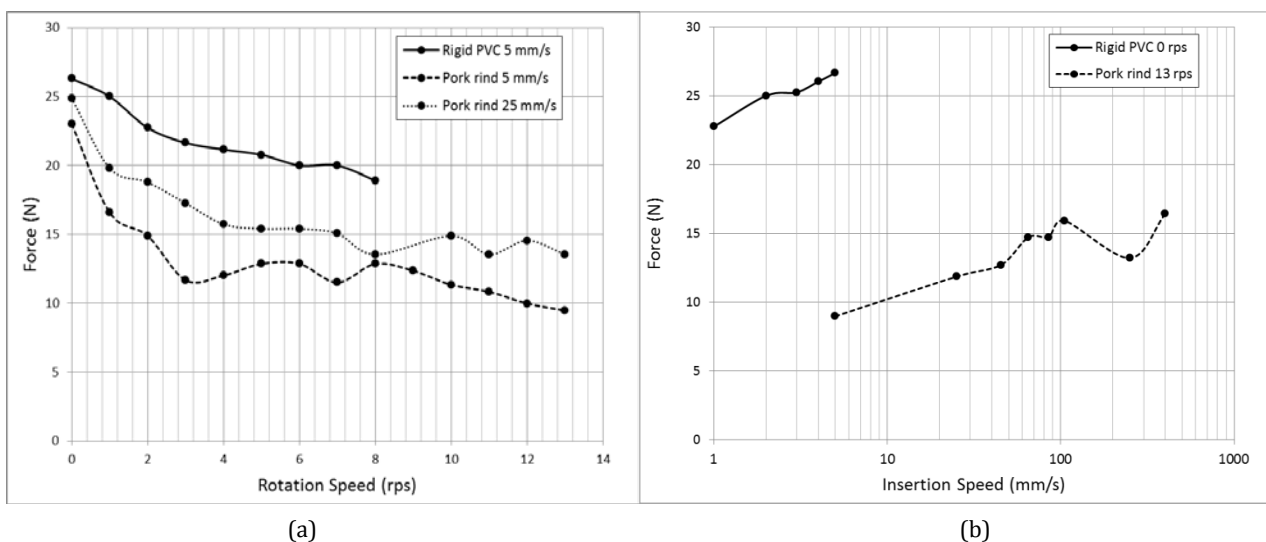


Figure 3-21: Maximum force measurements during needle insertion into pork rind samples, at varying (a) rotation speeds and (b) insertion speeds. An 18G brachytherapy needle was used in all insertions. The maximums of the PVC curves from Figure 3-20 are included for comparison.

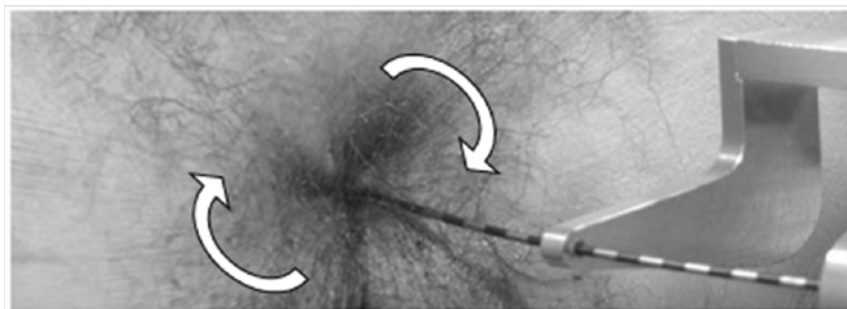


Figure 3-22: The effect of relatively slow (6 rps) clockwise rotation of the needle during insertion into fresh cadaveric skin. Note how the skin has been twisted by the needle point and how the needle is bent due to the high perforation force required to pass the skin at this slow insertion speed.

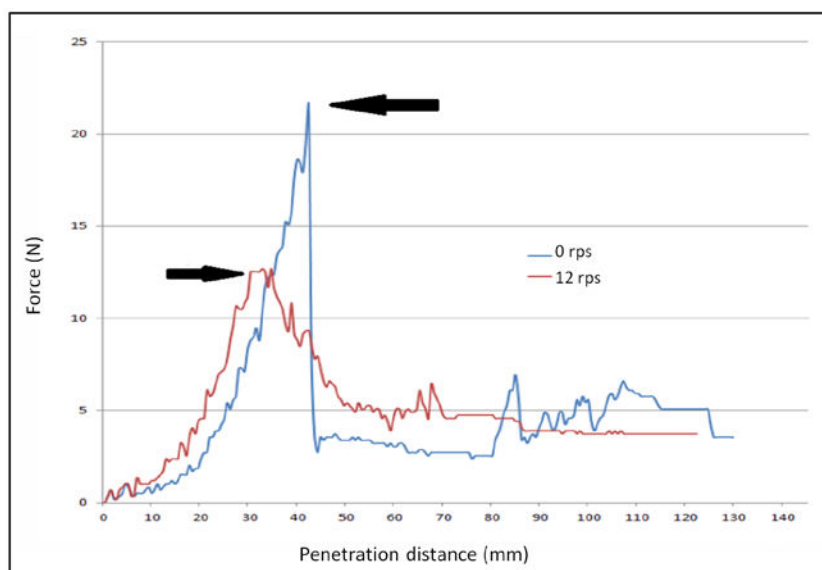


Figure 3-23: Force measurements during needle insertion into a fresh cadaver through the perineum at 12 mm/s. The perineal skin penetration point for each insertion is marked with black arrows.

Cadaver tests

Although these experiments are very promising, they are still not the same as real human tissue. So in addition to the animal samples, we were also able to do a number of insertions on embalmed and fresh (defrosted) cadavers. Insertions were done with the PROSPER robot through the perineum with a standard 17G Mick Ripple-Hub brachytherapy needle. Table 3-5 summarizes the main observations found during the fresh cadaver experiments for the various speed combinations tested. In both embalmed and fresh cadavers, we found that the needle tended to twist the tissue during rotation, instead of cutting it. This was in particular the case in the fibrous embalmed cadaver as well as at the soft skin of the fresh cadaver, as can be seen in Figure 3-22. In addition, in the fresh cadaver, we found that too low speeds of insertion (1 mm/s) required significant skin penetration force, enough, in fact, so as to bend the needle. In summary, the conditions that inserted smoothly were at high insertion (6 - 12 mm/s) and rotation (12 rps) speeds. Figure 3-23 shows the insertion force curve for insertion at 12 mm/s and rotation at 0 an 12 rps, showing an evident decrease in skin penetration force when using high rotation speed.

Tissue damage

All the above tests showed that needle rotation could decrease needle insertion force and consequently could help reduce tissue deformation. The effect of rotation on tissue damage is,

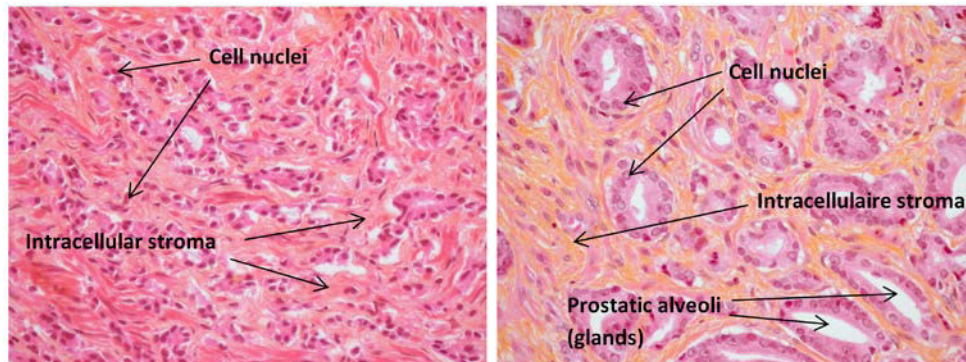


Figure 3-24: 400 × magnification of prostate adenocarcinoma tissue from (a) a defrosted fresh cadaver specimen and (b) a prostatectomy specimen (image courtesy of Dr. Agnès Ciapa, Actes Pathologie, Grenoble, France).

however, a vital aspect that needs to be determined before use on patients. Although high rotation speeds seem to be the best solution, it is unclear as to whether they do more damage than regular insertions without rotation. It is also unclear whether the twisting observed on the cadaveric tissue is caused in particular by the three-sided diamond-tip needle (designed for straight insertions, not for rotations) used during the experiments and whether it would be present in a bevel-tip or conical needle, for example. No information on these issues was found in the literature, other than two studies that have observed helical-shaped holes left by rotating needles in transparent artificial phantoms [223] [224].

We have begun experiments into these aspects on animal and cadaveric tissue. Initial steps have included inserting needles into deceased animal tissue and observing the effect of the rotation speed and needle type on the hole left in the tissue. To do so, we inserted the needles, plunged the samples into 10% formaldehyde solution for 48 hours without withdrawing the needles and then cutting down the length of the needle with a razor. No evident macroscopic differences were observed in any of the samples. The next step is, therefore, to make these observations on a microscopic level, in the form of a histological analysis. This has been initiated on a defrosted fresh cadaver prostate, however the technical aspects of the procedure need to be refined, in particular the marking of the needle holes in order to find them once the histology slides have been prepared. It is also unclear as to whether any significant differences will be noticeable, in particular because of the visible differences between truly fresh prostatic tissue and defrosted tissue, as shown in Figure 3-24.

Discussion

Getting a quantifiable idea of the effect of needle rotation on the needle insertion force and tissue integrity is not an easy task, especially because of the ethical and technical impossibility of performing such experiments on real patients. This is why we did progressive experiments from phantom material to in vitro animal tissue through to fresh cadaver tissue. The phantom tests allowed us to first establish the potential advantage of needle rotation. The animal tissue allowed us to verify these result on more realistic inhomogeneous material. Although none of the animal tissues tested were similar to human prostate tissue, it gave us a better feel for what to expect when traversing the skin, muscle and fat tissue of the perineum. The cadaver tests were as close as we could get to live human tissue, even though, as we saw, the tissue structure is modified after death and freezing. A logical next step would be to do tests on live animal tissue.

Regardless of the results, it is difficult to say whether rotation would cause increased clinically significant damage compared to the extensive damage already being done to the prostate in a conventional procedure (20 needles and aggressive localized radiation). In fact, how would one define clinically significant damage? Increased post-operative pain and increased amount or rate of oedema are two possibilities, but these are very difficult to measure. What is intuitively clear is that the less damage done, the better.

Regardless of these issues, this rotation study is currently in progress and shows some promise as to its potential reduction in tissue motion and deformation. Possible solutions that still need to be examined may involve using rotation only on specific portions of an insertion trajectory, such as at the skin or prostate capsule. In the following phantom study, which was done before the above-mentioned cadaver tests, needle rotation was used in order to maximize the effectiveness of our system.

The needle rotation results presented above were done in cooperation with Vincent Beix and Sebastien Briot during their internships.

3.3.3 Phantom study

The experiments conducted with the PROSPER system involved trying to insert seeds as close as possible to the glass targets embedded in the phantom prostates, using the gray control loop described in Figure 3-2 (page 38). The goal of the experiments was to determine how well the system was able to handle prostate motion and deformation and with what accuracy.

Materials and methods

Nine phantoms were constructed, each with 12 target beads embedded inside, giving 108 targets in total. After a first reference volume acquisition, the target beads in the phantom were located by hand at high zoom (at least 3x zoom), as shown in Figure 3-25. Using the first robot-probe calibration result in Table 3-3 (page 58), the target coordinates were sent to the robot, which proceeded to insert the needle accordingly. An 18 gauge diamond-tip Mick Ripple-Hub needle was used, with an insertion speed of 5 mm/s and a rotation speed of 8rps. We chose to include rotation in our experiments in order to maximize the effectiveness of our system. The

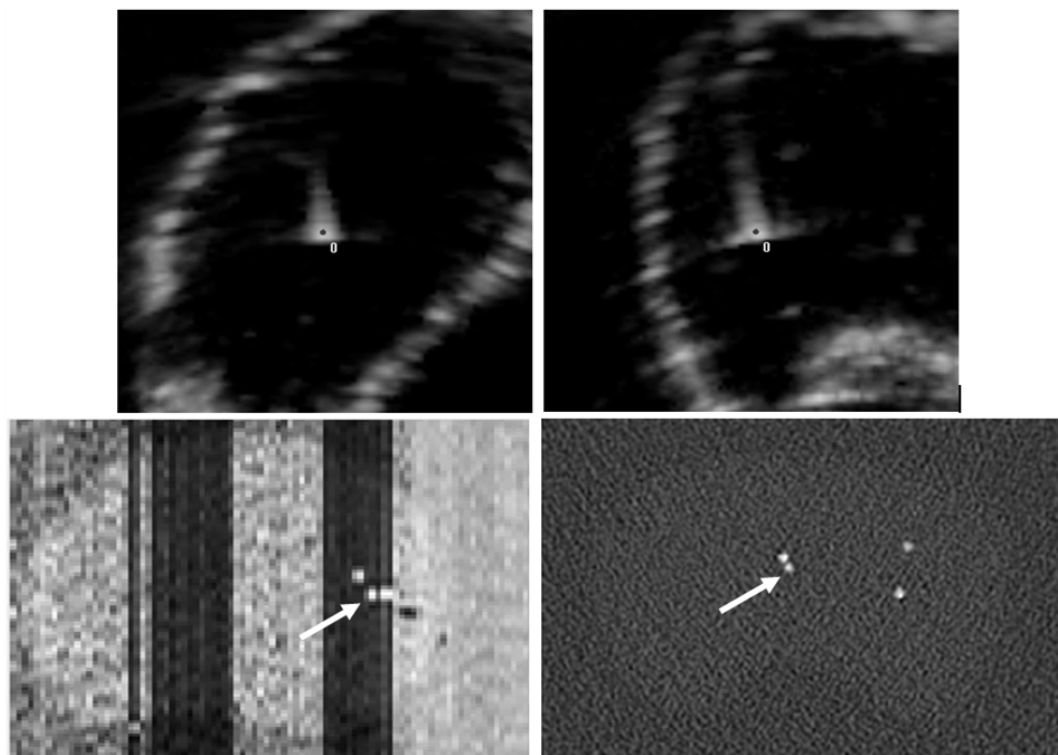


Figure 3-25: Sagittal (left) and transverse (right) cuts of a US volume (top) and a CT volume (bottom) acquisition of the prostate phantom, showing the prostate outline, target beads and inserted beads (marked by arrows in the CT images). Note in the sagittal CT view, the two inserted beads in line: the second bead being used to distinguish between inserted and target beads.

rotation speed was chosen based on the PVC experiments described in section 3.3.2 (page 64), in which we found that the needle force was most effective up to about 8 rps, beyond which the force did not decrease significantly (at least on our PVC material and up to the speeds available with our prototype). Once the needle was inserted, a second volume was acquired and the initial reference volume was registered to it. The deformation field was applied to the original segmented target location, and the new displaced target location was sent back to the robot. The robot then adjusted the needle depth to the closest point along the needle axis to this new target location. This was repeated until no further depth change could be made.

Once the needle was in place, the needle stylet was removed and a 1 mm diameter glass bead was inserted using a second stylet with its tip cut off, allowing the bead to be dropped exactly at the end of the needle cannula. To be able to distinguish the inserted bead from the target bead, the needle was then retracted a few millimeters, and a second bead was deposited in line with the first, acting as a marker for the CT images (see Figure 3-25).

Targets that were near the anterior surface of the prostate were approached at a 10° horizontal and vertical inclination to simulate pubic arch avoidance. All the other targets were approached in a horizontal, cranial-caudal direction, as in the conventional template-based brachytherapy technique.

The phantoms were then imaged in a Philips Brilliance 64 clinical CT scanner at a scanning resolution of 0.15 x 0.15 mm per pixel and 0.33 mm slice spacing. The target and inserted beads were segmented by hand, at high zoom in each phantom, and the distance between them was measured. During needle insertion, the total amount by which the robot corrected the needle depth after registration was recorded as well.

Results

The results of the experiment are shown in Table 3-6. The measurements done on each target are explained in Figure 3-26. Of the 108 available target beads, half were near the apex of the prostate, while the other half were near the base. Some target beads, primarily at the base of the prostate, were difficult to segment reliably and were consequently discarded, resulting in 50 measurements at the apex and 40 at the base.

The average amount by which the needle depth was corrected after image registration, was 4.36 mm for needles inserted at the apex and 6.94 mm at the base of the prostate. This can be understood as the amount of prostate motion in the needle insertion direction. The average

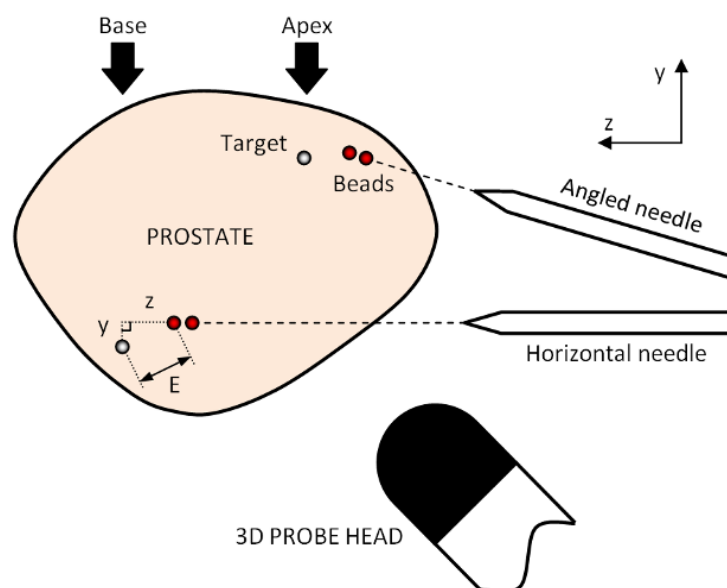


Figure 3-26: Illustration of the measurements done during phantom testing. E stands for Euclidean distance. The x-direction comes out of the page.

Table 3-6: Phantom experiment results, showing the distances between the target and inserted beads as measured in the CT images. The results are stratified by their spatial locations inside the prostate (in patient coordinates). All distance and depth values are in mm. The mean distance column represents the x, y and z projections of the Euclidean distance onto the needle axis. All distance measurements were done after depth correction.

Location	# of beads	Mean Euclidean distance (STD)	p Value	Mean distance (STD)			Mean depth correction (STD)	p Value
				x	y	z		
Apex	50	2.28 (0.73)	< 0.001*	1.15 (0.77)	0.94 (0.66)	1.37 (0.79)	4.36 (1.73)	< 0.001*
Base	40	3.86 (1.27)		2.40 (1.72)	1.52 (0.96)	1.91 (1.00)	6.94 (1.71)	
Center	28	2.73 (1.05)	0.002*	1.57 (1.27)	1.14 (0.77)	1.45 (0.73)	5.36 (2.38)	0.6
Right	32	3.76 (1.38)		2.45 (1.66)	1.44 (1.05)	1.83 (0.94)	5.32 (2.23)	
Left	30	2.38 (0.90)		1.04 (0.82)	0.99 (0.62)	1.53 (1.04)	5.21 (2.23)	
Anterior	52	2.92 (1.18)	0.59	1.51 (1.23)	1.16 (0.87)	1.76 (0.98)	5.04 (2.28)	0.18
Posterior	38	3.07 (1.40)		1.97 (1.62)	1.25 (0.84)	1.41 (0.80)	5.83 (1.92)	
Horizontal	67	3.08 (1.31)	0.28	1.78 (1.51)	1.20 (0.81)	1.69 (0.92)	5.26 (2.36)	0.18
Angled	23	2.68 (1.15)		1.50 (1.11)	1.19 (0.98)	1.37 (0.90)	5.85 (1.35)	
Overall	90	2.98 (1.27)		1.70 (1.42)	1.20 (0.85)	1.61 (0.92)	5.35 (2.20)	

Euclidean distance between the centers of the target and inserted beads was 2.98 mm for all the insertions. The distance in the horizontal cranial-caudal depth direction (i.e. in the needle insertion direction) was 1.61 mm.

Looking at the results based on their spatial location within the prostate, we can make a number of observations. First of all, the mean distance between the centers of the target and inserted beads at the apex was significantly less than at the base (2.28 mm at the apex, 3.83 mm at the base, $p < 0.001$). Accordingly, the amount of depth correction required at the base was significantly greater than at the apex (4.36 mm at the apex, 6.94 at the base, $p < 0.001$). The accuracy of angled needles compared to horizontal needles was not significantly different, although the former tended to be about 5% more accurate. There was also no significant difference between anterior and posterior insertions with a high p-value caused by the proximity of the two means and the relatively large spread (standard deviation) of the data. To lower this p-value, more insertions would have to be done. Where we do notice a significant difference is between left and right targets (3.76 mm on the right, 2.38 mm on the left, $p = 0.002$).

A large majority of the targets required only one single depth correction to reach the final insertion point, while about 5% required two or more corrections.

Timewise, an entire bead insertion, with one depth correction and two image acquisitions and registrations, took less than 3 minutes. Acquisition of the image volume by the 3D Ultrasonix probe took 17 seconds, while registration took 7 seconds (on the 40 MHz, 1.0 GB of RAM Ultrasonix RP system, running Windows XP Professional).

Sources of error

As described in section 2.5 (page 29), it is important to break down the sources of error in the experiments, in order to better understand the results. The sources of error can be split into extrinsic errors, specific to the experiment, and intrinsic errors specific to the robotic system itself. Figure 3-27 illustrates where the various sources of error occurred during the experiment.

One extrinsic error comes from the initial segmentation of the target beads in the reference US images. The amount of error attributed to this manual segmentation is difficult to quantify, however, the high zoom used during segmentation could allow us to estimate an error on the order of a voxel width or two, in addition to the error attributed to the image resolution itself (0.33 mm^3), resulting in a root sum of squares (RSS) error of 0.47 mm. This error means the initial target position sent to the robot was already inaccurate. Afterwards, once the result

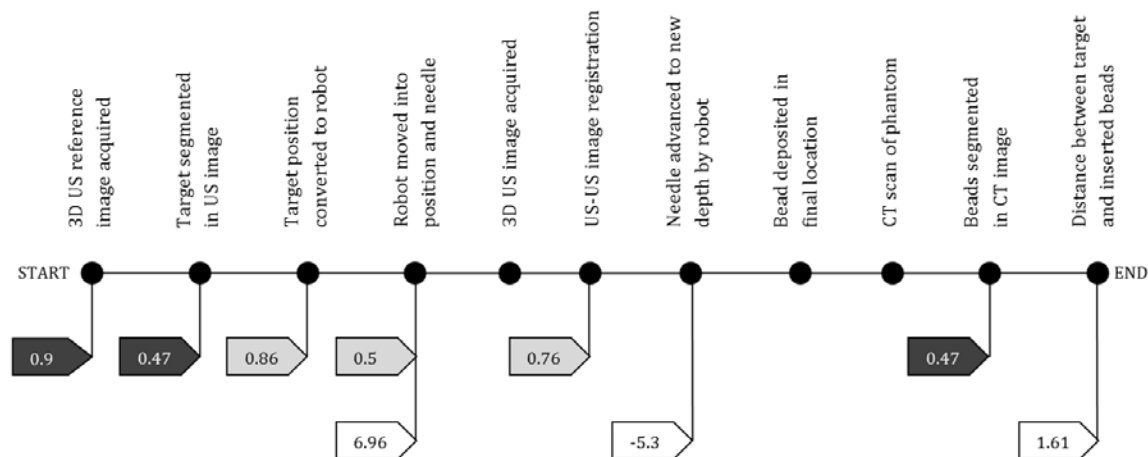


Figure 3-27: Rough timeline of the phantom experiment with the corresponding errors estimated or measured at each corresponding step (in mm). The light gray boxes represent the intrinsic system errors. The dark gray boxes represent the extrinsic experimental errors. The white boxes represent the measured distances between target and inserted beads (where 6.96 mm is the distance before depth correction, -5.3 mm is the amount corrected by the system in the z-direction and 1.61 mm is the final mean distance in the z-direction).

was obtained, in the form of the CT image, a similar manual segmentation error was also present (0.47 mm as well). The total RSS segmentation error affecting the accuracy measurements could therefore, be estimated at 0.66 mm.

Another extrinsic source of error that affected the results was the speed of sound used in the reconstruction of the US images, which, as described in section 3.3.1 (page 58), was found to be 1380 ± 20 mm/s and therefore a maximum error of 0.9 mm for the deepest targets. Combining this with the segmentation error results in a RSS measurement error of 1.1 mm.

The sources of error intrinsic to the PROSPER system itself include the kinematic (0.5 mm) and robot-probe calibration (0.86 mm) errors described in the previous sections, as well as the US-US image registration error (0.76 mm). Combining these with the measurement error would give an RSS error of 1.68 mm, which approaches the 1.61 mm mean final accuracy measured in the needle direction during the experiments.

Analysis

The purpose of this phantom experiment was to determine how well the PROSPER system was able to compensate for prostate motions and deformations due to needle insertion by adjusting only along the needle line. The results show that in our synthetic phantoms, needle insertion caused significant motion, on the order of 4 to 7 mm. Without the registration step, the resulting seed distribution would have been significantly offset from the planned distribution. By correcting the needle depth based on the prostate motion, the accuracy of the system in the needle insertion direction was improved by 75% to less than 2 mm, which is an encouraging result, given it includes non-negligible measurement errors and errors inherent to the experiment itself.

The overall mean accuracy of 2.98 mm for all the tests was above the 2 mm goal set in section 3.2.1. A significant part of this error came from the targets being off-axis from the needle line (i.e. x and y errors), which can be attributed in part to the rotation of the phantom prostate during insertion. As described in section 3.3.1, the realism of this rotation in the phantom model was uncertain making it difficult to know how representative this overall error is. This accuracy does, however, compare favorably to the other proposed computer-assisted brachytherapy systems listed in Table 2-1 (page 22) which mostly range between 1 and 3 mm. All of these systems were evaluated on static, non-deformable or low-deformation phantoms

without mention of motion correction, so our result is especially encouraging, as it includes prostate motion.

The essential conclusion drawn from the experiments was that the system was capable of reducing the errors caused by prostate mobility in the cranial-caudal direction in a quantifiable manner. This was true for the different depths of insertion and approach angles tested. In the conventional template-based technique, clinicians can adjust the dose plan in the cranial-caudal direction, but this is done by eye and is approximate, making it difficult to ensure an accurate dose distribution. Although further definitive *in vivo* studies need to be done, it has been stated in the literature that the primary axis of prostate mobility during brachytherapy is along the needle insertion axis [72] [74].

The spatially stratified results present some significant differences between different areas of the prostate. The discrepancy between apex and base targeting accuracies can be explained in part by the phantom's prostate rotation. Although the cranial-caudal direction was the primary axis of mobility, our experiments did confirm that prostate rotation affects the results significantly. During needle insertion, the target was not only pushed in the z-direction, but also rotated away from the needle insertion axis, making the target unreachable without re-inserting the needle at a different approach angle. The deeper the insertion, the more the prostate rotated. It was also noticed that peripheral needles caused more rotation than central needles, as could be expected. An important future step for the success of any prostate needle insertion system would, therefore, be to determine the degree to which this occurs *in vivo* and to provide ways of mitigating this error, such as predicting motion with biomechanical models [225] or reducing prostate motion with stabilizing needles [75].

The differences between apex and base accuracies can also be attributed in part to the poorer US characteristics at the base. With an end-fire probe, the prostate base is further from the transducers than the apex, resulting in poorer resolution and increased reconstruction and measurement errors. This could be eliminated by the use of a side-fire probe (as mentioned in section 3.2.4, page 53) which would make the apex and base at equal depths from the US transducers.

The discrepancy between left and right insertions can be explained by the fact that this prototype tends to flex slightly about its forward vertical joint (J3 in Figure 3-7, page 44) during insertion, causing slight deviation of the needle tip towards the phantom's right. This deviation, in combination with the motion of the prostate, which tends to rotate about the probe head, created a cumulative deviation effect resulting in an increased error on the right side and a decreased error on the left side.

3.4 Discussion

The phantom study described in the previous section has shown promising results with respect to the potential added value of the system's organ tracking capabilities. Targeting accuracy with respect to the mobile prostate is improved, potentially allowing for the planned dose distribution to be achieved with higher fidelity. Because of the high concentration of radioactive seeds in the gland, and the proximity of important organs, such as nerve bundles, seminal vesicles, the urethra and the rectum, this could lead to a reduced rate of complications, such as incontinence and impotence. In addition, with the robot's ability to angle needles, cases in which the pubic arch shadows part of the prostate could become viable and easier to execute. The system does not add significant bulk to the conventional OR equipment and leaves the operating site accessible to the clinicians. It is also compatible with existing needles and seed applicators.

Perhaps one of the common critiques that could be made about the system is with respect to the automation of the needle insertion. As with any robotic device that takes over part of a manual act, clinicians could be hesitant to allow automation for two reasons: 1) patient safety and 2) the loss of tactile feedback during needle insertion. The first reason would evidently

require validation and redundancy measures to reduce the risk sufficiently to justify the increase in accuracy obtained. The second reason would not necessarily be a drawback since the needle depth is always known with respect to the prostate, due to the robot-probe calibration and so tactile feedback is no longer as necessary. If, however, automation were eventually to be a serious constraint, it would be very simple to modify the robot architecture such that the insertion DOF would be left entirely manual and the robot would simply position a mechanical constraint in order to restrict the insertion to the calculated depth.

Another important issue to discuss is the effect of needle insertion and progressive seed deposition on image quality and hence on the accuracy of the registration algorithm. The needle traces and seeds would add high intensity regions in the image that could adversely affect the registration between the current “dirty” image and the “clean” reference image. As mentioned in section 3.2.5 (page 54), the algorithm was originally developed in the context of prostate biopsies, and has been extensively tested on clinical cases [82]. During these clinical trials, certain elements were observed that are to our advantage. Although needle traces after needle removal were very evident in our phantom and cadaver tests, they are, in fact, very rarely observable in the clinical cases, as they fill with fluid (blood), which re-establishes an acoustic connection. Note that during the biopsies, a dozen needles were inserted and removed without observing any problem with the algorithm. In addition, the needle volume is very small when compared to the total image volume, making its impact very limited; the registration algorithm is quite robust, in fact, to localized changes in image intensity. As far as needle presence in the image is concerned, our system is based on a single-needle tactic, so only one needle is ever present in the image at a time. Our phantom experiments, as well as the clinical biopsy trials have clearly shown that this does not cause problems for our algorithm. Regardless, since we know the current location of the needle in the image, we could therefore ignore it during registration by applying an image mask [82]. This can also be done for the deposited seeds and will be the subject of future study.

As far as the robotic manipulator is concerned, the prototype developed during this thesis has underlined the need for a number of future design objectives. First of all, the weight and size of the prototype, although relatively small as it is, could be reduced. The main bulk of this prototype comes from the off-the-shelf stepper motors used to power the four parallel linear stages. By replacing them with smaller brushless servomotors, this bulk could be significantly decreased. The off-the-shelf linear stages are also not ideal for this application, as the carriages should be stiffer in order to make the robot more robust to user handling and needle forces. A slightly larger workspace could also be useful, such that higher needle inclination could be achieved throughout the volume of larger prostates.

One of the two main research objectives that still needs to be considered is improving the management of prostate rotational motions during needle insertion in order to further increase the system’s accuracy. The use of two or three pre-inserted stabilizing needles is the simplest solution, but needs to be examined with care since it could cause unnecessary added damage to the tissue and its efficacy in clinical situations is not clear in the literature. Another simple solution would be to withdraw the needle and re-insert it with an offset estimated by the clinician in order to counteract the rotation. Other more complex solutions would be to predict the motion using biomechanical models of the prostate and to use needle steering during insertion.

Another aspect would be an in depth clinical study to define how the prostate deforms and moves during needle insertion *in vivo*, as few detailed and accurate studies exist in the literature that quantify the 6 DOF translations, rotations and deformations that the gland experiences during brachytherapies [73] [72] [74] [186]. The other essential research objective, as mentioned in the section 3.3.2 (page 64), would be to determine whether needle rotation is clinically viable in terms of tissue damage.

As a final remark, the advantages of the PROSPER system are not only limited to brachytherapy. The system would be very adapted to targeted transperineal biopsies and focal therapy. Both of these applications go hand in hand since accurate focal therapy requires

accurate, localized diagnosis and both are affected by prostate mobility in the same way as brachytherapy. In addition, only small modifications to the insertion module would be necessary in order to adapt the robot to other types of therapies, such as RF ablation and cryotherapy.

Chapter 4: LPR – CT and MRI-guided abdominal and thoracic puncture robot

4.1 System description	77
4.1.1 Clinical incentive	77
4.1.2 General layout	77
4.1.3 Clinical workflow	78
4.2 Technical design	80
4.2.1 Technical constraints	80
4.2.2 Robot description	81
<i>Mechanical description</i>	81
<i>Robot workspace</i>	84
<i>Electronics description</i>	85
<i>Robot fixation</i>	85
<i>Sterilization</i>	86
4.2.3 Robot Kinematics	87
<i>Forward kinematics</i>	87
<i>Inverse kinematics</i>	90
4.2.4 Cable stretch	91
<i>Material choice</i>	92
<i>Cable tension</i>	92
<i>Housing curvature</i>	93
<i>Cable stretch calibration</i>	94
4.2.5 Robot-image calibration	96
<i>Fiducial design</i>	96
<i>Image processing</i>	97
<i>Coordinate frames</i>	102
4.2.6 User interface	103
4.3 Pre-clinical evaluation	105
4.3.1 MRI and CT compatibility	106
<i>CT compatibility</i>	106
<i>MRI compatibility</i>	106
4.3.2 CT and MRI phantom study	109
<i>Materials and methods</i>	109
<i>Results</i>	112
<i>Sources of error</i>	114
<i>Analysis</i>	115
4.4 Discussion	116

The Light Puncture Robot (LPR) is a CT and MRI-guided interventional radiology robot for needle-based diagnosis and treatments. Its main goal is essentially the same as the PROSPER robot: to percutaneously insert a needle into an internal target with high accuracy. Because of this similarity, the general research path followed to create it and validate its potential clinical value is nearly identical: definition of the clinical and technical constraints, design of the clinical protocol, design of the manipulator architecture, construction of a proof-of-concept prototype,

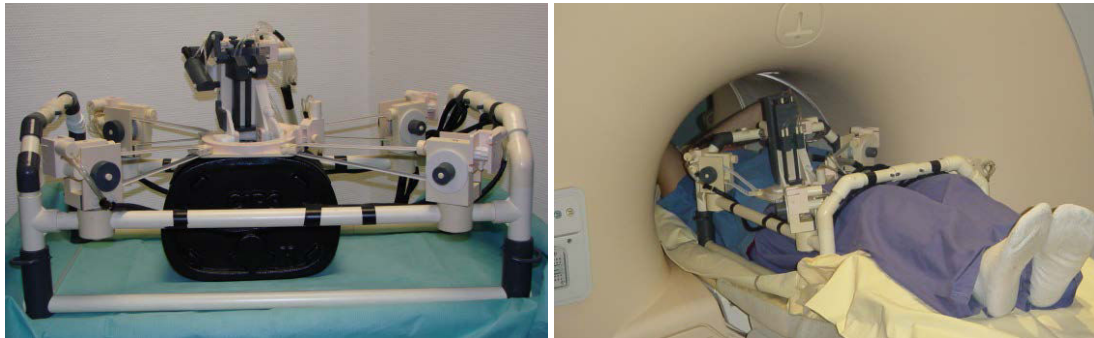


Figure 4-1: First version of the Light Puncture Robot (LPR) [85].

kinematic calibration, definition of an image-to-robot calibration technique, and phantom validation testing. Its clinical setting, however, makes its technical and design constraints quite different, giving rise to other research challenges.

The LPR project dates from 2004 and has seen the extensive development and testing (phantom and live animal testing) of a first prototype system, shown in Figure 4-1 [86] [85] [84]. As mentioned in section 2.1, this first prototype was not entirely suitable for clinical use. Firstly, although the needle insertion module was light and relatively compact, the size of the surrounding frame limited the size of patient that could fit inside. Secondly, the pneumatic actuators, although fully MR and CT-compatible, resulted in slow motions and significant noise during pressure-release. Thirdly, 32 pneumatic cables were necessary to control the robot, making installation difficult and the risk of pressure loss due to air leaks a constant issue. Finally, and most importantly, after much thought and brainstorming, it was realized that the prototype as it was, was impractical (if not impossible) to sterilize due to its large overall size and direct contact with the patient. A new prototype iteration was clearly necessary to improve on these issues.

The goal of the LPR project is to provide increased needle targeting accuracy with greater ease and fewer image acquisitions, in particular for difficult, out-of-plane anatomically constrained insertions (such as between the ribs). The originality of the project, with respect to other robotic systems (see section 2.2, page 20), is its multi-modality and its generic design, adapted to a large spectrum of needle-based IR procedures. This improves its potential clinical value for both patients (by offering a greater number of possible interventions) and hospitals (by offering a more generic tool, usable in more situations). As we can see in Table 2-1 (page 22), compared to most other robotic IR solutions in the literature, the LPR also presents the particularity of being patient-mounted, allowing it to move with the patient's body in case of involuntary motion.

The new prototype was designed by Nabil Zemiti, a postdoc in our laboratory. At the beginning of this thesis, construction of this prototype had already been started and the actuators chosen. The purpose of this thesis was to fine-tune the prototype, design and build the electronics for controlling the system, define the fiducial material used to find the robot in the images, program an automatic fiducial segmentation routine for robot-image calibration, design and program the control software for piloting the robot and implement the whole system in order to carry out feasibility tests to justify a clinical version.

This chapter describes the design and testing of the new LPR prototype, following the same layout as Chapter 3. It begins with a general description of the proposed system, its clinical constraints, its layout in the imaging room and the proposed clinical workflow. The technical details of the new prototype are then describe, including its mechanics, electronics, kinematics as well as the technique used to calibrate it with the image coordinates. The chapter ends with a description of the various pre-clinical tests done on the system, in particular the CT and MRI compatibility tests, sterilization tests and phantom target accuracy tests.

4.1 System description

4.1.1 Clinical incentive

As we have described in section 1.1 (page 3), IR has become a very important medical field, offering a large range of interventions. The main advantage of IR is its ability to provide highly accurate diagnoses and treatments in a very minimally invasive manner. This, coupled with an increase in medical imaging quality and availability, has led to IR being used for increasingly challenging procedures and by an increasing number of radiologists.

At the CHUG, our partner radiologists have expressed the need for developing a technique for facilitating the accurate targeting of internal lesions, in particular for challenging situations involving oblique insertion paths and tight insertion corridors. Two solutions have been conceived from this need. The first involves a CT navigation system now commercialized by the start-up IMACTIS (Grenoble, France) [13]. Their solution uses a hand-held needle guide and magnetic motion tracking system to allow the radiologist to automatically scroll through a 3D CT volume by moving the needle above the patient. It helps the radiologist to align the needle along the desired trajectory, simplifying this often spatially complex task.

Although the IMACTIS system presents clear benefits over the conventional navigation-less technique, it is only compatible with CT imaging. Indeed, the radiologists at the CHUG have conveyed the need for a multimodal technique that would allow targeting under both CT and MRI guidance and hence allowing them to take advantage of the complementary information acquired by each modality. The LPR system was conceived from this need.

4.1.2 General layout

The general layout of the new LPR system is shown in Figure 4-2. It consists of certain elements that are located inside the imaging room and other elements that are in the imaging

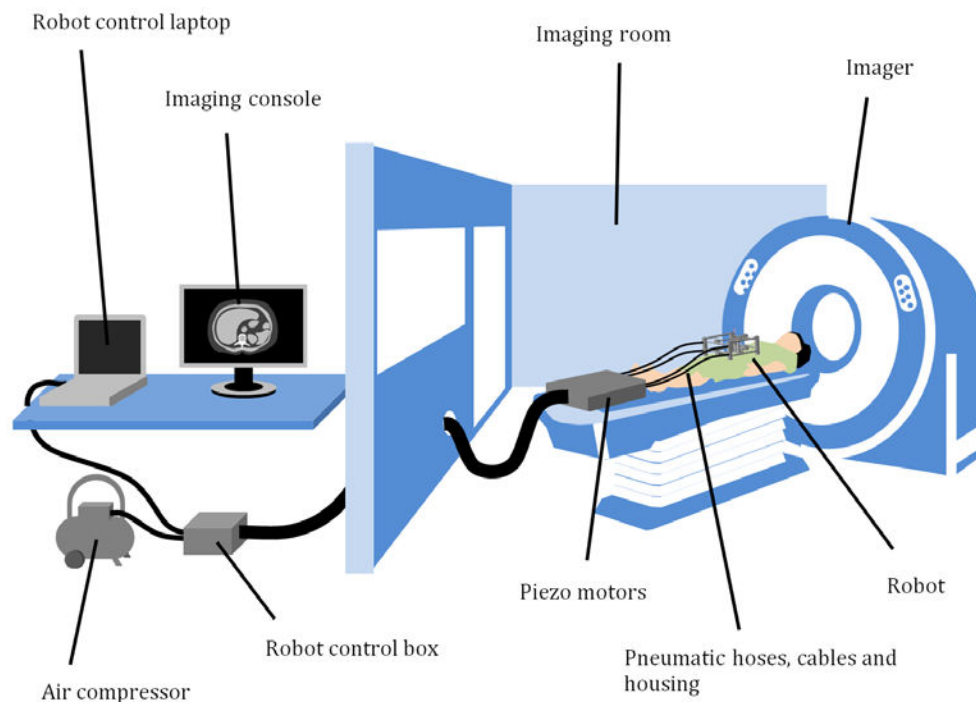


Figure 4-2: General layout of the various components of the LPR system within the imaging room.

control room. The robotic needle manipulator is strapped to the patient's body. The motors used to move the robot are placed at the patient's feet on the imaging table and remotely actuate the robot's joints through Bowden cable systems. This allows the motors to be permanently outside of the imaging tunnel, reducing the risk of image artifacts and making the structure on the patient's body lighter. Pneumatics are used to clamp and insert the needle in order to provide the strength and rapid action required by these binary motions.

The control box used to control the motors and pneumatics is located outside of the imaging room to prevent any effect on imaging compatibility, in particular for MRI interventions. The electrical motor cables and pneumatic actuation hoses that supply the motor box, pass through the control hatch between the imaging room and the control room. Air pressure can be provided either by the hospital air supply that is usually found in or near the imaging rooms, by bottled medical air, or by a portable electric compressor. The whole system is controlled by a single laptop pc that is connected to the hospital's DICOM server in order to receive images automatically.

4.1.3 Clinical workflow

The goal of the LPR's clinical workflow is not to change the conventional workflow as described in Figure 1-1 (page 2), but rather to render certain steps more efficient and repeatable, namely the needle insertion steps.

Table 4-1 compares the various steps between the conventional CT-guided technique and the robotic technique proposed for the LPR system. The patient is first installed on the imaging table in dorsal, ventral or lateral decubitus position. The radiologist then determines the approximate location of needle insertion on the patient's body by visual or palpation landmarks. Next, in the conventional technique, a CT-visible linear marker is taped on the patient's body

Table 4-1: Comparison between the conventional and robotic IR workflows. The LPR technique follows the same steps as the conventional technique except where indicated in the LPR column. The radiologist location column shows when the radiologist must move from the patient's side to the control room and back.

Step	Conventional technique	LPR technique	Radiologist location	
			Conventional	LPR
1	Patient installed		By patient	By patient
2	Approximate insertion point located			
3	Marker installed	Robot installed		
4	First image acquired		In control room	In control room
5	Target located and insertion point defined in image			
6	Insertion point located on patient with respect to marker	Needle automatically positioned and oriented above insertion point by robot	By patient	
7	Alignment of needle along insertion path			
8	First shallow needle insertion	No insertion yet		
9	Image acquired		In control room	
10	Verification of needle insertion point and trajectory <i>If KO go to step 11. If OK go to step 12.</i>	Automatic verification <i>Fewer KOs?</i>		
11	Realignment of needle trajectory <i>Back to step 9</i>	Automatic realignment of needle trajectory by robot	By patient	
12	Measurement of distance left to target in image <i>If target reached go to step 14. Else go to step 13.</i>	Automatic measurement	In control room	
13	Small needle insertion <i>Back to step 9.</i>		By patient	
14	Image acquired		In control room	
15	Prepare for diagnostic or therapeutic act	Needle released and robot removed	By patient	By patient

that is used as a reference point for finding the precise insertion point. This step is unnecessary in the robotic technique because the robot can automatically locate itself in the images, as will be described in section 4.2.5 (page 96). Instead, at this point, the robot is installed on the patient using straps to hold it in place.

Next, a volume image is taken of the patient, requiring the radiologist to leave the imaging room and enter the control room. For the robotic technique, the fiducial markers on the robot need to be visible in the image in order for the automatic calibration routine to work. This requires a larger FOV than that typically required in the conventional technique. The target and insertion points are then chosen manually in the image by the radiologist. This is done by first choosing the target and then extending a line out to the patient's skin along a viable insertion path that minimizes the risk of puncturing dangerous tissue.

The following two steps (6 and 7) of the conventional technique are the most challenging steps for the radiologist, that require him or her to return to the imaging room and keep the desired needle trajectory in his or her memory. To find the insertion point, the radiologist uses the CT-visible marker on the patient's skin as a reference point. The distance between this marker and the insertion point, measured in the image, is used to find the insertion location on the patient's skin. The needle orientation along the desired insertion path is the difficult part since no accurate reference is available to align the needle to. For this reason, radiologists often favour vertical insertion paths or paths that at least remain in the image plane (usually transverse). In the latter case, the angle within the image plane is estimated from the vertical or from the laser lines projected onto the patient by the CT scanner, and often requires the help of a second person in the control room who can compare the desired angle on the image screen with the angle applied by the radiologist. If more complex, out of plane insertions are required, this procedure becomes even more challenging. In addition, the radiologist must sterilize him or herself in order to handle the needle.

In the LPR technique, these two steps are automatically handled by the robot, allowing the radiologist to remain in the control room, in front of the images, and indeed, remain there until the end of the procedure. The software automatically locates the robot in the image and then moves the needle into position above the insertion point and along the desired insertion orientation. This significantly speeds up these steps and allows for any orientation to be chosen without jeopardizing the ease of the operation. In addition, this can all be done without withdrawing the patient from the imaging tunnel, which is useful in particular for MRI-guided procedures where the tunnel is very deep.

Next, in the conventional technique, the radiologist inserts the needle partially until the needle stays in place. He or she then leaves the room again for a second image acquisition that is used to verify the needle insertion point and direction. If the needle is not properly aligned, it is usually withdrawn and a new partial insertion is done. In the robotic technique, since the robot is holding the needle in place, this control image can be done without inserting the needle, reducing the trauma (albeit minor and superficial) of multiple needle reinsertions. Because of the accuracy of the robot, the number of these realignment steps that are necessary to get the needle on the right track can hopefully be reduced if not completely eliminated compared to the conventional technique. This once again potentially speeds up the intervention and decreases the radiation dose received by the patient by reducing the number of images needed. In addition, the verification of the needle position in the image is done automatically with the LPR, based on the robot's position in the image, instead of the radiologist visually checking the image. This is particularly important in MRI since the needle is not directly visible and its position can only be determined from the susceptibility artifact that it leaves in the patient's tissue.

Once the needle is appropriately positioned and aligned, the radiologist returns to the patient's side and applies a further small insertion to a depth dependent on the proximity of dangerous anatomical features, the necessity to pass from one organ to another in a single shot (to prevent the needle tip from lacerating the connective tissue or organ surfaces while the patient breathes and the organs move), and the skill of the radiologist. At each insertion depth, a control image can be taken to check if the needle is still on the path and to measure the

remaining depth to reach the target. The needle can sometimes be partially retracted and its direction can be realigned to a certain degree in order to correct its path. This is possible with the LPR robot as well.

Once the target is reached, the diagnostic or therapeutic act can be done. In the robotic technique, the needle is released and the robot is removed in order free the operating site.

From the above comparison, we can notice the important difference in the number of times the radiologist needs to go between the patient's side and the control room. This, in itself, is perhaps not a clinical advantage (although it could reduce the procedure time), however, since the radiologist is fully sterilized, he or she needs to take care in order not to brush against the non-sterile environment between the imaging room and the control room.

The potential advantages of the robotic technique are therefore to make the procedure less image intensive and easier, in particular for more complex, out of plane insertions. It also makes it possible to do such procedures under MRI guidance using standard closed-bore MRI machines. It is important to note that, although a number of the robotic steps are automated, they are all ultimately verified by the radiologist in the images; no step is initiated without the validation of the radiologist.

4.2 Technical design

This section describes the technical aspects of the LPR system. This includes a description of the technical constraints imposed by the clinical setting, a description of the pre-clinical prototype developed and constructed, its kinematics, and the automatic calibration method used to find the robot in the images.

4.2.1 Technical constraints

The clinical setting of the LPR system is very different from PROSPER. This is mainly due to the type of image guidance used to control the robot: CT and MRI as opposed to US. The patient position and the needle approach direction is also an important factor. Unlike the transperineal access used in PROSPER which is fairly constrained by the patient's legs, the LPR's access through the skin of the patient's abdomen results in a fairly generic access that could benefit from a larger robotic workspace.

The major technical constraints that we adhered to during the design of our prototype were the following:

- *4 DOF for needle positioning*: three for x-z positioning of the needle tip and two for needle orientation in the transverse and sagittal planes.
- *1 DOF for needle insertion*.
- *Automated needle gripping*: to allow incremental insertion steps.
- *Visibility*: must be segmentable in both CT and MRI modalities.
- *Image compatibility*: the robot must be entirely compatible with the CT and MRI imaging modalities.
- *Size constraints*: the robot must be able to fit inside the CT and MRI tunnels while mounted to a patient.
- *Translational workspace*: should have a relatively large x-z workspace (minimum 100 × 100 mm) to give the radiologist more flexibility in the initial positioning of the robot on the patient, without necessarily requiring an initial image.
- *Orientation workspace*: large pitch and yaw inclinations ($\pm 30^\circ$) to give a large range of needle orientations.
- *Robot mounting*: the robot must be mounted to the patient in order to follow his or her movements during the intervention.

- *Needle compatibility*: must be compatible with existing needles of varying diameters.
- *Safety*: must ensure the safety of the patient and operating room staff.
- *Sterilization*: must meet IR sterilization constraints.

The desired accuracy of the LPR system depends on the minimal size of lesion that the system is likely to be used on. Lesion size is not, of course, the only criterion used to determine whether a lesion requires IR-based diagnosis or treatment. Other criteria, such as lesion location, lesion dispersion, lesion density, lesion appearance, lesion growth rate, patient symptoms and patient history are important in the clinician's decision. It is difficult, therefore, to pinpoint an exact minimum lesion size that the system would be expected to deal with, in particular because of the large array of IR procedures accessible to the system. Since the needle trajectory often passes near neighbouring vital tissues, the needle's orientation accuracy is also important.

According to our partner radiologists, the minimum size of lesion likely to be targeted using CT or MRI is 10 mm in diameter, although this depends highly on the organ and clinical problem. Smaller lesions can be difficult to locate in the images and are often not considered clinically serious enough to warrant invasive diagnosis or treatment. Indeed, for lung cancer, the US-based International Early Lung and Cardiac Action Program (IELCAP), recommends biopsy of nodules between 5.0 and 15.0 mm in diameter having a 20 to 50% growth rate over 3 months [226] [227]. We therefore chose a desired accuracy of less than 5 mm, which would allow lesions with at least a 10 mm diameter to be successfully targeted.

To take into account the needle's orientation accuracy, we choose to extend the targeting accuracy along the entire needle's insertion length, making a 10 mm diameter cylinder spanning from the skin insertion point down to the target, within which the needle must remain. By knowing the size of this cylindrical insertion zone, the radiologist can choose an appropriate insertion trajectory that stays at least 5 mm away from neighbouring vital tissues.

Although 5 mm is largely sufficient for the majority of interventions, if the robot is to target interventions, such as spinal injections and joint infiltrations, its accuracy must be significantly higher. The epidural space, commonly targeted during spinal injections, has been measured to range from 1.1 to 6.5 mm depending on its rostral-caudal location [228]. For these particular interventions, the ideal desired accuracy would therefore have to be less than 1 mm, allowing lesions with at least a 2 mm diameter to be targeted.

4.2.2 Robot description

This section describes the mechanical architecture of the LPR manipulator, its workspace, the electronics used to control it, its fixation to the patient as well as its sterilization.

Mechanical description

The pre-clinical prototype of the LPR robot built during this thesis is shown in Figure 4-3. It is based on a 5 DOF parallelogram design, in which the needle is held by two parallel platforms, 85 mm apart, and that enables planar translation of the needle in the x-z plane and inclination about the x and z axes. The needle is held by two independent grippers, the upper one being mounted on a vertical slider and providing the needle insertion force, as shown in Figure 4-4. The frame is strapped to the patient's body to follow external movements.

Needle insertion is done incrementally by sequentially activating the two needle grippers and the insertion slider (see Figure 4-4). The stroke distance is regulated by a controllable stop designed during this thesis that blocks the vertical slider's path at a desired depth. The stop height is regulated by a screw connected to a set of reduction gears.

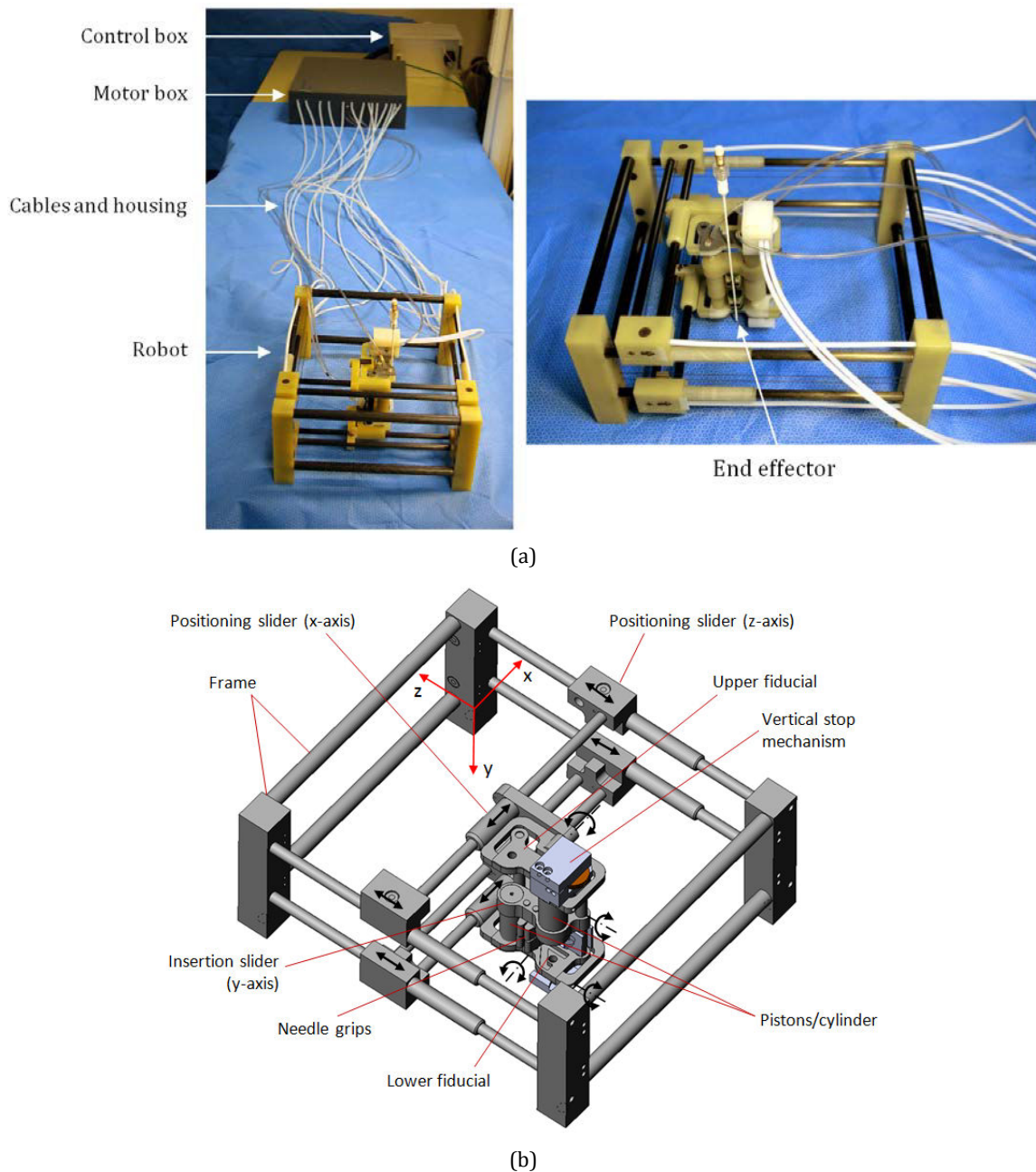


Figure 4-3: The new LPR robot architecture. (a) A photograph of the prototype LPR system (left) and close-up of the robot (right) showing the end effector location at the needle's tip. (b) A CAD drawing showing the various components and degrees of freedom of the robot.

Translation of the four x and z sliders is achieved through four Shinsei USR60-E3N ultrasonic motors. Their torque (max. 1 Nm) and speed (rated 100 rpm) ratings are easily sufficient for the low friction characteristics of the robot. As studies have shown that these motors are capable of affecting an MRI image when powered inside the tunnel [182], it was decided to house them in a separate container placed on the scanner or MRI bed, at the patient's feet. They are connected to the robot by 1.5 m long cables and housing, ensuring that they are never inside the tunnel. As shown in Figure 4-5, each motor activates a pair of rack and pinions, which in turn pull the cables to translate their respective robot slider. The cable housing is made of Teflon, to reduce cable friction, while the cables are made of low stretch 0.4 mm diameter Spectra thread, typically used in archery. Separating the motors from the robot also reduces the robot's weight on the patient's body by 1.5 kg (total motor weight).

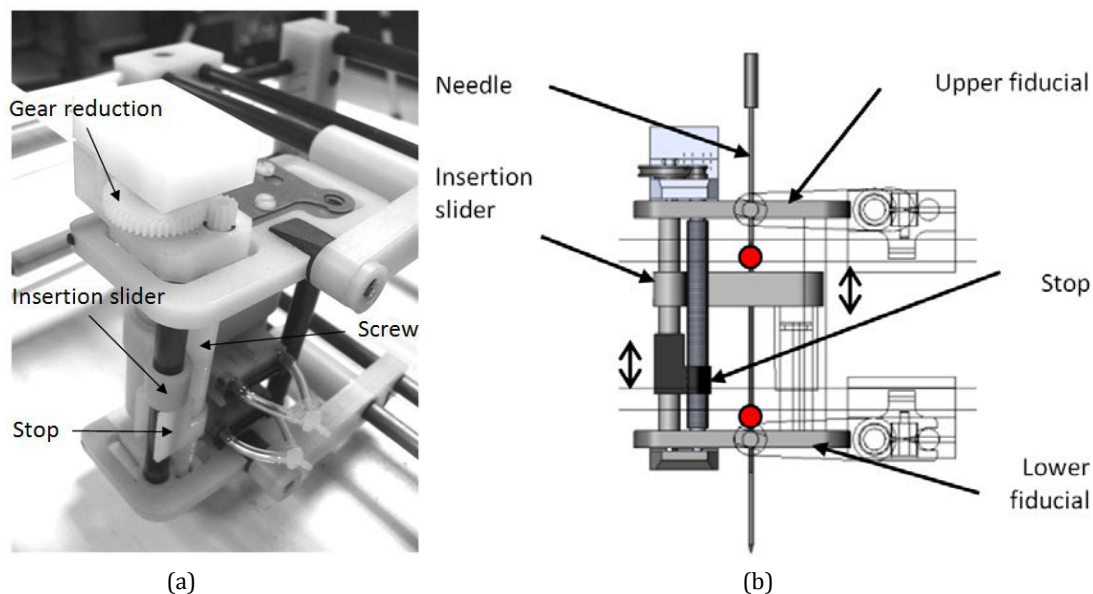


Figure 4-4: Stop mechanism for setting the insertion stroke. (a) Photograph of the prototype system. (b) CAD drawing highlighting the essential parts of the system. The needle grips locations are not shown but their positions are marked by red circles. The lower grip is stationary and the upper grip moves with the insertion slider.

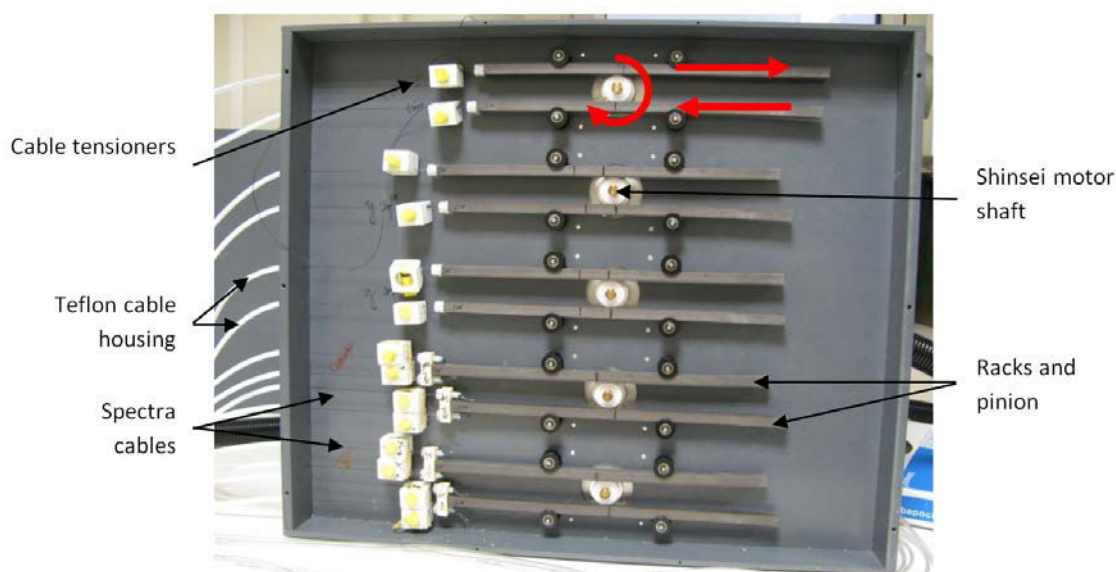


Figure 4-5: LPR motor box. The ultrasonic motors are mounted to the backside of the box. Each activated robot joint has a cable attached to its opposite sides that run through the cable housing to this motor box. When a motor turns, the pinion gear attached to its shaft activates the two symmetrical racks and subsequently pulls on one cable and releases the other.

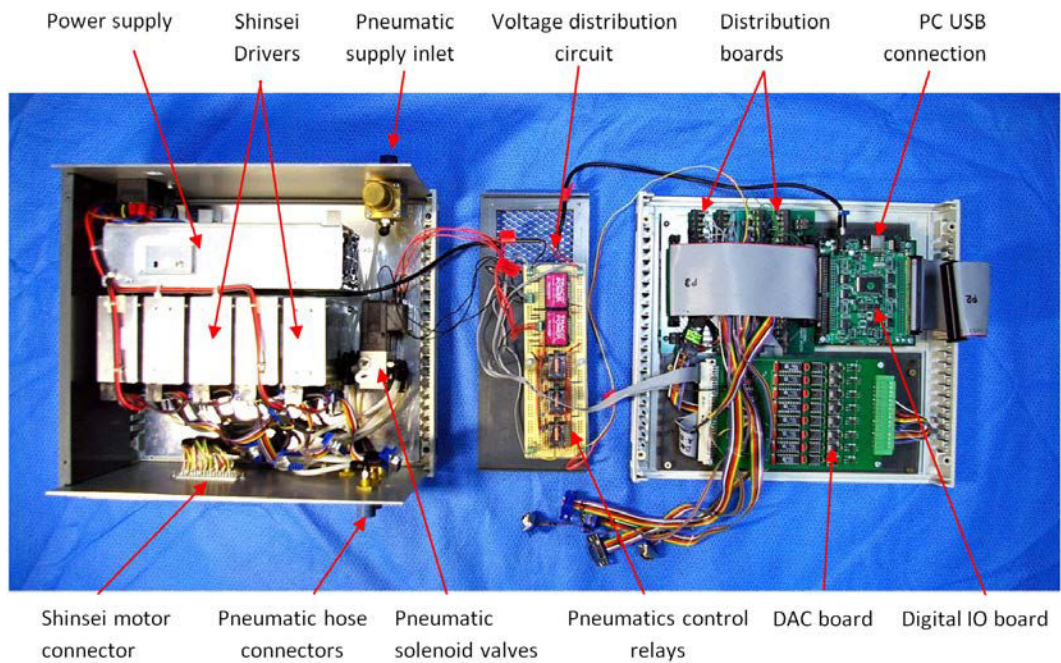
While the insertion stop mechanism is controlled by an ultrasonic motor, the insertion and retraction of the insertion slider as well as the two needle grippers are powered by pneumatics. Pneumatics were chosen in order to give sufficient power and speed to these vital elements of the robot. At a typical hospital air pressure of 4 bars, the needle insertion force is > 50 N, while the gripping force is 8 N. The latter increases to 13N at 5 bars, which is largely enough for typical needle insertion forces. The gripping force could be increased by increasing the area of contact and coefficient of friction between the grippers and the needle.

All the robot and motor unit materials consist of a combination of CT and MRI-compatible delrin, epoxy resin, carbon fiber and nylon materials. As will be described in section 4.2.5 (page 96), two fiducials are used to automatically locate the needle in the CT or MRI images. The fiducials are mounted on both parallel platforms as close as possible to the needle shaft,

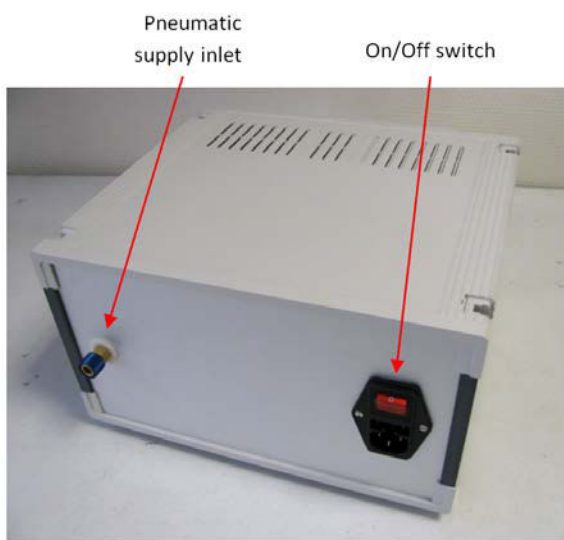
allowing for direct and accurate tracking of the needle position and inclination in the image (see Figure 4-4).

Robot workspace

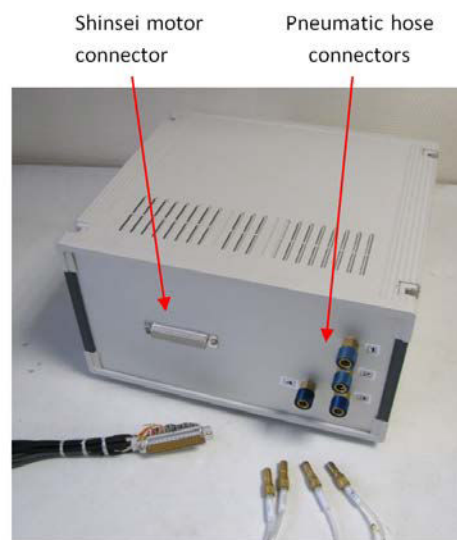
The robot manipulator has 5 DOFs, as shown in Appendix 3. It allows maximum planar translations of 135 mm in the x-direction and 120 mm in the z-direction, giving sufficient margin so that the clinician does not need to be very accurate in the initial positioning of the robot on the patient. In this prototype, inclination is limited to a range of 24° to -32° about the x-axis and 10° to -20° about the z-axis. In a clinical version, this range could easily be increased by slightly redimensioning the insertion module. The insertion stroke can be adjusted between 0 and 35 mm, allowing the clinician to choose the appropriate depth for each insertion step.



(a)



(b)



(c)

Figure 4-6: The electronics box used to control the LPR robot. (a) Inside view. (b) PC-side view. (c) Robot-side view.

Because of the dual grip system, the robot has no maximum needle depth, which depends rather on the needle length and the space available in the imaging tunnel.

Electronics description

The electronics used to control the robot is all contained in a single control box, as shown in Figure 4-6. The main component groups include a digital input/output (DIO) board for receiving the PC's commands and distributing them to the various components, the Shinsei motor drivers that convert the desired motor speed and direction signals into motor signals and the pneumatic solenoid valves that control the needle grips and insertion slider. Since the Shinsei motor drivers require an analog signal to set the motor speed, a digital-to-analog converter (DAC) board is used. Electrical relays are used to control whether the pneumatic solenoid valves are on or off. A power supply provides the general 24 V DC current to the control box which is then converted by a small voltage distribution circuit that supplies all the above-mentioned components with their various DC input voltages. The PC communicates with the control box through a single USB cable and the motor connector and pneumatic hose connectors all fit through the small 5 cm diameter control hatches found in the imaging rooms.

Robot fixation

The interface between the robot frame and the patient's body has not yet been constructed. Its function is to allow the robot to be solidly and comfortably fixed to the patient. It must hold the robot in place so that it does not move during needle insertion and so that it moves with the body in case of patient motion. It must also ensure that no superficial irritation or discomfort arises over the potentially hour-long intervention.

Two fixation solutions have been envisioned: taping the robot to the patient's skin with medical adhesive and strapping the robot down with straps running around the body of the patient. The first solution could potentially allow for more rapid installation but would be prone to motion during needle insertion because of skin flexibility. It would also cause problems with body hair. The strap solution, therefore, seems to be more adapted, although it requires a more thought out installation procedure with the non-sterile straps passing near the sterile zone. To get a preliminary idea of how solid strap fixation was, we strapped the LPR prototype to two volunteers of opposing physiques, using simple nylon straps tightened snugly around the body at breath inspiration. Pulling vertically on the frame of the robot with a dynamometer to around 60 N caused only a few mm of motion. Pulling horizontally to around

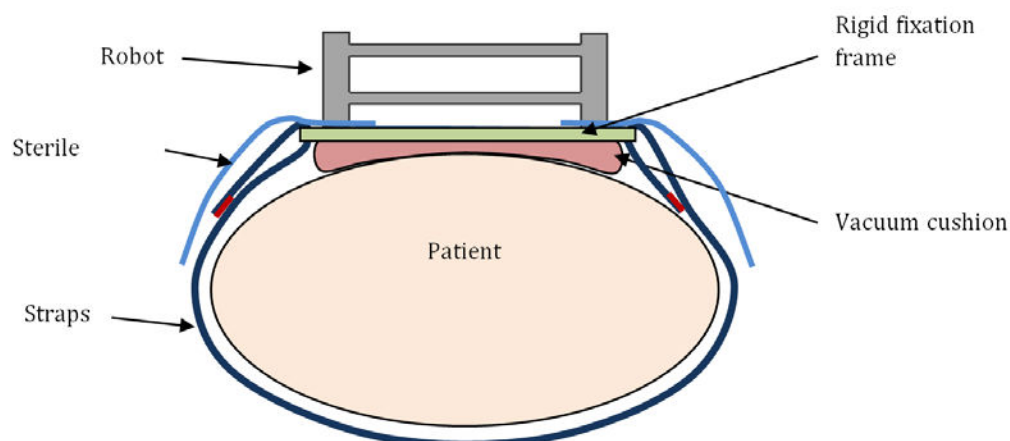


Figure 4-7: Schematic showing the proposed robot fixation system. The vacuum cushion is mounted to a rigid frame, both with an open window in the center, the size of the robot's workspace. These are placed on the sterile patient's body and fixed in place with the straps. They are then covered with a sterile drape with a similar access window and the sterile robot is clipped overtop.

10 N caused little more, showing the feasibility of the solution. Straps also have the advantage of restraining to a certain extent the external motion caused by respiration.

To be comfortable and to fit on any body type, the robot-patient interface must ideally mold to the patient's body. Foam padding could be used, but this would likely affect the rigidity of the fixation. An ergonomically shaped shell could be used, but this would be impossible to adapt to every body shape. The solution of using a mouldable vacuum cushion, proposed by [169] and commonly used for patient fixation in MRI and CT applications, seems like the most adapted to the large variety of body types and the rigidity required. The details of the solution are still being investigated, however the proposed setup is shown in Figure 4-7.

Sterilization

Compared to the PROSPER system, the LPR system is used in a less stringent operating environment. Typical CT and MRI rooms are open to the external environment, with no filtering of the air and no stringent entrance rules (such as hospital attire, masks, hairnets, etc.). That said, during an image-guided needle intervention, the sterility conditions around the operating site are practically identical. The needle must be handled by a sterile person and the patient must be draped appropriately to avoid any chance of the radiologist touching a non-sterile area (see Figure 1-3, page 6).

Like the PROSPER robot, the LPR robot operates within the sterile zone and therefore, all parts that are in direct contact with the needle must be sterile and all exposed parts that may come in contact with the radiologist must also be sterile. Since the needle is located within the confines of the robot's frame, requiring the clinician to reach inside to handle the needle, and since there are many moving elements that would be difficult to simply cover with sterile covers or drapes, it was decided to sterilize the entire robot and part of the cables leading to the motor unit. Any potential air leaks coming from the pneumatic system were deemed irrelevant, as the air in the imaging room is untreated, ambient air.

Autoclave sterilization was initially considered, however it would be very difficult to ensure the reliability of the many joints, plastic components and smooth surfaces needed for precise actuation of the robot. Instead, the robot was designed to fit into the STERRAD NX chamber available at the CHUG which is less demanding on the robot materials. Three aspects for successful sterilization were explored.

First, to fit into the sterilization chamber (170 x 300 x 600mm) it is necessary to disconnect the robot from the motor unit. A method of rapidly disconnecting the cables and housing between the robot and motor box is currently being developed, a preliminary version being shown in Figure 4-8. This will allow the entire robot and nearby cables to be placed in the sterilization chamber at once.

Second, as the compatibility of the carbon fiber bars used as sliders for the x and z joints of the robot with hydrogen peroxide gas was unknown, we decided to test this. We passed two carbon fiber samples through 25 normal sterilization cycles using the STERRAD NX machine. Visual microscopic comparison of the surfaces of these samples with non-sterilized samples, showed no evidence of surface decomposition, micro-fractures, or delamination of the fibers. Bend to fracture tests on these sample bars also showed no noticeable change in fracture strength and fracture mode.

Third, as temperature is not an acting sterilization agent in the sterilization technique chosen, it is necessary that all parts of the robot be reachable by the gas. This is especially the case for the cables hidden inside the 1.5 mm inside diameter cable housing, which during robot operation will emerge within close range of the needle, as they are pulled in and out. To verify the successful sterilization inside the cable housing, an experiment was undertaken in which 4 Spectra cables were impregnated with *Geobacillus Stearothermophilus* spores (standard bacterium used for validation of sterilization studies, including autoclave and gas-based techniques) and inserted into 30cm lengths of cable housing. Three of these were passed through a single STERRAD sterilization cycle, along with a batch of control spores in an open Eppendorf tube. The three sterilized samples, the control spores and the one non-sterilized

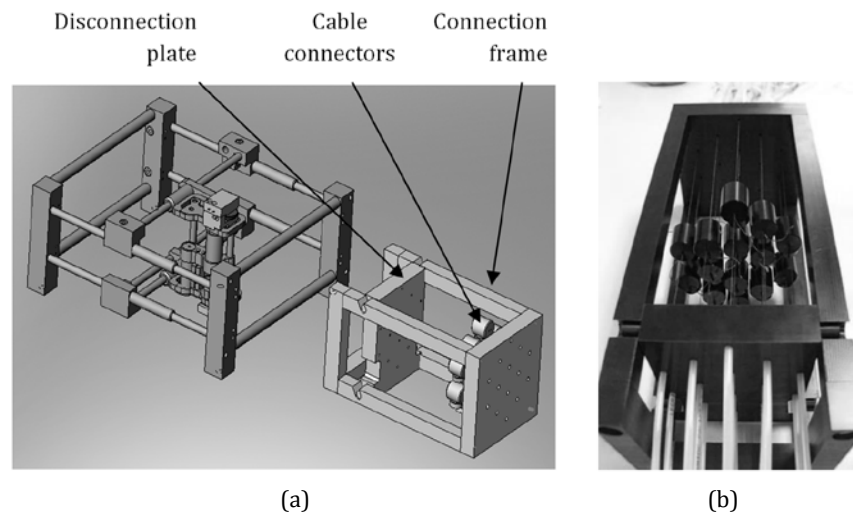


Figure 4-8: (a) CAD drawing of a preliminary prototype cable/housing connector used to disconnect the robot for sterilization. (b) Photograph of the built prototype. The idea consists in a connection frame that splits the cable housing in two. The disconnection plate separates from the frame and is sterilized with the robot while the connection frame remains connected to the motor box. The cables have connectors that allow them to be disconnected individually. A new, lighter version is being designed which allows all of the cables to be connected or disconnected simultaneously, thus preventing the risk of connecting together the wrong cables and significantly speeding up the procedure.

sample, were then put into cultivation at 60°C, and the optical densities (OD) were measured using a spectrometer for each cultivation solution at 24h and 72h. At both instances, only the non-sterilized sample showed any sign of bacterial proliferation (OD = 0.952, compared to OD < 0.014 for sterilized samples), confirming that the cables were successfully sterilized.

The two latter tests were used to confirm the feasibility of using STERRAD to sterilize the robot. However, before using it on a real patient, a set of sterilization tests on the entire robot as is, will be necessary in order to fully confirm its proper sterilization. For the CE marking of new medical devices such tests must be done by an external certified laboratory specialized in such tests.

The sterilization results discussed in this section were done in cooperation with Adeline Robert during her internship, and further details can be found in her report [229].

4.2.3 Robot Kinematics

The LPR manipulator's kinematic diagram is shown in Figure 4-9. Although the LPR prototype looks quite different from the PROSPER prototype, their kinematics are very similar. They are both parallelogram-type manipulators that rely on two pairs of parallel prismatic actuated joints to drive a set of five revolute joints. They can both be split into two kinematic chains leading from the base frame to the end effector. The difference comes in the orientation of the revolute joints and the lack of a fifth actuated joint in the LPR. This allows orientation of the LPR robot's end effector around a fixed point. Indeed, the needle's tip is located at the end effector in the home position (before insertion).

Forward kinematics

The likeness of the LPR manipulator to the PROSPER manipulator makes the solution of its forward kinematics practically identical. Indeed, as for PROSPER, the approach involves first calculating the location of frames 3 and 7 from the DH link transformations of each respective kinematic chain and then locating frame 9 by finding the intersection between the circle of constant radius A_7 and the sphere of constant radius A_9 .

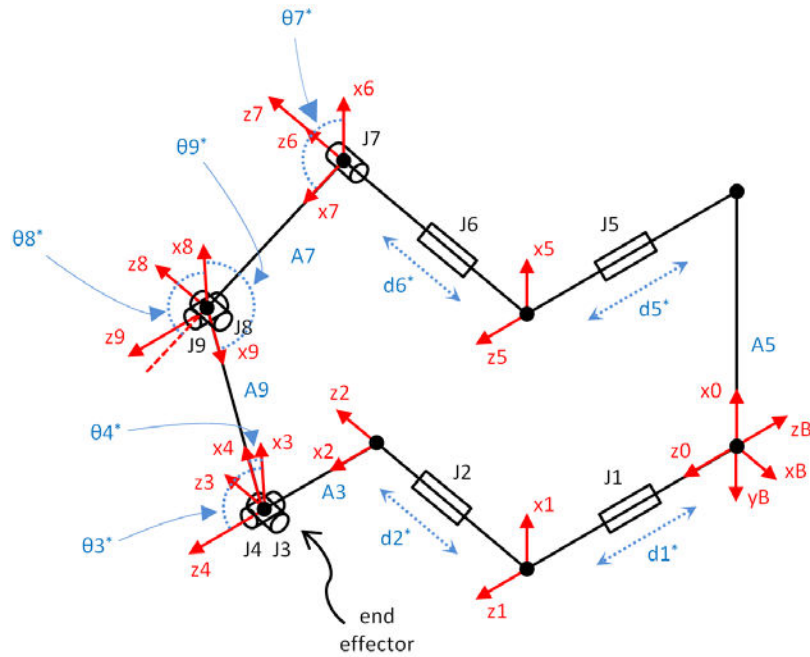


Figure 4-9: LPR manipulator kinematic diagram. The letter J represents the robot’s various joints. The thetas represent the variable angular positions of the revolute joints. Lowercase d’s represent the variable distances attributed to the robot’s actuated prismatic joints. Upper case A’s represent fixed link lengths. The reference frames attached to each of the manipulator’s links are shown in red, with only the x and z axes shown. The robot’s end effector is located at reference frame 4 but with a -90° rotation about the z-axis such that the y-axis points towards J9. The end effector location can be seen in Figure 4-3b. Before insertion, the needle tip is located at the end effector.

Table 4-2: The LPR robot’s DH parameters. Angles θ and α are written in degrees. Asterisks denote the mobile joint variables. All other values are constant regardless of the robot’s pose.

Link (i-1→i)	d_i ($x_{i-1} \rightarrow x_i$ along z_i)	θ_i ($x_{i-1} \rightarrow x_i$ about z_i)	a_{i-1} ($z_{i-1} \rightarrow z_i$ along x_{i-1})	α_{i-1} ($z_{i-1} \rightarrow z_i$ about x_{i-1})
<i>Chain 1</i>				
B→0	0	90	0	180
0→1	$d1^*$	0	0	0
1→2	$d2^*$	-90	0	-90
2→3	0	$\theta3^*$	A3	0
3→4	0	$\theta4^*$	0	90
4→ee	0	-90	0	0
<i>Chain 2</i>				
0→5	$d5^*$	0	A5	0
5→6	$d6^*$	0	0	-90
6→7	0	$-\theta7^*$	0	0
7→8	0	$\theta8^*$	A7	0
8→9	0	$-\theta9^*$	0	90
9→4	0	180	A9	0

The DH parameters for the LPR robot are listed in Table 4-2. The link transformations for the robot’s two kinematic chains are as follows:

Chain 1:

$$T_{Bee}^1(d_1^*, d_2^*, \theta_3^*, \theta_4^*) = T_{B0} \cdot T_{01} \cdot T_{12} \cdot T_{23} \cdot T_{34} \cdot T_{4ee} \tag{4.1}$$

Chain 2:

$$T_{Bee}^2(d_5^*, d_6^*, \theta_7^*, \theta_8^*, \theta_9^*) = T_{B0} \cdot T_{05} \cdot T_{56} \cdot T_{67} \cdot T_{78} \cdot T_{89} \cdot T_{94} \cdot T_{4ee} \tag{4.2}$$

As in PROSPER, the length variables d^* represent all the known actuated joint variables and the angular θ^* variables are the unknown revolute joint variables. We use the first chain to calculate our forward kinematics.

To find the unknown joint angles θ_3 and θ_4 , we first find the positions of frames 3 and 7 using their respective link transformations from the base frame:

$$T_{B3}(d_1^*, d_2^*, \theta_3^*) = T_{B0} \cdot T_{01} \cdot T_{12} \cdot T_{23} = \begin{bmatrix} 0 & 0 & -1 & -d_2^* \\ -\sin \theta_3^* & -\cos \theta_3^* & 1 & 0 \\ -\cos \theta_3^* & \sin \theta_3^* & 0 & -d_1^* - A3 \\ 0 & 0 & 0 & 1 \end{bmatrix} \quad 4.3$$

$$T_{B7}(d_5^*, d_6^*, \theta_7^*) = T_{B0} \cdot T_{05} \cdot T_{56} \cdot T_{67} = \begin{bmatrix} 0 & 0 & -1 & -d_6^* \\ -\cos \theta_7^* & -\sin \theta_7^* & 1 & -A5 \\ -\sin \theta_7^* & \cos \theta_7^* & 0 & -d_5^* \\ 0 & 0 & 0 & 1 \end{bmatrix} \quad 4.4$$

Next, we find the intersection of the **sphere** of radius $A9$ centered at frame 3 and the **circle** of radius $A7$ centered at frame 7:

$$(x - x_3)^2 + (y - y_3)^2 + (z - z_3)^2 = r_9^2 \quad 4.5$$

$$(y - y_7)^2 + (z - z_7)^2 = r_7^2 \quad 4.6$$

$$x = -d_6^* \quad 4.7$$

where:

$$\begin{aligned} x_3 &= -d_2^* \\ y_3 &= 0 \\ z_3 &= -d_1^* - A3 \\ r_9 &= A9 \\ y_7 &= -A5 \\ z_7 &= -d_5^* \\ r_7 &= A7 \end{aligned} \quad 4.8$$

which gives:

$$y_9 = y_3 + \frac{(R^2 - r_7^2 + P^2)(y_9 - y_3)}{2P^2} \pm \sqrt{R^2 - \left(\frac{R^2 - r_7^2 + P^2}{2P}\right)^2} \frac{(z_9 - z_3)}{P} \quad 4.9$$

$$z_9 = z_3 + \frac{(R^2 - r_7^2 + P^2)(z_9 - z_3)}{2P^2} \mp \sqrt{R^2 - \left(\frac{R^2 - r_7^2 + P^2}{2P}\right)^2} \frac{(y_9 - y_3)}{P} \quad 4.10$$

where:

$$R = \sqrt{r_9^2 - (-d_6^* - x_3)^2} \quad 4.11$$

$$P = \sqrt{(y_3 - y_9)^2 + (z_3 - z_9)^2} \quad 4.12$$

and because of the elbow-out configuration we can always choose the smallest y and the smallest z solutions. Like for the PROSPER kinematics, P is the distance between the centers of the sphere and circle. Therefore, if $P = (r_9 + r_7)$, then the robot is at a singularity point, with links A9 and A7 fully stretched out. This and $P > (r_9 + r_7)$ should never occur if the robot limits are carefully chosen.

In summary:

$$(x_3, y_3, z_3) = (-d_2^*, 0, -d_1^* - A3) \quad 4.13$$

$$(x_7, y_7, z_7) = (-d_6^*, -A5, -d_5^*) \quad 4.14$$

$$(x_9, y_9, z_9) = (-d_6^*, \text{Equation 4.9}, \text{Equation 4.10}) \quad 4.15$$

And the subsequent unknown joint angles θ_3^* and θ_4^* , required to solve the forward kinematics equation 4.1, are:

$$\theta_3^* = \text{asin}\left(\frac{y_9 - y_3}{\sqrt{A9^2 - (x_9 - x_3)^2}}\right) \quad 4.16$$

$$\theta_4^* = \text{asin}\left(\frac{x_9 - x_3}{A9}\right) \quad 4.17$$

The solution was successfully verified against the Solidworks CAD model, like for the PROSPER kinematics.

Inverse kinematics

Like the forward kinematics, the method for solving the inverse kinematics of the LPR manipulator is the same as for the PROSPER manipulator. Recall that the solution involves working backwards from the end effector and progressively locating the various unknown joints variables. The LPR solution is, in fact, simpler than for PROSPER because the only unknown joint variables are θ_7^* and θ_9^* .

We are given the homogeneous transformation from the robot's base to the end effector:

$$T_{Bee} = \begin{bmatrix} R_{xx} & R_{yx} & R_{zx} & x_{ee} \\ R_{xy} & R_{yy} & R_{zy} & y_{ee} \\ R_{xz} & R_{yz} & R_{zz} & z_{ee} \\ 0 & 0 & 0 & 1 \end{bmatrix} \quad 4.18$$

The location of frame 9 can be found from the link transformation:

$$T_{B9} = T_{Bee} \cdot T_{4ee}^{-1} \cdot T_{94}^{-1} \quad 4.19$$

where the transformations T_{4ee} and T_{94} are constant, as defined in the forward kinematics (see DH parameters in Table 4-2).

As shown in Figure 4-10, the location of J7 can be determined by looking at the circle described by rotating link A7 about J9. We know that the y -coordinate of frame 7 must be located at $-A5$, so we can solve the set of equations:

$$(y - y_9)^2 + (z - z_9)^2 = A7^2 \quad 4.20$$

$$y = -A5 \quad 4.21$$

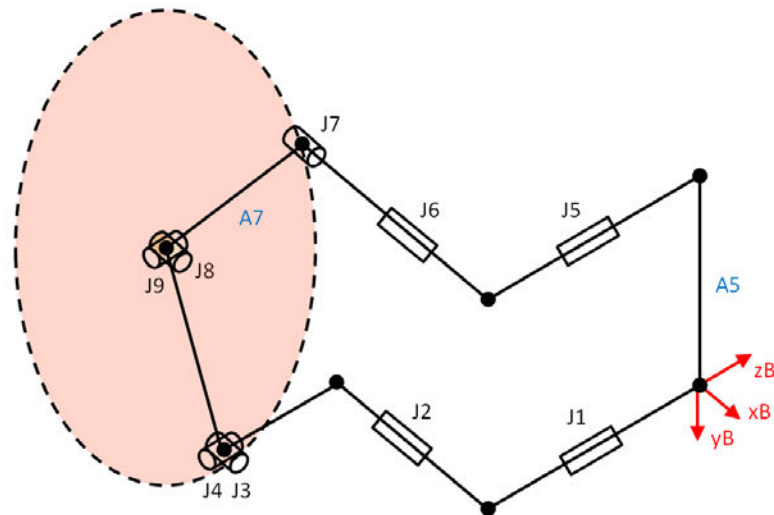


Figure 4-10: Circular path described by rotating joint A7 about J9.

which gives:

$$z = \sqrt{A7^2 - (-A5 - y_9)^2} + z_9 \quad 4.22$$

The location of frame 7 is therefore:

$$(x_7, y_7, z_7) = (x_9, -A5, \text{Equation 4.22}) \quad 4.23$$

The actuated joint variables can then be easily found from the locations of the end effector and frame 7:

$$d_1^* = -(z_{ee} + A3) \quad 4.24$$

$$d_2^* = -x_{ee} \quad 4.25$$

$$d_5^* = -z_7 \quad 4.26$$

$$d_6^* = -x_7 \quad 4.27$$

Once again, this solution was successfully verified against the CAD model of the robot.

4.2.4 Cable stretch

The use of Bowden cables to actuate the robot inevitably means that inaccuracies due to cable stretch must be taken into account. As the motors start moving and pulling on the cables, there is a latency and inaccuracy in the subsequent robot joint motion at the other end of the cables. This is caused by the stretch of the cables and housing as they overcome the static friction in the system.

Material choice

Material choice for the Bowden cables was important in order to reduce the cable stretch to a minimum. Table 4-3 shows the various properties of the chosen cables and housing. 90% Dyneema® (ultra-high molecular density polyethylene - UHMDPE) archery serving thread (Majesty Serving Thread, BCY Fibers, Middletown CT) was chosen for the cables because of its very high stiffness, thin diameter and availability. For the cable housing, Teflon® (polytetrafluoroethylene - PTFE) tubing was used with an outside diameter (OD) of 5 mm and inside diameter (ID) of 1.5 mm, which were the thinnest ID tubes encountered. Teflon is much more elastic than Dyneema, however because of the large cross-sectional area of the housing, the resultant stretch over its total 1.5 m length is very similar to that of the cables for the same applied force.

The friction that the system must overcome, comes from two sources: the friction in the mechanical joints of the robot manipulator and the friction in the Bowden cable system itself. Low coefficient of friction material couplings, such as smooth carbon fiber tubing with epoxy runners ($\mu_s \cong 0.4$) were used for the prismatic joints. The coefficient of friction between the Teflon cable housing and the Dyneema cables can be estimated at around $\mu_s \cong 0.05$, as measured by [230] for Teflon against polyethylene.

Cable tension

To diminish the stretch in the cables, one could suggest pre-loading the cables to try to decrease the stretching phase at the beginning of motion. However, this is not effective in our system, since each prismatic joint is stretched between an opposing pair of cables (to pull the joint in both directions). Pre-loading therefore increases the overall friction in the system (in particular the friction between the cables and the housing), thus increasing the cable stretch. Indeed, we measured, using precision caliper, the approximate difference in motion inaccuracy between the requested motor distance and the actual distance travelled by the joints for a pre-load force of 70 N and a pre-load force of around 5 N. The former resulted in 5 mm inaccuracies while the latter resulted in 1 mm inaccuracies.

In addition to increased friction, a pre-loaded system is affected by creep over time, which is a known detrimental property of UHMDPE fibers under constant loading. [231] report the creep behavior of Dyneema fibers over time. From their results, we can plot the resultant elongation due to creep if our cables were to be loaded with a tensile force of 50N (Figure 4-11).

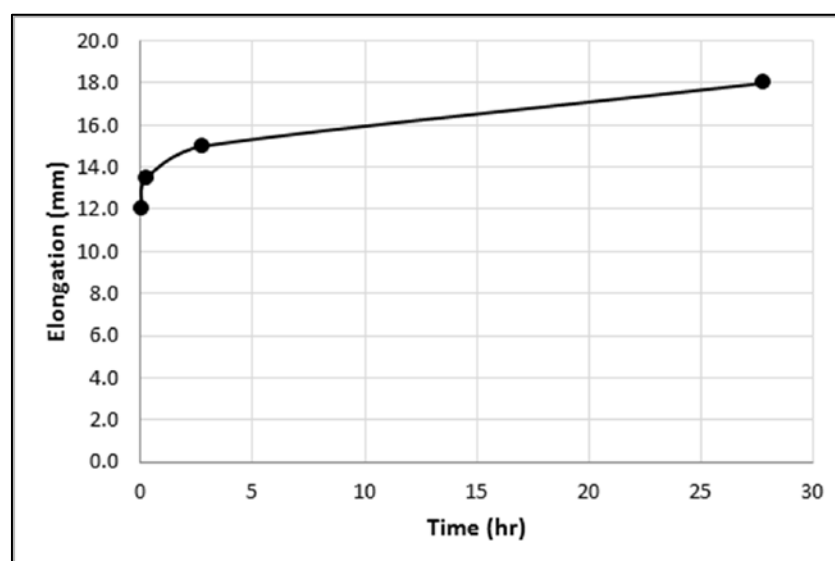


Figure 4-11: Elongation over time due to creep of a 1.5 m long 0.381 mm diameter Dyneema string loaded with a 60 N tensile force.

The plot shows two distinct regions, explained by [232]: a first region of rapid elongation over the first hour or so, followed by a second slower and constant region of elongation. The first region consists predominantly of reversible (elastic) elongation, while the second region consists of irreversible elongation. If we look, therefore, at the second region only, the irreversible creep can be estimated as 3 mm over a period of 24 hours. This means that if the cables in our system were to be pre-loaded, their pre-load tension would decrease over time, requiring adjustment at each use of the robot. We verified this with our particular setup by measuring the tensile force in our Dyneema cables over a one hour period, upon initial loading of 70 N. We found a rapid decrease in force (approximately 25% decrease) over the first half hour, followed by a more steady decrease (approximately 5% decrease) for the second half hour.

In conclusion, the ideal cable tension for our system, in terms of reducing cable stretch inaccuracies and creep, should be as low as possible; in other words, just enough tension to make the cables taught so as to avoid backlash due to sagging cables (on the order of 5 N).

Housing curvature

Another important aspect of Bowden cables is the effect of the curvature or wrap angle of the system on force transmission. In a perfectly straight system, the friction between the cable and the inside walls of the housing is zero since they do not touch. If the housing is curved, the cable comes into contact with the housing. This creates two effects: 1) increased friction between the cable and the housing and 2) modified cable pre-load due to the radius of curvature. These two effects could in turn affect the repeatability of the system by modifying its

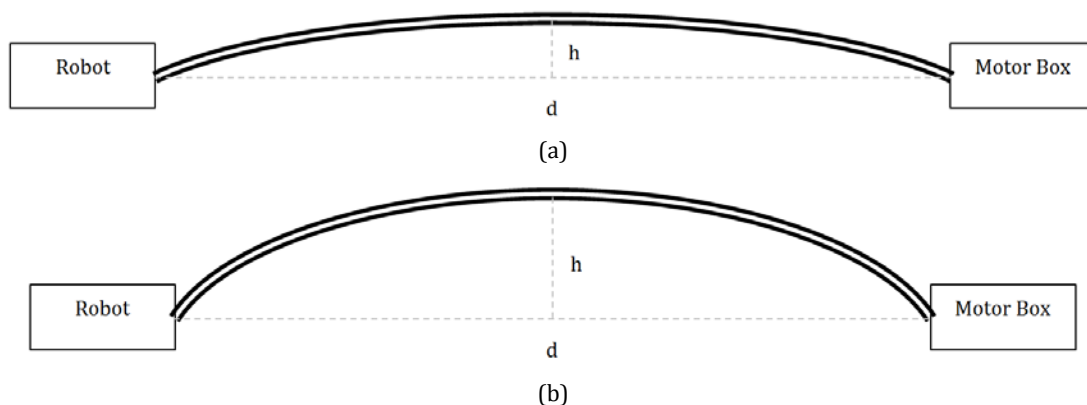


Figure 4-12: (a) Sketch of low cable housing curvature between the robot and motor box. (b) High cable housing curvature.

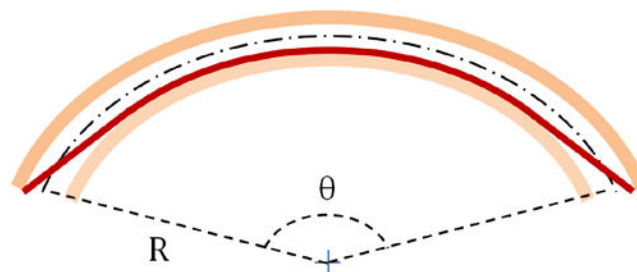


Figure 4-13: Sketch illustrating the path followed by the cable (red) within the curved housing (orange). At each end of the housing, the cable is in contact with the outer side of the housing, while throughout the center, it is in contact with the inner side. R represents the radius of curvature of the housing and θ the arc angle. The neutral centreline of the housing is assumed to be constant for all curvatures (i.e. 1.5 m).

working conditions depending on the curvature.

In our system, it is impossible for the housing to be perfectly straight due to its flexibility, therefore the curvature necessarily has some effect. Under normal operating conditions, the robot is placed on the patient's torso and the motor box beyond the patient's feet such that the cables are as stretched out as possible. The overall radius of curvature of the housing should not therefore vary significantly between interventions. In addition, during a single intervention, the cables should scarcely move at all.

To quantify the effect of curvature under normal operating conditions, we can compare the effect of a low curvature and a relatively "high" curvature. Figure 4-12 shows these situations, in which we define a low curvature as having a curvature height (h) of 100 mm and a high curvature having a height of 200 mm. To determine the difference in curvature-induced pre-load in the cables, we can find, for each of these two situations, the effective cable length from the robot end to the motor end of the housing, as shown in Figure 4-13. The resulting difference in cable length between the two curvatures is 0.3 mm for our Bowden system, which translates to a 0.02% difference in pre-load force. This can be considered as a very minor difference that would not noticeably affect the pre-load-induced creep.

To determine the difference in curvature-induced friction, we can use the force transmission efficiency equation presented by [233] which approximates the efficiency between the input and output forces of a Bowden cable system having a wrap angle θ and a coefficient of friction between cable and housing μ :

$$\frac{F_{output}}{F_{input}} \cong e^{-\mu\theta} \quad 4.28$$

Our system, with a μ of 0.05, results in a 2.7% decrease in transmission efficiency (and hence increase in friction) between the low and high curvatures described in the previous paragraph. If we assume the cables are pre-loaded with 5 N of force, this would mean a difference of 0.13 N between the two curvatures, which is a minor difference.

Table 4-4 summarizes the differences between low and high curvatures. The above analysis allows us to assume little effect is to be expected from variations in the cable housing curvature within "normal" working conditions. To decrease this effect even more, ideally the ID of the housing should be better matched to the cable diameter in order to reduce the space between them.

Cable stretch calibration

Since it is impossible to completely eliminate cable stretch, the resulting inaccuracies between the motor positions and their respective joint positions must be mitigated through software. Indeed, the software that allows the motors to move to a certain desired position

Table 4-4: Summary of the effects of cable housing curvature on cable friction and pre-load. The first four elements are defined in Figure 4-12 and Figure 4-13.

	Low curvature	High curvature
h (mm)	100	200
d (mm)	1482	1426
R (mm)	2800	1370
θ	31°	63°
Cable length (mm)	1499.74	1499.44
Elongation (mm)	0.26	0.56
Transmission efficiency	97.4%	94.7%
Friction force at 5N pre-load (N)	0.13	0.27

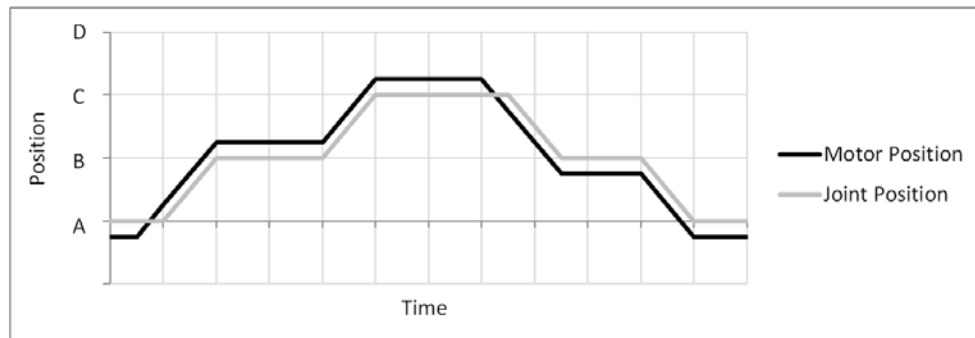


Figure 4-14: Timing chart showing a sample motion sequence for a single motor of the LPR robot. It shows the offset due to cable stretch between the requested motor position at one end of the cable and the actual resulting joint position at the other end of the cable. The plot should be read from left to right, with the offset represented by the vertical height difference between the black and gray curves. See text for an explicit description.

includes an offset that makes up for the hysteresis caused by cable stretch.

Figure 4-14 illustrates how this offset is applied by comparing the motor's motion to the resulting joint motion which, if the offset is properly calibrated, corresponds with the desired robot motion. At the beginning of the sequence, the joint is at its home position (A), abutted against the robot frame and the motor is in a negative offset position. The position B is then requested and the motor starts moving (first rising diagonal line on the black curve). A lag is seen in the joint motion as the cable stretches (first rising diagonal line on the gray curve). The motor overshoots the position B by the pre-calibrated offset in order to bring the lagging joint there. Next, the position C is requested and the motor starts moving again (second rising diagonal line on the black curve). Since the cable is already stretched, the joint begins moving simultaneously (second rising gray curve). The motor once again applies an offset, bringing the joint to position C. Next, a request is sent to move the motor back to position B. The motor starts moving (first descending diagonal line on the black curve) and must go beyond position C before the joint starts moving, in order to take back the cable stretch from the previous motions and apply a stretch in the other direction. At position B, the motor applies a negative offset, bringing the joint to the requested position. The final motion (last descending diagonal line) brings the motor back to a negative offset position and the joint back to home, abutted against the robot frame.

In the experiments that will be described below, calibration of the offset for each motor was done by applying motions to the motors and measuring the resulting difference at each prismatic joint with a caliper. Offset calibration was verified before each separate experiment. Since cable tension in this prototype was adjusted manually, the offsets for the five motors varied between 1 to 4 mm. Ideally, the cable tension should be accurately adjusted using a cable tensiometer.

The accuracy and repeatability of the calibrated offsets was verified by moving each joint to a same position a number of times and taking manual caliper measurements. The results for the four position motors were well below 0.5 mm. The fifth motor, used to adjust the insertion depth, was verified by inserting a needle to a depth of 80 mm at a stroke depth of 20 mm and the resulting tip depth was measured. The accuracy and repeatability over 20 insertions was also less than 0.5 mm. These results were deemed excellent given the relatively large bearing play and the imprecise cable tension of this prototype.

Because of our decision of not using position sensors on the robot structure itself, our control over the cable tension is vital in the final accuracy of the joint positions. In the end, however, any inaccuracies in joint positioning would not be critical to the patient's safety or the success of the insertion since the radiologist always verifies the actual needle position in the image before actually inserting. As will be explained in the following section, this is done by segmenting fiducials linked to the needle position and visible in both CT and MR images.

4.2.5 Robot-image calibration

As opposed to PROSPER, the LPR system uses intra-operative robot-image calibration. This means that the robot location is found in each individual image. It was decided not to use position sensors on the robot joints because MRI-compatible sensing options are typically very expensive. For this reason, robot-image calibration is vital to the accuracy of the system. The two fiducials incorporated into the parallel platforms shown in Figure 4-4 (page 83) are used to determine the location of the robot and needle in the image. This section describes the design of these fiducials, the automatic image processing routine used to segment them in CT and MR images and the coordinate frame manipulations used to register the robot space to the image space.

Fiducial design

The fiducials can be seen in Figure 4-15. Because of space constraints, instead of using a 3D fiducial, two distinct planar shapes were machined into the parallel platforms of the insertion module. These shapes can be filled with specific material visible in CT and MR images. Because they move with the needle, they can be used to determine its position and orientation in the image.

To ensure reliable and accurate localization of these fiducials, the following constraints were applied in their design:

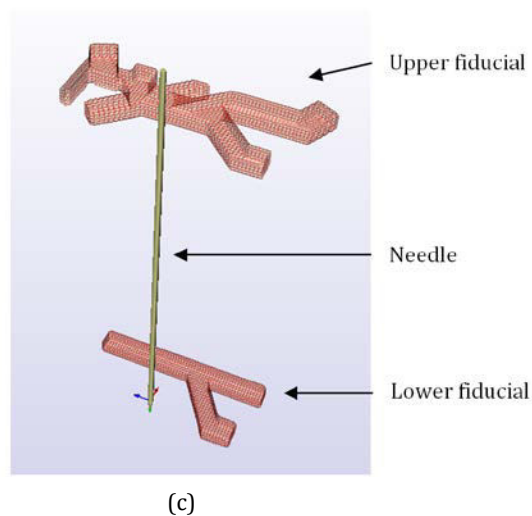


Figure 4-15: Photographs of the exposed (a) upper (top view) and (b) lower (underside view) fiducials used to locate the robot in the CT and MR images. The approximate location of the needle axis is shown on by a red dot in each image. (c) Mesh model of the fiducials with respect to the needle.

- *Asymmetry*: each planar fiducial must be asymmetrical in at least two directions in order to ensure unambiguous registration in three dimensions.
- *Shape*: numerous branches, in order to increase the number of recognizable features.
- *Orientation*: each fiducial should be oriented in the plane normal to the needle axis, in order to take advantage of the typically higher resolution transverse imaging plane and reduce the partial volume effect. The image volume used to locate the fiducials is reconstructed from a set of 2D images. These images are most often in the transverse plane, with inter-slice spacing usually much greater than the planar resolution of the images themselves. If the thin fiducials were to be oriented in the transverse imaging plane, a larger percentage of the fiducials would be hidden in the inter-slice spacing, significantly affecting the registration accuracy.
- *Location*: as close to the needle axis as possible and the two as spread apart as possible, in order to reduce errors due to construction tolerances.
- *Fill material*: the fiducial shapes should be filled with material that is distinguishable from the rest of the robot in CT and visible in MRI T1 and T2-weighted sequences.

Numerous materials were tested with which to fill the machined spaces of the fiducials. Initially, a material was sought that would be visible in both CT and MRI sequences. Gadolinium-doped water was initially tried, however, even when mixed with gelatin, it was very difficult to obtain a fully water-tight seal to prevent evaporation over time. In addition, gadolinium as an MRI contrast agent only has a significant effect on T1-weighted images and not on T2-weighted images.

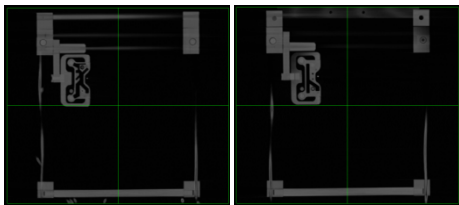
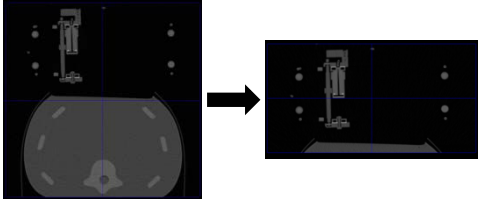
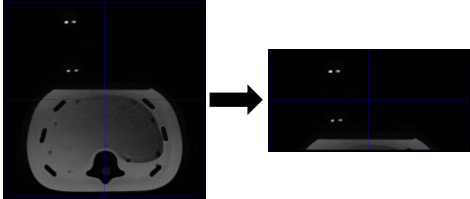
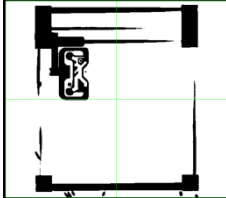
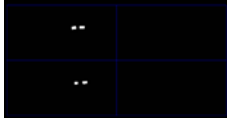
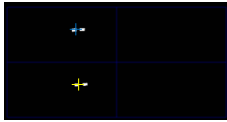
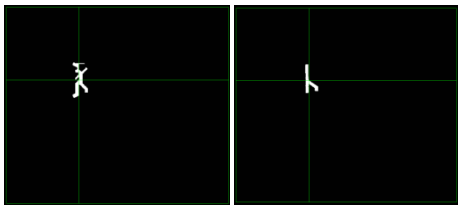
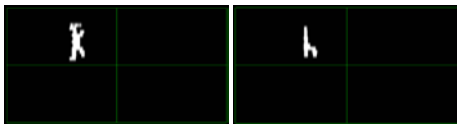
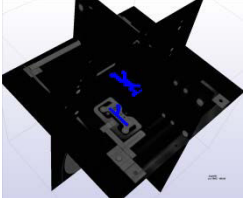
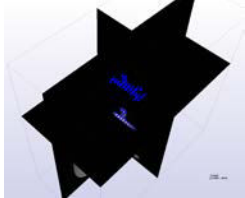
In the end, no material at all (empty space) was used for CT images, as this made a very stable black fiducial image, highly contrasted from the plastic material into which the fiducial shape was milled. For MRI images, soft PVC, like that used in the PROSPER phantom (see section 3.3.1, page 58), was chosen, as it was easily visible in both T1 and T2 images and because it was significantly more stable over time than water-based materials. Although segmentation of the PVC phantoms was very consistent and reliable during the phantom tests that will be described below, in the end, PVC was not an ideal choice due to a chemical shift artifact discovered posteriorly (see Sources of error in section 4.3.2, page 109). Ideally, these fiducials would in fact be factory-made, disposable cartridges, filled with the appropriate contrast agent according to the imaging modality being used. These cartridges would simply be installed at the beginning of each intervention, ensuring ideal imaging.

Image processing

Since the calibration must be done for every new image, one of the main goals of the robot-image calibration was for it to be fully automatic, with no necessary interaction from the user. An image processing routine therefore had to be developed that would segment the fiducials from a CT or MR image volume and subsequently register the known fiducial model to the segmented image. The steps used for this procedure are shown in Table 4-5 and are made up of standard processing routines. Table 4-6 lists the various parameters used in each relevant step for both imaging modalities.

The first step involves reducing the original 16-bit DICOM image to an 8-bit grayscale image. This is done to reduce the size of the image and hence free up memory. Next, the patient's anatomy is cropped out of the image to reduce the size even further and to speed up the subsequent segmentation routine. The cropping routine assumes that the robot is always located in the top portion of the image, with the patient anatomy below it. It works on the middle 2D transverse slice of the image volume. As shown in Figure 4-16, a search region is swept up the image from bottom to top, summing the pixel intensities and giving a total

Table 4-5: Image processing routine used to automatically segment and register the fiducials in both CT and MR image volumes. The Italicized text in between parentheses contains explanations of the images found in each row of the table.

Image processing step	CT	MRI
1. Convert to 8 bit <i>(coronal cuts showing upper and lower fiducials)</i>		
2. Crop out patient anatomy <i>(transverse cuts showing transition from full image to cropped image)</i>		
3. Threshold <i>(thresholded binary images. CT → coronal cut, MRI → transverse cut)</i>		
4. Find connected components		
5. Volume-threshold the connected components <i>(transverse cuts of resulting thresholded binary images)</i>		
6. Find centres of mass of connected components <i>(images showing centres of mass of various components)</i>		
7. Distance-threshold the connected components <i>(coronal cuts of resulting segmented upper and lower fiducials)</i>		
8. Extract white pixels into mesh of points <i>(extracted mesh of points overlaid on original image)</i>		
9. Register mesh of points with fiducial model	See Figure 4-18 (page 100).	See Figure 4-18 (page 100).

intensity for each region. The ratio of the current and previous regions' total intensities is then calculated. The search ends when it finds a region k whose ratio from the previous region k-1 is less than a certain threshold. In both CT and MR images, the patient anatomy has by far the highest concentration of high intensity pixels, giving an easily distinguishable drop of total intensity in the regions above the anatomy. The bottom of region k-1 is used as the crop line, leaving a sliver of patient anatomy in the image.

Table 4-6: Parameters used during each image processing step during the automatic segmentation of all CT and MRI images taken during the experiments described in section 4.3.2.

Step	Parameter	CT	MRI (T1 and T2)
Crop patient anatomy	Search box height	8% of image height	8% of image height
	Gradient threshold ratio	0.1	0.1
Threshold	Lower threshold	0	10
	Upper threshold	25	255
Volume threshold	Lower volume	500 mm ³	500 mm ³
	Upper volume	2500 mm ³	2500 mm ³
Distance threshold	Distance	85 ± 3.5 mm	85 ± 3.5 mm

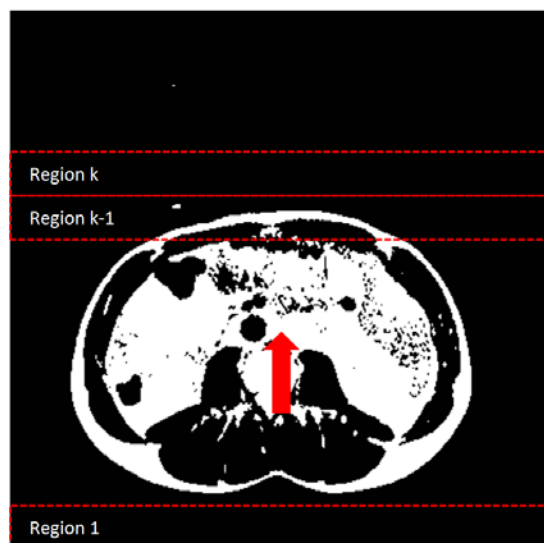


Figure 4-16: Schematic showing the search routine used to find the top of the patient's anatomy in an Otsu-filtered MR image. Region 1 is the first search box. The height used to crop the image is the bottom of region k-1. The height of the search boxes are approximately to scale.

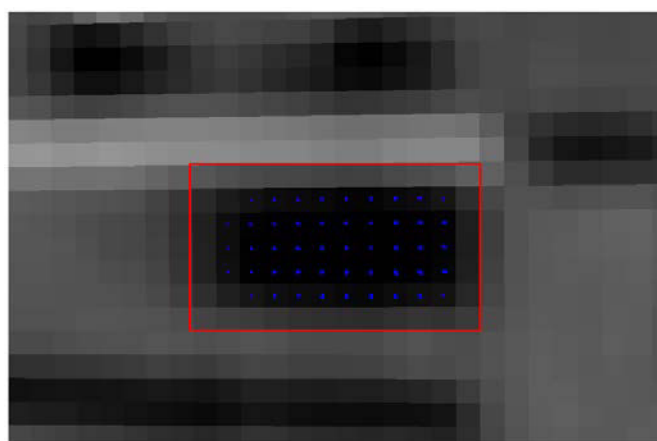


Figure 4-17: Zoomed transverse view of a CT image showing a portion of the upper fiducial (black pixels) with the segmented pixel centres shown in blue. The estimated true fiducial shape is shown by the red rectangle. Because of the finite resolution of the image (0.67×0.67 mm in this case), the edges of the fiducial are blurred and don't fall within the thresholding range defined in step 3 of the calibration routine (see Table 4-5). The fiducial is therefore under-segmented, resulting in a systematic underestimation of the fiducial's volume.

The cropped image is then thresholded based on calibrated low and high grayscale values. For CT images, the threshold range lies between 0 and 10 since the fiducial is empty. For MR images, both T1 and T2-weighted, the threshold range is the opposite, that is from 25 to 255

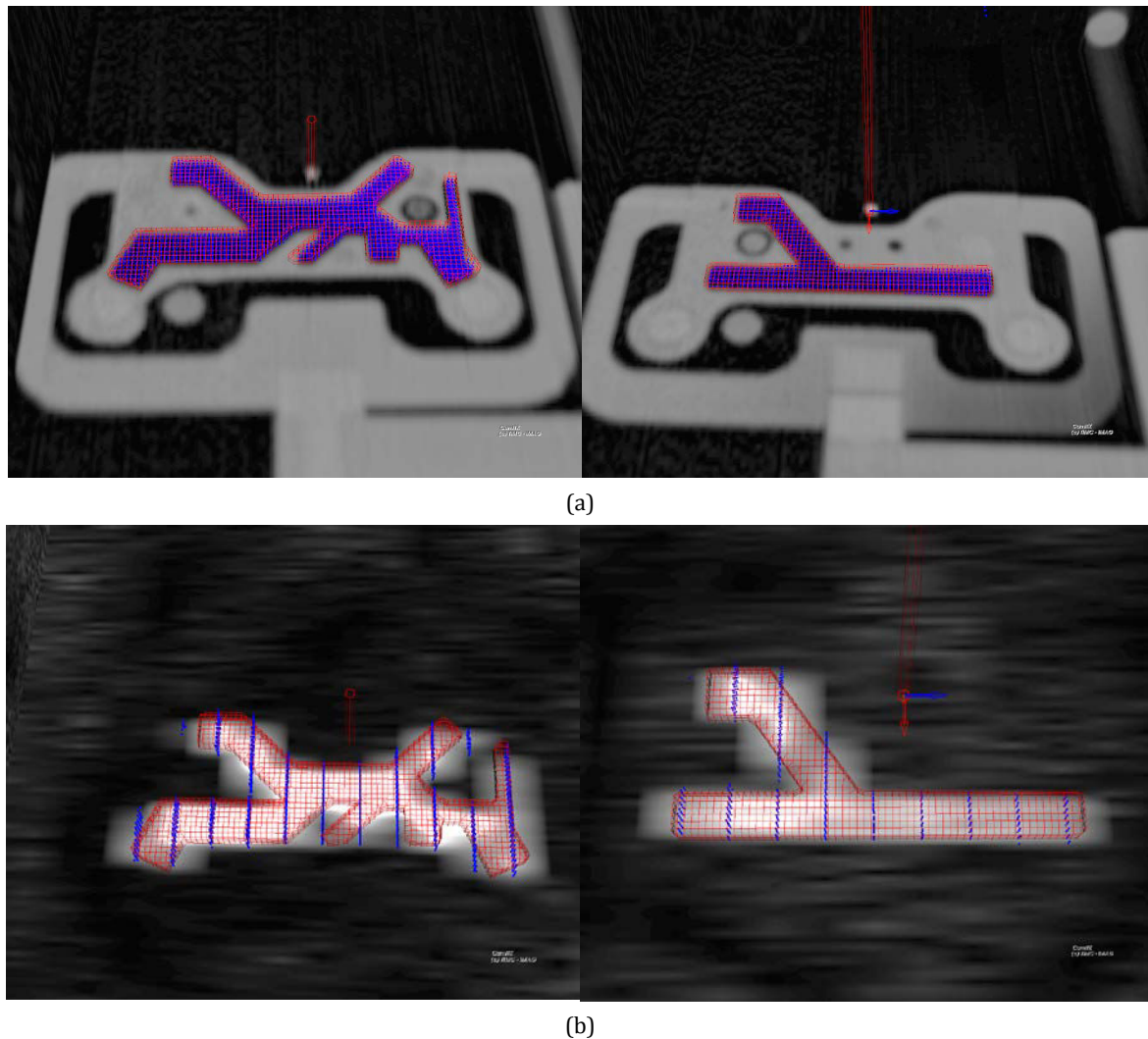


Figure 4-18: Screen captures showing the fiducial mesh (red) registered to the segmented cloud of points (blue), overlapping a coronal view of the original image in (a) a CT volume and (b) a MR volume. Note that the brightness and contrast of the images has been increased for better visualization. In the CT images, we can see that the model of the needle (red cylinder) is very well aligned with the actual needle in the image (bright spot).

since the fiducial signal is surrounded by essentially empty signals (which tend to be noisier than empty space in CT images).

Next, a connected components analysis is run on the thresholded volume, grouping together all the connected white pixels. A volume thresholding is then done to exclude all the components that are either too small or too large to be the fiducials. The true lower fiducial volume is 1338.08 mm^3 and the upper fiducial volume is 2203.62 mm^3 , as measured from the CAD model. A much larger volume threshold range was used, in particular in the lower threshold value, in order to account for inevitable segmentation inaccuracies, such as image resolution and edge segmentation inaccuracies, as explained in Figure 4-17.

Because of the large volume thresholding range used in the previous step, a number of unwanted components remain selected, therefore a further thresholding is necessary to eliminate them. This is done by measuring the distance between the centres of mass of the components. Since the two fiducials have a constant distance of 85 mm between them, this is enough to isolate them amongst the remaining components. Further thresholding could be done, such as comparing the axes of inertia or the planar alignment of the components, but this was not found necessary in any of the images tested.

Once the two fiducials are segmented, a cloud of points is created from the coordinates of the centres of all the segmented pixels. A mesh model of the two fiducials (constructed from

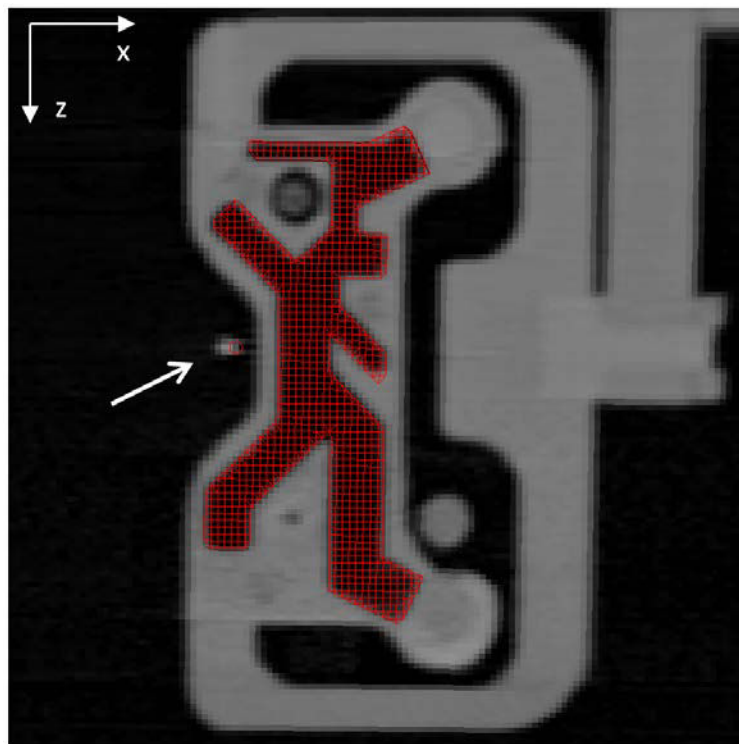


Figure 4-19: Location of the needle with respect to the upper fiducial in a CT image (marked by arrow). The registered fiducial model is overlaid in red, with the registered needle location shown as a faint circle beside the white spot of the actual needle in the image. Note the misalignment in the x-direction of the visible white needle compared to the registered red needle, as explained in the text.

Table 4-7: Mean error between the registered needle location and the needle segmented in the CT images for two image resolutions.

Image resolution (mm)	Fiducial	Registration error (mm)			
		x	y	z	E
0.67 × 0.67 × 0.6	Upper	1.26 ± 0.29	-0.14 ± 0.34	-0.31 ± 0.37	1.39 ± 0.33
	Lower	1.39 ± 0.19	-0.10 ± 0.18	-0.18 ± 0.23	1.43 ± 0.21
0.67 × 0.67 × 2.0	Upper	1.27 ± 0.35	-0.06 ± 0.25	-1.06 ± 0.85	1.86 ± 0.30
	Lower	1.40 ± 0.17	0.03 ± 0.12	-0.66 ± 1.07	1.84 ± 0.22

their CAD models) is then registered to this cloud of segmented points using standard rigid iterative closest point (ICP) registration [234]. Figure 4-18 shows screen captures of the result in both a CT and an MR volume. The mesh model was generated using the work described in [235] and consisted of 4860 nodes creating an even and fine mesh of hexahedra (with 0.77 mm cubic dimensions) throughout and mixed-element patterns at the fiducial edges. The meshes node points were used during the registration.

The above routine worked fully automatically for all the CT and MRI-guided phantom tests that will be described in section 4.3.2 (page 109). They were also successfully tried on a number of volunteer images taken in the MRI.

The resulting registration accuracy was measured using the CT images gathered during the phantom tests. As can be seen in Figure 4-19, the measurement was done by looking at the imaging plane parallel to each fiducial and comparing the actual visible needle position to the registered needle position. Segmentation of the needle in the image was done manually. A total of 16 CT images with a slice spacing of 0.6 mm, and 8 images with a more clinically realistic slice spacing of 2.0 mm were used, giving the results shown in Table 4-7. The main registration error was in the x-direction (see Figure 4-19 for direction), being around 1.3 mm. This was an error

found only after the experiments described in section 4.3.2 (page 109) and consisted of an inaccuracy in the model's distance between the needle axis and the fiducial (constructed from the original CAD model of the robot). It could very easily be rectified by adding the measured mean error to the needle's position in the x-direction. In the z (slice-thickness) direction, the error logically increased with increasing slice thickness, approximately giving a logical half a pixel error. No significant difference was noticed between the upper and lower fiducial registration errors. The mean registration error over all the CT images taken during the phantom experiments was 1.54 ± 0.33 mm. This registration error could not be measured in the MRI images because the needle was invisible.

Coordinate frames

Once a target and a skin insertion point have been chosen and the fiducials have been located in the image, the motor positions required to align the needle with the target insertion axis need to be determined.

Figure 4-20 illustrates the situation in which the needle is currently in a known position N with respect to the image frame S. Its position is defined by the transformation T^{SN} and is determined from the fiducial segmentation and registration routine described above. From the robot's forward kinematics, described in section 4.2.3 (page 87), we also know the transformation T^{RN} from the robot's frame R to the current needle frame N. The transformation from the image frame to the robot frame is therefore:

$$T^{RS} = T^{RN} \cdot T^{SN}^{-1} \quad 4.29$$

We can now use this transformation to determine by how much the motors must be moved to align the needle with the target axis A. The target axis is defined in image coordinates

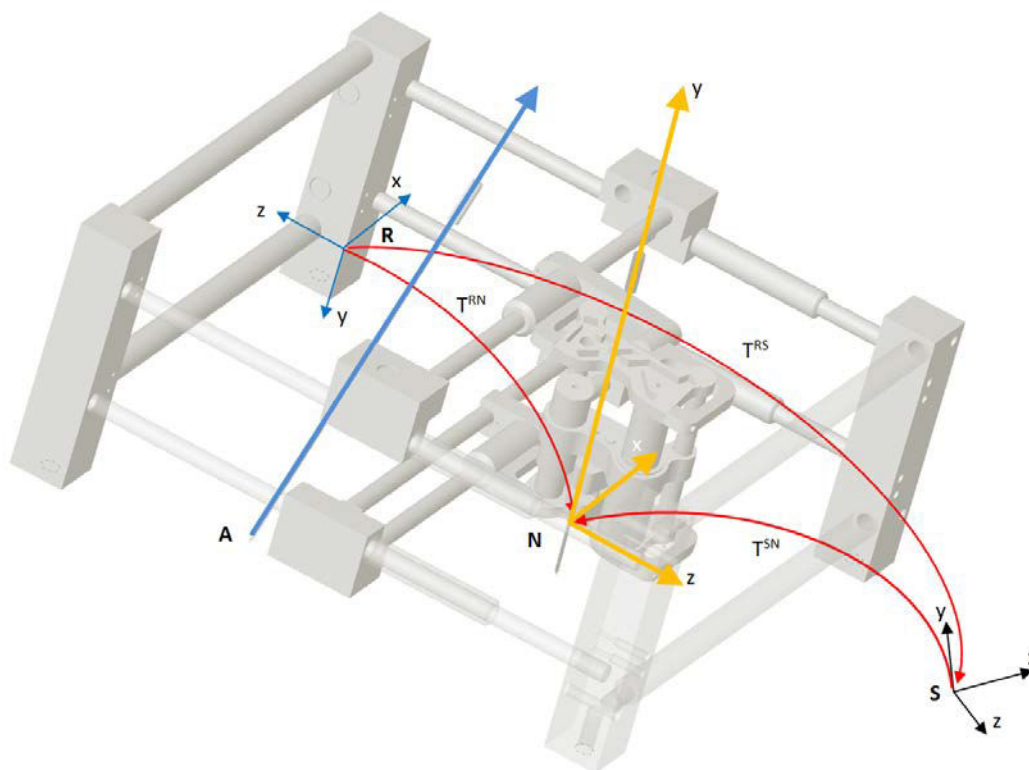


Figure 4-20: The transformations between image (S), robot (R) and current needle (N) frames that are required to determine how to position the robot's motors in order to align the needle with the target insertion axis (A).

by the chosen target point inside the patient, which we will call P^S , and the unit vector \vec{V}^S joining the target and skin insertion points. We can express these in robot coordinates through the following transformations:

$$P^R = T^{RS} \cdot P^S \quad 4.30$$

$$\vec{V}^R = T^{RS} \cdot \vec{V}^S \quad 4.31$$

We can now find the intersection between the axis A and the plane formed by the x and z axes of the robot frame. This is where the robot's end effector will have to be positioned. To do so, we can define the axis A by the following parametric equations:

$$x - P_x^R = t \cdot \vec{V}_x^R \quad 4.32$$

$$y - P_y^R = t \cdot \vec{V}_y^R \quad 4.33$$

$$z - P_z^R = t \cdot \vec{V}_z^R \quad 4.34$$

Since the x-z plane of the robot is at $y = 0$, we can solve for t :

$$t = -\frac{P_y^R}{\vec{V}_y^R} \quad 4.35$$

Giving us the desired robot end effector coordinates in the robot frame of reference:

$$\begin{aligned} x &= P_x^R + P_y^R \frac{\vec{V}_x^R}{\vec{V}_y^R} \\ y &= 0 \\ z &= P_z^R + P_y^R \frac{\vec{V}_z^R}{\vec{V}_y^R} \end{aligned} \quad 4.36$$

We can then use the inverse kinematics described in section 4.2.3 (page 87) to determine how to move the motors.

4.2.6 User interface

A user interface was designed for the system in C++ and using QT, VTK, ITK, and CamiTK. QT is a free development framework that provides a huge number of well documented classes for everything from data type handling all the way to GUI design. VTK and ITK are commonly used open-source medical image processing toolkits. CamiTK is an open source, multi-platform, modular toolkit specifically designed for computer assisted medical intervention software prototyping. It is developed and maintained in our TIMC-IMAG laboratory and has seen a dramatic increase in stability, scope and popularity over the last few years. It consists of a common core onto which users can plug self-programmed extensions, allowing them to be shared by others without the need for re-programming. It can handle a large number of medical image formats and, to date, its common extensions include image processing routines, surgical navigation extensions and biomechanical simulations. Developing a new extension for CamiTK is very easy, requiring only a small handful of lines of code, that in fact are now offered in template form. Extensions can be either 1) viewers for creating GUI's, 2) components for

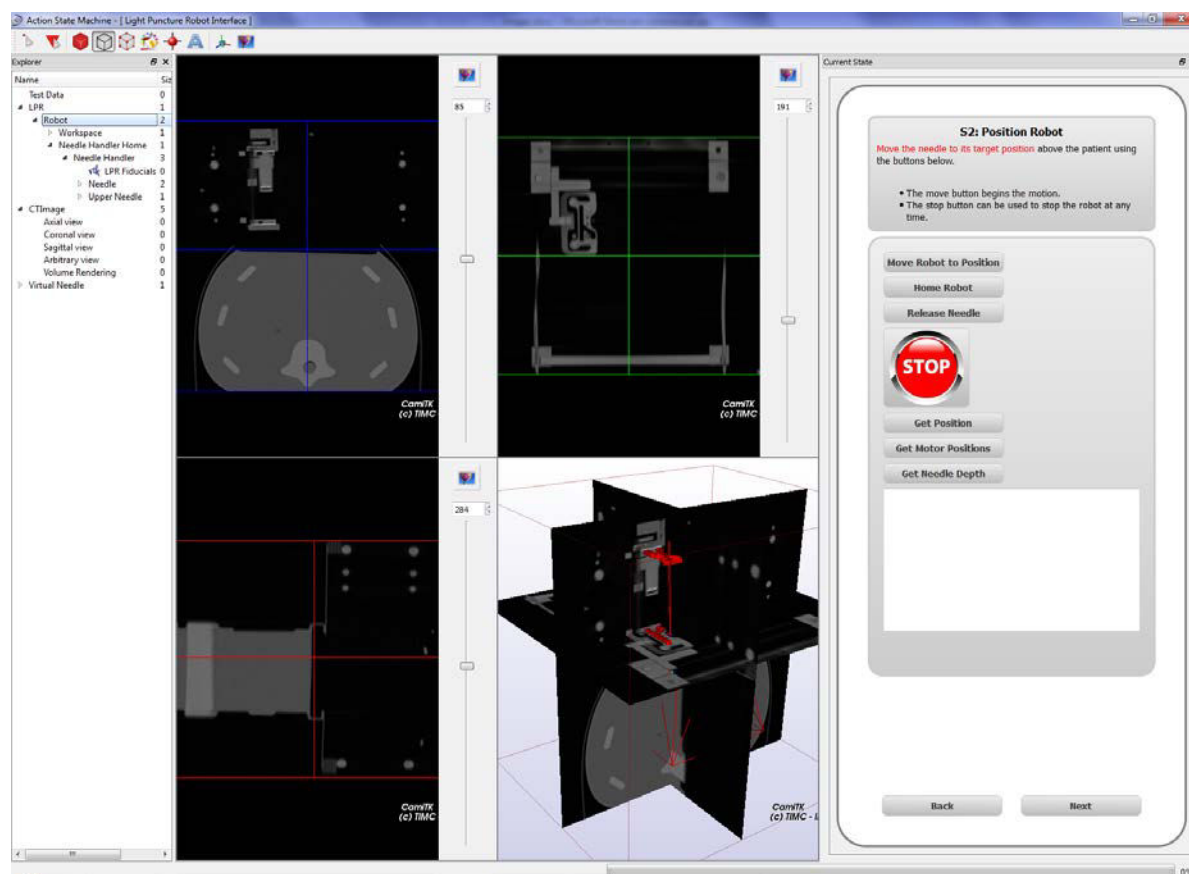


Figure 4-21: A screenshot of the GUI used to control the LRP system during the phantom tests. On the left is an explorer, listing the various data components currently loaded (in this case a set of test data, the model of the robot's upper and lower fiducials as well as its workspace, the current needle's position in the image, a CT image, and the virtual target needle position). The graphical components are displayed in the medical viewer in the center of the screen (showing axial, coronal, sagittal and 3D views). On the right is a description of the current state and the actions required from the user. The next and the back buttons allow the user to transition between states. The upper toolbar contains some display options.

storing data, such as images or meshes, and 3) actions for applying some sort of action on the stored data. More information can be found on the toolkit's website (<http://camitk.imag.fr/>).

For this LPR prototype system, a GUI extension available through CamiTK was used that is based on the UML state machine concept. It consists of a set of screens that each represent a stable state. Transitions are defined to move between states, obliging the user to follow a predefined protocol. The UML activity diagram of the developed protocol is shown in Appendix 4 and follows the workflow described in section 4.1.3 (page 78). The states and transitions were translated into an xml document which could then be fed into the CamiTK state machine viewer. A sample screen is described in Figure 4-21. The segmentation and registration routine described in the previous section was programmed into a CamiTK action and was applied here as a transition.

Figure 4-22 shows an overview of the control structure of the software. CamiTK acts as the core, linking all the various elements together and allowing a number of data, mesh and image components to be created. The Robot component is a generic component that holds the model of the fiducials and the current needle location. The Patient data component holds the information entered by the user pertaining to the current patient or test. The Dicom image component allows the images coming from the scanner to be opened and visualized. Reference frames are attached to the three visible components in order to allow them to interact together in the GUI. A library of C++ classes was also written to control this specific prototype, having a structure similar to that of the PROSPER robot (see Figure 3-14, page 56). It included a class for communicating with the IO card (see Electronics description in section 4.2.2, page 81), a low-

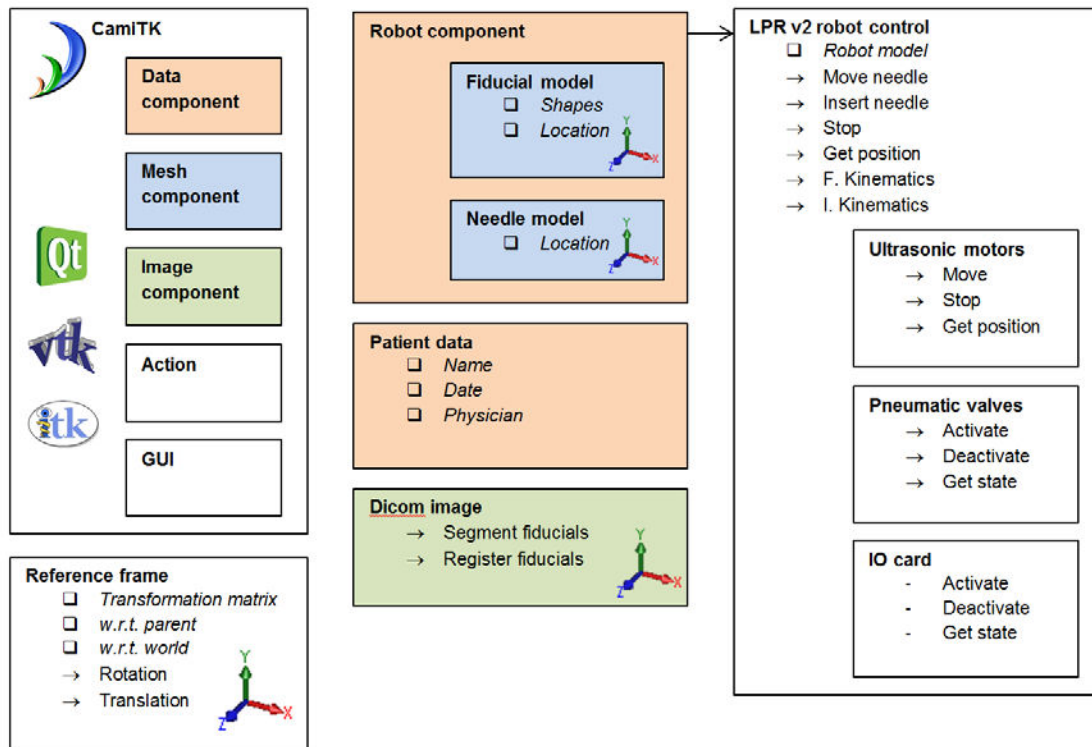


Figure 4-22: Block diagram showing the various elements making up the control structure of the LPR robot. CamiTK acts as the core, linking all the elements together. The Robot and Patient data components do not have a physical representation in the GUI and simply hold data. Reference frames are attached to the three components visible in the GUI, allowing them to interact with each other. The generic Robot component communicates with the Robot control library written specifically for this prototype. The square bullets represent the data held by each element, while arrow bullets represent the actions that can be applied on or from these elements.

level motor class instantiated by the five Shinsei motors within a high-level robot class for controlling the robot as a whole. The latter class included control commands, kinematics and workspace definitions. This library communicates with the generic Robot component, allowing its methods to be accessed from the GUI by the user.

The goal of this control structure was to keep it generic and modular in order to make it transposable to any future prototypes or clinical versions of the robot. Indeed, the only element that needs to be changed is the specific robot control library, depending on the actuators and communication protocols used as well as on the kinematic model of the robot.

4.3 Pre-clinical evaluation

To evaluate the new LPR system and its proposed workflow, phantom accuracy tests were done, similar to those described in the previous chapter for the PROSPER robot. The goal was to determine the system's overall accuracy in reaching targets within phantom anatomy, without considering needle bending and tissue deformation and under both CT and MRI guidance. Before being able to do so, it was important to study the robot's compatibility with the two imaging modalities, in order to ensure that its presence did not affect the image quality.

4.3.1 MRI and CT compatibility

CT compatibility

The CT compatibility of the robot was verified by taking an image of the entire robot on a phantom body and observing whether any visible artifacts were created in the image. The image was taken at the highest possible resolution, that is with a slice thickness of 0.7 mm, a reconstruction thickness of 0.6 mm and each slice having a pixel size of 0.67×0.67 mm. With a normal grayscale window level, no apparent artifacts were noticed throughout the volume. By augmenting the contrast and brightness of the image, some artifacts were brought out, as can be seen in Figure 4-23. These were exclusively aliasing artifacts due to under-sampling at sharp corners and in-plane faces. Their strength within the patient region of the image (i.e. below the robot) was on the order of 1% to 4% of the total 8-bit grayscale range, which is very minor. Indeed the strongest artifacts (3% to 4% strength) were only seen at the far edges of the robot frame, while the entire central region, within the robot's workspace, was only faintly affected (1% to 2% strength).

These aliasing artifacts could be reduced in part by filleting all of the robot's edges and corners. But regardless, since the robot is surrounded by empty space, its contrasting density will always create some minor aliasing.

MRI compatibility

MRI compatibility is more complex to evaluate than CT compatibility, since it relies not only on the objects present within the image bounds but also on objects located within range of the imager's magnetic field. Because of the inorganic and entirely non-metallic nature of the robot itself, we did not expect it to create any artifacts. The carbon fiber tubing used in the frame was perhaps the only concern due to the conductivity of the fibers. The motor box, however, containing the 5 ultrasonic motors, although located outside of the imaging tunnel, is in fact within the range of imager's magnetic field. It was therefore important to evaluate its impact on the signal to noise ratio of the images.

SNR tests were done early on, when the robot and motor box were first assembled and a choice of cable length between them had not yet been decided. A standard 3 L copper-sulphate MRI phantom bottle was used in a Philips Achieva 3T medical MRI scanner. Standard clinical THRIVE (T1-weighted) and BTFE (balanced gradient echo, mixed T1 and T2-weighted) sequences were taken, as detailed in Table 4-8. The entire bottle was imaged in different situations, notably with the motors at 4 different distances from the tunnel entrance, as shown in Table 4-9. The motors were not actuated, as would be the case when using the robot in a clinical protocol.

The SNR was calculated according to the NEMA standards [178] by determining the mean amount of signal emitted by the phantom bottle throughout all the slices of the 3D image, and compared to the standard deviation of the noise in the empty space area above the bottle, as shown in Figure 4-24:

$$SNR = \frac{Mean(Signal)}{Stdev(Noise)} \quad 4.37$$

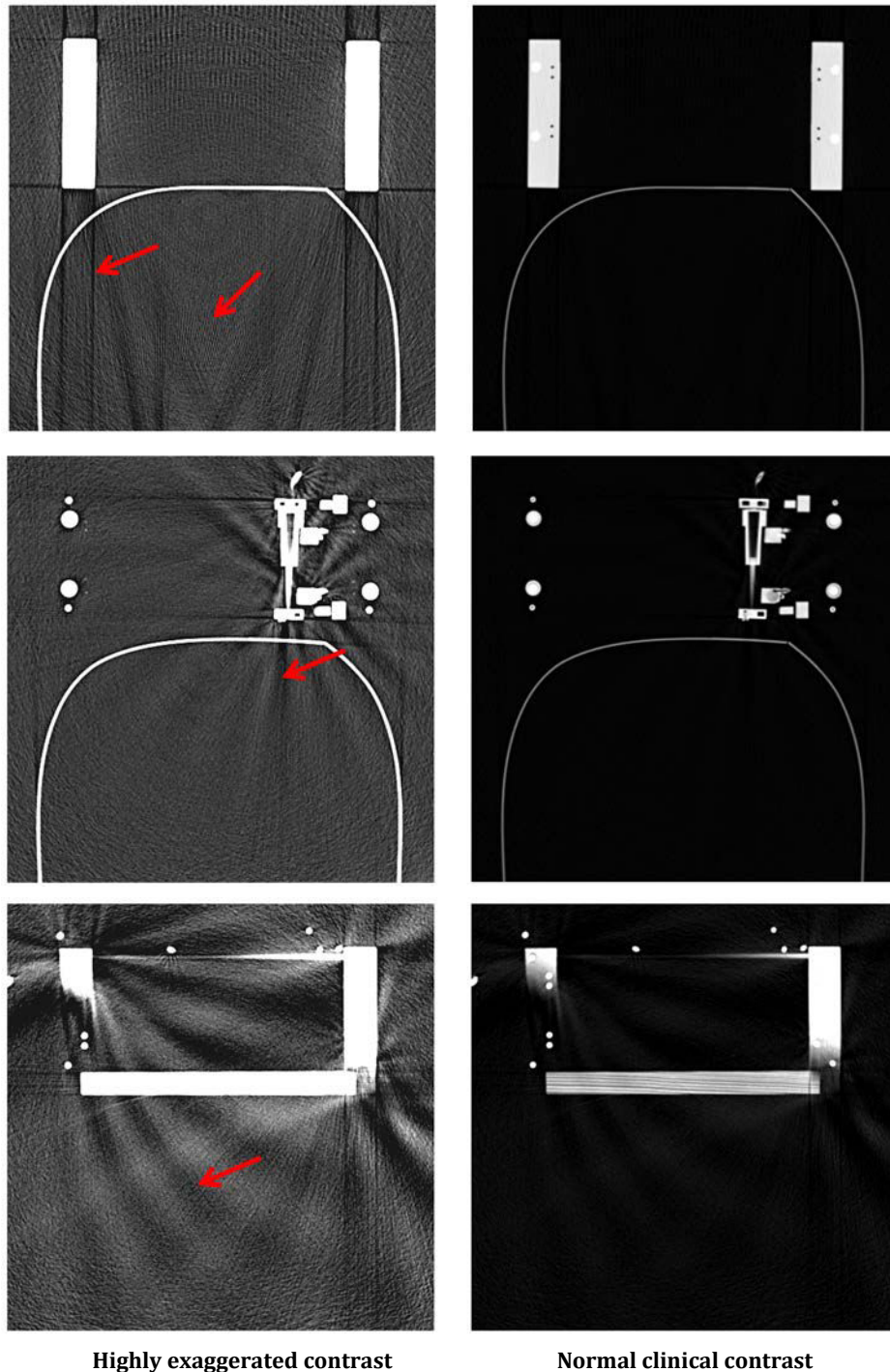


Figure 4-23: Three different transverse CT slices showing small very minor signs of aliasing artifacts. The left images are highly contrast and brightness-enhanced images (8-bit window level and width reduced to 0 - 15 grayscale values) to make the artifacts stand out. The right images are exactly the same images but in normal clinical contrast and brightness (full 8-bit window from 0 - 255 grayscale values). Of these normal images, only the bottom right image shows extremely minor artifacting due to undersampling at the robot frame's faces and corners, artifacts that would not affect the clinical readability of the images.

The results are shown in Figure 4-25. The only situation in which the SNR is noticeably reduced is in the THRIVE sequence, with the motors very close to the tunnel entrance, that is at 0.5 m. Although the effect is rather small, it was decided to place the motors at at least 1 m, to reduce the risk of the motors affecting the image SNR. The final choice of 1.5 m stemmed from this analysis along with the addition of half a meter in order to comfortably place the robot at a fairly tall patient's feet, directly on the imaging table.

Table 4-8: Imaging sequences used during the MRI SNR tests.

Imaging sequence	Resolution (pixels)	Slice spacing	Slice thickness	Slices	TR	TE	Flip angle
T1 Weighted High Resolution Isotropic Volume Exam (THRIVE)	384 × 384	2 mm	4 mm	80	3.03 ms	1.42 ms	10°
Balanced Turbo Field Echo (BTFE)	256 × 256	6.5 mm	5 mm	15	2.62 ms	1.31 ms	45°

Table 4-9: Experimental conditions during the MRI SNR tests.

Test #	Imaging sequence	Robot installed?	Motor distance	Motor state
1	THRIVE BTFE	No	-	-
2	THRIVE BTFE	Yes	0.5 m	OFF
3	THRIVE BTFE	Yes	1 m	OFF
4	THRIVE BTFE	Yes	2 m	OFF
5	THRIVE BTFE	Yes	3 m	OFF

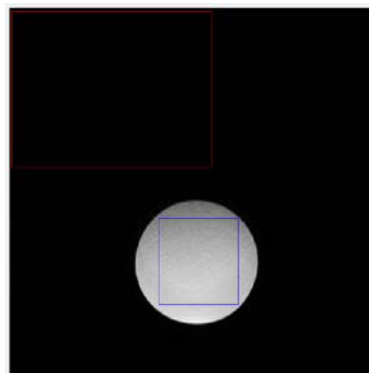


Figure 4-24: An MRI slice showing the two regions used to determine the signal (blue square within phantom bottle) and the noise of the image (red square at top left of image).

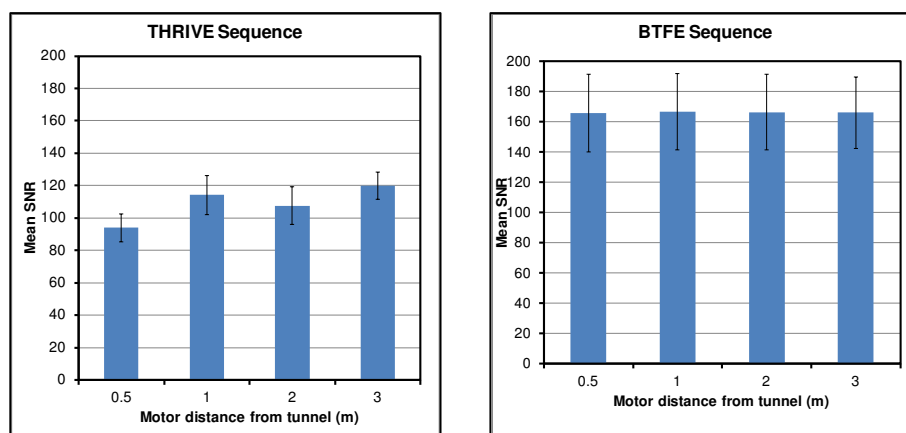


Figure 4-25: The SNR measured for the various situations considered during MRI compatibility testing.

Throughout all the MR imaging done during this thesis, the only other artifact that was noted with the presence of the robot, was a chemical shift artifact that will be explained in the following section.

4.3.2 CT and MRI phantom study

The CT and MRI phantom experiments conducted on the LPR system were similar to those conducted with the PROSPER system. Their goal was to examine the overall accuracy of the LPR system as a result of 1) the robot's kinematics, 2) the robot-image calibration and 3) the cable stretch calibration. In this case, target motion and needle bending was not considered so as to focus on the accuracy intrinsic to the system itself.

Materials and methods

The experiments were conducted by inserting a needle into a gelatin phantom with numerous targets embedded throughout. The phantom was constructed from the skeleton of an old CIRS thoracic phantom, as pictured in Figure 4-26. The structure was sealed all around, leaving the top open, and a viewing window was created on one side. 7 mm diameter plastic beads were strung throughout the interior on nylon thread, and the phantom was then filled with alimentary gelatin and set in the fridge overnight. Gelatin was used because of the very low resistance required to puncture it with a needle, eliminating needle bending and target motion issues. Once the gelatin was set, 1 mm diameter glass beads (like those used in the PROSPER phantom, section 3.3.1, page 58) were distributed throughout the phantom by inserting them through a hollow needle. The large plastic beads were intended to represent more clinically feasible targets, while the small glass beads were used to provide a more challenging target. The phantom was then placed within a plastic frame upon which the robot could be solidly mounted.

The CT experiments were done using a Siemens Somatom Sensation 16 CT scanner. The characteristics of all the performed insertions are summarized in Table 4-10. A total of 10 insertions were done, 6 of these using the finest slice thickness available on the imager (0.75 mm) and the rest using a coarser, more clinically viable thickness (3 mm). All insertions done with the fine images used the 1 mm diameter glass beads as targets. The insertions done with coarse images used the more realistic-sized 7 mm plastic beads, along with one deep glass bead target for the challenge.

The MRI experiments were done using a Philips Ingenia 1.5T wide-bore scanner, with a



Figure 4-26: Photograph of the phantom constructed and used for the LPR system's accuracy tests.

Table 4-10: Summary of the CT and MRI phantom tests done with the LPR system, organized by slice spacing and increasing insertion depth. All image volumes consisted of transverse slices. The MRI images had the following additional characteristics: T1-weighted (TR = 502 ms, TE = 10 ms, flip angle = 90°), T2-weighted (TR = 1158 ms, TE = 80 ms, flip angle = 90°). Transverse angles are in plane with the image slices and sagittal angles are in the slice-thickness direction.

Test #	Image						Target		Insertion angle	
	Sequence type	Resolution (pixels)	Pixel size (mm)	Slice thickness (mm)	Slice spacing (mm)	Number of slices	Type	Depth (mm)	Transverse	Sagittal
CT										
1	Fine	512 × 512	0.67 × 0.67	0.75	0.6	501	Glass	33	9.3°	0°
2	Fine	512 × 512	0.67 × 0.67	0.75	0.6	501	Glass	43	0°	0°
3	Fine	512 × 512	0.67 × 0.67	0.75	0.6	501	Glass	48	6.3°	0°
4	Fine	512 × 512	0.67 × 0.67	0.75	0.6	501	Glass	52	5.1°	-13.3°
5	Fine	512 × 512	0.67 × 0.67	0.75	0.6	501	Glass	62	-8.6°	15.1°
6	Fine	512 × 512	0.67 × 0.67	0.75	0.6	501	Glass	88	0°	0°
7	Coarse	512 × 512	0.67 × 0.67	3	2	151	Plastic	27	2.9°	-13.0°
8	Coarse	512 × 512	0.67 × 0.67	3	2	151	Plastic	51	0.7°	0°
9	Coarse	512 × 512	0.67 × 0.67	3	2	151	Plastic	73	-5.8°	0°
10	Coarse	512 × 512	0.67 × 0.67	3	2	151	Glass	92	0°	0°
MRI										
1	T1	480 × 480	0.73 × 0.73	5	5.3	35	Plastic	27	-1.5°	0°
2	T2	480 × 480	0.88 × 0.88	5	5.3	35	Plastic	48	0°	0°
3	T2	480 × 480	0.88 × 0.88	5	5.3	35	Plastic	55	0.9°	0°

bore diameter of 70 cm. Only 3 insertions were done, one using T1-weighted images and the other two using T2-weighted images. To improve fiducial visualization in this wide-bore scanner, in addition to the MRI's main body antenna, a pair of small doughnut-shaped Philips Flex M antennas were fixed to the side of the robot. Due to the 5.3 mm image spacing of these images, only the larger plastic beads were targeted.

The procedure used for all insertions was identical and constrained to the steps defined in the GUI described in section 4.2.6 (page 103). The robot was installed over the phantom on the scanner bed as shown in Figure 4-27 and Figure 4-28. A first image was taken of the entire robot and phantom. Random target and skin insertion points were chosen in this first image. The robot moved the needle automatically to the position above the insertion point. A second control image was then taken, for post-experiment analysis purposes only. This second image was not used to re-adjust the needle position, as the goal of the study was to determine the system's accuracy based on a single image, without any user-induced corrections (i.e. the worst case situation); it was only taken for post-experiment analysis and to adhere to the defined clinical protocol. The needle was then automatically inserted to the calculated depth and a final high-resolution image was taken. The DICOM images created by the imager during the experiments were directly passed to the robot control PC via a DICOM server. The needle used in all the experiments consisted of a 2 mm diameter carbon fiber rod, with its end sharpened into a conical tip. This was used instead of a metallic needle in order to eliminate image artifacts that would hinder the post-experiment analysis in both modalities.

The accuracy measurements were done on the final image. In the CT tests, this image had the same characteristics as images 1 to 6 in Table 4-10, in other words a voxel size of 0.67 × 0.67 × 0.6 mm. In the MRI tests, image size and resolution was identical between all three images for each experiment, as described in Table 4-10, in other words a voxel size of 0.73 × 0.73 × 5.3 mm for the T1 sequence and 0.88 × 0.88 × 5.3 mm for the T2 sequences. Measurements were done for all insertions on this final image by manually segmenting the needle tip and skin insertion points in the images at high zoom. These were then compared to the planned target and insertion points projected onto this final image. This projection could be done because the final image was taken in the exact same spatial configuration as the first image, without moving the robot or phantom on the scanner bed.



Figure 4-27: Photograph of the phantom experiment setup in the CT scanner room. The robot is placed over the phantom at the head of the scanner table. The motor box is placed at the feet of the scanner table. The work area, including control PC, control box and a compressor were placed within the imaging room in order to have a closer view of the robot motions during the experiments.

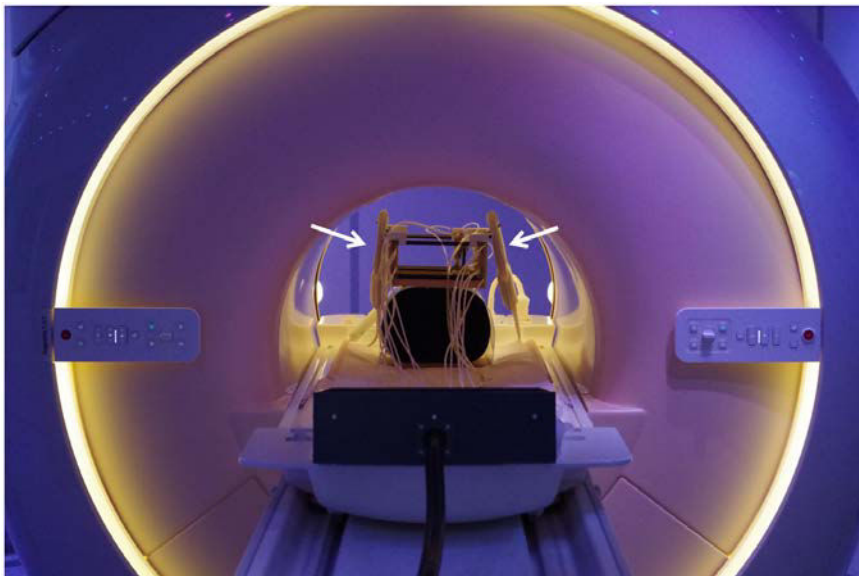


Figure 4-28: Photograph of the phantom experiment setup in the MRI scanner room. Here we see the robot and phantom within the scanner bore, with the motor box in the foreground, well outside the tunnel. The work area, including control PC, control box and compressor were all outside the imaging room. The white arrows point at the two Flex antennas installed on the side of the robot.

Note that these measurements differ from the measurements done in the PROSPER phantom tests described in section 3.3.3 (page 68), in which the target error was measured between the needle tip and the target segmented in the image. In PROSPER, this was done because to project the planned target location chosen in the US images into the CT images would have required a US-CT registration, hence adding registration errors to the measurement. The errors due to the segmentation of the beads were deemed easier to mitigate. In the LPR experiments, our ability to directly project the planned target positions into the final image eliminated both of the above registration and segmentation errors from the measurements.

Table 4-11: Results of the CT phantom tests done with the LPR system. Target error is the distance measured between the segmented needle tip and the planned target position. Angle error is the angular distance between the segmented needle axis and the planned needle direction. The x and y axes are the horizontal and vertical directions in the transverse imaging plane and the z-axis is in the slice-width (tunnel) direction. E stands for the Euclidean distance. In the Image type column, Fine refers to the images with 0.6 mm slice spacing while Coarse refers to the images with 2 mm slice spacing. Means and standard deviations are shown in bold font.

Test #	Image type	Target			Target error (mm)				Angle error	
		Type	Depth (mm)	Hit?	x	y	z	E	Transverse	Sagittal
CT										
1	Fine	Glass	33	No	3.3	3.3	-0.6	4.7	1.5°	-0.2°
2	Fine	Glass	43	Yes	1.3	1.3	1.2	2.2	0.8°	0.4°
3	Fine	Glass	48	No	2.0	3.3	0.0	3.9	0.8°	-0.2°
4	Fine	Glass	52	No	0.0	2.0	-3.0	3.6	2.0°	-0.2°
5	Fine	Glass	62	Yes	1.3	3.3	0.0	3.6	0.4°	0.2°
6	Fine	Glass	88	No	3.3	6.0	0.6	6.9	1.5°	0.2°
7	Coarse	Plastic	27	Yes	1.3	1.3	-3.0	3.5	0.6°	-0.8°
8	Coarse	Plastic	51	Yes	-0.7	0.0	-0.2	0.7	0.1°	-0.6°
9	Coarse	Plastic	73	Yes	-1.3	-0.7	0.6	1.6	-0.2°	-0.4°
10	Coarse	Glass	92	Yes	0.7	-0.7	2.4	2.6	0.6°	0.2°
Total Mean					1.1 ± 1.5	1.9 ± 2.1	-0.2 ± 1.7	3.3 ± 1.7	0.8 ± 0.7°	-0.1 ± 0.4°

Table 4-12: Results of the MRI phantom tests done with the LPR system.

Test #	Image type	Target			Target error (mm)				Angle error	
		Type	Depth (mm)	Hit?	x	y	z	E	Transverse	Sagittal
MRI										
1	T1	Plastic	27	Yes	-0.7	-1.5	0.0	3.1	-1.5°	0.0°
2	T2	Plastic	48	Yes	-1.8	-0.9	0.0	2.0	-1.6°	0.0°
3	T2	Plastic	55	Yes	0.4	0.0	0.0	0.4	-0.5°	0.0°
Mean					-0.7 ± 1.1	-0.8 ± 0.7	0.0 ± 0.0	1.3 ± 0.8	-1.2 ± 0.6°	0.0 ± 0.0°

A visual check of whether the needle hit the target or not was also done through the phantom's window to give a visual qualitative result of whether the target was hit or not. The distance between the needle tip and the planned target position was measured, as was the distance between the actual and planned insertion points. A point high up on the needle was also segmented, allowing the calculation of the resulting needle angles in the transverse and sagittal planes. These angles were compared to their respective planned angles.

Results

The results of the 10 CT experiments are shown in Table 4-11, while the results of the 3 MRI experiments are shown in Table 4-12. Of the seven 1 mm diameter glass beads targeted under CT guidance, three were actually hit by the needle. All of the 7 mm diameter plastic beads were hit in both modalities.

In the CT experiments, insertion depths ranged from 30 to 90 mm. The overall mean error between the final needle tip location and the planned target position was 3.3 ± 1.7 mm. The overall mean error at the insertion point was 1.7 ± 0.9 mm. The overall transverse and sagittal angular errors were $0.8 \pm 0.7^\circ$ and $-0.1 \pm 0.4^\circ$, respectively.

The total mean error in the y (depth) direction was the greatest, the error in the x (transverse, horizontal) direction was also > 1 mm, while the error in the z-direction was fairly low. Naturally, since the errors in the x-direction were larger than in the z-direction, the transverse angle error (about the z-axis) was greater than the sagittal (about the x-axis) error.

Looking now primarily at the first six insertions that used finely-spaced images errors tend to increase with depth, except the first insertion which happened to be the farthest away from the robot's home position. Indeed, errors also tend to increase with the motor distance travelled. This can be seen by normalizing the errors of each insertion with respect to the target depth and plotting the result on a bubble chart, as shown in Figure 4-29.

In the MRI experiments, the overall mean target error in the transverse plane was 1.3 ± 0.8 mm while the transverse angular error was $-1.2 \pm 0.6^\circ$. Note that the zero error in the z (slice-depth) direction, as seen at the bottom of Table 4-12, is not representative, due to the very large slice spacing of the images (over twice the size of the needle's diameter). This made any needle tip errors in the z-direction impossible to distinguish. The Euclidean error of the MRI results should not therefore be compared to the CT results. To measure the z-error, we could have either scanned the phantom after each needle insertion with a CT scanner with fine slice thickness (which would have involved significant planning and coordination, as the CT and MRI machines are not located in the same buildings!), or we could have done a high resolution control MRI image after each insertion (such images would have been very long, taking easily up to 20 minutes each. We did not have the MRI time to do so).

Time-wise, the procedure between the acquisition of the first image and the acquisition of the final image was typically about 20 minutes for the CT experiments and on the order of 30 to 45 minutes for the MRI experiments. The time for the automatic fiducial segmentation and registration procedure described in section 4.2.5 (page 96), was on the order of 40 seconds for the biggest size CT images, and dropping to 3 seconds for the smallest size MRI images. These times were measured on the robot control laptop, which consisted of a 2.80 GHz Intel Core i7 processor, 8 Gb of RAM and a 64-bit Windows 7 Professional platform.

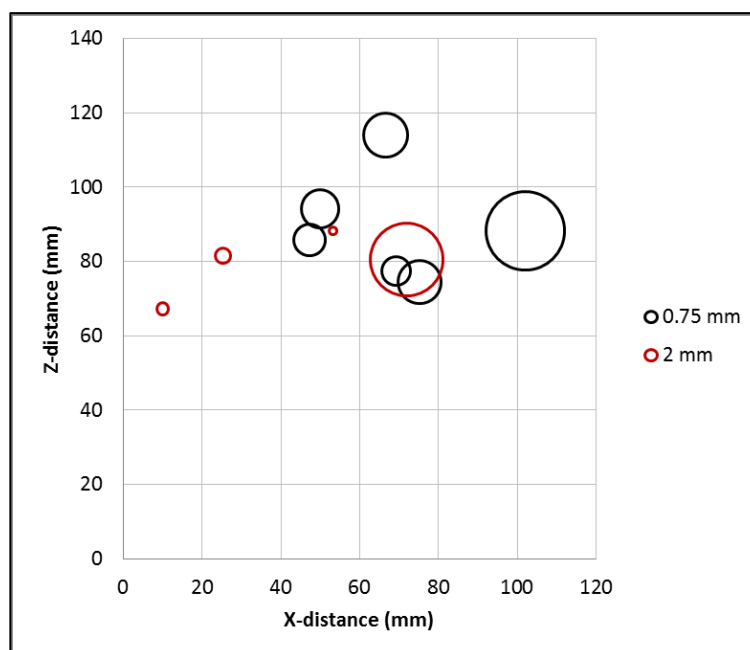


Figure 4-29: Bubble chart showing the amount of relative error at each insertion location. The relative errors are represented by the size of the circles and are the errors normalized to their respective insertion depths (in other words, circle diameter = error / depth, and therefore dimensionless). The x-axis represents the distance travelled by the robot's lower x-motor in order to place the needle in the insertion axis. The z-axis represents the distance travelled by the robot's lower z-motor. The centres of the circles therefore represent the distances travelled by the motors in the x and the z directions, with the robot's home position located at the graph's origin. Black circles are for insertions that used the finer-spaced images, while red circles are for the coarser images. What is important to see in this graph is that the circles get larger the further the motors move in the x and z directions (i.e. towards the upper right corner of the chart).

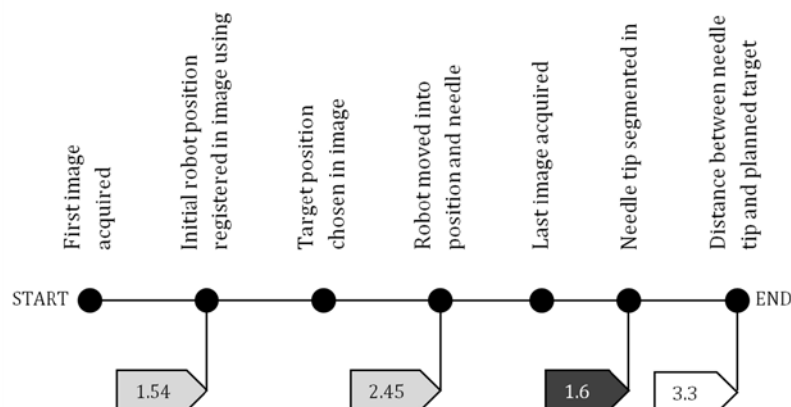


Figure 4-30: The progression of the various errors throughout the CT-guided LPR experimental procedure. The light gray boxes represent the intrinsic system errors. The dark gray boxes represent the extrinsic experimental errors. The white boxes represent the measured distance between the needle tip and the target.

Sources of error

A summary of the various errors encountered during the experiments are shown in Figure 4-30. The sources of experimental error were limited only to the segmentation of the needle tip in the final image. This segmentation was done manually and was therefore prone to human error. It was dependent 1) on the image resolution and 2) on the judgment made in choosing the actual pixel that represented the needle tip. The image resolution could have caused an error of up to 1 voxel. The maximum distance between two voxel centres in the fine CT images used to segment the needle tips is 1.1 mm. In the MRI images, as mentioned above, only the errors in the transverse slices are at all representative. The image resolution error in the transverse direction for the T1 and T2 images is therefore 1.0 mm and 1.2 mm, respectively.

The judgment error in choosing the actual needle tip was based on determining where along the length of the needle the tip actually lay. As we can see in Figure 4-31, the choice of needle tip is not evident and typically spanned between at least 2 voxels. An estimate of the judgement error would therefore be the distance between two voxels, i.e. the same as the image resolution error. The total estimated RMS error in the segmentation of the needle tip in the CT images is therefore 1.6 mm, while the error in the transverse plane of the T1 and T2 images is 1.5 mm and 1.8 mm, respectively.

The errors intrinsic to the LPR system itself were the robot-image calibration error of 1.54 mm (see section 4.2.5, page 96) and the cable-stretch error of 2.45 mm. The latter error was made up of the positioning error of the horizontal joints that position the needle along its desired insertion axis, and the insertion depth error due to the vertical insertion stop mechanism. The positioning error was estimated by calculating the effect of a 0.5 mm joint positioning error due to cable stretch (see section 4.2.4, page 91) on the final target position, as shown in Figure 4-32 and assuming an average depth of 60 mm, resulting in a 1.4 mm error. The insertion depth error was the accumulation of the stop's inaccurate position over the number of insertion strokes required to reach the average depth of 60 mm. Since 20 mm insertion strokes were used during the experiments, this led to a 1.5 mm error. The RMS sum of these two errors gave 2.45 mm. The resulting total intrinsic error was 3.0 mm.

The RMS sum of the intrinsic error and the needle tip segmentation error, gives a total error of 3.4 mm for the CT experiments, which is comparable to the total mean targeting error (3.3 mm) shown in Table 4-11 (page 112).

For the MRI tests, another very important error was discovered after completion of the experiments. This was that the PVC, oil-based fiducials were subject to a chemical shift artifact. Chemical shift artifact results from a slight difference in a material or tissue's resonant frequency, causing a miscalculation of its position in the frequency-encoding direction. Indeed,

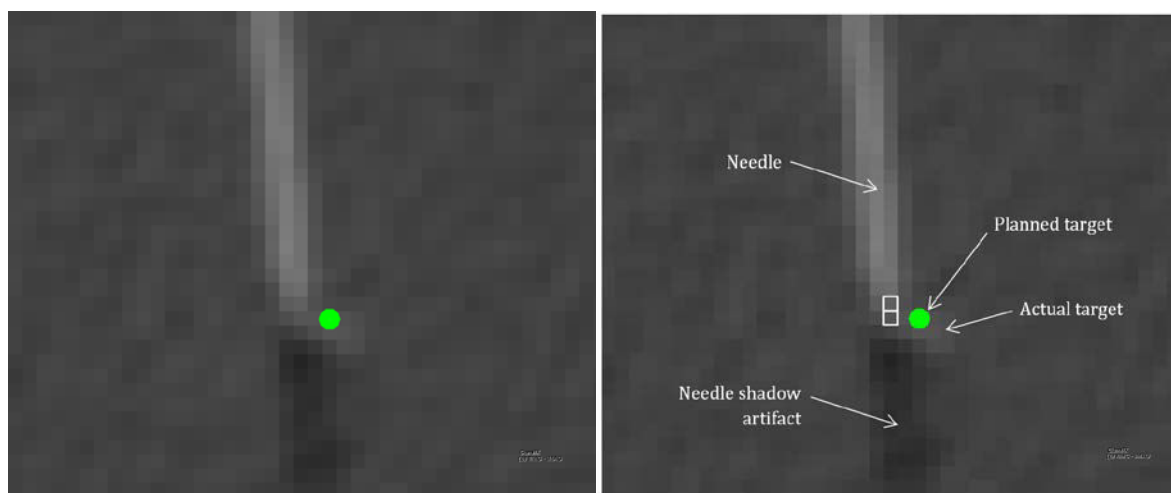


Figure 4-31: Zoomed screenshot of the needle tip in a 0.67×0.67 mm resolution CT image. The left image is the virgin image showing the location of the superimposed planned target. The right image is the same image but labelled. The two white squares represent the two pixels in which the needle tip is most likely to be found.

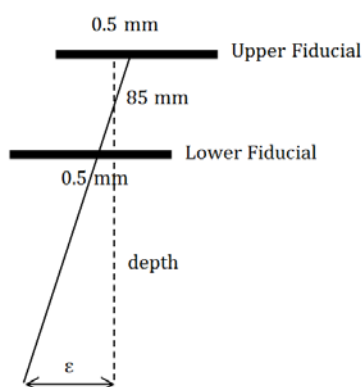


Figure 4-32: Resulting error ϵ at a given depth from the lower fiducial due to a 0.5 mm inaccuracy in joint positioning. 85 mm is the constant distance between the lower and upper fiducials.

an article was published on the subject in 1997 by Condon and Hadley, specifically for soft PVC materials, showing a shift of 2.4 mm. We did our own tests to determine the shift of our fiducials by taking two identical images except with the frequency and phase encoding directions switched. We did this for both the T1 and T2 images done in our experiments. Figure 4-33 shows the resulting segmented fiducials overlaid one on top of the other. The shift of the fiducials' centres of mass in the x (frequency encoding) direction are shown in Table 4-13 and are on the order of 1.5 mm in T1 images and 2 mm in T2 images in the negative x-direction. This likely explains the negative x-errors in the MRI targeting results in Table 4-12 (page 112).

Analysis

The results described above give an idea as to the system's overall accuracy (mean errors) and precision (standard deviation of the errors) when inserting to random targets, without considering needle-tissue interaction forces. Ideally, we would need to do more insertions, but experiments are long and highly dependent on the availability of the clinical imaging machines used. The only available times are either well after typical working hours, or during holiday

season, when the machines are reserved mainly for emergency use and an operator or radiologist is not always present to handle them.

An important point to keep in mind about the phantom experiments is that all the insertions were based on one single initial image. No control corrections were done on subsequent images to ensure the needle was properly aligned with the desired trajectory. This could have been done by registering the current needle position in the second image using the fiducials and measuring its distance from the desired trajectory so as to drive the motors closer. This, of course, would have improved the system's accuracy, depending on how many corrections were made. Indeed, this is the strength of the robot, because although it can do automatic motions, in the end, the desired accuracy is chosen by the radiologist based on what he or she sees and evaluates in the image. But for these experiments, we wished to determine the robot's accuracy alone, without any user input that would improve its chances of doing better. So the measured accuracies are very encouraging.

Some remarks can be made on the CT results presented in the previous sub-section. First of all, the increase in error with insertion depth can likely be attributed to the accumulation with each insertion step of any slight error in the stroke depth set by the insertion stopper. The difference between errors in the x and z directions could be explained by the smaller distribution of the insertion locations in the x-direction, as seen in Figure 4-29 (page 113).

In the CT-guided experiments, not enough insertions were done to make a reliable comparison between the finely (0.6 mm) spaced images and the coarser (2 mm) images, however, it should be noted that prototype's accuracy remains respectably below 5 mm.

4.4 Discussion

In this chapter, we showed that the LPR system is feasible as a potentially fast and reliable way of inserting needles to varying depths in a patient and along any inclination, both in and out of the imaging plane and using the same procedure in both CT and MRI modalities. The accuracy of the system was measured to be less than the 5 mm objective set in section 4.2.1 (page 80), for varying image resolutions, needle depths, inclinations and for both CT and MRI guidance. In addition, since both the target and insertion accuracies were within this 5 mm objective, we can conclude that the needle's trajectory fell within the cylindrical orientation objective, making even this initial prototype clinically viable in terms of both targeting and trajectory accuracy.

It is important to note that the measured accuracies were based on the system automatically reaching the target from a single initial image. In a real clinical situation, this would not be the case, as the user would always take a second image to verify and improve the needle's position before insertion. We could therefore expect the final targeting accuracy to improve. In addition, as mentioned in section 4.2.5 and Figure 4-19 (page 101), the systematic error caused by the miscalibration of the fiducial model used during the registration of the image and robot spaces could very easily be reduced, potentially improving the results significantly. The repeatability (standard deviation of the accuracy measurements) of 1.7 mm could also likely be decreased by eliminating the significant backlash in this prototype.

In the CT phantom experiments described in the previous section, we did a number of experiments with high resolution images in order to get an idea of the system's accuracy in the best of conditions. With these images, the measured 20 minute experiment times were quite long, as the images had to be transferred to the control PC and then processed by the LPR system. The coarser, more clinically viable images that used 3 mm slice thicknesses and 2 mm slice spacing during reconstruction, allowed for significantly higher transfer and processing rates. With the automatic segmentation routine, it was technically extremely simple and fast to move through the procedure and insert the needle.

In the MRI, we were unable to do more than three insertions. It is particularly difficult to reserve research time on this clinical MRI machine and to add salt to the wound, of the three

sessions we were generously given, two were hampered by technical issues with the MRI machine itself. However, it was clear from the experiments that the same ease and rapidity of use was true under MRI guidance. The important difference in MRI is that the quality of the fiducial visualization in the images is highly dependent on the antennas used. With just the body antenna of the 70 cm wide-bore MRI machine that we used, it was nearly impossible to get good images. We did do a number of preliminary compatibility tests in standard 1.5 T and 3 T 60 cm diameter MRI's well before doing the phantom tests, and the fiducials were noticeably more visible with just the standard body coil. Logically, therefore, antenna choice is a key factor.

MRI imaging times are another important factor, as depending on the sequence and slice thickness chosen, these can increase significantly when the large region of interest is required to capture not only the patient but the fiducials above as well. In the phantom experiments, the longer T2 images took on the order of 4 minutes, while the T1 images took about 1 to 2 minutes. For long sequences of many minutes, breath-hold techniques or breathing sensors would have to be used.

Regardless, in both CT and MRI, the imaging sequences and resolution must obviously be chosen by the radiologists with the patient's anatomy (and CT radiation safety) in mind, rather than the visibility of the fiducials. One idea, therefore, would be to use a regular patient-based sequence for the first image, with a slightly taller region of interest to include the robot. For the following control images used to reposition the needle, only the slices required to view the fiducials themselves would be necessary, at least until the radiologist deems it necessary to make another wider angle verification.

Some improvements could be made to this prototype to further improve its accuracy and reliability. First and foremost, the backlash in the joints could be significantly reduced, making joint calibration and repeatability much more accurate. In a clinical setting, insertion forces would be much greater than in the gelatin experiments described. Joint rigidity would therefore be an important aspect to improve upon. In addition, as mentioned before, cable tension would need to be equalized for all the joints, in order to improve the cable stretch calibration. Of course, the patient fixation system still needs to be developed, as well as the cable and housing disconnection system to allow the robot to fit into the STERRAD sterilization chamber.

In addition to design improvements, the presented LPR system makes a number of assumptions that simplify its clinical context, but that would have to be considered in a clinical version. Unlike with PROSPER, it assumes that the target position remains in place during needle insertion. Of course, depth correction can be done if the target is sufficiently precise as to be able to visualize its displacement. If however, like in the prostate, the target is an indistinguishable point within a larger organ, some sort of deformation compensation would have to be included, as in PROSPER.

Furthermore, the procedure is based on a breath-hold imaging sequence, in which each image is acquired and each insertion is done with the patient holding his or her breath with the same inspiration volume. This is common IR practice, however the robot could be used to allow the radiologist to take CT fluoroscopy or real-time MR images of the breathing patient and "shoot" the needle in at a given moment during the respiratory cycle. This is currently not possible without the robot, since the radiologist needs to be inside the imaging room, focused on holding and inserting the needle, rather than carefully looking at the images. Of course, in CT fluoroscopy, this also would entail the radiologist being exposed to repeated radiation; in MRI, it would be technically very difficult due to the depth of the imaging tunnel and the lack of space for the radiologist to hold the needle while looking at the imaging screen.

The LPR system therefore has a huge potential for providing easier, faster and more complex insertions under both CT and MRI guidance, with fewer images required to reach a target. Because of its versatility in positioning on the patient's body and its multi-modality, a large number of IR interventions would be available, along with the prospective for the development of new interventions, previously technically unfeasible.

Chapter 5: Conclusion

5.1 Thesis summary	118
5.2 Contributions	119
5.3 Perspectives	120
5.4 Publications	122

5.1 Thesis summary

In this thesis, we have discussed the design and validation of image-guided percutaneous computer and robotic assisted needle interventions. A number of aspects were discussed, including the types of clinical interventions open to such systems, the common types of imaging modalities used, the difficulties encountered in the conventional manual techniques and the advantages that robotic systems could bring. The particularities in the design of such systems were examined, focusing on how they were affected by the imaging modality, needle and the soft tissue interactions. The typical methods with which robotic systems can be calibrated with the images used to guide them were also discussed. An analysis of the validation and testing of such systems, along with the sources of error affecting their targeting accuracy were also described.

Two robots, PROSPER and LPR, were then described, that were designed, constructed and pre-clinically validated during this thesis. Although their overall goal of inserting a needle through the skin to a given target in the image was the same, resulting in very similar robot kinematics, their clinical settings were different. They each presented their own design challenges that covered the large spectrum of design and evaluation constraints outlined in Chapter 2, specific to needle insertion robots and summarized in Table 5-1.

Medical imaging constraints were widely covered by both systems, with the use of three of the four main image guidance modalities: US, CT and MRI. Image compatibility was an important issue in the LPR system, as the robot lies within the actual image space, potentially affecting image quality. Workspace compatibility had to be considered in both systems, as PROSPER's needle manipulation range had to fall within the relatively small and directionally constrained imaging volume of an endfire US probe, while the LPR had to fit inside the tight tunnel constraints of CT and MRI machines.

Both robotic architectures were designed keeping in mind the two phases of needle insertion procedures. More specifically, they both consisted of a positioning module and an insertion module that could be considered independent, with different technical constraints and consequently different actuation techniques. The insertion modules both took into account the possibility of accidental contact with hard bone, PROSPER putting into place a needle release mechanism and LPR being able to slide the needle in its grips upon hard contact.

The PROSPER project took into account soft-tissue constraints by experimenting with needle rotation and more importantly, by using a registration technique for intra-operative prostate motion and deformation tracking.

Robot fixation was explored differently by both systems, with the PROSPER system fixed to the surgical table and the LPR system mounted on the patient's body. The former could be justified because the patient is fully anaesthetized during prostate brachytherapies, making patient motion less likely. The latter, however, being much more prone to patient motion,

Table 5-1: Comparison of the various design constraints considered in the PROSPER and LPR systems.

Design constraint	PROSPER	LPR
Image compatibility		X
Workspace compatibility	X	X
Positioning module	X	X
Insertion module	X	X
Bone contact	X	X
Soft tissue motion and deformation	X	
Robot fixation	X	X
Pre-operative calibration	X	
Intra-operative calibration		X
Sterilization	X	X
Accuracy	X	X

required body-mounting to help reduce the risk of harming the patient once the needle was inserted.

The robot's fixation was closely related to the robot-image calibration techniques chosen for both systems. The PROSPER system took advantage of the small size and easy handling of US probes to use a one-time pre-operative calibration, bypassing the need to calibrate in the OR. The US probe was hence fixed rigidly to the robot manipulator. The LPR system, on the other hand, relies on intra-operative calibration, putting into place a fully automatic fiducial segmentation and registration method compatible with both CT and MRI.

The sterilization of both systems was considered, PROSPER leading to a solution based on sterile drapes and caps while the LPR robot being sterilized in its entirety, bringing about distinct design challenges.

Finally, both systems were evaluated in a pre-clinical setting on synthetic phantoms, in particular with respect to their targeting accuracies. The sources of error intrinsic to the systems and those related to the tests themselves were analyzed, including imaging errors, calibration errors, kinematic errors, and measurement errors. Both systems showed accuracies that fell within the technical and clinical goals set at the onset of the projects.

5.2 Contributions

The two robotic systems proposed in this thesis provide various technical and clinical contributions with respect to the conventional prostate brachytherapy and IR techniques as well as to the many other existing robotic systems described in Chapter 1 and Chapter 2.

With the PROSPER system, a novel approach to performing brachytherapies was proposed in which the robot was coupled to 3D TRUS imaging and a US registration algorithm to take into account prostate motion and deformation during insertion. A pre-clinical prototype was designed and built. The details of the robotic manipulator were described, including its design, its forward and inverse kinematics and the kinematic calibration tests used to improve its intrinsic mechanical accuracy. A unique robot-probe calibration technique was also described that allowed the robot to be calibrated to the 3D US images without needing to tilt the robot vertically into a water bath, as is done conventionally. The effect of needle rotation on needle-tissue interaction forces and on potential tissue damage was also described. A novel mobile prostate phantom was developed and studied in detail, that allowed experimentation on the system including prostate motion and deformation during insertion. Phantom tests were done to determine the viability and accuracy of using the system on a deformable medium. These tests showed that, on average, the robot was able to reduce the targeting error within the mobile phantom prostate from around 6 mm to 1.6 mm, in the needle insertion direction, which was well within the 2 mm clinical objective.

The expected clinical benefits of the PROSPER system are numerous. First of all, with an improved accuracy and its motion-tracking ability, the dose plans could be more accurately followed, resulting in higher dose conformity and therefore potentially fewer adverse side-effects, such as incontinence, impotence, and cancer recurrence. Technically, the brachytherapy would be easier to perform, as the matching of the image to the actual needle position would be done by the robot, potentially requiring fewer repeat insertions. The robot could also make the procedure available to patients with tight pubic arch constraints, by allowing urologists to pass the needles underneath and behind the bone using needle inclinations.

With the LPR system, an original cable-driven manipulator was proposed for performing CT and MRI-guided needle insertions. A pre-clinical prototype was also built and tested. The robotic manipulator, its kinematics, sterilization and cable stretch aspects were described. A fully automatic image processing routine was designed to locate the robot in the image intra-operatively and that worked in both imaging modalities. This allowed a clinical protocol to be designed and applied in a preliminary user interface. The CT and MRI compatibility of the robot was studied to ensure no image artifacts were caused by the robot's presence in the images. The system was tested in both modalities and evaluated in terms of its accuracy in reaching internal targets. The targeting accuracy was found to be less than 3.5 mm at depths ranging from 30 to 90 mm, with needle inclination accuracy remaining below 1°. These results were within the 5 mm clinical objective.

The novelty of the LPR system lies in a number of aspects. Firstly, its multi-modality greatly opens up its expected clinical benefit, providing radiologists with a versatile tool that can be used to take advantage of both CT and MRI's imaging particularities. Its fixation on the patient's body allows it to move with the patient, improving safety and comfort. The use of offset motors allows the robot structure to be lighter and less prone to image artifacts. Its accuracy and fully automatic registration routine, could allow the robot to be used in more complex situations, in which out-of-plane needle inclinations and close insertion tolerances are required. It would also potentially reduce the number of images required to reach the target, reducing the number of breath-holds required by the patient, decreasing the radiation exposure in CT interventions, eliminating the need for the radiologist to come and go between the patient and the control room, and shortening the overall procedure time. Finally, with regards to MRI, it could open up the possibility of doing interventions that currently are not technically feasible given the magnetic and space constraints of standard MRI machines.

5.3 Perspectives

The work in this thesis lay the foundations for the development of clinical prototypes of both systems. Indeed, work is already well under way to develop new versions that take into account the improvements enlightened during this thesis and that meet the regulatory demands for clinical trials.

The new PROSPER clinical prototype will fully take into account sterilization and draping of the system, fixation to the surgical table, an increased workspace to account for particular cases, such as patients with a highly constrained pubic arch and requiring large needle inclinations, increased rigidity to allow easier handling and greater insertion accuracy, faster motors to speed up the needle positioning and updated electronics to meet the electrical and electromagnetic norms required for OR use.

Before going on real patients, work also remains on the image processing and dosimetry aspects of the PROSPER system. The US-US registration technique's ability to track the prostate with the presence of volume deformations due to intraoperative oedema, in addition to image noise due to the increasing presence of seeds, must be validated on real patients. Also, the dose planning aspect of the system needs to be developed and incorporated, with the eventual goal of providing dynamic dose planning based on automatic intra-operative seed detection. These aspects were all out of the scope of this thesis.

The PROSPER robot was described in this thesis in the context of prostate brachytherapies, however, as mentioned, it could also be of great use for transperineal biopsies as well as for the growing trend of focal therapy. Transperineal biopsies are prescribed to patients who have contra-indications to the standard transrectal approach, such as prior rectal operations for example. Focal therapy of the prostate is an emerging field, with rapidly growing interest in urological circles. It relies on the accurate diagnosis of the gland, pinpointing the exact areas of tumor presence and therefore allowing a highly concentrated treatment in just these regions. The potential benefits of such treatment would be a reduced risk of adverse side-effects by offering a less aggressive treatment. Indeed, the high accuracy of the PROSPER system, along with its ability to track prostate motion, would make it ideal for such an accuracy-demanding procedure. Of course, an equally accurate diagnosis is vital to allowing even the consideration of such focal therapy.

With this in mind, an MRI-TRUS fusion algorithm, developed in our laboratory [236], could be a particularly useful addition to the PROSPER system, as it could allow the robot to focus its treatment on the lesions visible in the MRI image. It could also help speed up the manual segmentation of the prostate in the US images during the dose planning stage, as MRI scans are easier to segment and can be interpreted pre-operatively by the urologist in the calm of his or her office.

The PROSPER robot could also be of value in combination with the state-of-the-art research on flexible needles and needle steering. Because of the manipulator's rotational degree of freedom, which allows either continuous or discrete needle rotations, bevel-tip needles could be used to actively steer their natural curvature through the tissue and either to avoid obstacles or to improve their targeting accuracy. Indeed, needle steering could be a solution for taking into account the rotations of the prostate during insertion. This could be done by inserting the needle progressively and steering the needle in the direction of the prostate's rotation.

The LPR system is also being redesigned in view of doing first clinical trials. Like PROSPER, the new prototype will take into account sterilization, increased rigidity, increased workspace and clinically authorized electronics. Its fixation to the patient with straps and likely a vacuum cushion will also be put into place, allowing it to sit on the patient during the potentially extended period of the intervention. It will likely also include a second set of fiducials mounted on the robot's frame that would allow for the estimation of the robot's joint positions directly from the images. This would act as a substitution to the lack of sensors on the robot's joints.

Like with the PROSPER system, before going on patients, not only the mechanical and electronic aspects need to be certified, but also the software and GUI needs to be developed and tested within the confines of a quality control and risk analysis structure. This is currently under way with the goal of putting into place first clinical tests within the next year.

As mentioned before, the LPR robot could be used during real-time imaging, allowing the radiologist to progressively shoot the needle in as the patient breathes regularly and when the desired target moves in line with the needle axis (ideally at the end of expiration, when breathing is momentarily paused). In addition to this, research has begun on the subsequent teleoperation of the robot. Very preliminary tests have already been done showing a radiologist's ability to point and shoot the robot over an illustrative geographical distance (Montpellier-Grenoble) using an Omega device (Force Dimension, Nyon, Switzerland) and TCP internet protocol. The goal would not necessarily be to control the robot from a large distance, but rather to allow the radiologist to actively act on the position and insertion of the needle, following the patient's motions. A wealth of research directions will stem from this, including force feedback (requiring the installation of sensors on the robot) and target motion tracking.

5.4 Publications

The following works were published during this thesis:

Peer-reviewed journal papers:

- **N. Hungr**, M. Baumann, J. A. Long, J. Troccaz, "A 3-D Ultrasound Robotic Prostate Brachytherapy System With Prostate Motion Tracking," *IEEE Transactions on Robotics*, vol. 28, no. 6, pp. 1382-1397, 2012. [[PROSPER](#)]
- **N. Hungr**, J. A. Long, V. Beix, J. Troccaz, "A realistic deformable prostate phantom for multimodal imaging and needle-insertion procedures," *Medical Physics*, vol. 39, no. 4, pp. 2031-2041, 2012. [[PROSPER](#)]
- J. A. Long, **N. Hungr**, M. Baumann, J. L. Descotes, M. Bolla, J. Y. Giraud, J. J. Rambeaud, J. Troccaz, "Development of a Novel Robot for Transperineal Needle Based Interventions: Focal Therapy, Brachytherapy and Prostate Biopsies," *The Journal of Urology*, vol. 188, no. 4, pp. 1369-1374, 2012. [[PROSPER](#)]

Peer-reviewed conference articles:

- **N. Hungr**, C. Fouard, A. Robert, I. Bricault, P. Cinquin, "Interventional Radiology Robot for CT and MRI Guided Percutaneous Interventions," *MICCAI*, pp. 137-144, 2011. [[LPR](#)]
- **N. Hungr**, J. Troccaz, N. Zemiti, N. Tripodi, "Design of an ultrasound-guided robotic brachytherapy needle insertion system" *EMBC*, pp. 250-253, 2009. [[PROSPER](#)]

Patent:

- M. Baumann, **N. Hungr**, A. Leroy, J. Troccaz, V. Daanen, "Control System and Method for Precisely Guiding a Percutaneous Needle Toward the Prostate" *US Patent Application*, No. 20120245455, 2012. [[PROSPER](#)]

References

- [1] Société Française de Radiology (SFR), "La radiologie interventionnelle en France," Fédération de Radiologie Interventionnelle (FRI), 2010.
- [2] INCa, "Radiologie interventionnelle en cancérologie. Etat des lieux," Boulogne-Billancourt, 2009.
- [3] The Royal College of Radiologists, "Clinical Radiology UK Workforce Report 2011," 2012.
- [4] "Specialties & Subspecialties," 2012. [Online]. Available: http://www.abms.org/who_we_help/physicians/specialties.aspx. [Accessed 12 February 2013].
- [5] E. I. Bluth, B. W. Short and S. Willis-Walton, "2012 ACR Commission on Human Resources Workforce Survey," *Journal of the American College of Radiology*, vol. 9, no. 9, pp. 625-629, September 2012.
- [6] M. O. Baerlocher, R. Owen, A. Poole and M.-F. Giroux, "Interventional radiology deserves formal recognition as a distinct medical subspecialty: a statement from the Canadian Interventional Radiology Association," *Journal of vascular and interventional radiology*, vol. 19, no. 1, pp. 9-12, January 2008.
- [7] "OECD Health Data 2012 - Frequently Requested Data," Organisation for Economic Co-operation and Development (OECD), 2012.
- [8] R. Smith-Bindman, D. L. Miglioretti, E. Johnson, C. Lee, H. Spencer Feigelson, M. Flynn, R. T. Greenlee, R. L. Kruger, M. C. Hornbrook, D. Roblin, L. I. Solberg, N. Vanneman, S. Weinmann and A. E. Williams, "Use of Diagnostic Imaging Studies and Associated Radiation Exposure for Patients Enrolled in Large Integrated Health Care Systems, 1996-2010," *The Journal of the American Medical Association*, vol. 307, no. 22, pp. 2400-2409, 2012.
- [9] M. Peikari, T. K. Chen, A. Lasso, T. Heffter and G. Fichtinger, "Effects of Ultrasound Section-Thickness on Brachytherapy Needle Tip Localization Error," *MICCAI 2011*, vol. LNCS 6891, no. 1, pp. 299-306, 2011.
- [10] K. Perisinakis, J. Damilakis, N. Theocharopoulos, G. Papadokostakis, A. Hadjipavlou and N. Gourtsoyiannis, "Patient Exposure and Associated Radiation Risks from Fluoroscopically Guided Vertebroplasty or Kyphoplasty," *Radiology*, vol. 232, pp. 701-707, 2004.
- [11] S. Balter, J. W. Hopewell, D. L. Miller, L. K. Wagner and M. J. Zelefsky, "Fluoroscopically Guided Interventional Procedures: A Review of Radiation Effects on Patients' Skin and Hair," *Radiology*, vol. 254, pp. 326-341, February 2010.
- [12] D. L. Miller, E. Vañó, G. Bartal, S. Balter, R. Dixon, R. Padovani, B. Schueler, J. F. Cardella and T. de Baère, "Occupational Radiation Protection in Interventional Radiology: A Joint Guideline of the Cardiovascular and Interventional Radiology Society of Europe and the Society of Interventional Radiology," *Cardiovascular and Interventional Radiology*, vol. 33, no. 2, pp. 230-239, April 2010.

- [13] A. Moreau-Gaudry, E. Chipon, P. Durand, L. Carrat and I. Bricault, "Première évaluation du Service Médical Rendu d'un système de navigation pour l'assistance des gestes de radiologie interventionnelle sous scanner," in *Recherche en Imagerie et Technologies (RITS)*, Rennes, 2011.
- [14] P. P. Dendy, "Radiation risks in interventional radiology," *The British Journal of Radiology*, vol. 81, pp. 1-7, 2008.
- [15] S. Leng, J. A. Christner, S. K. Carlson, M. Jacobsen, T. J. Vrieze, T. D. Atwell and C. H. McCollough, "Radiation Dose Levels for Interventional CT Procedures," *American Journal of Roentgenology*, vol. 197, no. 1, pp. W97-103, July 2011.
- [16] G. R. Kim, J. Hur, S. M. Lee, H.-J. Lee, Y. J. Hong, J. E. Nam, H. S. Kim, Y. J. Kim, B. W. Choi, T. H. Kim and K. O. Choe, "CT fluoroscopy-guided lung biopsy versus conventional CT-guided lung biopsy: a prospective controlled study to assess radiation doses and diagnostic performance," *European Radiology*, vol. 21, p. 232-239, 2011.
- [17] M. Sarti, W. P. Brehmer and S. B. Gay, "Low-Dose Techniques in CT-guided Interventions," *RadioGraphics*, vol. 32, pp. 1109-1119, July 2012.
- [18] S. Tatli, P. R. Morrison, K. Tuncali and S. G. Silverman, "Interventional MRI for Oncologic Applications," *Techniques in Vascular and Interventional Radiology*, vol. 10, pp. 159-170, 2007.
- [19] R. C. Semelka, "Whole-Body Screening: MRI vs CT -- A Clinician's Perspective," 9 September 2004. [Online]. Available: http://www.medscape.org/viewarticle/488088_print. [Accessed 7 March 2013].
- [20] J.-W. Kwek, C.-H. Thng, P.-H. Tan, J. S.-P. Yuen, J. B.-K. Khoo, S.-T. Quek, J. T.-S. Ho, K.-P. Tan and C. W.-S. Cheng, "Phased-array Magnetic Resonance Imaging of the Prostate with Correlation to Radical Prostatectomy Specimens: Local Experience," *Asian Journal of Surgery*, vol. 27, no. 3, pp. 219-224, July 2004.
- [21] J. Nakashima, A. Tanimoto, Y. Imai, M. Mukai, Y. Horiguchi, K. Nakagawa, M. Oya, T. Ohigashi, K. Marumo and M. Murai, "Endorectal MRI for prediction of tumor site, tumor size, and local extension of prostate cancer," *Urology*, vol. 64, pp. 101-105, 2004.
- [22] M. G. Swanson, D. B. Vigneron, L. Z. Tabatabai, R. G. Males, L. Schmitt, P. R. Carroll, J. K. James, R. E. Hurd and J. Kurhanewicz, "Proton HR-MAS Spectroscopy and Quantitative Pathologic Analysis of MRI/3D-MRSI-Targeted Postsurgical Prostate Tissues," *Magnetic Resonance in Medicine*, vol. 50, p. 944-954, 2003.
- [23] C. K. Kim, B. K. Park and B. Kim, "Localization of prostate cancer using 3T MRI: comparison of T2-weighted and dynamic contrast enhanced imaging," *Journal of Computer Assisted Tomography*, vol. 30, no. 1, pp. 7-11, January/February 2006.
- [24] V. A. Morgan, S. Kyriazi, S. E. Ashley and N. M. DeSouza, "Evaluation of the Potential of Diffusion-Weighted Imaging in Prostate Cancer Detection," *Acta Radiologica*, vol. 48, no. 6, pp. 695-703, 2007.
- [25] K. Kitajima, Y. Kaji, Y. Fukabori, K.-i. Yoshida, N. Sukanuma and K. Sugimura, "Prostate Cancer Detection With 3 T MRI: Comparison of Diffusion-Weighted Imaging and Dynamic Contrast-Enhanced MRI in Combination With T2-Weighted Imaging,"

- Journal of Magnetic Resonance Imaging*, vol. 31, pp. 625-631, 2010.
- [26] B. R. Sequeiros, R. Ojala, J. Kariniemi, J. Perälä, J. Ninimäki, H. Reinikainen and O. Tervonen, "MR-Guided Interventional Procedures: A Review," *Acta Radiologica*, vol. 6, pp. 576-586, 2005.
- [27] G. C. Kagadis, K. Katsanos, D. Karnabatidis, G. Loudos, G. C. Nikiforidis and W. R. Hendee, "Emerging technologies for image guidance and device navigation in interventional radiology," *Medical Physics*, vol. 39, no. 9, pp. 5768-5781, September 2012.
- [28] A. R. Padhani, D.-M. Koh and D. J. Collins, "Whole-Body Diffusion-weighted MR Imaging in Cancer: Current Status and Research Directions," *Radiology*, vol. 261, no. 3, pp. 700-711, December 2011.
- [29] A. R. Gillams, "Image guided tumour ablation," *Cancer Imaging*, vol. 5, pp. 103-109, 2005.
- [30] D. F. Saldanha, V. L. Khatani, T. C. Carrillo, F. Y. Yap, J. T. Bui, M. G. Knuttinen, C. A. Owens and R. C. Gaba, "Current Tumor Ablation Technologies: Basic Science and Device Review," *Seminars in Interventional Radiology*, vol. 27, no. 3, pp. 247-254, 2010.
- [31] M. Ahmed, C. L. Brace, F. T. Lee and S. N. Goldberg, "Principles of and Advances in Percutaneous Ablation," *Radiology*, vol. 258, no. 2, pp. 351-369, February 2011.
- [32] Y. Ni, S. Mulier, Y. Miao, L. Michel and G. Marchal, "A review of the general aspects of radiofrequency ablation," *Abdominal Imaging*, vol. 30, pp. 381-400, 2005.
- [33] B. Zhang, M. Moser, E. Zhang and W. J. Zhang, "Radiofrequency ablation technique in the treatment of liver tumours: review and future issues," *Journal of Medical Engineering & Technology*, vol. 37, no. 2, pp. 150-159, 2013.
- [34] B. Rubinsky, C. Y. Lee, J. Bastacky and G. Onik, "The Process of Freezing and the Mechanism of Damage during Hepatic Cryosurgery," *Cryobiology*, vol. 27, pp. 85-97, 1990.
- [35] A. Kapoor, N. J. Touma and R. El Dib, "Review of the efficacy and safety of cryoablation for the treatment of small renal masses," *Canadian Urological Association Journal*, vol. 7, no. 1, pp. E38-E43, January 2013.
- [36] C. Pusceddu, B. Sotgia, R. M. Fele and L. Melis, "CT-guided thin needles percutaneous cryoablation (PCA) in patients with primary and secondary lung tumors: A preliminary experience," *European Journal of Radiology*, vol. xxx, pp. xxx-xxx, 2013.
- [37] G. Onik, "Percutaneous Image-Guided Prostate Cancer Treatment: Cryoablation as a Successful Example," *Techniques in Vascular and Interventional Radiology*, vol. 10, pp. 149-158, 2007.
- [38] C. J. Simon, D. E. Dupuy and W. W. Mayo-Smith, "Microwave Ablation: Principles and Applications," *RadioGraphics*, vol. 25, pp. S69-S83, 2005.
- [39] T. J. Vogl, R. Straub, K. Eichler, D. Woitaschek and M. G. Mack, "Malignant Liver Tumors Treated with MR Imaging-guided Laser-induced Thermotherapy: Experience with Complications in 899 Patients (2,520 lesions)," *Radiology*, vol. 225, no. 2, pp.

- 367-377, 2002.
- [40] C. M. Moore, M. Emberton and S. G. Bown, "Photodynamic Therapy for Prostate Cancer- An Emerging Approach for Organ-Confined Disease," *Lasers in Surgery and Medicine*, vol. 43, pp. 768-775, 2011.
 - [41] L. Blendis, "Percutaneous ethanol ablation of small hepatocellular carcinomas: twenty years on," *Gastroenterology*, vol. 130, no. 1, pp. 280-282, January 2006.
 - [42] M. G. Harisinghani, D. A. Gervais, P. F. Hahn, C. H. Cho, K. Jhaveri, J. Varghese and P. R. Mueller, "CT-guided Transgluteal Drainage of Deep Pelvic Abscesses: Indications, Technique, Procedure-related Complications, and Clinical Outcome," *RadioGraphics*, vol. 22, pp. 1353-1367, 2002.
 - [43] M. M. Maher, D. A. Gervais, M. K. Kalra, B. Lucey, D. V. Sahani, R. Arellano, P. F. Hahn and P. R. Mueller, "The Inaccessible or Undrainable Abscess: How to Drain It," *Radiographics*, vol. 24, pp. 717-735, 2004.
 - [44] S. I. Seldinger, "Catheter replacement of the needle in percutaneous arteriography," *Acta Radiologica*, vol. 39, no. 5, pp. 368-376, 1953.
 - [45] J. Fritz, T. Niemeyer, S. Clasen, J. Wiskirchen, G. Tepe, B. Kastler, T. Nägele, C. W. König, C. D. Claussen and P. L. Pereira, "Management of Chronic Low Back Pain: Rationales, Principles, and Targets of Imaging-guided Spinal Injections," *RadioGraphics*, vol. 27, pp. 1751-1771, 2007.
 - [46] A. Loizides, S. Peer, M. Plaikner, V. Spiss, K. Galiano, J. Obernauer and H. Gruber, "Ultrasound-guided injections in the lumbar spine," *Medical Ultrasonography*, vol. 13, no. 1, pp. 54-58, 2011.
 - [47] J. Obernauer, K. Galiano, H. Gruber, R. Bale, A. A. Obwegeser, R. Schatzer and A. Loizides, "Ultrasound-guided versus Computed Tomography-controlled facet joint injections in the middle and lower cervical spine: a prospective randomized clinical trial," *Medical Ultrasonography*, vol. 15, no. 1, pp. 10-15, March 2013.
 - [48] M. H. Maurer, N. Schreiter, M. de Bucourt, C. Grieser, D. M. Renz, T. Hartwig, B. Hamm and F. Streitparth, "Cost comparison of nerve root infiltration of the lumbar spine under MRI and CT guidance," *European Radiology*, January 2013.
 - [49] National Electrical Manufacturers Association, "Determination of Signal-to-Noise Ratio (SNR) in Diagnostic Magnetic Resonance Imaging," National Electrical Manufacturers Association, 2008.
 - [50] National Electrical Manufacturers Association, "Determination of Image Uniformity in Diagnostic Magnetic Resonance Images," National Electrical Manufacturers Association, 2008.
 - [51] G. Schaeffers, "Testing MR Safety and Compatibility: An Overview of the Methods and Current Standards," *IEEE Engineering in Medicine and Biology Magazine*, pp. 23-27, May/June 2008.
 - [52] E. Lermite, C. Aubé, P. Pessaux and J.-P. Arnaud, "Thermo-ablation par radiofréquence des tumeurs hépatiques," *Presse Médicale*, vol. 36, no. 7-8, pp. 1127-1134, July/August 2007.
 - [53] J. M. Hernández-García, M. A. Reina, A. Prats-Galino and J. A. De Andrés, "Morphologic

- Study of Nerve Root and Types of Needle Used in Transforaminal Injections," *Regional Anesthesia and Pain Medicine*, vol. 36, no. 3, pp. 278-281, May/June 2011.
- [54] Institut National du Cancer, "La situation du cancer en France en 2012," Institut National du Cancer, 2012.
- [55] American Cancer Society, "Cancer Facts & Figures 2013," American Cancer Society, Atlanta, 2013.
- [56] V. Scattoni, C. Maccagnano, G. Zanni, D. Angiolilli, M. Raber, M. Roscigno, P. Rigatti and F. Montorsi, "Is extended and saturation biopsy necessary?," *International Journal of Urology*, vol. 17, pp. 432-449, 2010.
- [57] V. Scattoni, A. Zlotta, R. Montironi, C. Schulman, P. Rigatti and F. Montorsi, "Extended and Saturation Prostatic Biopsy in the Diagnosis and Characterisation of Prostate Cancer: A Critical Analysis of the Literature," *European Urology*, vol. 52, pp. 1309-1322, 2007.
- [58] G. Onik, M. Miessau and D. G. Bostwick, "Three-Dimensional Prostate Mapping Biopsy Has a Potentially Significant Impact on Prostate Cancer Management," *Journal of Clinical Oncology*, vol. 27, no. 26, pp. 4321-4326, September 2009.
- [59] R. Sanchez-Salas, N. Miranda, R. Valero, M. Sánchez-Encinas, A. Ouzzane, M. Galiano, F. Rozet, E. Barret and X. Cathalineau, "The impact of saturation biopsy in decision making for low risk prostatic carcinoma after prior positive biopsy," in *5th International Symposium on Focal Therapy and Imaging in Prostate & Kidney Cancer*, 2012.
- [60] E. Barret, Y. Ahallal, R. Sanchez-Salas, M. Galiano, J.-M. Cosset, P. Validire, P. Macek, M. Durand, D. Prapotnich, F. Rozet and X. Cathelineau, "Morbidity of Focal Therapy in the Treatment of Localized Prostate Cancer," *European Urology*, vol. 63, pp. 618-622, 2013.
- [61] R. T. Schulte, D. P. Wood, S. Daignault, R. B. Shah and J. T. Wei, "Utility of Extended Pattern Prostate Biopsies for Tumor Localization: Pathologic Correlations following Radical Prostatectomy," *Cancer*, vol. 113, no. 7, pp. 1559-1565, October 2008.
- [62] J. T. Wei, "Limitations of a Contemporary Prostate Biopsy: The Blind March Forward," *Urologic Oncology*, vol. 28, no. 5, pp. 546-549, 2010.
- [63] P. Mozer, M. Baumann, G. Chevreau, A. Moreau-Gaudry, S. Bart, R. Renard-Penna, E. Comperat, P. Conort, M.-O. Bitker, E. Chartier-Kastler, F. Richard and J. Troccaz, "Mapping of Transrectal Ultrasonographic Prostate Biopsies - Quality Control and Learning Curve Assessment by Image Processing," *Journal of Ultrasound in Medicine*, vol. 28, no. 4, pp. 455-460, April 2009.
- [64] P. Stattin, E. Holmberg, J.-E. Johansson, L. Holmberg, J. Adolfsson and J. Hugosson, "Outcomes in Localized Prostate Cancer: National Prostate Cancer Register of Sweden Follow-up Study," *Journal of the National Cancer Institute*, vol. 102, no. 13, pp. 950-958, July 2010.
- [65] G. Lu-Yao, P. C. Albertsen, D. F. Moore, W. Shih, Y. Lin, R. S. DiPaola, M. J. Barry, A. Zietman, M. O'Leary, E. Walker-Corkery and S.-L. Yao, "Outcomes of localized prostate cancer following conservative management," *The Journal of the*

- American Medical Association*, vol. 302, no. 11, pp. 1202-1209, September 2009.
- [66] P. Grimm and J. Sylvester, "Advances in Brachytherapy," *Reviews in Urology*, vol. 6, no. Suppl. 4, pp. S37-S48, 2004.
- [67] U. Lindner and J. Trachtenberg, "Focal therapy for localized prostate cancer - choosing the middle ground," *Canadian Urological Association Journal*, vol. 3, no. 4, pp. 333-335, August 2009.
- [68] G. Onik, "Rationale for a "Male Lumpectomy," a Prostate Cancer Targeted Approach Using Cryoablation: Results in 21 Patients with at Least 2 Years of Follow-Up," *Cardiovascular and Interventional Radiology*, vol. 31, pp. 98-106, 2008.
- [69] D. S. Ellis, T. B. Manny and J. C. Rewcastle, "Focal Cryosurgery Followed by Penile Rehabilitation as Primary Treatment for Localized Prostate Cancer: Initial Results," *Urology*, vol. 70, no. Suppl 6A, pp. 9-15, 2007.
- [70] S. Langley, H. U. Ahmed, B. Al-Qaisieh, D. Bostwick, L. Dickinson, F. Gomez Veiga, P. Grimm, S. Machtens, F. Guedea and M. Emberton, "Report of a consensus meeting on focal low dose rate brachytherapy for prostate cancer," *BJU International*, vol. 109, no. Suppl 1, pp. 7-16, February 2012.
- [71] J. E. Dawson, T. Wu, T. Roy, J. Y. Gu and H. Kim, "Dose effects of seeds placement deviations from pre-planned positions in ultrasound guided prostate implants," *Radiotherapy and Oncology*, vol. 32, no. 3, pp. 268-270, September 1994.
- [72] N. N. Stone, J. Roy, S. Hong, Y. C. Lo and R. G. Stock, "Prostate gland motion and deformation caused by needle placement during brachytherapy," *Brachytherapy*, vol. 1, no. 3, pp. 154-160, 2002.
- [73] V. Lagerburg, M. A. Moerland, J. J. W. Lagendijk and J. J. Battermann, "Measurement of prostate rotation during insertion of needles for brachytherapy," *Radiotherapy and Oncology*, vol. 77, no. 3, pp. 318-323, December 2005.
- [74] R. Taschereau, J. Pouliot, J. Roy and D. Tremblay, "Seed misplacement and stabilizing needles in transperineal permanent prostate implants," *Radiotherapy and Oncology*, vol. 55, no. 1, pp. 59-63, April 2000.
- [75] T. K. Podder, J. Sherman, D. Rubens, E. Messing, J. Strang, W. S. Ng and Y. Yu, "Methods for prostate stabilization during transperineal LDR brachytherapy," *Physics in Medicine and Biology*, vol. 53, no. 6, pp. 1563-1579, March 2008.
- [76] S. V. Sejpal, V. Sathiaseelan, I. B. Helenowski, J. M. Kozlowski, M. F. Carter, R. B. Nadler, D. P. Dalton, K. T. McVary, W. W. Lin, J. E. Garnett and J. A. Kalapurakal, "Intra-operative pubic arch interference during prostate seed brachytherapy in patients with CT-based pubic arch interference of ≤ 1 cm," *Radiotherapy & Oncology*, vol. 91, no. 2, pp. 249-254, May 2009.
- [77] J. M. Cosset, J. M. Hannoun-Lévi, D. Peiffert, M. Delannes, P. Pommier, N. Pierrat, P. Nickers, L. Thomas and L. Chauveinc, "Curiethérapie du cancer prostatique par implants permanents : le point en 2013," *Cancer/Radiothérapie*, vol. 17, no. 2, pp. 111-117, April 2013.
- [78] S. Nag, D. Beyer, J. Friedland, P. Grimm and R. Nath, "American Brachytherapy Society (ABS) recommendations for transperineal permanent brachytherapy of prostate cancer," *International Journal of Radiation Oncology, Biology, Physics*, vol. 44, no.

4, pp. 789-799, July 1999.

- [79] S. A. Tincher, R. Y. Kim, M. P. Ezekiel, T. Zinsli, J. B. Fiveash, D. A. Raben, A. J. Bueschen and D. A. Urban, "Effects of pelvic rotation and needle angle on pubic arch interference during transperineal prostate implants," *International Journal of Radiation Oncology, Biology, Physics*, vol. 47, no. 2, pp. 361-363, May 200.
- [80] M. Baumann, P. Mozer, V. Daanen and J. Troccaz, "Towards 3D ultrasound image based soft tissue tracking: A transrectal ultrasound prostate image alignment system," in *Proceedings of the International Conference on Medical Image Computing and Computer-Assisted Intervention (MICCAI)*, 2007.
- [81] M. Baumann, P. Mozer, V. Daanen and J. Troccaz, "Prostate biopsy assistance system with gland deformation estimation for enhanced precision," in *Proceedings of the International Conference on Medical Image Computing and Computer-Assisted Intervention (MICCAI)*, 2009.
- [82] M. Baumann, P. Mozer, V. Daanen and J. Troccaz, "Prostate biopsy tracking with deformation estimation," *Medical Image Analysis*, vol. 16, no. 3, pp. 562-576, April 2011.
- [83] J. Long, V. Daanen, A. Moreau-Gaudry, J. Troccaz, J. Rambeaud and J. Descotes, "Prostate biopsies guided by three-dimensional real-time (4-D) transrectal ultrasonography on a phantom: Comparative study versus two-dimensional transrectal ultrasound-guided biopsies," *European Urology*, vol. 52, no. 4, pp. 1097-1114, October 2007.
- [84] E. Taillant, J. C. Avila-Vilchis, C. Allegrini, I. Bricault and P. Cinquin, "CT and MR compatible Light Puncture Robot : architectural design and first experiments," in *Lecture Notes in Computer Science (MICCAI)*, Saint-Malo, 2004.
- [85] I. Bricault, N. Zemiti, E. Jouniaux, C. Fouard, E. Taillant, F. Dorandeu and P. Cinquin, "A Light Puncture Robot for CT and MRI Interventions: Designing a New Robotic Architecture to Perform Abdominal and Thoracic Punctures," *IEEE Engineering in Medicine and Biology Magazine*, vol. 27, no. 3, pp. 42-50, May-June 2008.
- [86] N. Zemiti, I. Bricault, C. Fouard, B. Sanchez and P. Cinquin, "LPR: A CT and MR-Compatible Puncture Robot to Enhance Accuracy and Safety of Image-Guided Interventions," *IEEE/ASME Transactions on Mechatronics*, vol. 13, no. 3, pp. 306-315, June 2008.
- [87] E. Dombre, P. Poignet and F. Pierrot, "Design of Medical Robots," in *Medical Robotics*, 1st ed., J. Troccaz, Ed., 2011, pp. 141-176.
- [88] L. A. Sanchez, M. Q. Le, K. Rabenorosa, C. Liu, N. Zemiti, P. Poignet, E. Dombre, A. Menciassi and P. Dario, "A Case Study of Safety in the Design of Surgical Robots: The ARAKNES Platform," in *Proceedings of the 12th International Conference IAS-12*, Jeju Island, 2013.
- [89] A. Krieger, R. C. Susil, A. Tanacs, G. Fichtinger, L. L. Whitcomb and E. Atalar, "A MRI Compatible Device for MRI Guided Transrectal Prostate Biopsy," *Proceedings of the International Society for Magnetic Resonance in Medicine*, 2002.
- [90] R. C. Susil, A. Krieger, A. J. Derbyshire, A. Tanacs, L. L. Whitcomb, G. Fichtinger and E. Atalar, "System for MR Image-guided Prostate Interventions: Canine Study,"

Radiology, vol. 228, no. 3, pp. 886-894, 2003.

- [91] A. Krieger, R. C. Susil, C. Ménard, J. A. Coleman, G. Fichtinger, E. Atalar and L. L. Whitcomb, "Design of a Novel MRI Compatible Manipulator for Image Guided Prostate Interventions," *IEEE Transactions on Biomedical Engineering*, vol. 52, no. 2, pp. 306-313, February 2005.
- [92] A. Krieger, I. Iordachita, S.-E. Song, N. B. Cho, P. Guion, G. Fichtinger and L. L. Whitcomb, "Development and Preliminary Evaluation of an Actuated MRI-Compatible Robotic Device for MRI-Guided Prostate Intervention," in *IEEE International Conference on Robotics and Automation*, Anchorage, 2010.
- [93] A. Krieger, I. I. Iordachita, P. Guion, A. K. Singh, A. Kaushal, C. Ménard, P. A. Pinto, K. Camphausen, G. Fichtinger and L. L. Whitcomb, "An MRI-Compatible Robotic System with Hybrid Tracking for MRI-Guided Prostate Intervention," *IEEE Transactions on Biomedical Engineering*, vol. 58, no. 11, pp. 3049-3060, November 2011.
- [94] H. Xu, A. Lasso, P. Guion, A. Krieger, A. Kaushal, A. K. Singh, P. A. Pinto, J. Coleman, R. L. Grubb, J.-B. Lattouf, C. Ménard, L. L. Whitcomb and G. Fichtinger, "Accuracy analysis in MRI-guided robotic prostate biopsy," *International Journal of Computer Assisted Radiology and Surgery*, vol. [Epub ahead of print], March 2013.
- [95] A. Krieger, S.-E. Song, N. B. Cho, I. I. Iordachita, P. Guion, G. Fichtinger and L. L. Whitcomb, "Development and Evaluation of an Actuated MRI-Compatible Robotic System for MRI-Guided Prostate Intervention," *IEEE/ASME Transactions on Mechatronics*, vol. 18, no. 1, pp. 273-284, September 2012.
- [96] M. G. Schouten, J. Ansems, W. K. J. Renema, D. Bosboon, T. W. J. Scheenen and J. J. Fütterer, "The accuracy and safety aspects of a novel robotic needle guide manipulator to perform transrectal prostate biopsies," *Medical Physics*, vol. 37, no. 9, pp. 4744-4750, September 2010.
- [97] D. Yakar, M. G. Schouten, D. G. H. Bosboom, J. O. Barentsz, T. W. J. Scheenen and J. J. Fütterer, "Feasibility of a Pneumatically Actuated MR-compatible Robot for Transrectal Prostate Biopsy Guidance," *Radiology*, vol. 260, no. 1, pp. 241-247, July 2011.
- [98] M. G. Schouten, J. G. R. Bomers, D. Yakar, H. Huisman, E. Rothgang, D. Bosboom, T. W. J. Scheenen, S. Misra and J. J. Fütterer, "Evaluation of a robotic technique for transrectal MRI-guided prostate biopsies," *European Radiology*, vol. 22, no. 2, pp. 476-483, February 2012.
- [99] H. Elhawary, A. Zivanovic, M. Rea, B. L. Davies, C. Besant, D. McRobbie, N. M. Desouza, I. Young and M. U. Lamperth, "A Modular Approach to MRI-Compatible Robotics," *IEEE Engineering in Medicine and Biology Magazine*, vol. 27, no. 3, pp. 35-41, June 2008.
- [100] H. Elhawary, Z. T.-H. Tse, M. Rea, A. Zivanic, B. L. Davies, C. Besant, N. M. Desouza, D. McRobbie, I. Young and M. U. Lamperth, "Robotic system for transrectal biopsy of the prostate: real-time guidance under MRI," *IEEE Engineering in Medicine and Biology Magazine*, vol. 29, no. 2, pp. 78-86, March-April 2010.
- [101] G. Fichtinger, A. Krieger, R. C. Susil, A. Tanacs, L. L. Whitcomb and E. Atalar, "Transrectal Prostate Biopsy Inside Closed MRI Scanner with Remote Actuation,

- under Real-Time Image Guidance," in *Lecture Notes in Computer Science (MICCAI)*, Tokyo, 2002.
- [102] K. Chinzei, N. Hata, F. A. Jolesz and R. Kikinis, "MR Compatible Surgical Assist Robot: System Integration and Preliminary Feasibility Study," in *Lecture Notes in Computer Science (MICCAI)*, Pittsburgh, 2000.
- [103] K. Chinzei and K. Miller, "MRI Guided Surgical Robot," in *Proceedings of the 2001 Australian Conference on Robotics and Automation*, Sydney, 2001.
- [104] S. P. DiMaio, S. Pieper, K. Chinzei, N. Hata, S. J. Haker, D. F. Kacher, G. Fichtinger, C. M. Tempany and R. Kikinis, "Robot-assisted needle placement in open MRI: System architecture, integration and validation," *Computer Aided Surgery*, vol. 12, no. 1, pp. 15-24, January 2007.
- [105] M. R. van den Bosch, M. R. Moman, M. van Vulpen, J. J. Battermann, E. Duiveman, L. J. van Schelven, H. de Leeuw, J. J. W. Lagendijk and M. A. Moerland, "MRI-guided robotic system for transperineal prostate interventions: proof of principle," *Physics in Medicine and Biology*, vol. 55, no. 5, pp. N133-N140, March 2010.
- [106] G. S. Fischer, S. P. DiMaio, I. I. Iordachita and G. Fichtinger, "Robotic Assistant for Transperineal Prostate Interventions in 3T Closed MRI," in *Lecture Notes in Computer Science (MICCAI)*, Brisbane, 2007.
- [107] G. S. Fischer, I. I. Iordachita, C. Csoma, J. Tokuda, S. P. DiMaio, C. M. Tempany, N. Hata and G. Fichtinger, "MRI-Compatible Pneumatic Robot for Transperineal Prostate Needle Placement," *IEEE/ASME Transactions on Mechatronics*, vol. 13, no. 3, pp. 295-305, June 2008.
- [108] S. E. Song, N. B. Cho, G. Fischer, N. Hata, C. Tempany, G. Fichtinger and I. I. Iordachita, "Development of a Pneumatic Robot for MRI-guided Transperineal Prostate Biopsy and Brachytherapy: New Approaches," in *IEEE International Conference on Robotics and Automation*, Anchorage, 2010.
- [109] H. Su, I. I. Iordachita, X. Yan, G. A. Cole and G. S. Fischer, "Reconfigurable MRI-Guided Robotic Surgical Manipulator: Prostate Brachytherapy and Neurosurgery Applications," in *33rd Annual International Conference of the IEEE EMBS*, Boston, 2011.
- [110] R. Seifabadi, S. E. Song, A. Krieger, N. B. Cho, J. Tokuda, G. Fichtinger and I. I. Iordachita, "Robotic system for MRI-guided prostate biopsy: feasibility of teleoperated needle insertion and ex vivo phantom study," *International Journal of Computer Assisted Radiology and Surgery*, vol. 7, no. 2, pp. 181-190, March 2012.
- [111] J. Tokuda, S. E. Song, G. S. Fischer, I. I. Iordachita, R. Seifabadi, N. B. Cho, K. Tuncali, G. Fichtinger, C. M. Tempany and N. Hata, "Preclinical evaluation of an MRI-compatible pneumatic robot for angulated needle placement in transperineal prostate interventions," *International Journal of Computer Assisted Radiology and Surgery*, vol. 7, no. 6, pp. 949-957, November 2012.
- [112] S. E. Song, N. Hata, I. I. Iordachita, G. Fichtinger, C. Tempany and J. Tokuda, "A workspace-orientated needle-guiding robot for 3T MRI-guided transperineal prostate intervention: evaluation of in-bore workspace and MRI compatibility," *The International Journal of Medical Robotics*, vol. 9, no. 1, pp. 67-74, March 2013.

- [113] R. Seifabadi, N. B. J. Cho, S. E. Song, J. Tokuda, N. Hata, C. M. Tempny, G. Fichtinger and I. Iordachita, "Accuracy study of a robotic system for MRI-guided prostate needle placement," *The International Journal of Medical Robotics and Computer Assisted Surgery*, vol. 9, no. 3, pp. 205-316, September 2013.
- [114] A. A. Goldenberg, J. Trachtenberg, W. Kucharczyk, Y. Yi, M. Haider, L. Ma, R. Weersink and C. Raoufi, "Robotic System for Closed-Bore MRI-Guided Prostatic Interventions," *IEEE/ASME Transactions on Mechatronics*, vol. 13, no. 3, pp. 374-379, June 2008.
- [115] J. Cepek, B. Chronik, U. Lindner, J. Trachtenberg and A. Fenster, "Development of an MRI-Compatible Device for Prostate Focal Therapy," in *Lecture Notes in Computer Science (MICCAI)*, Nice, 2012.
- [116] J. Cepek, B. A. Chronik, U. Lindner, J. Trachtenberg, S. R. H. Davidson, J. Bax and A. Fenster, "A system for MRI-guided transperineal delivery of needles to the prostate for focal therapy," *Medical Physics*, vol. 40, no. 1, pp. 012304-1-15, January 2013.
- [117] H. Su, W. Shang, G. A. Cole, K. Harrington and G. S. Fischer, "Haptic System Design for MRI-Guided Needle Based Prostate Brachytherapy," in *IEEE Haptics Symposium*, Waltham, 2010.
- [118] H. Su, A. Camilo, G. A. Cole, N. Hata, C. M. Tempny and G. S. Fischer, "High-field MRI-compatible needle placement robot for prostate interventions," *Studies in Health Technology and Informatics*, vol. 163, pp. 623-629, 2011.
- [119] H. Su, M. Zervas, G. A. Cole, C. Furlong and G. S. Fischer, "Real-time MRI-Guided Needle Placement Robot with Integrated Fiber Optic Force Sensing," in *IEEE International Conference on Robotics and Automation*, Shanghai, 2011.
- [120] S. Eslami, G. S. Fischer, S. E. Song, J. Tokuda, N. Hata, C. M. Tempny and I. I. Iordachita, "Towards Clinically Optimized MRI-guided Surgical Manipulator for Minimally Invasive Prostate Percutaneous Interventions: Constructive Design," in *IEEE International Conference on Robotics and Automation (ICRA)*, Karlsruhe, 2013.
- [121] S. Abdelaziz, L. Esteveny, P. Renaud, B. Bayle, L. Barbé, M. de Mathelin and A. Gangi, "Design considerations for a novel MRI compatible manipulator for prostate cryoablation," *International Journal of Computer Assisted Radiology and Surgery*, vol. 6, no. 6, p. 811-819, November 2011.
- [122] S. Abdelaziz, "Développement d'un système robotique pour la radiologie interventionnelle sous IRM," Strasbourg, 2012.
- [123] S. E. Song, J. Tokuda, K. Tunkali, C. M. Tempny and N. Hata, "Development and preliminary evaluation of an ultrasonic motor actuated needle guide for 3T MRI-guided transperineal prostate interventions," in *Medical Imaging 2012: Image-Guided Procedures, Robotic Interventions, and Modeling*, San Diego, 2012.
- [124] M. Muntener, A. Patriciu, D. Petrisor, D. Mazilu, H. Bagga, L. Kavoussi, K. Cleary and D. Stoianovici, "Magnetic resonance imaging compatible robotic system for fully automated brachytherapy seed placement," *Urology*, vol. 68, no. 6, pp. 1313-1317, December 2006.
- [125] A. Patriciu, D. Petrisor, M. Muntener, D. Mazilu, M. Schär and D. Stoianovici, "Automatic Brachytherapy Seed Placement Under MRI Guidance," *IEEE Transactions on*

Biomedical Engineering, vol. 54, no. 8, pp. 1499-1506, August 2007.

- [126] M. Muntener, A. Patriciu, D. Petrisor, M. Schär, D. Ursu, D. Y. Song and D. Stoianovici, "Transperineal prostate intervention: robot for fully automated MR imaging-system description and proof of principle in a canine model," *Radiology*, vol. 247, no. 2, pp. 543-549, May 2008.
- [127] J. A. Cunha, I. C. Hsu, J. Pouliot, M. Roach, K. Shinohara, J. Kurhanewicz, G. Reed and D. Stoianovici, "Toward adaptive stereotactic robotic brachytherapy for prostate cancer: Demonstration of an adaptive workflow incorporating inverse planning and an MR stealth robot," *Minimally Invasive Therapy*, vol. 19, no. 4, p. 189-202, August 2010.
- [128] H. S. S. Ho, P. Mohan, E. D. Lim, D. L. Li, J. S. P. Yuen, W. S. Ng, W. K. O. Lau and C. W. S. Cheng, "Robotic ultrasound-guided prostate intervention device: system description and results from phantom studies," *The International Journal of Medical Robotics and Computer Assisted Surgery*, vol. 5, no. 1, pp. 51-58, March 2009.
- [129] H. Ho, J. S. P. Yuen, P. Mohan, E. W. Lim and C. W. S. Cheng, "Robotic Transperineal Prostate Biopsy: Pilot Clinical Study," *Urology*, vol. 78, no. 5, pp. 1203-1208, November 2011.
- [130] L. Phee, D. Xiao, J. Yuen, C. F. Chan, H. Ho, C. H. Thng, C. Cheng and W. S. Ng, "Ultrasound Guided Robotic System for Transperineal Biopsy of the Prostate," in *Proceedings of the 2005 IEEE International Conference on Robotics and Automation*, Barcelona, 2005.
- [131] J. Bax, D. Smith, L. Bartha, J. Montreuil, S. Sherebin, L. Gardi, C. Edirisinghe and A. Fenster, "A compact mechatronic system for 3D ultrasound guided prostate interventions," *Medical Physics*, vol. 38, no. 2, pp. 1055-1069, February 2011.
- [132] H. Bassan, T. Hayes, R. V. Patel and M. Moallem, "A Novel Manipulator for 3D Ultrasound Guided Percutaneous Needle Insertion," in *IEEE International Conference on Robotics and Automation*, Rome, 2007.
- [133] B. L. Davies, S. J. Harris and E. Dibble, "Brachytherapy—an example of a urological minimally invasive robotic procedure," *International Journal of Medical Robotics and Computer Assisted Surgery*, vol. 1, no. 1, pp. 88-96, June 2004.
- [134] Y. D. Zhang, T. K. Podder, W. S. Ng, J. Sherman, V. Mistic, D. Fuller, E. M. Messing, D. J. Rubens, J. G. Strang, R. Brasacchio and Y. Yu, "Semi-automated Needling and Seed Delivery Device for Prostate Brachytherapy," in *Proceedings of the 2006 IEEE/RSJ International Conference on Intelligent Robots and Systems*, Beijing, 2006.
- [135] Y. Yu, T. K. Podder, Y. Zhang, W. S. Ng, V. Mistic, J. Sherman, L. Fu, D. Fuller, E. Messing, D. Rubens, J. Strang and R. Brasacchio, "Robot-Assisted Prostate Brachytherapy," in *Lecture Notes in Computer Science (MICCAI)*, Copenhagen, 2006.
- [136] Y. Yu, T. K. Podder, Y. D. Zhang, W. S. Ng, V. Mistic, J. Sherman, D. Fuller, D. J. Rubens, J. G. Strang, R. A. Brasacchio and E. M. Messing, "Robotic system for prostate brachytherapy," *Computer Aided Surgery*, vol. 12, no. 6, pp. 366-375, November 2007.
- [137] T. K. Podder, I. Buzurovic, K. Huang, T. Showalter, A. P. Dicker and Y. Yu, "Reliability of EUCLIDIAN: An autonomous robotic system for image-guided prostate

- brachytherapy," *Medical Physics*, vol. 38, no. 1, pp. 96-106, January 2011.
- [138] T. K. Podder, W. S. Ng and Y. Yu, "Multi-channel robotic system for prostate brachytherapy," in *Proceedings of the 29th Annual International Conference of the IEEE EMBS*, Lyon, 2007.
- [139] S. E. Salcudean, T. D. Prananta, W. J. Morris and I. Spadinger, "A Robotic Needle Guide for Prostate Brachytherapy," in *IEEE International Conference on Robotics and Automation*, Pasadena, 2008.
- [140] J. Kettenbach, G. Kronreif, M. Figl, M. Fürst, W. Birkfellner, R. Hanel and H. Bergmann, "Robot-assisted biopsy using ultrasound guidance: initial results from in vitro tests," *European Radiology*, vol. 15, no. 4, pp. 765-771, April 2005.
- [141] G. Kronreif, M. Fürst, W. Ptacek, M. Kornfeld and J. Kettenbach, "Robotic System for Image Guided Therapie – B-RobII," in *International Workshop on Robotics in Alpe-Adira-Danube Region*, Balaton, 2006.
- [142] G. Fichtinger, J. Fiene, C. W. Kennedy, G. Kronreif, I. I. Iordachita, D. Y. Song, E. C. Burdette and P. Kazanzides, "Robotic Assistance for Ultrasound Guided Prostate Brachytherapy," in *Lecture Notes in Computer Science (MICCAI)*, Nice, 2007.
- [143] G. Fichtinger, J. P. Fiene, C. W. Kennedy, G. Kronreif, I. I. Iordachita, D. Y. Song, E. C. Burdette and P. Kazanzides, "Robotic assistance for ultrasound-guided prostate brachytherapy," *Medical Image Analysis*, vol. 12, no. 5, pp. 535-545, October 2008.
- [144] D. Y. Song, E. C. Burdette, J. Fiene, E. Armour, G. Kronreif, A. Deguet, Z. Zhang, I. I. Iordachita, G. Fichtinger and P. Kazanzides, "Robotic needle guide for prostate brachytherapy: Clinical testing of feasibility and performance," *Brachytherapy*, vol. 10, no. 1, pp. 57-63, January-February 2011.
- [145] B. Schulz, K. Eichler, P. Siebenhandl, T. Gruber-Rouh, C. Czerny, T. J. Vogl and S. Zangos, "Accuracy and speed of robotic assisted needle interventions using a modern cone beam computed tomography intervention suite: a phantom study," *European Radiology*, vol. 23, no. 1, pp. 198-204, January 2013.
- [146] D. Stoianovici, J. A. Cadeddu, R. D. Dernaree, S. A. Basile, R. H. Taylor, L. L. Whitcomb, W. N. Sharpe and L. R. Kavoussi, "An Efficient Needle Injection Technique and Radiological Guidance Method for Percutaneous Procedures," in *Lecture Notes in Computer Science*, Grenoble, 1997.
- [147] D. Stoianovici, L. L. Whitcomb, J. H. Anderson, R. H. Taylor and L. R. Kavoussi, "A modular surgical robotic system for image guided percutaneous procedures," in *Lecture Notes in Computer Science (MICCAI)*, Cambridge, 1998.
- [148] A. Patriciu, D. Stoianovici, L. L. Whitcomb, T. Jarrett, D. Mazilu, A. Stanimir, I. I. Iordachita, J. Anderson, R. Taylor and L. R. Kavoussi, "Motion-Based Robotic Instrument Targeting under C-Arm Fluoroscopy," in *Lecture Notes in Computer Science (MICCAI)*, Pittsburgh, 2000.
- [149] K. Masamune, G. Fichtinger, A. Patriciu, R. C. Susil, R. H. Taylor, L. R. Kavoussi, J. H. Anderson, I. Sakuma, T. Dohi and D. Stoianovici, "System for Robotically Assisted Percutaneous Procedures with Computed Tomography Guidance," *Computer Aided Surgery*, vol. 6, no. 6, pp. 370-383, 2001.

- [150] G. Fichtinger, T. L. DeWeese, A. Patriciu, A. Tanacs, D. Mazilu, J. H. Anderson, K. Masamune, R. H. Taylor and D. Stoianovici, "System for Robotically Assisted Prostate Biopsy and Therapy with Intraoperative CT Guidance," *Academic Radiology*, vol. 9, no. 1, pp. 60-74, January 2002.
- [151] D. Stoianovici, K. Cleary, A. Patriciu, D. Mazilu, A. Stanimir, N. Craciunoiu, V. Watson and L. Kavoussi, "AcuBot: A Robot for Radiological Interventions," *IEEE Transactions on Robotics and Automation*, vol. 19, no. 5, pp. 927-930, October 2003.
- [152] K. Cleary, w, V. Watson, D. Lindisch, R. H. Taylor, G. Fichtinger, S. Xu, C. S. White, J. Donlon, M. Taylor, A. Patriciu, D. Mazilu and D. Stoianovici, "Precision placement of instruments for minimally invasive procedures using a "Needle Driver" robot," *International Journal of Medical Robotics and Computer Assisted Surgery*, vol. 1, no. 2, pp. 40-47, January 2005.
- [153] S. Shah, A. Kapoor, J. Ding, P. Guion, D. Petrisor, J. Karanian, W. F. Pritchard, D. Stoianovici, W. J. Wood and K. Cleary, "Robotically assisted needle driver: evaluation of safety release, force profiles, and needle spin in a swine abdominal model," *International Journal of Computer Assisted Radiology and Surgery*, vol. 3, no. 1-2, pp. 173-179, June 2008.
- [154] R. Pollock, P. Mozer, T. J. Guzzo, J. Marx, B. Matlaga, D. Petrisor, B. Vigar, S. Badaan, D. Stoianovici and M. E. Allaf, "Prospects in Percutaneous Ablative Targeting: Comparison of a Computer-Assisted Navigation System and the AcuBot Robotic System," *Journal of Endourology*, vol. 24, no. 8, pp. 1269-1272, August 2010.
- [155] M. H. Loser and N. Navab, "A New Robotic System for Visually Controlled Percutaneous Interventions under CT Fluoroscopy," in *Lecture Notes in Computer Science (MICCAI)*, Pittsburgh, 2000.
- [156] E. Hempel, H. Fischer, L. Gumb, T. Höhn, H. Krause, U. Voges, H. Breitwieser, B. Gutmann, J. Durke, M. Bock and A. Melzer, "An MRI-Compatible Surgical Robot for Precise Radiological Interventions," *Computer Aided Surgery*, vol. 8, no. 4, pp. 180-191, 2003.
- [157] S. Zangos, C. Herzog, K. Eichler, R. Hammerstingl, A. Lukoschek, S. Guthmann, B. Gutmann, U. J. Schoepf, P. Costello and T. J. Vogl, "MR-compatible assistance system for puncture in a high-field system: device and feasibility of transgluteal biopsies of the prostate gland," *European Radiology*, vol. 17, no. 4, pp. 1118-1124, April 2007.
- [158] A. Melzer, B. Gutmann, T. Remmele, R. Wolf, A. Lukoscheck, M. Bock, H. Bardenheuer and H. Fischer, "INNOMOTION for percutaneous image-guided interventions: principles and evaluation of this MR- and CT-compatible robotic system," *IEEE Engineering in Medicine and Biology Magazine*, vol. 27, no. 3, pp. 66-73, May-June 2008.
- [159] S. Zangos, A. Melzer, K. Eichler, C. Sadighi, A. Thalhammer, B. Bodelle, R. Wolf, T. Gruber-Rouh, D. Proschek, R. Hammerstingl, C. Müller, M. G. Mack and T. V. Vogl, "MR-compatible assistance system for biopsy in a high-field-strength system: initial results in patients with suspicious prostate lesions," *Radiology*, vol. 259, no. 3, pp. 903-910, June 2011.
- [160] B. Schell, K. Eichler, M. G. Mack, C. Müller, J. M. Kerl, C. Czerny, M. Beeres, A.

- Thalhammer, T. J. Vogl and S. Zangos, "Robot-Assisted Biopsies in a High-Field MRI System – First Clinical Results," *Fortschr Röntgenstr*, vol. 184, no. 1, pp. 42-47, January 2012.
- [161] E. G. Christoforou, I. Seimenis, E. Andreou, E. Eracleous and N. V. Tsekos, "A novel, general-purpose, MR-compatible, manually actuated robotic manipulation system for minimally invasive interventions under direct MRI guidance," *The International Journal of Medical Robotics and Computer Assisted Surgery*, vol. [Epub ahead of print], April 2013.
- [162] N. V. Tsekos, A. Özcan and E. Christoforou, "A prototype manipulator for magnetic resonance-guided interventions inside standard cylindrical magnetic resonance imaging scanners," *Journal of Biomechanical Engineering*, vol. 127, no. 6, pp. 972-980, November 2005.
- [163] "Robotic manipulators with remotely-actuated joints: Implementation using drive-shafts and u-joints," in *Proceedings of the 2006 IEEE International Conference on Robotics and Automation*, Orlando, 2006.
- [164] E. Christoforou, E. Akbudak, A. Ozcan, M. Karanikolas and N. V. Tsekos, "Performance of interventions with manipulator-driven real-time MR guidance: implementation and initial in vitro tests," *Magnetic Resonance Imaging*, vol. 25, no. 1, pp. 69-77, January 2007.
- [165] N. V. Tsekos, E. Christoforou and A. Özcan, "A General-Purpose MR-Compatible Robotic System: Implementation and Image Guidance for Performing Minimally Invasive Interventions," *IEEE Engineering in Medicine and Biology Magazine*, vol. 27, no. 3, pp. 51-58, 2008.
- [166] G. Cole, J. Pilitsis and G. S. Fischer, "Design of a Robotic System for MRI-Guided Deep Brain Stimulation Electrode Placement," in *IEEE International Conference on Robotics and Automation*, Kobe, 2009.
- [167] Y. Wang, G. A. Cole, H. Su, J. G. Pilitsis and G. S. Fischer, "MRI Compatibility Evaluation of a Piezoelectric Actuator System for a Neural Interventional Robot," in *31st Annual International Conference of the IEEE EMBS*, Minneapolis, 2009.
- [168] G. Cole, K. Harrington, H. Su, A. Camilo, J. Pilitsis and G. S. Fischer, "Closed-Loop Actuated Surgical System Utilizing Real-Time In-Situ MRI Guidance," in *12th International Symposium on Experimental Robotics (ISER)*, New Delhi and Agra, 2010.
- [169] B. Maurin, "Conception et réalisation d'un robot d'insertion d'aiguille pour les procédures percutanées sous imageur scanner," Strasbourg, 2005.
- [170] "A Robotized Positioning Platform Guided by Computed Tomography : Practical Issues and Evaluation," in *Proceedings 2006 IEEE International Conference on Robotics and Automation (ICRA)*, Orlando, 2006.
- [171] B. Maurin, B. Bayle, O. Piccin, J. Gangloff, M. de Mathelin, C. Doignon, P. Zanne and A. Gangi, "A Patient-Mounted Robotic Platform for CT-Scan Guided Procedures," *IEEE Transaction on Biomedical Engineering*, vol. 55, no. 10, pp. 2417-2425, October 2008.
- [172] O. Piccin, L. Barbé, B. Bayle and M. de Mathelin, "A Force Feedback Teleoperated Needle Insertion Device for Percutaneous Procedures," *The International Journal*

- of Robotics Research*, vol. 28, no. 9, pp. 1154-1168, September 2009.
- [173] B. Maurin, C. Doignon, J. Gangloff, B. Bayle, M. de Mathelin, O. Piccin and A. Gangi, "CTBot: A Stereotactic-Guided Robotic Assistant for Percutaneous Procedures of the Abdomen," in *Proceedings of SPIE: Medical Imaging*, San Diego, 2005.
- [174] C. J. Walsh, N. C. Hanumara, A. H. Slocum, J. A. Shepard and R. Gupta, "A Patient-Mounted, Telerobotic Tool for CT-Guided Percutaneous Interventions," *Journal of Medical Devices*, vol. 2, pp. 011007-1-10, March 2008.
- [175] A. Seitel, C. J. Walsh, N. C. Hanumara, J. A. Shepard, A. H. Slocum, H. P. Meinzer, R. Gupta and L. Maier-Hein, "Development and evaluation of a new image-based user interface for robot-assisted needle placements with the Robopsy system," in *SPIE Proceedings*, Lake Buena Vista, 2009.
- [176] F. Wu, M. Torabi, A. Golden, M. Werner, A. Yamada, N. Hata, H. Su, G. Cole, G. Fischer, D. Frey, C. J. Walsh and K. Tuncali, "Compact, Patient-Mounted MRI-guided Robot for Accurate Positioning of Multiple Cryoablation Probes," in *Fifth National Image Guided Therapy Workshop*, Boston, 2012.
- [177] E. Taillant, J. C. Avila-Vilchis, C. Allegrini, I. Bricault and P. Cinquin, "CT and MR compatible Light Puncture Robot : architectural design and first experiments," in *Lecture Notes in Computer Science (MICCAI)*, Saint-Malo, 2004.
- [178] National Electrical Manufacturers Association, "Determination of Signal-to-Noise Ratio (SNR) in Diagnostic Magnetic Resonance Imaging," 2008.
- [179] G. Schaeffers, "Testing MR Safety and Compatibility - An Overview of the Methods and Current Standards," *IEEE Engineering in Medicine and Biology Magazine*, vol. 27, no. 3, pp. 23-27, May/June 2008.
- [180] T. O. Woods, "Standards for medical devices in MRI: present and future," *Journal of Magnetic Resonance Imaging*, vol. 26, no. 5, pp. 1186-1189, November 2007.
- [181] R. Gassert, A. Yamamoto, D. Chapuis, L. Dovat, H. Bleuler and E. Burdet, "Actuation Methods for Applications in MR Environments," *Concepts in Magnetic Resonance Part B (Magnetic Resonance Engineering)*, vol. 29B, no. 4, pp. 191-209, 2006.
- [182] G. S. Fischer, A. Krieger, I. I. Iordachita, C. Csoma, L. L. Whitcomb and G. Fichtinger, "MRI Compatibility of Robot Actuation Techniques - A Comparative Study," in *Lecture Notes in Computer Science (MICCAI)*, 2008.
- [183] D. J. van Gerwen, J. Dankelman and J. J. van den Dobbelsteen, "Needle-tissue interaction forces - A survey of experimental data," *Medical Engineering & Physics*, vol. 34, no. 6, pp. 665-680, July 2012.
- [184] J. Sherman, T. K. Podder, V. Mistic, L. Fu., D. Fuller, B. Winey, E. M. Messing, D. J. Rubens, J. G. Strang, R. Brasacchio and Y. Yu, "Efficacy of Prostate Stabilizing Techniques during Brachytherapy Procedure," in *Proceedings of the 28th IEEE EMBS Annual International Conference*, New York City, 2006.
- [185] H. Xu, A. Lasso, S. Vikal, P. Guion, A. Krieger, A. Kaushal, L. L. Whitcomb and G. Fichtinger, "MRI-Guided Robotic Prostate Biopsy: A Clinical Accuracy Validation," in *Lecture Notes in Computer Science (MICCAI)*, Beijing, 2010.
- [186] T. De Silva, A. Fenster, J. Bax, C. Romagnoli, J. Izawa, J. Samarabandu and A. D. Ward,

- "Quantification of prostate deformation due to needle insertion during TRUS-guided biopsy: Comparison of hand-held and mechanically stabilized systems," *Medical Physics*, vol. 38, no. 3, pp. 1718-1731, March 2011.
- [187] N. Abolhassani, R. Patel and M. Moallem, "Needle insertion into soft tissue: A survey," *Medical Engineering & Physics*, vol. 29, no. 4, pp. 413-431, May 2007.
- [188] A. Sotiras, C. Davatzikos and N. Paragios, "Deformable Medical Image Registration: A Survey," *IEEE Transactions on Medical Imaging*, vol. 32, no. 7, pp. 1153-1190, July 2013.
- [189] A. Majewicz, S. P. Marra, M. G. van Vledder, M. Lin, M. A. Choti, D. Y. Song and A. M. Okamura, "Behavior of Tip-Steerable Needles in ex vivo and in vivo Tissue," *IEEE Transactions on Biomedical Engineering*, vol. 59, no. 10, pp. 2705-2715, October 2012.
- [190] N. Pagoulatos, D. R. Haynor and Y. Kim, "A fast calibration method for 3-D tracking of ultrasound images using a spatial localizer," *Ultrasound in Medicine & Biology*, vol. 27, no. 9, pp. 1219-1229, September 2001.
- [191] T. K. Chen, T. Heffter, A. Lasso, C. Pinter, P. Abolmaesumi, E. C. Burdette and G. Fichtinger, "Automated intraoperative calibration for prostate cancer brachytherapy," *Medical Physics*, vol. 38, no. 11, pp. 6285-6299, November 2011.
- [192] A. Krieger, G. Metzger, G. Fichtinger, E. Atalar and L. L. Whitcomb, "A Hybrid Method for 6-DOF Tracking of MRI-Compatible Robotic Interventional Devices," in *Proceedings of the 2006 IEEE International Conference on Robotics and Automation (ICRA)*, Orlando, 2006.
- [193] D. Pfeiffer, S. Sutlief, W. Feng, H. M. Pierce and J. Kofler, "AAPM Task Group 128: Quality assurance tests for prostate brachytherapy ultrasound systems," *Medical Physics*, vol. 35, no. 12, pp. 5471-5489, December 2008.
- [194] B. R. Condon and D. M. Hadley, "Solid Localization Marker for MR Imaging," *Radiology*, vol. 204, no. 2, pp. 577-580, August 1997.
- [195] U.S. Food and Drug Administration, "Medical Device Innovation Initiative White Paper - CDRH Innovation Initiative," 2011.
- [196] A. Moreau-Gaudry and L. Pazart, "Développement d'une innovation technologique en santé : le cycle CREPS, Concept - Recherche - Essais - Produit - Soins," *Ingénierie et Recherche Biomédicale*, vol. 31, no. 1, pp. 1-68, February 2010.
- [197] L. Barbe, B. Bayle, M. de Mathelin and A. Gangi, "In Vivo Model Estimation and Haptic Characterization of Needle Insertions," *The International Journal of Robotics Research*, vol. 26, no. 11-12, pp. 1283-1301, November 2007.
- [198] R. E. Peschel and J. W. Colberg, "Surgery, brachytherapy, and external-beam radiotherapy for early prostate cancer," *The Lancet Oncology*, vol. 4, no. 4, pp. 233-241, 2003.
- [199] J. E. Dawson, T. Wu, T. Roy, J. Y. Gu and H. Kim, "Dose effects of seeds placement deviations from pre-planned positions in ultrasound guided prostate implants," *Radiotherapy and Oncology*, vol. 32, no. 3, pp. 268-170, September 1994.
- [200] P. L. Roberson, V. Narayana, D. L. McShan, R. J. Winfield and P. W. McLaughlin, "Source

- placement error for permanent implant of the prostate," *Medical Physics*, vol. 24, no. 2, pp. 251-257, February 1997.
- [201] M. Bues, E. J. Holupka, P. Meskell and I. D. Kaplan, "Effect of random seed placement error in permanent transperineal prostate seed implant," *Radiotherapy and Oncology*, vol. 79, no. 1, pp. 70-74, April 2006.
- [202] Y. Su, B. J. Davies, K. M. Furutani, M. G. Herman and R. A. Robb, "Dosimetry accuracy as a function of seed localization uncertainty in permanent prostate brachytherapy: increased seed number correlates with less variability in prostate dosimetry," *Physics in Medicine and Biology*, vol. 52, no. 11, pp. 3105-3119, June 2007.
- [203] C. S. McGill, J. A. Schwartz, J. Z. Moore, P. W. McLaughlin and A. J. Shih, "Precision grid and hand motion for accurate needle insertion in brachytherapy," *Medical Physics*, vol. 38, no. 8, pp. 4749-4759, August 2011.
- [204] J. J. Craig, *Introduction to Robotics Mechanics and Control*, Third ed., Upper Saddle River, NJ: Pearson Education, Inc., 2005.
- [205] L. J. Everett and C. Y. Lin, "Kinematic calibration of manipulators with closed loop actuated joints," in *Proceedings of the IEEE International Conference on Robotics and Automation (ICRA)*, Philadelphia, 1988.
- [206] M. Baumann, "A 3d ultrasound-based tracking system for prostate biopsy distribution quality insurance and guidance," 2008.
- [207] N. Bilaniuk and G. S. K. Wong, "Erratum: Speed of sound in pure water as a function of temperature," *Journal of the Acoustical Society of America*, vol. 99, no. 5, pp. 3257-3257, 1996.
- [208] K. S. Arun, T. S. Huang and S. D. Blostein, "Least-Squares Fitting of Two 3-D Point Sets," *IEEE Transactions on Pattern Analysis and Machine Intelligence*, Vols. PAMI-9, no. 5, pp. 698-700, September 1987.
- [209] N. Hungr, J. A. Long, V. Beix and J. Troccaz, "A realistic deformable prostate phantom for multimodal imaging and needle-insertion procedures," *Medical Physics*, vol. 39, no. 4, pp. 2031-2041, April 2012.
- [210] R. Lefrançois and R. S. Sloboda, "A medical needle drive for the study of interstitial implant mechanics," *Medical Engineering & Physics*, vol. 25, no. 3, pp. 255-258, April 2003.
- [211] M. De Brabandere, C. Kirisits, R. Peeters, K. Haustermans and F. Van den Heuvel, "Accuracy of seed reconstruction in prostate postplanning studied with a CT- and MRI-compatible phantom," *Radiotherapy and Oncology*, vol. 79, no. 2, pp. 190-197, May 2006.
- [212] S. P. DiMaio and S. E. Salcudean, "Needle insertion modelling and simulation," in *Proceedings of the IEEE International Conference on Robotics and Automation (ICRA)*, Washington DC, 2002.
- [213] J. R. Crouch, C. M. Schneider, J. Wainer and A. M. Okamura, "A velocity-dependent model for needle insertion in soft tissue," *Lecture Notes in Computer Science (MICCAI)*, vol. 8, no. Pt. 2, pp. 624-632, 2005.
- [214] J. Bax, D. Cool, L. Gardi, K. Knight, D. Smith, J. Montreuil, S. Sherebrin, C. Romagnoli and

- A. Fenster, "Mechanically assisted 3D ultrasound guided prostate biopsy system," *Medical Physics*, vol. 35, no. 12, pp. 5397-5410, 2008.
- [215] X. Wen and S. E. Salcudean, "Detection of brachytherapy seeds using 3D transrectal ultrasound," in *Proceedings of the Annual International Conference of the IEEE Engineering in Medicine and Biology Society (EMBC)*, Vancouver, 2008.
- [216] E. Dehghan, X. Wen, R. Zahiri-Azar, M. Marchal and S. E. Salcudean, "Needle-tissue interaction modeling using ultrasound-based motion estimation: Phantom study," *Computer Aided Surgery*, vol. 13, no. 5, pp. 25-280, 2008.
- [217] G. M. Spirou, A. A. Oraevsky, I. A. Vitkin and W. M. Whelan, "Optical and acoustic properties at 1064 nm of polyvinyl chloride-plastisol for use as a tissue phantom in biomedical optoacoustics," *Physics in Medicine and Biology*, vol. 50, no. 14, pp. N141-153, July 2005.
- [218] E. L. Madsen, G. R. Frank, T. A. Krouskop, T. Varghese, F. Kallel and J. Ophir, "Tissue-mimicking oil-in-gelatin dispersions for use in heterogeneous elastography phantoms," *Ultrasonic Imaging*, vol. 25, no. 1, pp. 17-38, January 2003.
- [219] D. Fontanarosa, S. van der Meer, E. Harris and F. Verhaegen, "A CT based correction method for speed of sound aberration for ultrasound based image guided radiotherapy," *Medical Physics*, vol. 38, no. 5, pp. 2665-2673, 2011.
- [220] D. Pfeiffer, S. Sutlief, W. Feng, H. M. Pierce, and J. Kofler, "AAPM Task Group 128: Quality assurance tests for prostate brachytherapy ultrasound systems," *Medical Physics*, vol. 35, no. 12, pp. 5471-5489, December 2008.
- [221] K. J. Parker, S. R. Huang, R. M. Lerner, F. Lee, D. Rubens and D. Roach, "Elastic and ultrasonic properties of the prostate," in *Proceedings of the IEEE Ultrasonics Symposium*, Baltimore, 1993.
- [222] T. A. Krouskop, T. M. Wheeler, F. Kallel, B. S. Garra and T. Hall, "Elastic moduli of breast and prostate tissues under compression," *Ultrasonic Imaging*, vol. 20, no. 4, pp. 260-274, 1998.
- [223] M. A. Meltsner, N. J. Ferrier and B. R. Thomadsen, "Observations on rotating needle insertions using a brachytherapy robot," *Physics in Medicine and Biology*, vol. 52, no. 19, pp. 6027-6037, October 2007.
- [224] S. Badaan, D. Petrisor, C. Kim, P. Mozer, D. Mazilu, L. Gruionu, A. Patriciu, K. Cleary and D. Stoianovici, "Does needle rotation improve lesion targeting?," *The International Journal of Medical Robotics and Computer Assisted Surgery*, vol. 7, no. 2, pp. 138-147, June 2011.
- [225] E. Dehghan and S. E. Salcudean, "Needle insertion parameter optimization for brachytherapy," *IEEE Transactions on Robotics*, vol. 25, no. 2, pp. 303-315, April 2009.
- [226] C. I. Henschke, "International Early Lung Cancer Action Program: Enrollment and Screening Protocol," New York, 2011.
- [227] C. I. Henschke, D. F. Yankelevitz and J. P. Smith, "Definition of a positive test result in computed tomography screening for lung cancer: a cohort study," *Annals of Internal Medicine*, vol. 158, no. 4, pp. 246-252, February 2013.

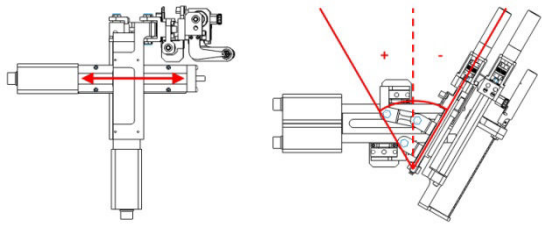
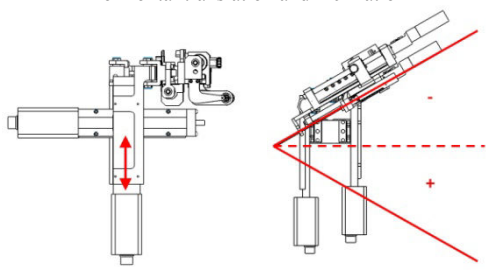
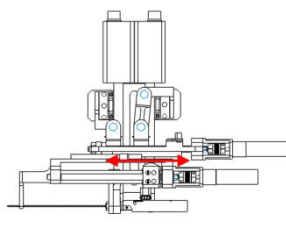
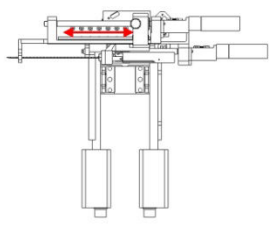
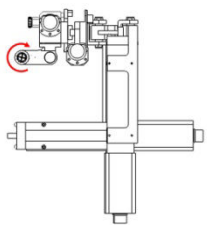
- [228] A. F. Reynolds, P. A. Roberts, M. Pollay and P. H. Stratemeier, "Quantitative anatomy of the thoracolumbar epidural space," *Neurosurgery*, vol. 17, no. 6, pp. 905-907, December 1985.
- [229] A. Robert, "Évolution d'un système robotique de ponction abdominale sous scanner et IRM en vue de sa stérilisation," Laboratoire TIMC-IMAG, La Tronche, 2010.
- [230] S. B. Ainbinder and L. M. Liberman, "Polymeric pairs having a low coefficient of friction," *Polymer Mechanics*, vol. 9, no. 5, pp. 825-827, September/October 1973.
- [231] L. E. Govaert and P. J. Lemstra, "Deformation behavior of oriented UHMW-PE fibers," *Colloid & Polymer Science*, vol. 270, pp. 455-464, 1992.
- [232] M. J. N. Jacobs, Creep of gel-spun polyethylene fibres : Improvements by impregnation and crosslinking, 1 ed., U. o. Eindhoven, Ed., Eindhoven, 1999.
- [233] P. Letier, A. Schiele, M. Avraam, M. Horodinca and A. Preumont, "Bowden Cable Actuator for Torque-Feedback in Haptic Applications," in *EuroHaptics*, Paris, 2006.
- [234] P. J. Besl and N. D. McKay, "A method for registration of 3-D shapes," *IEEE Transactions on Pattern Analysis and Machine Intelligence*, vol. 14, no. 2, pp. 239-256, February 1992.
- [235] C. Lobos, "A set of mixed-elements patterns for domain boundary approximation in hexahedral meshes," *Studies in Health Technology and Informatics*, vol. 184, pp. 268-272, 2013.
- [236] S. Martin, M. Baumann, V. Daanen and J. Troccaz, "MR prior based automatic segmentation of the prostate in TRUS images for MR/TRUS data fusion," in *IEEE International Symposium on Biomedical Imaging (ISBI)*, Rotterdam, 2010.
- [237] D. Stoianovici, J. A. Cadeddu, R. D. Demaree, S. A. Basile, R. H. Taylor, L. L. Whitcomb, W. N. Sharpe and L. R. Kavoussi, "An Efficient Needle Injection Technique and Radiological Guidance Method for Percutaneous Procedures," *Lecture Notes in Computer Science*, vol. 1205, pp. 295-298, 1997.
- [238] T. K. Podder, J. Sherman, D. Fuller, E. M. Messing, D. J. Rubens, J. G. Strang, R. A. Brasacchio and Y. Yu, "In-vivo Measurement of Surgical Needle Intervention Parameters: A Pilot Study," in *Proceedings of the 28th IEEE EMBS Annual International Conference*, New York, 2006.
- [239] T. K. Podder, D. P. Clark, D. Fuller, J. Sherman, W. S. Ng, L. Liao, D. J. Rubens, J. G. Strang, E. M. Messing, Y. D. Zhang and Y. Yu, "Effects of Velocity Modulation during Surgical Needle Insertion," in *Proceedings of the 2005 IEEE Engineering in Medicine and Biology 27th Annual Conference*, Shanghai, 2005.
- [240] T. Podder, D. Clark, J. Sherman, D. Fuller, E. Messing, D. Rubens, J. Strang, R. Brasacchio, L. Liao, W. S. Ng and Y. Yu, "In vivo motion and force measurement of surgical needle intervention during prostate brachytherapy," *Medical Physics*, vol. 33, no. 8, pp. 2915-2922, August 2006.
- [241] M. Peikari, T. K. Chen, A. Lasso, T. Heffter and G. Fichtinger, "Effects of Ultrasound Section-Thickness on Brachytherapy Needle Tip Localization Error," in *Lecture Notes in Computer Science (MICCAI)*, Toronto, 2011.

- [242] J. N. Morelli, V. M. Runge, F. Ai, U. Attenberger, L. Vu, S. H. Schmeets, W. R. Nitz and J. E. Kirsch, "An Image-based Approach to Understanding the Physics of MR Artifacts," *RadioGraphics*, vol. 31, pp. 849-866, 2011.
- [243] C. S. McGill, J. A. Schwartz, J. Z. Moore, P. W. McLaughlin and A. J. Shih, "Effects of insertion speed and trocar stiffness on the accuracy of needle position for brachytherapy," *Medical Physics*, vol. 39, no. 4, pp. 1811-1817, April 2012.
- [244] B. Maurin, B. Bayle, J. Gangloff, P. Zanne, M. de Mathelin and O. Piccin, "A Robotized Positioning Platform Guided by Computed Tomography : Practical Issues and Evaluation," in *Proceedings 2006 IEEE International Conference on Robotics and Automation (ICRA)*, Orlando, 2006.
- [245] K. Masamune, E. Kobayashi, Y. Masutani, M. Suzuki, T. Dohi, H. Iseki and K. Takakura, "Development of an MRI-Compatible Needle Insertion Manipulator for Stereotactic Neurosurgery," *Journal of Image Guided Surgery*, vol. 1, pp. 242-248, 1995.
- [246] C. Lobos, "A set of mixed-elements patterns for domain boundary approximation in hexahedral meshes," *Studies in Health Technology and Informatics*, vol. 184, pp. 268-272, 2013.
- [247] V. Lagerburg, M. A. Moerland, M. K. Konings, R. E. van de Vosse, J. J. W. Lagendijk and J. J. Battermann, "Development of a tapping device: a new needle insertion method for prostate brachytherapy," *Physics in Medicine and Biology*, vol. 51, no. 4, pp. 891-902, February 2006.
- [248] M. Heverly, P. Dupont and J. Triedman, "Trajectory Optimization for Dynamic Needle Insertion," in *Proceedings of the 2005 IEEE International Conference on Robotics and Automation (ICRA)*, Barcelona, 2005.
- [249] M. K. Feldman, S. Katyal and M. S. Blackwood, "US Artifacts," *RadioGraphics*, vol. 29, pp. 1179-1189, 2009.
- [250] C. W. Burckhardt, P. Flury and D. Glauser, "Stereotactic Brain Surgery - Integrated MINERVA system meets demanding robotic requirements," *IEEE Engineering in Medicine and Biology*, vol. 14, no. 3, pp. 314-317, May/June 1995.
- [251] J. F. Barrett and N. Keat, "Artifacts in CT: Recognition and Avoidance," *RadioGraphics*, vol. 24, pp. 1679-1691, 2004.
- [252] N. Abolhassani, R. Patel and M. Moallem, "Control of soft tissue deformation during robotic needle insertion," *Minimally Invasive Therapy and Allied Technologies*, vol. 15, no. 3, pp. 165-176, 2006.
- [253] "URobotics - Urology Robotics at Johns Hopkins," Johns Hopkins University, [Online]. Available: <http://urobotics.urology.jhu.edu/projects/PneuStep/>. [Accessed 04 September 2013].
- [254] "Ultrasonic Motors Development and Support Company - SHINSEI CORPORATION," Shinsei Corporation, [Online]. Available: <http://www.shinsei-motor.com/English/>. [Accessed 04 September 2013].
- [255] "PiezoMotor: Simplicity in motion," PiezoMotor AB, [Online]. Available: <http://www.piezomotor.se/>. [Accessed 04 September 2013].

- [256] V. Beix, "Etude d'un système robotisé d'insertion d'une aiguille pour la curiethérapie de la prostate," Laboratoire TIMC-IMAG, La Tronche, 2009.
- [257] S. Briot, "Etude sur l'insertion d'aiguille pour la curiethérapie automatisée de la prostate," Laboratoire TIMC-IMAG, La Tronche, 2013.

Appendix 1: PROSPER workspace

The PROSPER pre-clinical prototype, DOFs and range of motion.

Motor #	Motor type	Range of motion	DOF
POSITIONING MODULE			
1 and 7	Zaber TLLS Stepper motor	T: 105 mm I: $\pm 30^\circ$	 <p>Horizontal translation and inclination</p>
2 and 8	Zaber TLLS Stepper motor	T: 105 mm I: $\pm 30^\circ$	 <p>Vertical translation and inclination</p>
5	Faulhaber 2057 Brushless motor Planetary gearhead (3.71:1)	T: 90 mm	 <p>Z -translation</p>
INSERTION MODULE			
6	Faulhaber 2057 Brushless motor Planetary gearhead (3.71:1)	T: 105 mm	 <p>Needle insertion</p>
	Faulhaber 1536 Brushless motor Spur gearhead (6.3:1)	R: 0 to 12 rps	 <p>Needle rotation</p>

Appendix 2: Prostate phantom article

A realistic deformable prostate phantom for multimodal imaging and needle-insertion procedures

Nikolai Hungr^{a)}

UJF-Grenoble 1/CNRS/TIMC-IMAG UMR 5525 (Equipe GMCAO), Grenoble, F-38041, France

Jean-Alexandre Long

Clinique Universitaire de Chirurgie urologique et Transplantation rénale, CHU Grenoble, 38043 Grenoble Cedex 9, France

Vincent Beix and Jocelyne Troccaz

UJF-Grenoble 1/CNRS/TIMC-IMAG UMR 5525 (Equipe GMCAO), Grenoble, F-38041, France

(Received 20 October 2011; revised 17 January 2012; accepted for publication 13 February 2012; published 22 March 2012)

Purpose: Phantoms are a vital step for the preliminary validation of new image-guided procedures. In this paper, the authors present a deformable prostate phantom for use with multimodal imaging (end-fire or side-fire ultrasound, CT and MRI) and more specifically for transperineal or transrectal needle-insertion procedures. It is made of soft polyvinyl chloride (PVC) plastic and includes a prostate, a perineum, a rectum, a soft periprostatic surrounding and embedded targets for image registration and needle-targeting. Its main particularity is its realistic deformability upon manipulation.

Methods: After a detailed manufacturing description, the imaging and mechanical characteristics of the phantom are described and evaluated. First, the speed of sound and stress-strain relationship of the PVC material used in the phantom are described, followed by an analysis of its storage, imaging, needle-insertion force, and deformability characteristics.

Results: The average speed of sound in the phantom was measured to be 1380 ± 20 m/s, while the stress-strain relationship was found to be viscoelastic and in the range of typical prostatic tissues. The mechanical and imaging characteristics of the phantom were found to remain stable at cooler storage temperatures. The phantom had clearly distinguishable morphology in all three imaging modalities, with embedded targets that could be precisely segmented, resulting in an average US-CT rigid registration error of 0.66 mm. The mobility of the phantom prostate upon needle insertion was between 2 and 4 mm, with rotations between 0° and 2° , about the US probe head.

Conclusion: The phantom's characteristics compare favorably with *in vitro* and *in vivo* measurements found in the literature. The authors believe that this realistic phantom could be of use to researchers studying new needle-based prostate diagnosis and therapy techniques. © 2012 American Association of Physicists in Medicine. [<http://dx.doi.org/10.1118/1.3692179>]

Key words: deformable phantom, prostate, needle insertion, multi-modal imaging, PVC

I. INTRODUCTION

Prostate cancer is the third most deadly cancer in men in western developed countries, with 33 720 and 70 821 deaths estimated in 2011 in the United States¹ and in 2008 in Europe,² respectively. Indeed, the importance of this disease on public health is such that it has attracted an abundance of research in improved diagnostics and therapy over the last decade. Percutaneous transperineal and transrectal interventions for the diagnosis and treatment of prostate cancer have seen particular attention due to their minimally invasive approaches. In recent years, important developments have been made in computer and robot-assisted image-guided needle insertion technology. The most common imaging modality used for such prostate techniques is ultrasound (US), due to its harmless, inexpensive, and easily accessible nature. CT and MRI, however, have also seen a lot of research attention because of their complementary imaging characteristics.

For any new developments in the field, anthropomorphic phantom-testing is a prerequisite before doing animal or human testing. Prostate phantoms are artificial models of the prostatic environment that emulate soft tissue mechanical and imaging characteristics. A wide variety of such phantoms have been developed, typically to meet certain simplified project-specific needs. Phantom applications have included the evaluation of needle insertion accuracy, the validation of biomechanical models, testing of image processing algorithms, preliminary studies on new treatment methods, and surgeon training, amongst others.

In this paper, we describe a deformable prostate phantom that we developed and that we believe could be of potential use to the research community. We begin the paper with a description of the context and reasoning for the development of our phantom followed by a review of existing prostate phantoms, their characteristics, and particularities. We then discuss the various phantom materials cited in the literature and what material we chose for our phantom. We then

describe our phantom in detail, including its ingredients and construction recipe. In the second half of the paper, we describe the phantom's mechanical and imaging characteristics, concluding with a discussion of its novelty, usefulness, and limitations.

I.A. Context

In our laboratory, we have developed a robotic brachytherapy needle insertion system, which uses a robotic needle insertion device coupled to a 3D US registration software to track prostate motion intraoperatively. The prototype of the robotic device and the US registration software have both been described in previous publications.^{3–5} The primary goal of our system is to improve accuracy and efficiency of seed deposition in prostate brachytherapy by taking into account tissue mobility during needle insertion.

The first step for bringing this project to clinical trials was to run a phantom study to determine the system's accuracy, efficiency, ergonomics, and reliability. The novelty of our system is its ability to track prostate motion; so, it was vital that our phantom be able to simulate prostate motions during needle insertion. For this purpose, we were interested in developing a prostate phantom that had the following anatomical morphology:

- prostate: to validate our registration technique;
- general periprostatic tissue: to hold the prostate in place while allowing prostate mobility;
- skin of the perineum: to simulate realistic needle–tissue interactions during insertion;
- rectum: to allow for realistic insertion of either an end-fire or a side-fire US probe;
- urethra: (optional) to make the US images more realistic for both dose planning and image registration.

The phantom study that we carried out involved the insertion of a number of inert brachytherapy seeds in the phantom using US guidance, based on a mock seed plan conceived beforehand. Accuracy was measured by comparing the deposited seeds to the dose plan using postimplant CT imaging. Beads placed within the phantom during construction were used either as targets or for US-CT image registration.

I.B. Prior art

A large number of prostate phantoms have been described in the literature over the last decade: everything from very simple uniform blocks, to more complex and realistic multi-component phantoms, to commercialized tissue-equivalent phantoms. Their main features are (1) to reproduce the anatomy of the prostate environment, (2) to emulate the soft-tissue feel either for applying surface pressure or for needle insertion, and (3) to emulate the imaging characteristics of the prostate, whether it is x-ray, MRI, or US based. The variety of phantoms designed nearly equals the variety of prostate applications being researched.

The simplest phantoms are uniform single-component phantoms. Their simplicity has been used for preliminary studies in a very controlled environment, such as the initial

validation of new needle insertion instruments^{6–8} as well as the validation of image processing techniques such as brachytherapy seed segmentation.⁹ Uniform phantoms impregnated with a matrix of visible fiducials have also been built for experimental validation of biomechanical models.^{10–12}

For prostate-based percutaneous procedures, multi-component phantoms are more useful as they introduce more realistic anatomical conditions, both mechanically and for imaging. Some examples of such phantoms can be seen in the work by Bax *et al.*¹³ and Long *et al.*,¹⁴ both of which include a prostate suspended in background material. A number of studies have also used an industrial prostate phantom commercialized by CIRS (Computerized Imaging Reference Systems, Inc).^{15,16} This phantom consists of prostate and seminal vesicles embedded in surrounding tissue and has a perineal surface, along with a rectum and urethra. None of these phantoms were designed to simulate prostate motion.

Few publications exist that describe the use of a phantom specifically for prostate motion evaluation. The earliest “mobile prostate phantom” that we found in the literature was described by McGahan *et al.*¹⁷ and was used to determine errors caused by external probe pressure during radiotherapy. The hard prostate, made of clay, makes this phantom, however, inappropriate for needle insertion. Only two other mobile phantoms were found that were designed specifically for needle insertion. Both use a harder prostate encapsulated in softer surrounding polyvinyl chloride (PVC) material. In Dehghan *et al.*,¹⁸ the phantom has a rectum as well as a stiffer inclusion linking the prostate to the base of the phantom in an attempt to reproduce the prostate's rotation about the pubic bone. Needle insertion into the phantom resulted in axial prostate motions of <4 mm. The phantom described by Sherman *et al.*¹⁹ has the added characteristic of including a perineal surface, simulated with a 2 cm layer of stiffer material. The phantom was used in a vertical orientation, with two orthogonal US probes for visualization. Vitamin E capsules were embedded in the phantom to provide specific targets for motion tracking. Target motions up to 11 mm were reported during needle insertion.

These last two mobile phantoms were the closest to our design objectives, and we used them as inspiration for our own design. Our initial building block was therefore the use of a harder prostate embedded in a softer surrounding. Our main goal was then to improve the anatomical realism, adapt the phantom for transrectal ultrasound applications, and ensure its multimodality to generalize its usability. The resulting phantom was found to have very satisfying mechanical and imaging characteristics that we report in this paper in detail.

I.C. Phantom materials

To satisfy our design constraints, we had to choose an appropriate material for our phantom. Some of the most common base materials used in phantom construction are agarose, gelatin, polyvinyl alcohol (PVA-C), polyvinyl chloride (PVC), silicone, and the proprietary commercialized material Zerdine (CIRS). Their mechanical and imaging

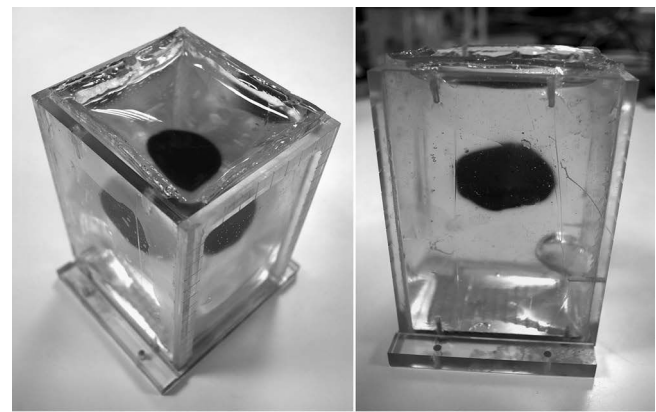
characteristics are described by various sources, comparing them to real tissue. Table I summarizes the various properties of these materials found in the literature. A detailed description of each of these materials can be consulted as electronic supplemental material.⁴¹

We experimented with all of the above materials, settling on the following conclusions: agarose and gelatin are too fragile for the type of motions we require, especially when low concentrations are used for the surrounding periprostatic material; the CIRS phantoms do not have evident deformation during needle insertion and are expensive, making them impractical for tests requiring multiple phantoms; PVA-C has a very complex and lengthy preparation procedure, which makes it challenging for multicomponent structures; and silicone has inappropriate acoustic properties. Our choice was therefore PVC, which provides the best compromise between mechanical and imaging characteristics. It has a sufficiently large range of elastic modulus all the while remaining resistant to rough handling (needle puncture, probe pressure, etc.) and is inexpensive and simple to manufacture.

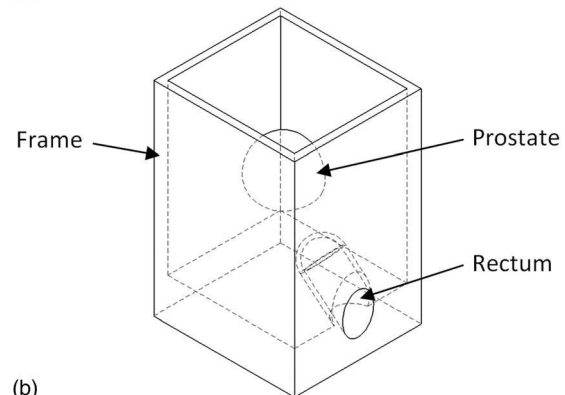
II. MATERIALS AND METHODS

II.A. Phantom description

The phantom that we developed is shown in Fig. 1. It consists of four distinct regions made of PVC mixtures of various elasticities. Soft PVC can be bought from companies that specialize in fishing lure construction, such as M-F Manufacturing Co., Inc. (Ft. Worth, TX),^{18,26,38} or, in our case, Bricoleurre (Mont Saint Aignan, France). The PVC used in our phantoms consists of a mixture of PVC polymer solution and the softener diethyl hexyl adipate. Our provider sells PVC in a number of different premixed polymer-softener mixtures, the stiffest being a “super rigid” mixture, whose exact ratio of polymer-softener is proprietary and could not



(a)



(b)

Fig. 1. (a) Photograph of the phantom with mobile prostate and rectum. (b) CAD drawing of phantom. Note that the rectum shown in this figure is meant for end-fire US probes. For side-fire probes, a cylindrical rectum is used, as shown in Fig. 11.

be obtained. Based on this super rigid mixture, various softer mixtures can be obtained by adding an appropriate amount of softener solution. The PVC mixtures that we used during our experiments and in our phantom are listed in Table II.

TABLE I. Properties of the typical soft materials used in phantom construction, as found in the literature. All values were reported at room temperature.

Material	Density (kg/m ³)	Young's modulus (kPa)	Speed of sound (m/s)	Attenuation (dB/cm/MHz)	Measurement frequency (MHz)	T1 relax. time (ms)	T2 relax. time (ms)	Ref.
Agarose	1036 ± 22					1207 ± 168	66 ± 9	9
Agarose			1546	0.5	2.0–10.0			20
Agarose	1040 ± 11		1050 ± 30	0.08 ± 0.02	5			21
Agar		7.6–195						22
PVA-C			1520–1540	0.075–0.22	3.0–8.0	718–1034	108–175	23
PVA-C	1028–1054	0.2–6	1525–1560					24
PVA-C	1100 ± 50		1570 ± 20	0.58 ± 0.02	5			21
PVA-C	1015–1027		1524.4–1570.5	1.4–2.9	2.2			25
PVC	1000 ± 40		1400 ± 20	0.56 ± 1.01	0.61–1.25			26
PVC			1395	1.05–1.37	4.5–8.0			27
PVC		10–100						11
Silicone	1070 ± 30		1030 ± 60	2.8 ± 0.28	5			21
Silicone		0.2–2						8
Silicone		25.8						10
Zerdine			1420–1650	0.1–1.5	2.0–10.0			28
Zerdine			1538	0.7	4			20
Gelatin		4.8–158	1555–1598					22
Gelatin		104 ± 3	1538	0.1–0.19	2.5–8.0	1610	416	27

TABLE II. Ratios of hardener to softener used to make the various PVC mixtures used in our phantom. ρ is density, c is speed of sound, E is elastic modulus, and H is Hounsfield.

Mixture name	Hardener (%)	Softener (%)	ρ (kg/m ³)	c (m/s)	E (kPa)	H. unit
Super rigid (hardener)	100	0	-	-	200	-
Rigid	75	25	0.98	1580	150	100–110
Standard	50	50	0.91	1440	100	60–80
Soft	25	75	0.93	1420	50	30–50
Super soft	10	90	0.74	1360	3	–20–15

As described in Sec. I, the anatomy that we wished to simulate with our phantom includes (1) the perineum, (2) the rectum, (3) the prostate, (4) the surrounding periprostatic tissue, and (5) an optional urethra for imaging purposes. The perineum acts as the first “tougher” skin barrier through which the needle must traverse. It also provides a structural frame to maintain the phantom’s form. The rectum accepts an end-fire US probe and is strong enough to resist rough handling during probe placement. The prostate has a colored capsule that makes it visible both to the human eye as well as in ultrasound images. The prostate is hard enough to be mobile but soft enough to be deformable upon needle insertion, as will be described in Sec. III. The periprostatic tissue suspends the prostate in place within the phantom. It is soft enough to allow for sufficient prostatic mobility during ultrasound probe handling and needle insertion.

II.B. Phantom construction

The construction of the phantom is illustrated in Fig. 2. It requires simple equipment: a laboratory hot plate, a 1.5 l pot, a 300 ml beaker, and an optional vacuum chamber. Material costs for a single phantom are on the order of \$20 to \$25 US. A single phantom takes about 5 h to make (3 h for the frame, 1 h for the prostate, and 1 h for the surrounding material and overall assembly) and requires 12 h of curing time after final assembly. Multiple phantoms can be made in parallel if the equipment is available. Two moulds were constructed, one for the frame and rectum and one for the prostate. The former [Fig. 2(a)] was made of aluminum and was a negative of the frame and rectum seen in Fig. 1. The prostate mould was an approximation of a prostate geometry imprinted into fast-drying silicone paste.

To make the 9 × 10 × 15 cm frame, a standard mixture (see Table II) is heated in the pot at a hot plate temperature of 450 °C for 30 min, until polymerized. The solution is poured into the aluminum mould and cooled at room temperature. An appropriate molding technique must be used to ensure that no air remains trapped in the mould: in addition to appropriate mould orientation with respect to gravity, the mould can be placed in a vacuum chamber for 1–2 min immediately after pouring of the PVC. It is helpful to preheat the mould on a heating element to prevent the PVC from curing too quickly around the thin walls, thus trapping the escaping air bubbles. This procedure, including cooling, takes about 3 h.

For the prostate, the same standard PVC mixture is heated in a 300 ml beaker at 450 °C for 20 min [Fig. 2(b)]. As soon

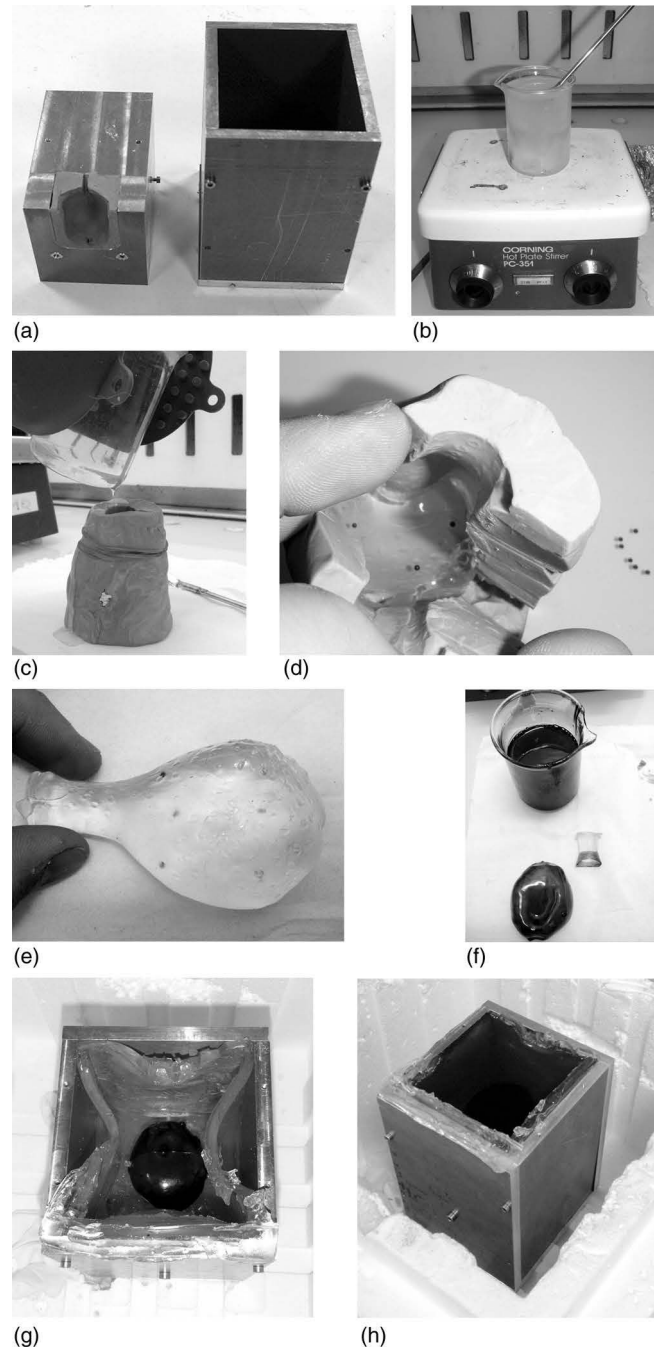


Fig. 2. Steps during construction of the prostate phantom. (a) Mould used to shape the outer frame of the phantom. (b) Heating of the PVC mixture. (c) Pouring the molten PVC into the prostate mould. (d) Placing the targets onto the first layer of the prostate. (e) The final prostate shape. (f) Coating the prostate with an echogenic stained PVC mixture. (g) Putting the prostate in place inside the frame. (h) Allowing the phantom to cool overnight.

as full polymerization has occurred, the beaker is ideally placed into the vacuum chamber for 1–2 min. The pressure change induces a boiling effect. Upon pressure release, all air bubbles disappear from the solution, and it can be poured carefully into the mould [Fig. 2(c)]. At this stage, it is possible to embed reference targets inside the prostate. This is done by pouring the PVC into the mould in layers, briefly letting each layer to cool at its surface just enough to place the targets without them sinking (about 3–4 min) and then covering them with the next layer of PVC [Fig. 2(d)]. The beaker can be kept on very low heat (hot plate temperature of 100 °C) during this procedure to keep it from curing.

Two types of targets were tested: glass and polymer clay beads. One millimeter diameter glass beads can be obtained from laboratory equipment merchants and have good US and CT imaging characteristics. Polymer clay targets can be shaped into 1 mm diameter beads and baked in an oven at 130 °C for 20 min. Similar to soft PVC, polymer clay is a PVC-based material sold for hobbies and crafts. It has good US, CT, and MRI imaging characteristics. Its advantage over glass beads is that it does not cast a white shadow in US images, keeping the image clear. Glass beads are, however, more easily and precisely distinguishable in the image.

The prostate mould is made with a 2 to 3 cm tail on its base [Fig. 2(e)]. This allows it to be held with ease during coating of the prostate capsule material. The capsule material is made by heating standard PVC in a beaker and, once polymerized, mixing in a scattering agent. In our phantoms, we used 0.2 g of the biological staining agent toluidine blue for 200 ml of PVC material. This made the prostate contour not only echogenic in ultrasound but also made it blue and visible within the surrounding transparent PVC. The prostate is dipped once or twice into the stained PVC solution, depending on the desired capsule thickness. Once cooled, the prostate tail can be cut off and the exposed base can be redipped into the stained PVC to complete the capsule [Fig. 2(f)]. The prostate and capsule take approximately 1.5 h to make.

The suspension of the prostate within the frame and surrounding material is done by first pouring an initial layer of super soft PVC periprostatic material (heated at 450 °C for 20 min) to the appropriate height, letting it cure enough to place the prostate in position [Fig. 2(g)] and then filling up the rest of the frame. If no bubbles are desired, each layer can be placed in the vacuum chamber for 1–2 min as described above. Additionally, a small amount of scattering agent can be mixed with the periprostatic material to increase its echogenicity for more realistic ultrasound images. Curing of this very soft PVC at this stage takes much longer and ideally should be left overnight [Fig. 2(h)].

An optional urethra can be included in the prostate. For this, a thin tube is inserted into the prostate mould before pouring. This makes a hole through the prostate which can then be filled with a mixture of standard PVC and scattering agent before creating the prostate capsule. Another variation to the phantom is to place targets outside of the prostate, into the periprostatic material. This is done by layering, in the same way as for the prostate.

PVC is amenable to layering. Although layers of different elasticities can be separated by hand, they bond together amply for needle-insertion purposes. Bonding is improved when the second layer is poured before complete cooling of the first layer, as it allows the polymer chains between layers to blend together. An important precaution to note during the preparation of soft PVC is not to overheat the PVC, as it burns very quickly (overheating is evident as the solution turns dark yellow). Stirring is therefore very important. Magnetic stirrers were not found to be ideal, as the PVC tends to solidify prematurely around it during heating. A more efficient technique is to stir regularly by hand and then use the vacuum chamber to eliminate bubbles.

III. PHANTOM CHARACTERISTICS

The phantom has a number of distinct characteristics, both in its mechanical behavior and in its imaging compatibility. Its primary feature is the mobility of the prostate both when manipulating an ultrasound probe in the rectum and when inserting a needle. In addition, the different anatomical regions in the phantom are clearly distinguishable in US, CT, and MRI. These properties will be discussed in further detail in the sections that follow.

III.A. Speed of sound

In order to acquire accurate ultrasound images of the phantom, it was necessary to know the speed of sound in the PVC material used. The speed of sound was measured by fixing an US transmitter at a set distance from the floor of a water-filled basin. The speed of sound of the water was calculated based on its temperature and the distance between the transducer and the basin as measured in the image. A sample of the PVC material was then placed between the transducer and basin floor, and the distance was measured again. A simple proportion calculation gave us then a value for the speed of sound in the PVC:

$$c_{PVC} = c_{water} \frac{d_{water}}{d_{PVC}}.$$

The experiment was repeated over the range of PVC mixtures used in the phantom, and the results are shown in Table II. The first three measurements were carried out by medical ultrasound transducer manufacturer, Vermon, in their research facility, using material specifically designed for this purpose (notably, a 3.5 MHz emitting transducer coupled to a receiving transducer on the floor of the water basin). Due to technical reasons, Vermon was unable to do the fourth measurement; so, it was done in our laboratory using an 8 MHz linear array US transmitter connected to an Ultrasonix Sonix TOUCH ultrasound machine.

The values that we measured were compared to results published in the literature. Spirou *et al.*²⁶ report a speed of sound of 1400 ± 20 m/s. It is unclear, however, how their PVC material compares to the various mixtures that we tested. Madsen *et al.*²⁷ report a similar value of 1395 m/s, but with no details on how the values were measured and what

type of PVC mixture was used. Nevertheless, both reported values fall within the range of our measurements. With these results, we were able to determine the speed of sound with which to acquire US images of the phantom with minimal distortion error. To do so, we took the speed of sound at the two extreme depths of the prostate: one at the point closest to the probe head, and one at the point farthest from the probe head, as shown in Fig. 3. The two speeds were calculated based on the depth-weighted average of PVC mixtures that the sound wave must travel through. The final speed of sound used for the phantom was taken as the average of these two extremes: 1380 ± 20 m/s. The variability in speed of sound due to the varying depths of PVC mixtures would cause an error of $\pm 1.5\%$ of the distance from the probe head. For the shallowest areas (~ 20 mm from the probe head), this would amount to about 0.3 mm, while for the deepest areas of the prostate (~ 60 mm), the error could be up to 0.9 mm. We consider this variability reasonable, as it is less than the variability due to tissue differences reported *in vivo*.^{30,31}

We verified the speed of sound by manually segmenting the prostate in a 3D US image and comparing it to the true volume of the prostate. The US volume was reconstructed at 1380 m/s with an Ultrasonix 4DEC9-5 end-fire probe connected to an Ultrasonix RP ultrasound machine, giving a $299 \times 299 \times 299$ image with a voxel dimension of 0.33 mm. The true volume was determined during construction of the phantom by measuring the volume of water displaced when submerging the prostate. The segmented volume of the prostate was 47.2 cm^3 compared to the true measured volume of 47.0 cm^3 . The proximity of the two results leads us to believe that the chosen speed of sound was suitable.

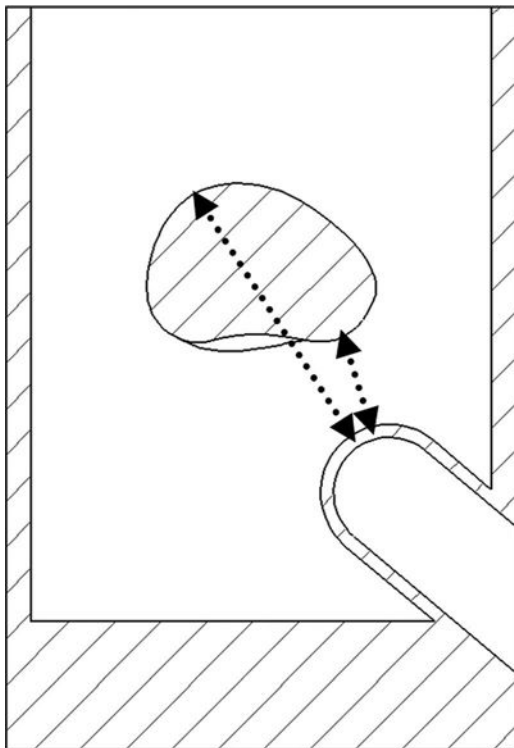


FIG. 3. The shallowest and deepest trajectories from the probe head, used to calculate the range of sound speeds in the phantom.

III.B. Stress-strain relationship

To compare the PVC material's elastic properties to those of prostatic soft tissue, the stress-strain relationship of the various mixtures was studied. The compression stress-strain relationship was measured using a Gabo Eplexor (Ahlden, Germany) mechanical characterization machine, as shown in Fig. 4. Five 16 mm diameter cylindrical samples of the five different PVC mixtures described in Table II were prepared and allowed to settle overnight. A 25 N force transducer was used to measure a 35% compression-decompression cycle at 0.5 mm/s for each sample. The same measurements were also made on three sets of identical samples prepared 11 days before, in order to study the stability of the samples over time. These stability results will be described in Sec. III C.

The resulting stress-strain curves are shown in Fig. 5. For all the samples, the curve shows viscoelastic behavior, with an increase in elastic modulus with increasing strain and a hysteretic effect between compression and decompression cycles (caused by the relaxation of the material during deceleration of the compressor). A quadratic polynomial fit to the samples is shown in Fig. 5. To get an idea of the difference in elasticity of the five PVC mixtures used, we can make a linear approximation of the first part of the stress-strain curves (up to 20% compression strain). The results are shown in Table II and correspond with published results for both PVC and *in vitro* prostate tissue.³²⁻³⁴

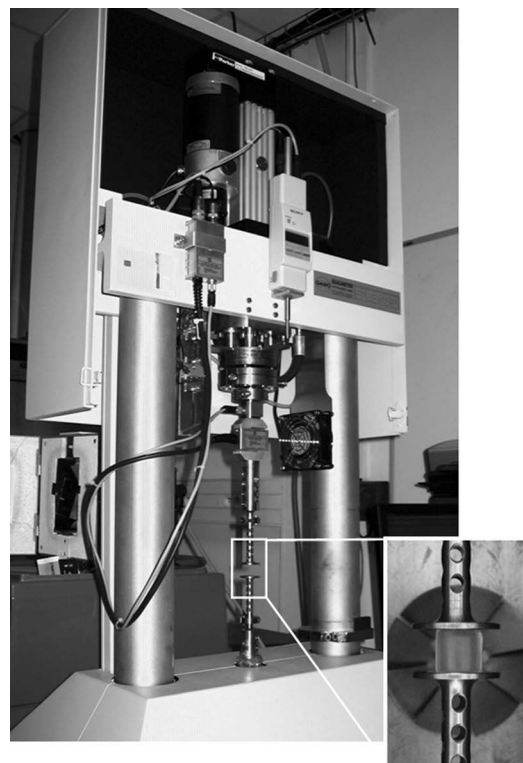


FIG. 4. Mechanical characterization machine used to measure the compression stress-strain relationship of the PVC samples. The inlayed image shows a sample in place between the compression rods.

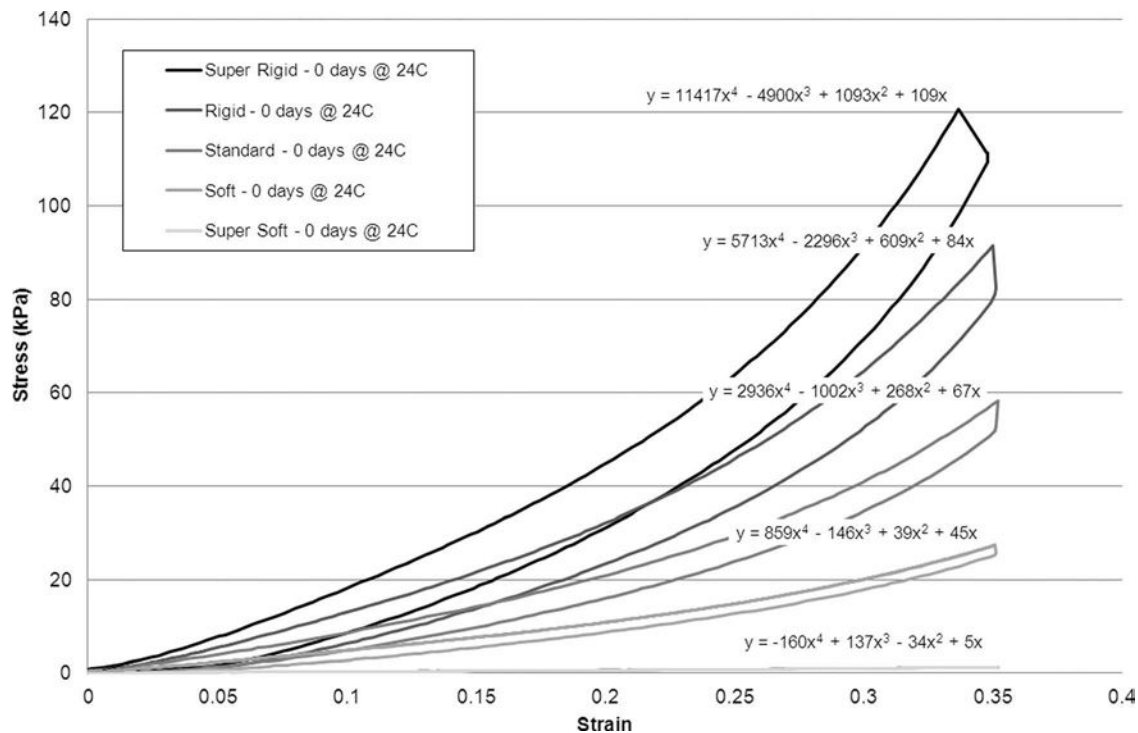


FIG. 5. Stress-strain curves for the five sets of PVC samples. The displayed equations represent the polynomial fits for the compression phase (upper part) of each curve.

III.C. Phantom storage characteristics

The ability to store a phantom without a change in its properties over time is an important aspect in phantom design. Extensive testing of systems often requires phantoms to be made in batches in advance, before actually beginning the experiments. It is very important, therefore, that the phantom properties remain consistent throughout the testing period. We carried out two experiments to verify the response of our PVC phantom over time with respect to its two primary properties described above: speed of sound and stress-strain. The main goal was to determine the best storage conditions for our phantom.

The first experiment involved measuring the compression stress-strain relationship for various PVC samples stored (1) at room temperature (between 23 °C and 25 °C), (2) in the fridge (4.5 °C), and (3) in the freezer (−21 °C). The resulting stress-strain relationships can be seen in the electronic supplemental material.⁴¹ The results show that the stress-strain relationship follows a steeper curve with increasing storage temperature. In other words, the higher the storage temperature, the stiffer the PVC becomes over time. The freezer would therefore seem to be the best storage environment for PVC, in order to conserve its mechanical elasticity.

In the second experiment, we constructed three small sample phantoms with an echogenic inclusion, similar in property to the true phantom. These samples were once again stored at room temperature, in the fridge, and in the freezer and observed visually and with ultrasound, over a period of 26 days. The sample stored in the freezer showed noticeably less changes in visual aspect, compared to the other samples. To analyze the 3D US images of the samples, the volume of the

echogenic inclusion visible in the images was measured. The results can be seen in Fig. 6 and show an increase in inclusion volume over time, with the freezer samples being less affected than the room temperature samples. This volume change can be attributed to an increase in speed of sound, which is a reasonable assumption, given the increase in stiffness of PVC over time, as described in the previous paragraph (see also measured speeds for mixtures of various stiffnesses in Table II).

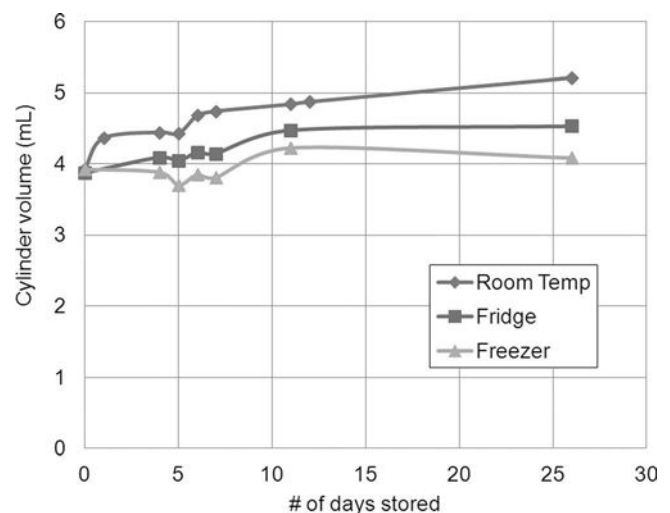


FIG. 6. Volume over time of the segmented inclusions for the three samples stored at different temperatures. The uneven jumps in the curves are likely the result of slight image inconsistencies caused by variable probe pressure or the presence of air bubbles in the ultrasound gel applied at the probe–phantom interface.

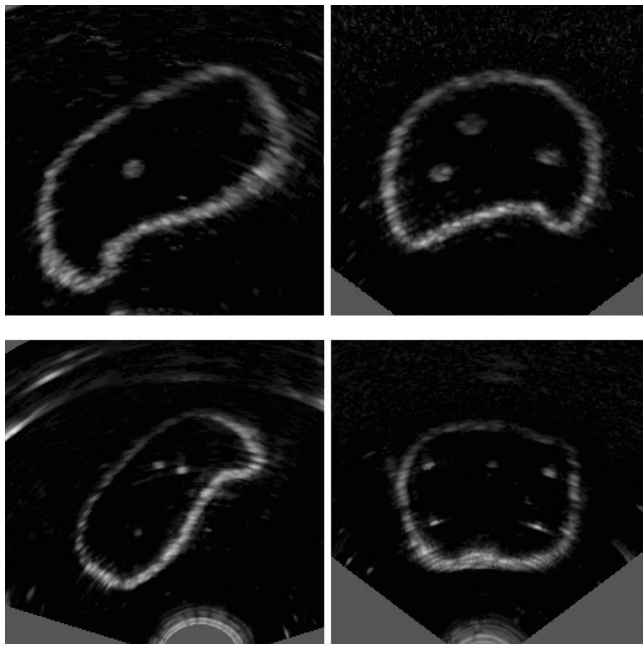


FIG. 7. Sagittal (left images) and transverse (right images) cuts of 3D ultrasound volumes taken of two different phantoms. The top images are of a phantom with 3 mm polymer clay targets embedded in the prostate, while bottom images show a phantom embedded with 1 mm glass targets. Note that the oblique angle of the prostate in the sagittal images is due to the use of an obliquely placed end-fire probe.

Based on these results and observations, it was evident that it was best to store the phantoms in the freezer, at low temperatures, to minimize changes in mechanical and imaging properties. Please note that interested readers can refer to the detailed description of the experiments and their results in the electronic supplemental material.⁴¹

III.D. Imaging characteristics

Phantoms that are visible in multiple imaging modalities are valuable, because they do not restrict their use to just a single type of image-guided procedure. Complementary information can also be extracted from the different imaging modalities and combined to provide a more complete analysis of the phantom tests. For example, the distribution of brachytherapy seeds inserted under US guidance can be analyzed in a CT scan volume. An important aspect of our phantom design was, therefore, its multimodality.

We have tested our phantom in the three primary volumetric imaging modalities: ultrasound, CT, and MRI. US images of the phantom can be seen in Fig. 7. The prostate capsule, which is blue to the naked eye, stands out as the white outer boundary of the prostate. The figure shows two types of embedded targets: the polymer clay targets cast a small black shadow and their outline can be clearly seen; the glass targets cast slight white shadows that allow for very easy and accurate segmentation. A 3D prostate registration algorithm developed in our laboratory for biopsy targeting and brachytherapy guidance^{3,4} was tested and works flawlessly.

The main disadvantage of this phantom, like with the majority of synthetic phantoms, is that needle insertions leave permanent traces in the US images. In our experience, this limited us to about 15 to 20 insertions per phantom, before the image became too degraded for effective use. At this point, the registration algorithm started showing inaccuracies in certain noisier areas of the volumes.

Figure 8 shows a CT and an MR image of the phantom. In the CT image, the PVC mixtures used in the phantom are clearly distinguishable because of their different densities. The Hounsfield units for the various PVC mixtures were determined and are listed in Table II. In the MR image, the phantom is equally visible, with the prostate, prostate capsule, and urethra clearly distinguishable. The polymer clay and glass targets are visible in both modalities and are easily segmented.

To check the segmentation accuracy of the targets in the images, we compared US and CT images of 8 phantoms embedded with 8 to 12 glass targets each. The targets were segmented manually at high zoom in each US and CT image. The clouds of segmented US points were then rigidly registered to the corresponding CT points using Arun least squares fitting.³⁵ The average registration error for all eight phantoms was 0.66 mm. This error is very reasonable, as it includes the segmentation errors from both modalities. A similar test including MR images was not done because of availability constraints for the high-demand clinical MR machines at our disposal.

III.E. Needle-insertion force

To study the mechanical behavior of our phantom specifically during needle insertion, we measured the axial force

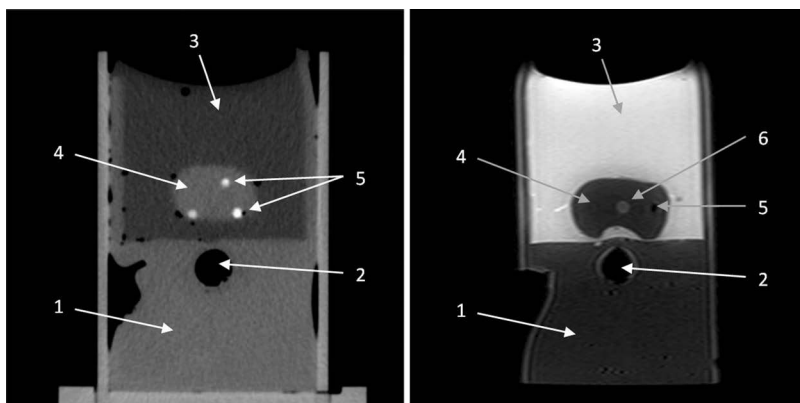


FIG. 8. Transverse cuts of a CT (left) and an MR (right) volume of two different phantoms. The left phantom has polymer clay embedded targets. The right phantom has a urethra. (1) Frame, (2) rectum, (3) periprostatic material, (4) prostate, (5) polymer clay targets, and (6) urethra.

required to push a 19 gauge diamond-tip Mick Ripple-Hub needle (Mick Radio-Nuclear Instruments, Inc.) into the prostate. This was done by mounting a Flexiforce A201 force sensor (Tekscan) onto the brachytherapy needle insertion robot described in Hung *et al.*⁵ and calibrating it by applying known forces on the needle tip. A plot of the insertion force measured by the force sensor during insertion through the perineum and into the prostate of our phantom is seen in Fig. 9. The different regions of the phantom through which the needle traverses can be distinguished and are labeled in the figure. A first maximum is reached, at 1.8 N, when traversing the perineum. The force then decreases through the periprostatic region, until it reaches the prostate. It then increases as it travels through the prostate, until the needle is stopped. At this point, we see a decrease in the force, as the material relaxes around the needle. This multistep behavior is comparable to the *in vitro* liver puncture curve reported by Maurin *et al.*,³⁶ the dog prostate tests described by Kataoka *et al.*,³⁷ as well as the *in vivo* force measurements done by Podder *et al.*²⁹ during live brachytherapy.

Although the axial force curve has a characteristic shape for prostate needle puncture, our partner urologists have mentioned that the increasing friction felt the deeper the needle is pushed is not realistic. In a real patient, blood lubricates the shaft of the needle, making the needle tip cutting force the primary force felt by the clinician, allowing them to feel the needle's progress through different tissues. The phantom, on the other hand, is not lubricated, and as the cutting force is relatively low compared to the friction between the PVC and the needle shaft, it is more difficult for the clinician to "read" the tissues with the needle.

III.F. Prostate motion

Prostate motion is the primary behavioral aspect that we wished to reproduce in our phantom. We wished to use it to

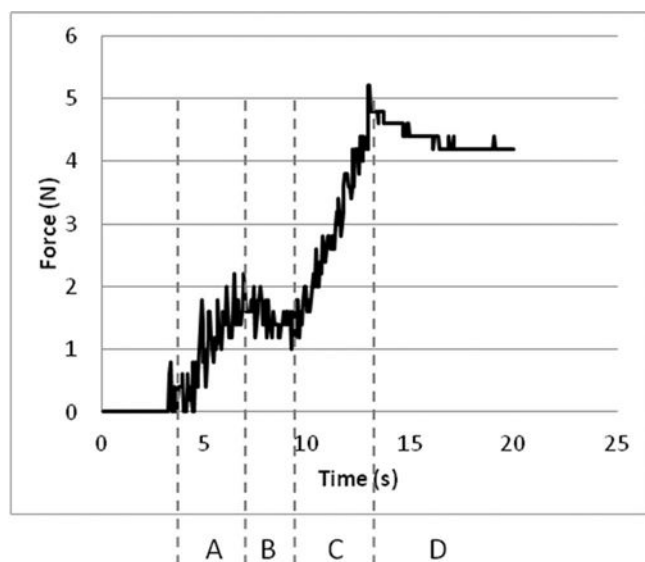


FIG. 9. Axial needle force measured during needle insertion into our phantom. A denotes the needle traversing the perineum. B denotes the super soft PVC before reaching the prostate. C denotes the prostate. D denotes the relaxation of the material after stopping needle motion.

evaluate our prostate tracking system for robotic brachytherapy. In the literature, it has been shown that prostate motion is important during needle insertion.^{38–40} It has been suggested that *in vivo* motion of the prostate is constrained by the ligament bundles holding the prostate to the pubic arch above, resulting in translation and rotation of the prostate.

To quantify the amount of motion caused by needle insertions in our phantom, we looked at the deformation fields calculated by our registration algorithm for five different insertion locations in the prostate, as shown in Fig. 10. The deformation fields were obtained by registering a reference 3D US image taken before insertion to a second image taken after needle insertion. Insertions were done using a robotic insertion device, using an 18 gauge Mick Ripple-Hub needle, with an insertion speed of 5 mm/s. After each insertion, an image volume was acquired to which the reference image taken before insertion was registered. A grid of 512 points evenly distributed throughout the prostate was taken from the resulting 3D deformation field and used to analyze the prostate motion. The center of mass of the points was used to quantify the amount of translation experienced by the prostate. The rotation of the prostate was extracted from the transformation matrix determined by rigidly registering the grid points from the before and after US volumes using Arun least squares fitting.³⁵ The results are shown in Table III for the five insertions done on a single phantom.

We found, as can be expected, that the prostate motion depended on the direction and location of insertion of the needle and was generally constrained to motion about the fixed US probe head inside the rectum. A needle inserted straight into the center of the prostate resulted in translational motion along the needle axis direction. An angled approach from the side of the prostate resulted in a translation of the

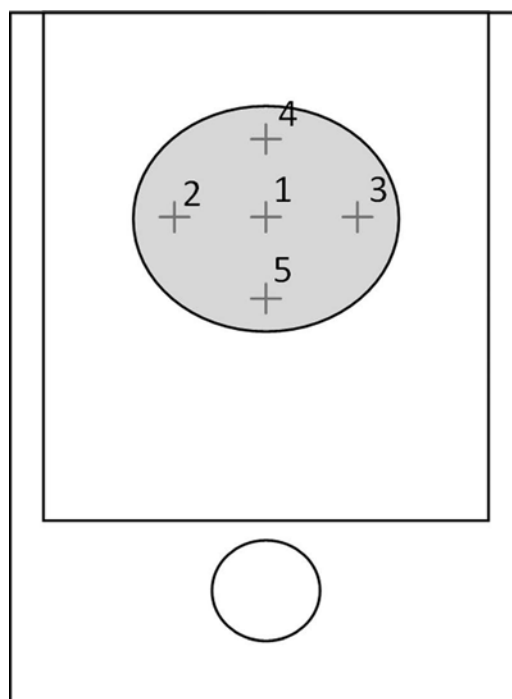


FIG. 10. Needle insertion locations used for phantom deformation testing.

TABLE III. Results showing the translation and rotation of the prostate during needle insertion into the phantom.

Insertion #	Translation (mm)	Rotation (°)		
		Coronal	Sagittal	Transverse
1	3.7	0.3	-0.2	0
2	2.3	1.0	0.3	0.9
3	2.4	-1.2	-0.4	-1.3
4	2.7	0	-2.1	-0.1
5	3.3	0.3	1.1	0

prostate along the needle axis direction coupled with a rotation about the probe head. The translation and the coronal-plane rotation of the phantom prostate were realistic, compared to the motions described in the literature. Rotation in the sagittal direction was, however, different, as rotation tended to be downward toward the rectum, rather than upward toward the pubic arch as suggested in the literature. But, as also mentioned in the literature, the sagittal-plane rotation is not as important as other motions and tends to be unpredictable in any case.³⁸ The measured translations and rotations correspond to published results measured *in vivo*: on the order of 3–10 mm of translation³⁹ and between 0° and about 10° of rotation.⁴⁰

III.G. Precautions

There are some precautions to be taken when using this phantom. Although the construction technique is quite simple,

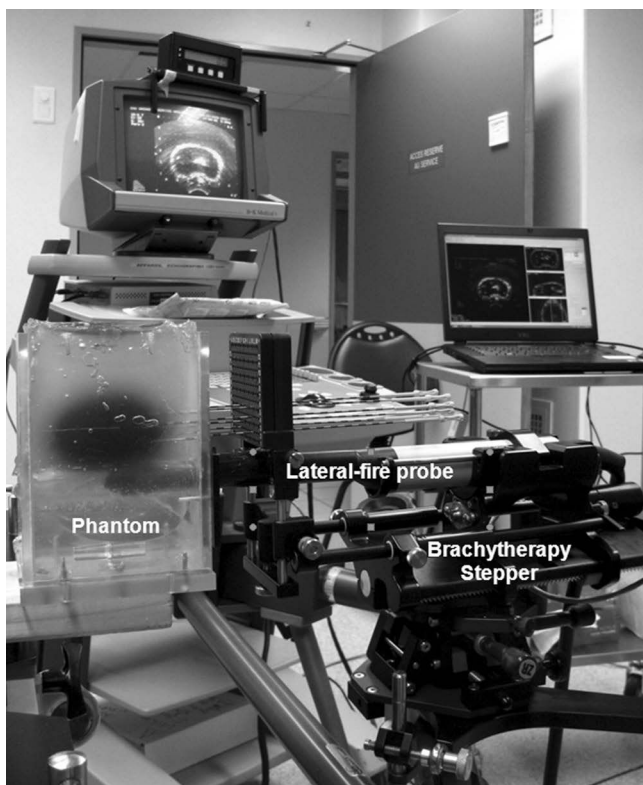


FIG. 11. Prostate phantom with a horizontal cylindrical rectum, being used with a side-fire US probe during a mock brachytherapy test.

it does require some caution in order to produce repeatable phantoms. The primary difficulty lies in the reduction of air bubbles. If a vacuum chamber is not used during construction, bubbles can become difficult to avoid. It is also important to heat the PVC material in the same way for each phantom, to ensure visible similarity, although differences in the heating procedure did not affect the imaging characteristics. Another precaution lies in the toxicity of the fumes emitted by the heated PVC. Although authorized for general public use, the fumes are very unpleasant to inhale, and the PVC should be handled under a fume hood during construction. The speed of sound, lower than the 1540 m/s used in standard US machines, may also be a difficulty for those unable to modify the sound speed used in their image reconstructions. Such a situation, however, is not wholly unreasonable, as the variations in speed of sound in the real prostatic environment are important.^{30,31} Although much better than water-based materials, the storage of PVC must nevertheless be handled with caution, and the phantoms should ideally be stored at cool temperatures. Finally, the material is also able to react with other types of PVCs; so, ultrasound probes should always be used with a protection cover to prevent possible damage.

IV. CONCLUSION

The prostate phantom described in this article has the characteristics of being realistically mobile upon needle insertion, as well as being visible to the naked eye and in US, CT, and MR images. We have used it for the preliminary validation of a new robotic brachytherapy system that includes 3D US-US registration. We believe that this phantom could be useful to other research teams working on similar prostate intervention technologies. Phantom validation is a necessary first step in most, if not all, new diagnostic or therapeutic techniques. A multitude of phantoms have, therefore, been described in the literature, but very few have the realistic mechanical and multimodal imaging characteristics presented above, and certainly none have been described to sufficient detail to allow for reproduction by interested readers.

The phantom is relatively fast to construct, does not require special tools for fabrication, and is inexpensive in material costs. For ultrasound applications, although only an end-fire probe version was described here, the rectum can easily be adapted to accept a side-fire probe, as shown in Fig. 11. The morphology of the phantom allows for both transrectal and transperineal needle approaches. The imaging characteristics of the phantom also make it useful for testing the accuracy of both feature-based and intensity-based deformable registration techniques.

ACKNOWLEDGMENTS

The authors would like to thank Dr. Ivan Bricault and the staff of the radiology department of the Grenoble University Hospital (CHU Grenoble) for their unfailing availability and willingness to scan our countless phantoms.

^{a)} Author to whom correspondence should be addressed. Electronic mail: Nikolai.Hungr@imag.fr

- ¹Cancer Society. Cancer Facts and Figures 2011. Available: <http://www.cancer.org> (January 13, 2012).
- ²J. Ferlay, D. M. Parkin, and E. Steliarova-Foucher, "Estimates of cancer incidence and mortality in Europe in 2008," *Eur. J. Cancer* **46**(4), 765–781 (2010).
- ³M. Baumann, P. Mozer, V. Daanen, and J. Troccaz, "Prostate biopsy assistance system with gland deformation estimation for enhanced precision," *Med. Image Comput. Comput. Assist. Interv.* **12**(Pt 1), 67–74 (2009).
- ⁴M. Baumann, P. Mozer, V. Daanen, and J. Troccaz, "Prostate biopsy tracking with deformation estimation," *Med Image Anal.* 2011 May 17. [Epub ahead of print].
- ⁵N. Hungr, J. Troccaz, N. Zemiti, and N. Tripodi, "Design of an ultrasound-guided robotic brachytherapy needle-insertion system," *Annual International Conference of the IEEE Engineering in Medicine and Biology Society-EMBC* (Minneapolis, 2009), pp. 250–253.
- ⁶R. Lefrançois and R. S. Sloboda, "A medical needle drive for the study of interstitial implant mechanics," *Med. Eng. Phys.* **25**(3), 255–258 (2003).
- ⁷Y. Yu, T. Podder, Y. Zhang, W. S. Ng, V. Mistic, J. Sherman, L. Fu, D. Fuller, E. Messing, D. Rubens, J. Strang, and R. Brasacchio, "Robot-assisted prostate brachytherapy," *Med. Image Comput. Comput. Assist. Interv.* **9**(Pt 1), 41–49 (2006).
- ⁸M. P. Ottensmeyer and J. K. Salisbury, "In vivo data acquisition instrument for solid organ mechanical property measurement," *Lect. Notes Comput. Sci.* **2208**, 975–982 (2001).
- ⁹M. De Brabandere, C. Kirisits, R. Peeters, K. Haustermans, and F. Van den Heuvel, "Accuracy of seed reconstruction in prostate postplanning studied with a CT- and MRI-compatible phantom," *Radiother. Oncol.* **79**(2), 190–197 (2006).
- ¹⁰A. E. Kerdok, S. M. Cotin, M. P. Ottensmeyer, A. M. Galea, R. D. Howe, and S. L. Dawson, "Truth cube: Establishing physical standards for soft tissue simulation," *Med. Image Anal.* **7**(3), 283–291 (2003).
- ¹¹S. P. DiMaio and S. E. Salcudean, "Needle insertion modeling and simulation," *Proceedings of the IEEE International Conference on Robotics and Automation-ICRA* (Washington, DC, 2002), pp. 2098–2105.
- ¹²J. R. Crouch, C. M. Schneider, J. Wainer, and A. M. Okamura, "A velocity-dependent model for needle insertion in soft tissue," *Med. Image Comput. Comput. Assist. Interv.* **8**(Pt 2), 624–632 (2005).
- ¹³J. Bax, D. Cool, L. Gardi, K. Knight, D. Smith, J. Montreuil, S. Sherbrin, C. Romagnoli, and A. Fenster, "Mechanically assisted 3D ultrasound guided prostate biopsy system," *Med. Phys.* **35**(12), 5397–5410 (2008).
- ¹⁴J. A. Long, V. Daanen, A. Moreau-Gaudry, J. Troccaz, J. J. Rambeaud, and J. L. Descotes, "Prostate biopsies guided by 3-dimension real-time (4D) transrectal ultrasound on a phantom. Comparative study versus 2D transrectal ultrasound guided biopsies," *Prog. Urol.* **17**(7), 1337–1342 (2007).
- ¹⁵X. Wen and S. E. Salcudean, "Detection of brachytherapy seeds using 3D transrectal ultrasound," *Proceedings of the Annual International Conference of the IEEE Engineering in Medicine and Biology Society* (Vancouver, BC, Canada, 2008), pp. 855–858.
- ¹⁶J. A. Cunha, I. C. Hsu, J. Pouliot, I. M. Roach, K. Shinohara, J. Kurhanewicz, G. Reed, and D. Stoianovici, "Toward adaptive stereotactic robotic brachytherapy for prostate cancer: Demonstration of an adaptive workflow incorporating inverse planning and an MR stealth robot," *Minimally Invasive Ther. Allied Technol.* **19**(4), 189–202 (2010).
- ¹⁷J. P. McGahan, J. Ryu, and M. Fogata, "Ultrasound probe pressure as a source of error in prostate localization for external beam radiotherapy," *Int. J. Radiat. Oncol., Biol., Phys.* **60**(3), 788–93 (2004).
- ¹⁸E. Dehghan, X. Wen, R. Zahiri-Azar, M. Marchal, and S. E. Salcudean, "Needle-tissue interaction modeling using ultrasound-based motion estimation: Phantom study," *Comput. Aided Surg.* **13**(5), 265–280 (2008).
- ¹⁹J. Sherman, T. K. Podder, V. Mistic, L. Fu, D. Fuller, B. Winey, E. M. Messing, D. J. Rubens, J. G. Strang, R. Brasacchio, and Y. Yu, "Efficacy of prostate stabilizing techniques during brachytherapy procedure," *Proceedings of the Annual International Conference of the IEEE Engineering in Medicine and Biology Society* (New York, NY, 2006), pp. 563–566.
- ²⁰J. E. Browne, K. V. Ramnarine, A. J. Watson, and P. R. Hoskins, "Assessment of the acoustic properties of common tissue-mimicking test phantoms," *Ultrasound Med. Biol.* **29**(7), 1053–1060 (2003).
- ²¹K. Zell, J. I. Sperl, M. W. Vogel, R. Niessner, and C. Haisch, "Acoustical properties of selected tissue phantom materials for ultrasound imaging," *Phys. Med. Biol.* **52**(20), N475–N484 (2007).
- ²²T. J. Hall, M. Bilgen, M. F. Insana, and T. A. Krouskop, "Phantom materials for elastography," *IEEE Trans. Ultrason. Ferroelectr. Freq. Control*, **44**(6), 1355–1365 (1997).
- ²³K. J. Surry, H. J. Austin, A. Fenster, and T. M. Peters, "Poly(vinyl alcohol) cryogel phantoms for use in ultrasound and MR imaging," *Phys. Med. Biol.* **49**(24), 5529–5546 (2004).
- ²⁴J. Fromageau, J. L. Gennisson, C. Schmitt, R. L. Maurice, R. Mongrain, and G. Cloutier, "Estimation of polyvinyl alcohol cryogel mechanical properties with four ultrasound elastography methods and comparison with gold standard testings," *IEEE Trans. Ultrason. Ferroelectr. Freq. Control*, **54**(3), 498–509 (2007).
- ²⁵C. U. Devi, R. M. Vasu, and A. K. Sood, "Design, fabrication, and characterization of a tissue-equivalent phantom for optical elastography," *J. Biomed. Opt.* **10**(4), 44020 (2005).
- ²⁶G. M. Spirou, A. A. Oraevsky, I. A. Vitkin, and W. M. Whelan, "Optical and acoustic properties at 1064 nm of polyvinyl chloride-plastisol for use as a tissue phantom in biomedical optoacoustics," *Phys. Med. Biol.* **50**(14), N141–N153 (2005).
- ²⁷E. L. Madsen, G. R. Frank, T. A. Krouskop, T. Varghese, F. Kallel, and J. Ophir, "Tissue-mimicking oil-in-gelatin dispersions for use in heterogeneous elastography phantoms," *Ultrason. Imaging* **25**(1), 17–38 (2003).
- ²⁸M. B. Zerhouni and M. Rachedine, "Ultrasonic calibration material and method," U.S. Patent 5196343 (Mar. 23, 1993).
- ²⁹T. Podder, D. Clark, J. Sherman, D. Fuller, E. Messing, D. Rubens, J. Strang, R. Brasacchio, L. Liao, W. S. Ng, and Y. Yu, "In vivo motion and force measurement of surgical needle intervention during prostate brachytherapy," *Med. Phys.* **33**(8), 2915–2922 (2006).
- ³⁰D. Fontanarosa, S. van der Meer, E. Harris, and F. Verhaegen, "A CT based correction method for speed of sound aberration for ultrasound based image guided radiotherapy," *Med. Phys.* **38**(5), 2665–2673 (2011).
- ³¹D. Pfeiffer, S. Sutlief, W. Feng, H. M. Pierce, and J. Kofler, "AAPM Task Group 128: Quality assurance tests for prostate brachytherapy ultrasound systems," *Med. Phys.* **35**, 5471–5489 (2008).
- ³²E. J. Chen, J. Novakofski, W. K. Jenkins, and W. D. O'Brien, "Young's modulus measurements of soft tissues with application to elasticity imaging," *IEEE Trans. Ultrason. Ferroelectr. Freq. Control* **43**(1), 271–275 (1996).
- ³³K. J. Parker, S. R. Huang, R. M. Lerner, F. Lee, D. Rubens, and Roach, "Elastic and ultrasonic properties of the prostate," *Proc. -IEEE Ultrason. Symp.* **2**, 1035–1038 (1993).
- ³⁴T. A. Krouskop, T. M. Wheeler, F. Kallel, B. S. Garra, and T. Hall, "Elastic moduli of breast and prostate tissues under compression," *Ultrason. Imaging* **20**(4), 260–274 (1998).
- ³⁵K. S. Arun, T. S. Huang, and S. D. Blostein, "Least-squares fitting of two 3-D point sets," *IEEE Trans. Pattern Anal. Mach. Intell.* **PAMI-9**(5), 698–700 (1987).
- ³⁶B. Maurin, L. Barbé, B. Bayle, P. Zanne, J. Gangloff, M. de Mathelin, A. Gangi, L. Soler, and A. Forgiione, "In vivo study of forces during needle insertions. Proceedings of the Medical Robotics," *Navigation and Visualisation Scientific Workshop* (Remagen, Germany, 2004).
- ³⁷H. Kataoka, T. Washio, K. Chinzei, K. Mizuhara, C. Simone, and A. M. Okamura, "Measurement of the tip and friction force acting on a needle during penetration," *Med. Image Comput. Comput. Assist. Interv.* **2002**, 216–223 (2002).
- ³⁸R. Taschereau, J. Pouliot, J. Roy, and D. Tremblay, "Seed misplacement and stabilizing needles in transperineal permanent prostate implants," *Radiother. Oncol.* **55**(1), 59–63 (2000).
- ³⁹N. N. Stone, J. Roy, S. Hong, Y. C. Lo, and R. G. Stock, "Prostate gland motion and deformation caused by needle placement during brachytherapy," *Brachytherapy* **1**(3), 154–160 (2002).
- ⁴⁰V. Lagerburg, M. A. Moerland, J. J. Legendijk, and J. J. Battermann, "Measurement of prostate rotation during insertion of needles for brachytherapy," *Radiother. Oncol.* **77**(3), 318–323 (2005).
- ⁴¹See supplementary material at <http://dx.doi.org/10.1118/1.3692179> for supplementary material 1: detailed description of the various materials considered during the design of our deformable prostate phantom: agarose, gelatin, Zerdine, PVA-C, silicone gel and PVC. Also, supplementary material 2: detailed description of the experiments done to determine the storage properties of our deformable prostate phantom (with additional figures).

SUPPLEMENTAL MATERIAL 1 – PHANTOM MATERIALS

Paper: “A realistic deformable prostate phantom for multi-modal imaging and needle-insertion procedures.”

Authors: Nikolai Hungr, Jean-Alexandre Long, Vincent Beix, Jocelyne Troccaz.

Note: Numbered refs. refer to references in the paper. Lettered refs. refer to reference list at the end of this document.

The following is a detailed description of the various materials considered during the design of our deformable prostate phantom.

Agarose is a plant-based jellifying agent typically used in microbiology as a bacterial growth medium, in molecular biology for protein separation by electrophoresis and in the food industry. It is sold in the form of a white powder that, once mixed with water, heated above 85°C and then cooled to below around 35°C, becomes a lightly opaque gelatinous substance. Its strength can be adjusted based on the dry-weight concentration of agarose used, its Young’s modulus ranging from 7.6 to 195 kPa according to Hall *et al.*²² De Brabandere *et al.*⁹ used an agarose phantom to evaluate the accuracy of a brachytherapy seed detection algorithm in CT and MR images. They chose agarose because its density and T1 and T2 MRI relaxation times are comparable to prostatic tissue. Bax *et al.*,¹³ on the other hand, used agarose for its tissue-equivalent speed of sound, to study the accuracy of an ultrasound guided biopsy robot. Although agarose has mechanical and imaging characteristics similar to those of soft tissues, its main limitation is its low toughness, making it fragile during handling.²⁷

Gelatin is another type of jellifying agent, derived from animal collagen and used primarily in the food and pharmaceutical industries. It is prepared identically to Agarose gel, but at lower temperatures, as it dissolves at around 40°C. Its strength depends not only on the dry-weight concentration used in the mixture, but also on the Bloom value of the gelatin used. Hall *et al.*²² report a similar range of Young’s modulus to that of agarose gels (4.8-159 kPa). They did, however, find that gelatin has a linear stress-strain curve, compared to the non-linear behavior of agarose, suggesting that gelatin is more suitable for elastography phantoms. A gelatin phantom was used by Lefrançois *et al.*⁶ to test the response of their needle insertion drive, while McGahan *et al.*¹⁷ constructed a gelatin-based phantom to explore the effect of external ultrasound probe pressure on prostate localization. Doyley *et al.*^a describe the testing of a prototype elastographic imaging system, using gelatin phantoms prepared with polyethylene granules as acoustic scattering agents. Like agarose gels, gelatin gels must be stored in either air-tight containers to prevent water evaporation, or in liquid baths at low temperatures.^{21,27}

A different class of tissue-equivalent materials used in phantoms is based on polymers. One such material is commercialized under the name of Zerdine® (Computerized Imaging Reference Systems,

Inc.) and was developed specifically for ultrasound calibration phantoms. It is a clear polyacrylamide substance, whose formulation can be adjusted to match a variety of soft-tissue acoustic properties. Its primary advantages over agarose and gelatin are its increased stability over time in room-temperature conditions as well as its improved strength and temperature resistance. As it is water based and its density can be controlled, it can also be used for CT and MR imaging, as demonstrated by Cunha *et al.*,¹⁶ for example, who used a Zerdine prostate phantom to validate their MRI robot's range of motion in both modalities. The same phantom was used by Wen *et al.*¹⁵ to validate an ultrasound brachytherapy seed detection algorithm. No published information was found on the range of elasticity that can be obtained with this material.

Another polymer-based hydrogel is polyvinyl alcohol cryogel (PVA-C), a solution that combines PVA compound with water. By subjecting the solution to repeated freeze-thaw cycles, a semi-transparent gel of various strengths can be made. The more cycles the material experiences, the harder it becomes. As summarized in Table I of the paper, a number of studies have shown its very similar mechanical and acoustic characteristics to those of human soft tissues. For this reason, it has often been recommended for use with ultrasound imaging.^{21,23-25} Its extensive use, however, in multi-component phantoms and needle insertion phantoms has been hindered by its complex preparation. The temperature cycles during preparation must be carefully controlled, taking on the order of 20 hours per cycle, and requiring specialized equipment, such as controlled rate freezer. To prevent dehydration over time, it must also be stored in a water bath at low temperatures.

A third polymer gel often used in phantoms is silicone gel. Primarily composed of silicon, oxygen and other organic side-groups, silicone gel comes in many varieties, depending, among others, on the curing characteristics, strength and environmental compatibility required. It is used in a large variety of applications, from industrial, to home, to medical. A typical variety used for phantom construction, is a room temperature vulcanization (RTV) silicone consisting of two compounds: a catalyst and a crosslinker. The compounds can be mixed in variable proportions to produce a clear gel of the required strength. Bubbles must be removed using a vacuum chamber. In their phantom material study, Zell *et al.*²¹ conclude that silicone materials are appropriate for long-term, stable phantoms, but their acoustic properties are not ideal for ultrasound applications. Kerdok *et al.*¹⁰ used silicone for soft-tissue modeling experiments, using Teflon beads scattered throughout the phantom as reference markers for CT-imaging. Ottensmeyer *et al.*⁸ used silicone for initial validation on a new soft-tissue mechanical property measurement instrument.

The final type of gel that we will present here is soft polyvinyl chloride (PVC), or plastisol. PVC is a combination of liquid polyvinyl chloride resin with a plasticizer, such as ethyl hexyl adipate. Different ratios of resin-to-plasticizer can be mixed and heated to around 150 - 200°C, which, upon cooling back to

room temperature, turn into clear rubber-like plastics with a range of different elasticities. Soft PVC in its uncured form is sold for home fabrication of soft fishing lures. Both Spirou *et al.*²⁶ and Madsen *et al.*²⁷ found its speed of sound for acoustic applications to be on the lower side of standard tissue values, hovering around 1400 m/s. Detailed information on its Young's modulus was not found in the literature, although DiMaio *et al.*¹¹ mention a range between 10 and 100 kPa is attainable. However, with its inexpensive and simple preparation, its resistance to rough handling, as well as its stability over time, it has often been used as a phantom material. Indeed, DiMaio *et al.*¹¹ used PVC to validate a needle insertion force model that they developed. The same team a few years later,¹⁸ again used a more complex PVC phantom to introduce a new experimental method of modeling needle-tissue interactions, using ultrasound. Another team used PVC phantoms for testing the needle insertion accuracy of a brachytherapy robot they designed,⁷ as well as for studying the effect of stabilizing the prostate with hooked and angled needles for brachytherapy.¹⁹

The materials detailed above are generally described in their pure form; however, many additives and mixtures have been reported in the literature. Additives are typically used to change the acoustic scatter properties for ultrasound applications,^{13,24,a-c} to modify the mechanical characteristics,²² or to improve the stability of the material over time.^d Other materials have also been presented for more specific uses, such as thermal ablation^{e-g} and others.^{14,h,i}

References:

- ^aM. M. Doyley, J. C. Bamber, F. Fuechsel and N. L. Bush, "A freehand elastographic imaging approach for clinical breast imaging: system development and performance evaluation," *Ultrasound Med. Biol.* 27(10), 1347-1357 (2001).
- ^bW. D. D'Souza, E. L. Madsen, O. Unal, K. K. Vigen, G. R. Frank and B. R. Thomadsen, "Tissue mimicking materials for a multi-imaging modality prostate phantom," *Med. Phys.* 28(4), 688-700 (2001).
- ^cE. L. Madsen, M. A. Hobson, H. Shi, T. Varghese, and G. R. Frank, "Tissue-mimicking agar/gelatin materials for use in heterogeneous elastography phantoms," *Phys. Med. Biol.* 50(23), 5597-55618 (2005).
- ^dB. W. Pogue and M. S. Patterson, "Review of tissue simulating phantoms for optical spectroscopy, imaging and dosimetry," *J. Biomed. Opt.* 11(4), 1-16 (2006).
- ^eZ. Bu-Lin, J. Bing, K. Sheng-Li, Y. Huang, W. Rong and L. Jia, "A polyacrylamide gel phantom for radiofrequency ablation," *Int. J. Hyperthermia*, 24(7), 568-576 (2008).
- ^fU. Lindner, N. Lawrentschuk, R. A. Weersink, O. Raz, E. Hlasny, M. S. Sussman, S. R. Davidson, M. R. Gertner and J. Trachtenberg, "Construction and evaluation of an anatomically correct multi-image modality compatible phantom for prostate cancer focal ablation," *J. Urol.* 184(1), 352-357 (2010).

^gM. McDonald, S. Lochhead, R. Chopra and M. J. Bronskill, “Multi-modality tissue-mimicking phantom for thermal therapy,” *Phys. Med. Biol.* 49(13), 2767-2778 (2004).

^hH. Kato, M. Kuroda, K. Yoshimura, A. Yoshida, K. Hanamoto, S. Kawasaki, K. Shibuya and S. Kanazawa, “Composition of MRI phantom equivalent to human tissues,” *Med. Phys.* 32(10), 3199-3208 (2005).

ⁱT. Kondo, M. Kitatuji and H. Kanda, “New Tissue Mimicking Materials for Ultrasound Phantoms,” *IEEE Ultrasonics Symposium*, (Rotterdam, The Netherlands, 2005) pp. 1664 – 1667.

SUPPLEMENTAL MATERIAL 2 – PHANTOM STORAGE PROPERTIES

Paper: “A realistic deformable prostate phantom for multi-modal imaging and needle-insertion procedures.”

Authors: Nikolai Hungr, Jean-Alexandre Long, Vincent Beix, Jocelyne Troccaz.

The following is a detailed description of the experiments done to determine the storage properties of our deformable prostate phantom.

In the first experiment, we carried out the same compression stress-strain measurements described in section III.B. of the paper, on 3 sets of PVC samples each stored at different temperatures for 11 days after fabrication. The first set was stored at room temperature (between 23°C and 25°C), the second in the fridge (4.5°C) and the third in the freezer (-21°C). The resulting stress-strain relationships can be seen in Figure Sup.1. We can see that, except for the standard samples, the stress-strain relationship follows a steeper curve with increasing storage temperature. In other words, PVC stored at room temperature becomes stiffer, while PVC stored in the freezer stiffens less quickly over time. Visually, over time, we noticed that the samples leached oil, predominantly in the room-temperature samples, while the colder samples remained more intact.

In the second experiment, we constructed three small sample models as shown in Figure Sup.2, similar in property to the true phantom. The models consisted of a 16 mm diameter cylinder made of standard PVC mixture stained with Toluidine Blue (like the material used for the prostate capsule) submerged in a super-soft PVC surrounding. Models were used because they were easier to manufacture and because the geometrical shape of the blue cylinder was easier to survey visually in terms of size and shape. One model was stored at room temperature, another in the fridge and the third in the freezer. The models were observed over a period of 26 days: photographs were taken of each model throughout the period, in order to follow any visual changes; at the same time, 3D ultrasound volumes were also taken, in order to monitor any changes visible in this imaging modality.

Visually, the cylinders showed leaching over time of the blue coloring into the surrounding super-soft material. Figure Sup.3 shows this phenomenon with sequential photographs of the models over the 26 days. The model stored at room temperature shows very rapid and evident leaching. The model stored in the fridge shows less leaching, while the freezer model shows minimal leaching. This leaching is consistent with the changes in mechanical properties described in the first experiment above: as the oil-based softening agent seeps out, the samples can be expected to become stiffer.

Figure Sup.4 shows a sample image of the ultrasound volumes taken of the models. Nine volumes were taken of each sample using an Ultrasonix 4DEC9-5 end-fire probe connected to an Ultrasonix RP

ultrasound machine. In order to determine whether the visual US properties changed over time, the cylindrical inclusion was singled out in each image and its volume measured. The volume was measured by thresholding the region of interest around the cylinders with the same intensity threshold range for each image, and then summing the resulting white pixels. The results are shown in Figure Sup.5. The volume increased for all three samples over the 26 days. Once again, the sample stored at room temperature showed a stronger change than the other two samples. The sample in the freezer showed noticeably less change in volume.

There are two possible reasons for these changes in volume. The first is evidently that the leaching of the blue scattering agent resulted in an increased volume being visualized in the US images. The diffusive character of this leaching was not, however evident in the images: even the sample with the strongest amount of leaching still displayed a sharp outline of the cylinder in the US image. This, therefore, pointed to the other reason for the change in volume, notably a change in speed of sound of the material. An increase in speed of sound would consequently increase the apparent size of the cylinder in the image, resulting in larger measured volumes. This is a reasonable assumption, given the increase in stiffness over time, as described above, which would result in an increase in speed of sound (see measured speeds for mixtures of various stiffnesses in Table II of the paper).

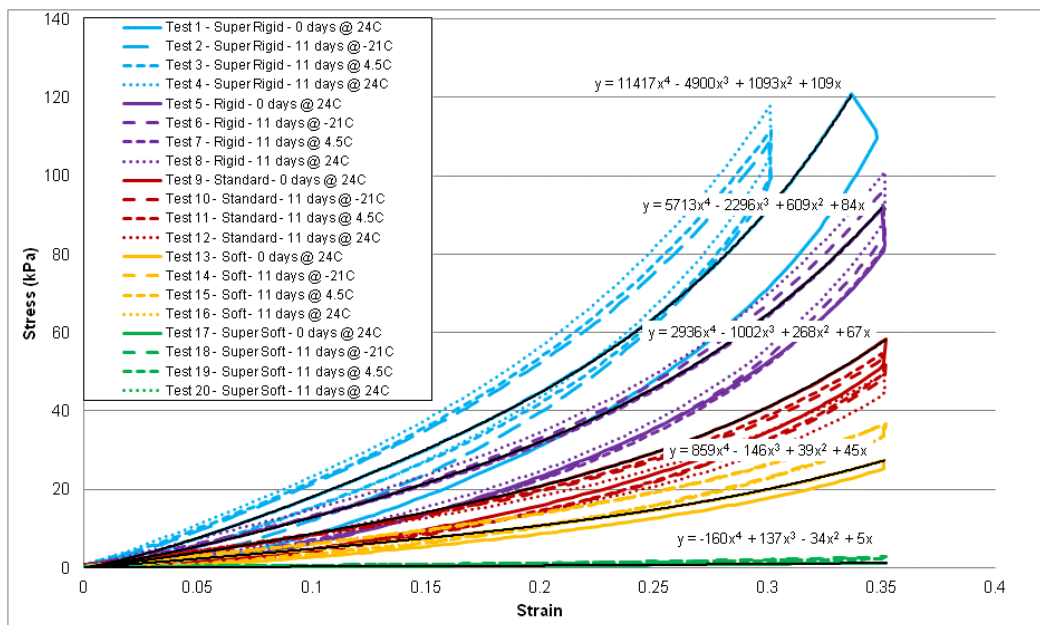
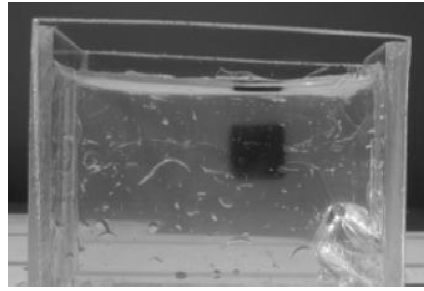
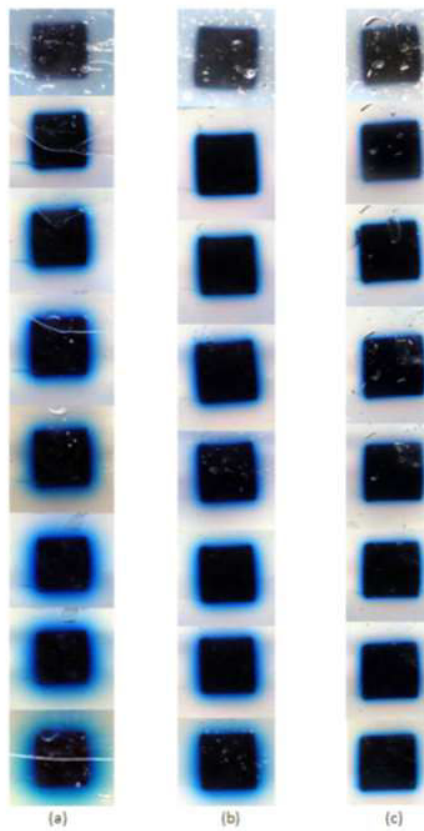


FIG. Sup.1. Stress-strain curves for the four sets of PVC samples stored at different temperatures: overnight at room temperature (0 days @ 24°C), eleven days in the freezer (11 days @ -21°C), eleven days in the fridge (11 days @ 4.5°C), and eleven days at room temperature (11 days @ 24°C). Polynomial fits for the compression phases of the overnight samples are traced in black.



. Small sample model of our phantom, used to observe its storage



. Close-up photographs showing the leaching of the sample models over a period of 26 days (samples grow older vertically downward). (a) Model stored at room temperature. (b) Model stored in the fridge. (c) Model stored in the freezer. Note the photographs are not homogeneously scaled: the most important aspect is the relative amount of leaching observable around the sample inclusion in each photograph.

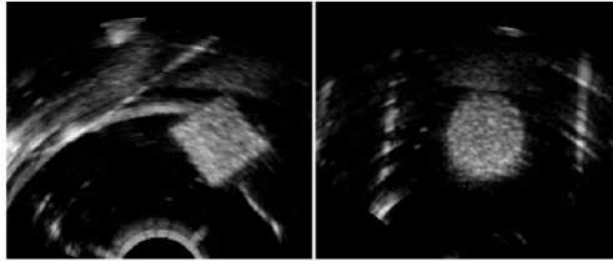


FIG. Sup.4. Sample ultrasound image of the leaching models. Left: sagittal cut. Right: transverse cut.

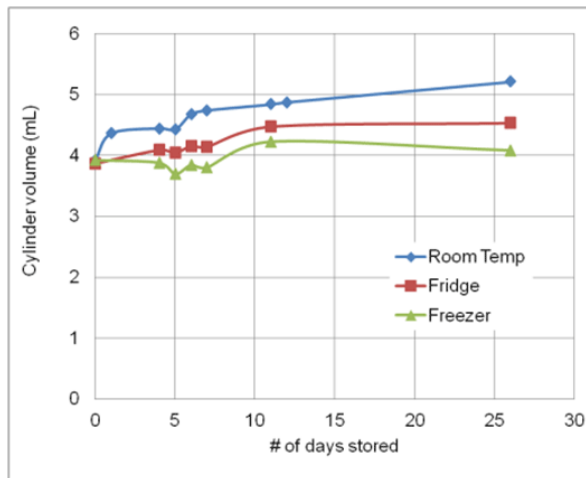
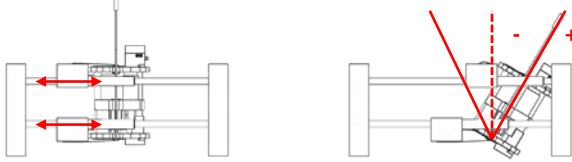
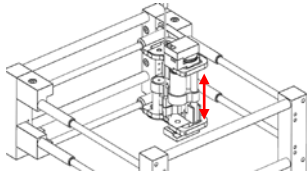


FIG. Sup.5. Volume over time of the thresholded inclusions for the three samples stored at different temperatures. The uneven jumps in the curves are likely the result of slight image inconsistencies caused by variable probe pressure or the presence of air bubbles in ultrasound gel applied at the probe-phantom interface.

Appendix 3: LPR workspace

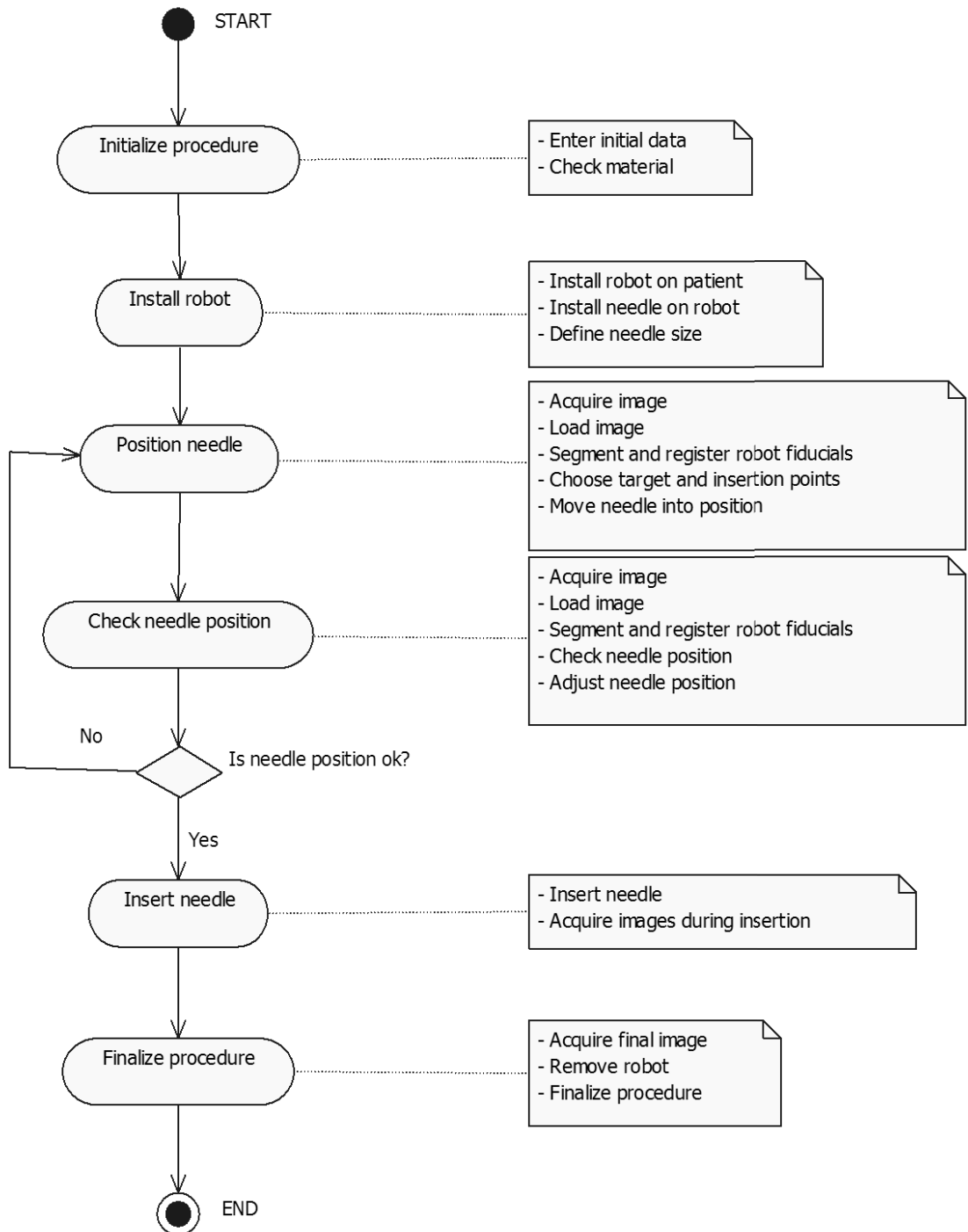
The LPR pre-clinical prototype's DOFs and range of motion.

Motors #	Range of motion	DOF
1 and 2	T: 120 mm I: +24° to -32°	 <p>Translation along z-axis and inclination about x-axis</p>
3 and 4	T: 135 mm I: +10° to -20°	 <p>Translation along x-axis and inclination about z-axis</p>
5	T: 35 mm	 <p>Insertion stroke distance</p>

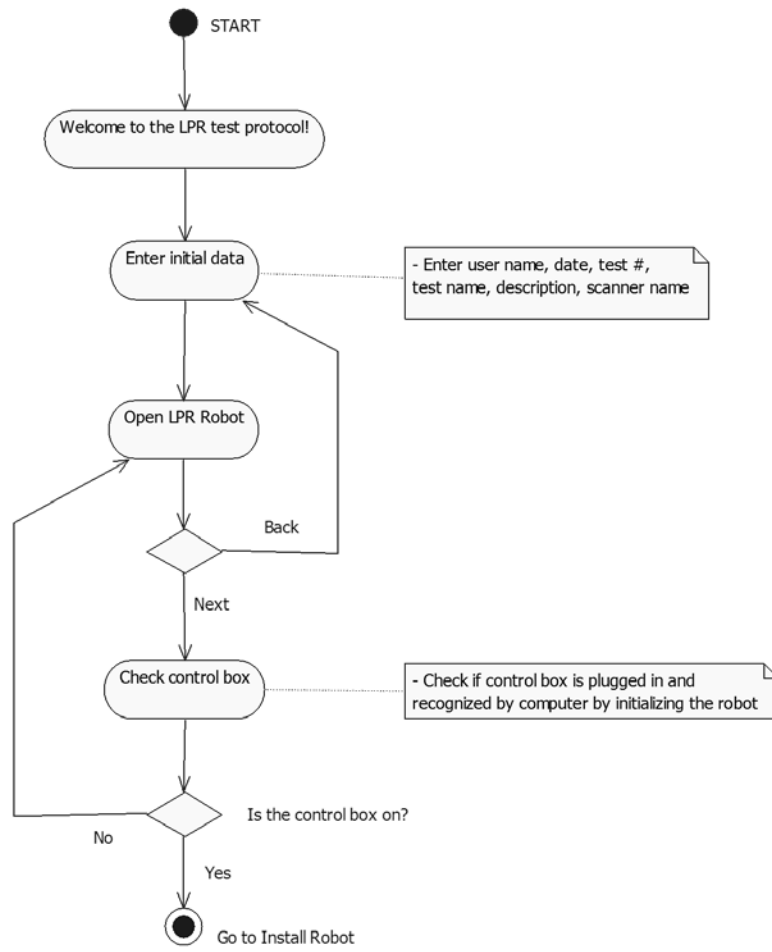
Appendix 4: LPR GUI protocol

UML activity diagram of the protocol used during the LPR phantom experiments.

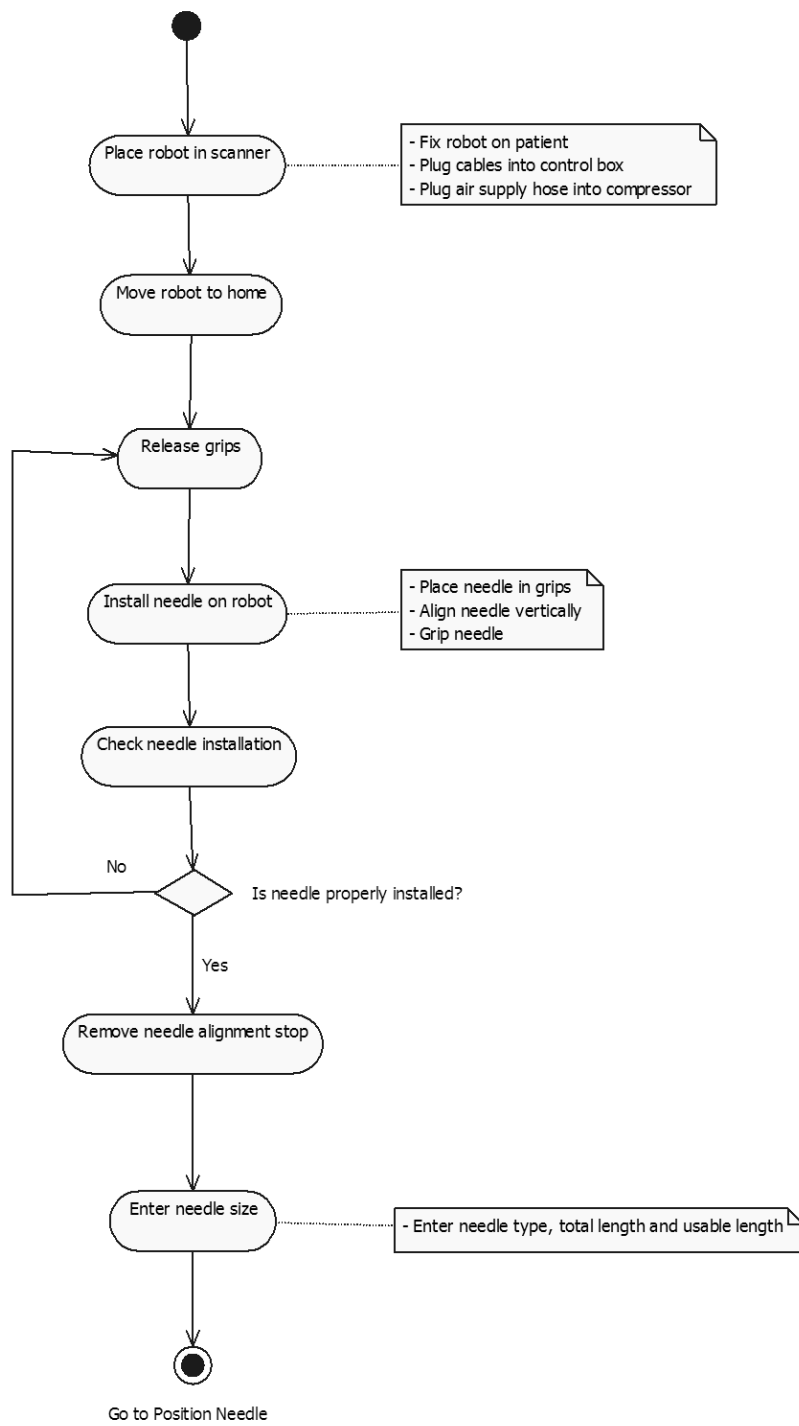
General Diagram:



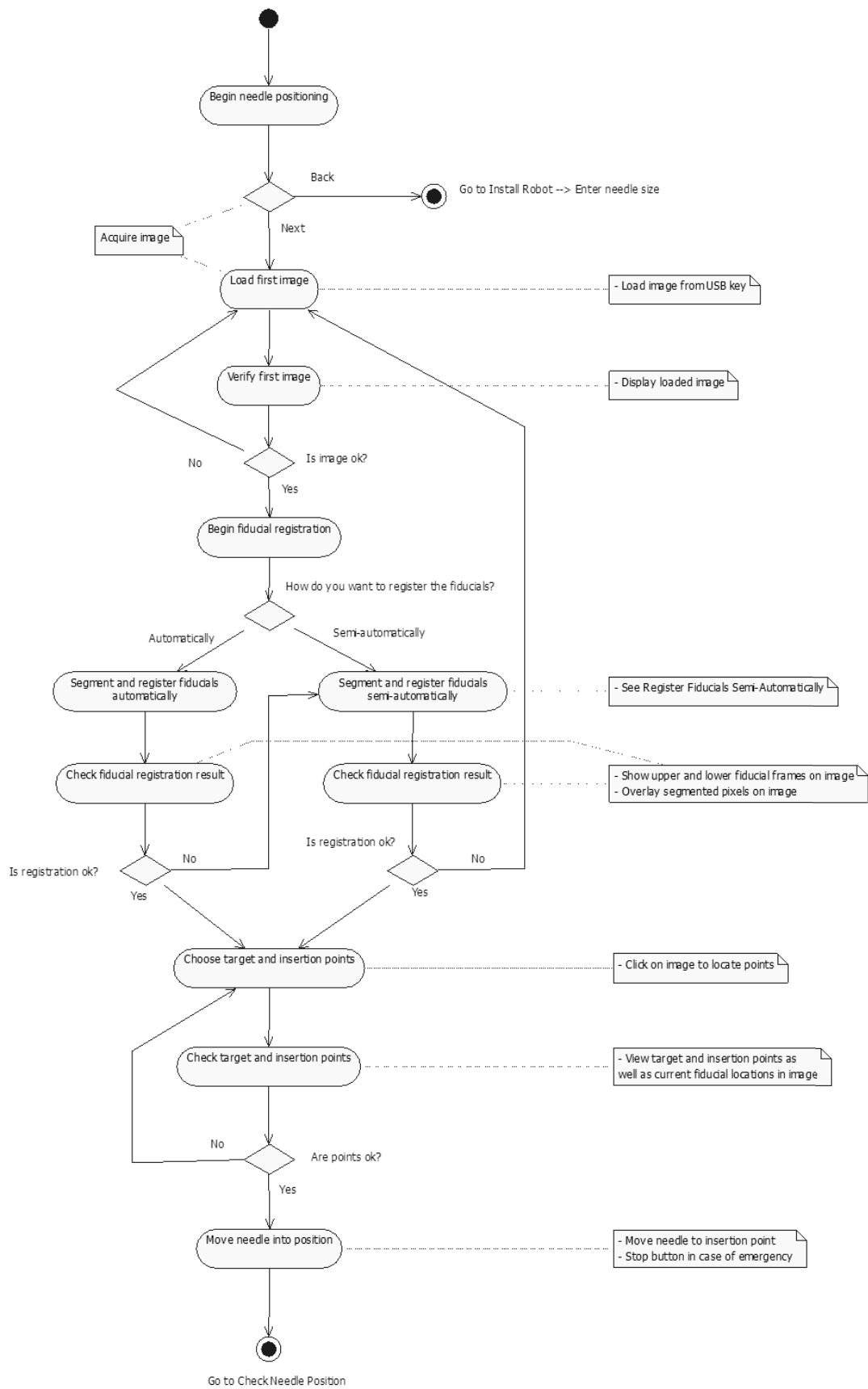
Initialize Procedure:



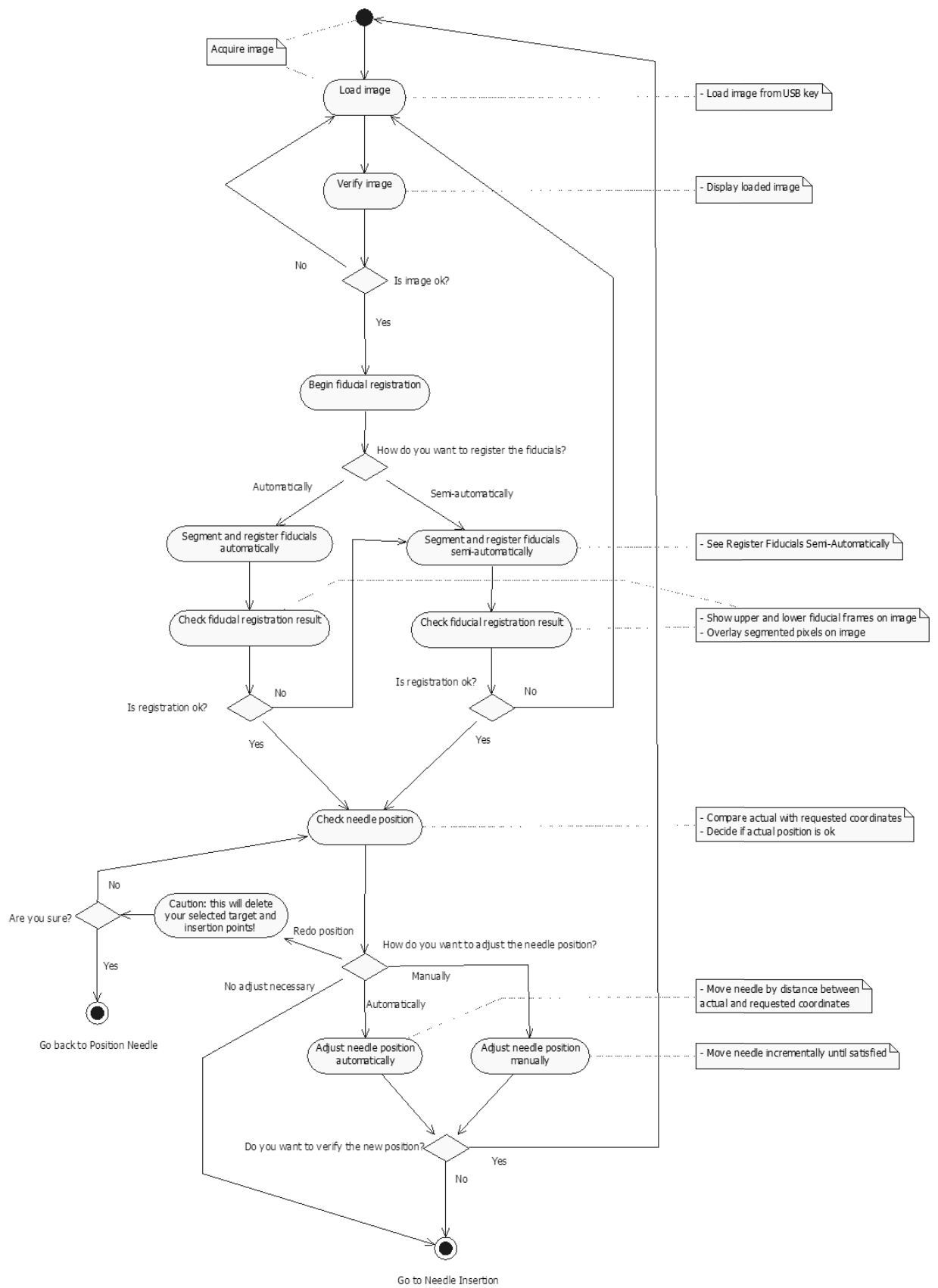
Install Robot:



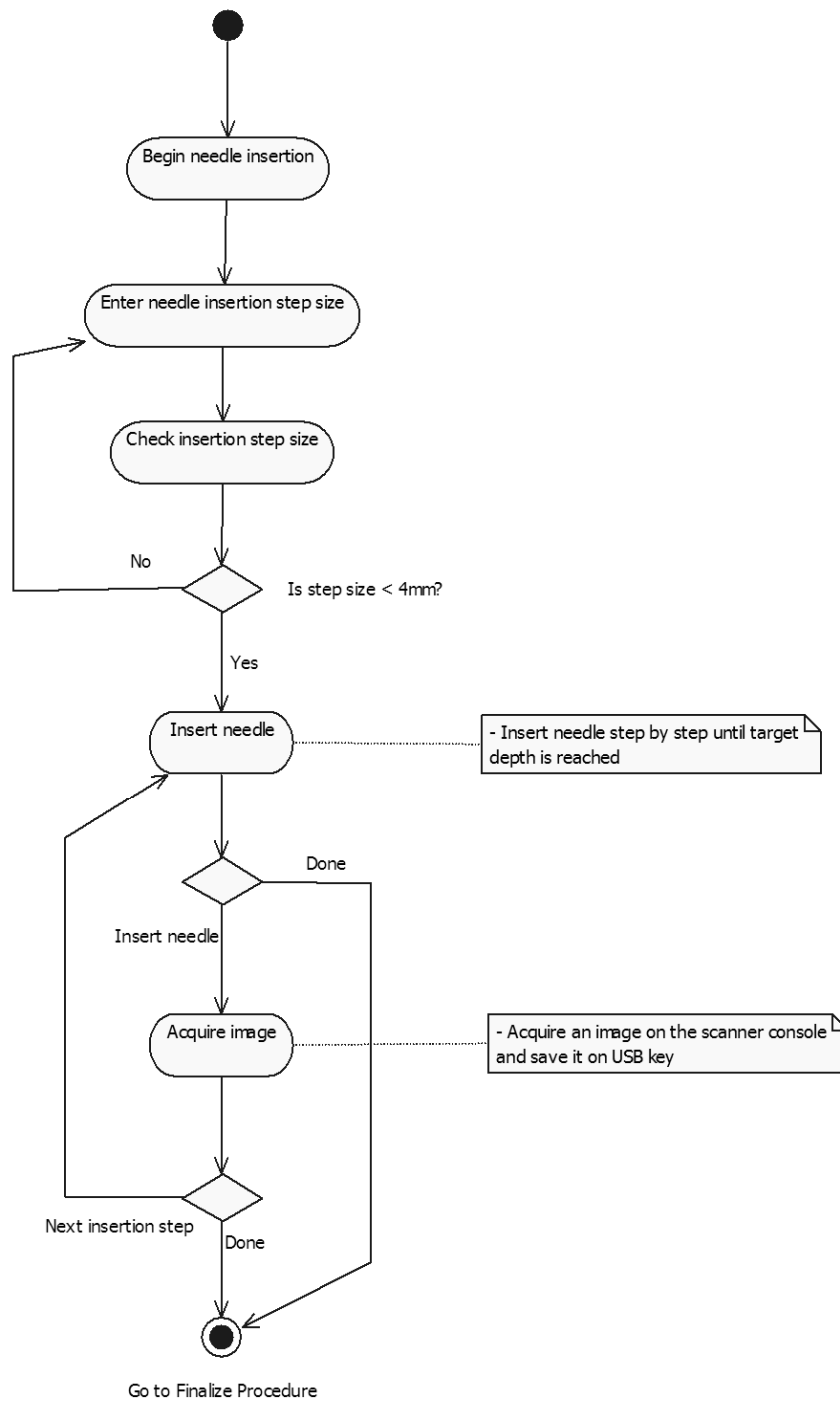
Position Needle:



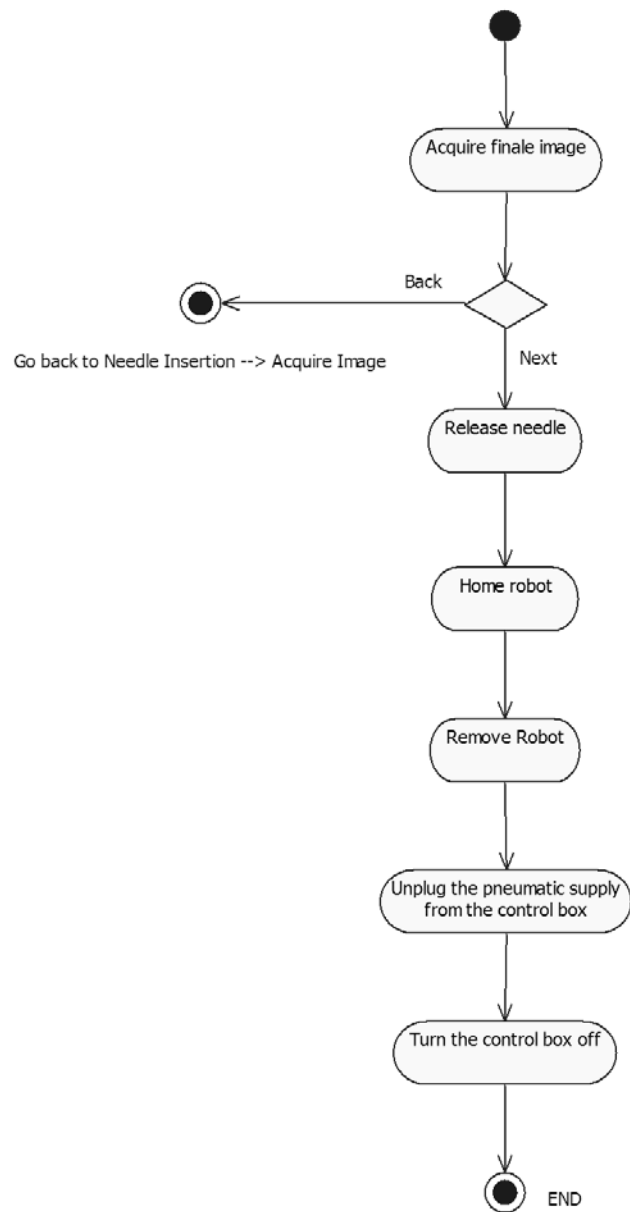
Check Needle Position:



Needle Insertion:



Finalize Procedure:



Appendix 5: Synthèse (Français)

Chapitre 1 : Introduction aux gestes percutanés guidés par imagerie médicale

Le contexte de cette thèse se situe dans l'assistance aux gestes percutanés en radiologie interventionnelle (RI). Ce premier chapitre introduit le domaine des gestes percutanés guidés par imagerie médicale en décrivant les modalités d'imagerie utilisées, les gestes diagnostiques et thérapeutiques communément réalisés ainsi que les difficultés auxquelles les cliniciens doivent faire face pour les accomplir. Les gestes d'intervention radiologique thoraciques et abdomino-pelviens sont distingués des gestes qui visent spécifiquement la prostate par voie transpérinéale à cause 1) de leur importance respective en tant que problèmes de santé publique, 2) des différentes modalités d'imagerie utilisées et 3) de l'emplacement particulier des ponctions sur le corps du patient.

La procédure utilisée pendant une ponction d'aiguille percutanée quelconque comporte les étapes suivantes : d'abord, un planning de la procédure est fait en préopératoire en s'appuyant sur des images médicales du patient ou des résultats d'analyses prises auparavant. Le patient est installé sur le lit de l'imageur et bénéficie d'une anesthésie locale ou générale. Une image du patient est prise et un planning peropératoire précis du geste est fait pour déterminer comment et où insérer la ou les aiguille(s). L'aiguille est ensuite insérée partiellement ou entièrement, selon la complexité du trajet. Cette insertion est soit guidée avec des images en temps réel, soit contrôlée après insertion par une image de contrôle. La trajectoire de l'aiguille peut être ajustée selon le retour des images. Une fois que toutes les aiguilles nécessaires mises en position, le diagnostic ou traitement peut être délivré. Les aiguilles sont ensuite retirées et une image post-opératoire est prise pour contrôler le résultat final.

Les gestes de RI abdomino-thoraciques peuvent être accomplis avec plusieurs types d'imagerie, notamment l'échographie, la fluoroscopie, la tomодensitométrie (TDM) et l'imagerie par résonance magnétique (IRM). L'échographie est la modalité la plus répandue à cause de sa disponibilité, sa relative facilité d'utilisation, sa nature non-invasive et sa capacité à prendre des images en temps réel. Divers types de sonde existent selon la profondeur et la taille de l'organe. Le guidage des aiguilles est fait soit à main levée, soit en utilisant un guide-aiguille monté directement sur la sonde échographique. Quelques désavantages de l'échographie sont la dépendance de la résolution des images par rapport à la profondeur de visualisation, sa susceptibilité aux artefacts qui peuvent modifier l'image, et l'effet de distorsion du faisceau ultrasonique qui rend la localisation précise d'aiguilles difficile.

La fluoroscopie est la deuxième modalité la plus utilisée pour les ponctions d'aiguilles. C'est une modalité qui permet de faire des projections radiographiques bi-dimensionnelles (2D) en temps-réel, permettant de suivre le mouvement des tissus. Cette modalité est souvent couplée avec des agents de contraste pour relever les détails des tissus en question utiles à mettre en évidence. La plupart des gestes guidés par fluoroscopie sont vasculaires, mais d'autres applications existent, telles que les infiltrations intra articulaires et les vertébroplasties. La fluoroscopie doit être utilisée avec précaution à cause de l'irradiation du patient et du radiologue qui doit tenir l'aiguille dans le champs des rayons X.

La TDM est une modalité qui est en train de devenir de plus en plus utilisée pour la RI. Elle permet d'acquérir des images volumiques 3D de n'importe quel endroit du patient avec une haute résolution. Comme pour l'échographie, la plupart des ponctions guidées par TDM sont faites à main levée, donc la trajectoire de l'aiguille planifiée sur les images dans la salle de contrôle doit être reproduite de mémoire par le radiologue sur le patient. Pour ce faire, les radiologues ont tendance à planifier des trajectoires avec une seule obliquité. Comme pour la fluoroscopie, l'irradiation du patient est un aspect important à considérer dans de tels gestes.

L'IRM est de loin la modalité la moins utilisée pour les ponctions d'aiguilles à cause de son coût élevé, de la disponibilité limitée et des problèmes de compatibilité du matériel avec le fort champ magnétique des machines. L'IRM est une modalité qui est très complémentaire de la TDM car elle apporte des informations très différentes aux radiologues d'une manière non-irradiante. Ses spécificités incluent la prise de plans dans n'importe quelle orientation, une excellente résolution de contraste des tissus mous, et la possibilité de détection de cancers. Le champ magnétique et les contraintes d'espace dans le tunnel des IRM les rendent difficilement adaptés aux gestes médicaux : le matériel utilisé doit être non-magnétique et non-conducteur et l'accès au patient est rendu très difficile à cause de la profondeur du tunnel.

Les gestes de ponction d'aiguilles les plus communs sont les biopsies, les ablations de tumeurs, les drainages, et les injections dans la colonne vertébrale. Les biopsies sont des gestes diagnostiques utilisés pour extraire des carottes de tissus pour analyse histologique. Les aiguilles utilisées varient selon l'organe ponctionnée et selon le type de biopsie. Une aiguille typique consiste en une canule avec une pointe coupante, un mandrin et un mécanisme de déclenchement. Les pointes des aiguilles sont souvent traitées en surface pour améliorer leur échogénicité et des aiguilles compatibles IRM existent aussi. Les biopsies peuvent être ciblées ou exploratoires pour soit cibler une zone particulière, ou pour systématiquement explorer une région entière.

L'ablation de tumeurs a pour but de détruire les cancers par l'application focalisée d'énergie ou de produits chimiques. Ces types de traitements du cancer sont en train de devenir de plus en plus communs, car ils sont minimalement invasifs, et la technologie utilisée pour délivrer l'énergie avec précision est en pleine évolution. L'ablation par radiofréquence est une des méthodes les plus répandues et consiste en l'application d'un courant électrique entre deux électrodes en forme d'aiguilles pour chauffer les cellules proches. Cette technique est souvent utilisée dans le foie, les reins et les poumons sous contrôle échographique, TDM ou même IRM. Des systèmes mono ou bipolaires peuvent être utilisés, les premiers consistant en une aiguille dite « interstitielle » et un patch de « mise à la terre » sur la peau du patient. Les systèmes bipolaires utilisent directement deux aiguilles insérées dans le tissu entre lesquelles le courant passe. La cryoablation est une technique qui utilise le froid pour tuer les cellules cancéreuses. Du gaz d'argon est mis en expansion au bout de l'aiguille pour créer les très basses températures nécessaires. La boule de glace peut être suivie sous échographie ou sous TDM. Cette technique est souvent utilisée pour les cancers du rein, de poumons ou de la prostate. D'autres méthodes d'ablation sont l'ablation par micro-ondes, par laser, par thérapie photodynamique et par application d'éthanol.

Les drainages consistent en l'utilisation de cathéters pour drainer des fluides accumulés dans le corps à cause d'inflammations ou d'hématomes. Des abcès peuvent se former n'importe où dans le corps et l'échographie ou la TDM peuvent être utilisés pour guider les cathéters en place. Les injections dans la colonne vertébrale sont utilisées pour administrer des médicaments antidouleurs ou anti-inflammatoires, ainsi que pour cimenter des vertèbres. La fluoroscopie est souvent utilisée à cause des images en temps-réel ainsi que de la très grande présence d'os.

Les avantages des gestes décrits ci-dessus par rapport à la chirurgie ouverte sont nombreux : ils sont minimalement invasifs, plus rapides, moins coûteux, et avec un temps de récupération beaucoup plus court. Ils présentent, par contre, certaines difficultés dues au fait que les cibles ne sont pas visibles à l'œil nu. La qualité des images médicales est donc primordiale pour assurer un suivi précis. Le matériel utilisé doit donc être compatible avec la modalité d'imagerie. Il est aussi souvent difficile de reproduire sur le patient ce qui a été planifié dans l'image, les double-obliques de la trajectoire de l'aiguille étant particulièrement difficiles et nécessitant plusieurs images de contrôle pendant l'insertion. Les cibles visées pendant ces gestes sont souvent petites et accessibles à travers des couloirs d'accès restreints, donc la précision est un aspect très important.

Dans cette thèse la prostate est différenciée des autres organes typiquement décrits par la radiologie interventionnelle. C'est une glande qui est soignée par des urologues plutôt que par

des radiologues et nécessite un accès très particulier, soit transrectal, soit transpérinéal. Elle a une taille normale entre 20 et 50 cc, et est très adaptée aux interventions à base d'aiguilles, étant visible sous échographie et IRM.

Les deux principales interventions percutanées pratiquées sur la prostate sont les biopsies et la curiethérapie. La biopsie est la méthode de référence pour le diagnostic du cancer de la prostate. Ces biopsies exploratoires consistent à prélever 12 carottes de tissu réparties dans la glande à travers le rectum sous échographie transrectale. Des biopsies transpérinéales sont aussi possibles en cas de contre-indication de la voie rectale.

La curiethérapie est un traitement du cancer de la prostate par l'irradiation localisée à faible dose de la glande. Une vingtaine d'aiguilles creuses sont insérées à travers le périnée du patient sous guidage échographique transrectal pour pouvoir déposer une centaine de petits grains radioactifs à travers la glande entière selon un planning fait auparavant. Un gabarit, nommé un « template », qui consiste en une grille de trous horizontaux espacés de 5 mm, est utilisé pour aligner les aiguilles avec l'image échographique. La sonde conventionnelle est une sonde biplan qui permet d'acquérir des images transverses ou sagittales. Les images étant 2D, un dispositif appelé « stepper » est nécessaire pour déplacer la sonde dans le rectum et pouvoir visualiser toute la prostate.

Le succès du traitement par curiethérapie dépend de la répartition homogène de la dose à travers la totalité de la glande, et ceci sans sur-doser les tissus avoisinants. Une grande précision du placement des aiguilles est donc cruciale. Ceci est rendu difficile par un certain nombre de complications. Pendant l'insertion des aiguilles et le déplacement de la sonde dans le rectum, la prostate a tendance à bouger et à se déformer, rendant la reproduction du planning dosimétrique difficile à assurer. De façon similaire, l'œdème de la prostate fait grossir la glande pendant l'opération par rapport au planning initial. En plus, l'utilisation du template contraint les aiguilles à une grille d'insertions horizontales tous les 5 mm. Ceci rends difficile d'atteindre des distributions de dose précises et aussi ne permet pas de contourner l'arche pubien quand celui-ci cache une partie de la prostate. La curiethérapie de la prostate est donc une procédure longue et répétitive nécessitant une bonne expérience du clinicien.

La robotique permettrait de faire face aux diverses difficultés exprimées dans ce chapitre.

Chapitre 2 : Robots de ponction d'aiguilles

Ce chapitre décrit comment la robotique et l'assistance par ordinateur peuvent potentiellement améliorer les interventions à base d'aiguilles avec comme résultat une simplicité et une efficacité accrues ainsi qu'une amélioration des bénéfices cliniques. La grande précision des robots pourraient mener à des procédures avec moins d'itérations donc de réinsertions et de prises d'images, particulièrement pour des trajectoires complexes.

Le tableau 2-1 donne un résumé détaillé des systèmes robotiques existant dans la littérature pour les ponctions abdomino-thoracique guidées par TDM ou IRM ainsi que pour les ponctions prostatiques guidées par IRM ou échographie. Une très grande variété de robots existe, avec diverses architectures, compatibilités d'imagerie, et caractéristiques. Par contre, très peu ont atteint le stade des tests cliniques sur de vrais patients à cause des strictes réglementations et de la complexité de la problématique.

Cette thèse décrit le développement de deux tels systèmes : le robot PROSPER (PROState par voie transPERinéale) pour la curiethérapie écho-guidée de la prostate et le robot LPR (Light Puncture Robot ou Robot de Ponction Léger) pour la radiologie interventionnelle guidée par TDM et IRM. La suite de ce chapitre décrit les particularités des systèmes robotiques de ponction d'aiguille et les diverses problématiques auxquelles il faut faire face lors de leur conception.

Une première série de contraintes pendant la conception de robots de ponction relève de la modalité d'imagerie utilisée. Le robot étant proche de l'imageur, il ne doit pas affecter la qualité des images. Pour l'échographie, il ne doit pas bloquer le trajet des faisceaux d'ultrasons,

alors qu'en TDM et IRM, des contraintes de matériaux doivent être respectées pour éviter des artefacts indésirables dans l'image. Pour ceci, les choix des actionneurs utilisés pour contrôler les robots sont importants, en particulier dans le cadre de systèmes IRM. Des options compatibles IRM incluent les moteurs spécialisés dénommés « ultrasoniques », l'utilisation de solutions pneumatiques, ou l'utilisation de moteurs déportés hors du champ magnétique. Un autre aspect important lié aux imageurs TDM et IRM, est la contrainte d'espace limité dans les tunnels dans lesquels sont positionnés les patients.

D'autres contraintes sont liées au fait de manipuler une aiguille. L'espace de travail nécessaire est typiquement assez restreint, comme le sont aussi les forces appliquées. Par contre, les insertions d'aiguilles se font parfois près de structures osseuses, donc les systèmes doivent pouvoir gérer l'éventuel contact de l'aiguille avec l'os.

Toutes les procédures percutanées peuvent être divisées en deux phases : une phase de positionnement de l'aiguille au-dessus de la peau du patient pour l'aligner avec la trajectoire désirée, et une phase d'insertion de l'aiguille selon cette trajectoire pour atteindre la cible à l'intérieur du patient. Un système robotique peut automatiser une ou les deux de ces parties, avec plus ou moins de degrés de liberté (DDL). La phase de positionnement comporte des translations pour placer la pointe de l'aiguille sur le point d'entrée ciblé et des orientations pour aligner l'aiguille à la trajectoire. La phase d'insertion peut comporter une insertion fractionnée pour pouvoir faire des images de contrôle pendant l'insertion ou une insertion continue dans le cas d'une imagerie en temps réel. L'aiguille peut être mise en rotation, comme une perceuse, pour essayer de diminuer les forces d'interaction entre l'aiguille et les tissus. L'aiguille peut aussi être tout simplement guidée par le robot, l'insertion étant faite par le clinicien lui-même.

Une dernière série de contraintes est liée aux tissus mous à travers lesquels les aiguilles doivent passer. La déformation des tissus ainsi que de l'aiguille elle-même sont des problèmes importants ; en effet dans le premier cas la position de la cible peut être modifiée par la tâche réalisée ; pour le second cas c'est le contrôle même de la trajectoire qui s'avère difficile. La déformation des tissus peut être gérée soit en essayant de la réduire en jouant sur la vitesse d'insertion ou éventuellement de rotation de l'aiguille ou en tenant les tissus avec des aiguilles d'ancrage, soit en suivant la déformation pendant l'insertion par des modèles déformables ou par le recalage d'images. La déformation des aiguilles peut être mise à profit pour pouvoir diriger la pointe vers sa cible par une technique dite de « needle steering ».

En plus de ces contraintes de conception du robot, il faut aussi considérer comment lier le robot aux images pour pouvoir simplement choisir une cible et laisser le robot se mettre en place en autonomie. Pour ce faire, il faut calibrer l'espace robot par rapport à l'espace image. Ceci peut être fait en préopératoire si le robot est lié physiquement à l'imageur (avec un bras codé ou un autre système de navigation) ou en per-opératoire si le robot est visible dans les images. Cette dernière technique nécessite des mires reconnaissables qui peuvent être segmentées dans l'image avec précision.

Du fait que ces robots sont guidés par l'imagerie médicale, des sources d'erreurs en découlent qui affectent la précision finale. La qualité des images est bien sûr un élément clé, la précision du calibrage entre le robot et l'imageur y étant étroitement liée. Si on voulait toujours prendre des images de très haute résolution, ceci n'est pas toujours faisable, notamment pour des raisons de rapidité de la prise d'image et des problèmes d'irradiation du patient dans la TDM. La résolution d'une image échographique a, de par le mode de formation de l'image, une dégradation de sa résolution en profondeur. Enfin, une autre source d'erreurs provient de l'identification des paramètres du modèle cinématique du robot réel. Le robot doit être calibré avec le modèle prédit pendant la phase de conception. Des imprécisions dans les moteurs ou capteurs de position ou des imprécisions dans les dimensions du robot peuvent créer des erreurs significatives en bout d'aiguille.

Tous les systèmes conçus pour être utilisés sur patients doivent être validés et testés au préalable pour assurer non seulement leur sécurité mais aussi pour évaluer leur service médical attendu. Les robots de ponction d'aiguilles sont des dispositifs médicaux à risque moyen (classe IIb selon la Directive Européenne) utilisés typiquement dans un environnement ouvert et non-

stérile tel que les salles d'imagerie TDM ou IRM. Ceci dit, ils travaillent tous à proximité de la zone stérile définie autour du point d'insertion sur le patient. Du coup, la stérilisation est une contrainte forte qui peut facilement invalider un concept. Il faut donc éviter toute contamination de l'aiguille soit directement par le robot, soit par biais du clinicien qui doit manipuler l'aiguille. Les systèmes peuvent être soit protégés par des housses stériles ou stérilisés entièrement. Les deux principales techniques de stérilisation utilisées au CHU de Grenoble sont la stérilisation par vapeur pressurisée et la stérilisation basse température par peroxyde d'hydrogène, chacune ayant ses propres contraintes et avantages.

La validation de systèmes robotiques suit le cycle normal d'un nouveau dispositif quelconque où des phases de prototypages et de tests précliniques se suivent pour donner un produit final prêt pour des premiers tests cliniques sur humain. Les tests précliniques consistent en des tests simplifiés pour valider certains aspects, tels que la précision ou l'utilisation d'une certaine méthodologie. Ces tests sont souvent faits sur des fantômes (représentations synthétiques de l'environnement réel) mais aussi sur des modèles animaux in vitro ou in vivo ainsi que sur des modèles cadavériques. Le but principal est de mettre en évidence le service médical potentiel attendu du produit pour justifier des études plus poussées sur humain.

Pendant cette thèse les concepts décrits dans ce chapitre pour la conception et le développement de robots de ponctions ont été mis en pratique dans le développement des systèmes PROSPER et LPR.

Chapitre 3 : PROSPER – Robot de ponction transpérinéale de la prostate guidé par échographie

Le système PROSPER a comme but d'améliorer la précision de délivrance de la dose pendant la curiethérapie de la prostate. Il consiste en un dispositif robotisé d'insertion d'aiguille couplé à une sonde échographique 3D pour donner un système capable de suivre les mouvements et déformations de la prostate pendant l'intervention. Ceci est fait par le biais d'une procédure automatique de recalage d'images échographiques qui permet de modifier le planning dosimétrique selon les déformations. Le système permet 1) d'avoir une meilleure correspondance entre le placement réel des grains et le planning, 2) de permettre une meilleure diversité de positionnements des grains pour améliorer la distribution de la dose dans la prostate et 3) de potentiellement ouvrir la disponibilité de la technique à plus de patients, en particulier ceux avec une plus grosse prostate ou avec un arc pubien contraignant.

Ce chapitre décrit la conception et le développement de ce système ainsi que les tests précliniques poursuivis pour valider le concept en préparation d'un prototype clinique. Le robot est rigidement relié à la sonde transrectale 3D permettant un calibrage préopératoire entre l'espace robot et l'espace image. L'utilisation d'une sonde 3D permet d'acquérir une image volumique de toute la prostate sans avoir à déplacer la sonde dans le rectum, ce qui limite les bougés et déformations éventuelles.

La procédure robotique envisagée est la suivante : le système est mis en place et une première image de référence de la prostate est prise. Cette image est utilisée pour planifier la distribution des grains. Le robot insère ensuite une aiguille pour atteindre une première cible. Une deuxième image est prise et recalée avec l'image de référence pour déterminer si la cible a bougé par rapport à la position de référence. Si la cible est encore atteignable en profondeur, le robot pousse l'aiguille plus loin jusqu'à l'atteindre. Sinon, l'aiguille est retirée et réinsérée avec un décalage estimé pour prendre en compte la déviation de la cible, comme dans la méthode conventionnelle. Si l'arc pubien est touché, la cible peut être atteinte en inclinant l'aiguille pour contourner l'os. Une fois la cible atteinte, le grain est libéré. Ceci est ensuite répété pour tous les grains.

Pour accomplir cette tâche, le manipulateur robotique a été conçu respectant les contraintes techniques suivantes. 5 DDL étaient nécessaires pour pouvoir positionner et

orienter l'aiguille devant le périnée. 2 DDL étaient incorporés dans le module d'insertion, un pour l'insertion et un pour faire tourner l'aiguille autour de son axe. L'espace de travail devait permettre au robot d'atteindre au moins le même volume de travail permis par le « template » classique (60 x 60 mm) en plus des 30 degrés d'inclinaison dans les plans sagittal et coronal. Le robot devait être facile à manipuler tout en laissant au clinicien un accès facile à l'aiguille pour l'insertion des grains et avoir un poids de moins de 5 kg pour une meilleure manipulation. Il devait être compatible avec les aiguilles et distributeurs de grains standard. La sécurité du patient et des cliniciens était primordiale ainsi que sa compatibilité avec les conditions stériles de la procédure. La précision visée pour ce système était de moins de 2 mm pour le système entier et inférieure à 1 mm pour le robot tout seul sans l'imagerie.

Un prototype pour une utilisation en laboratoire a été conçu et construit. Le manipulateur comporte un module de positionnement sur lequel est installé un module d'insertion. Le module de positionnement utilise une architecture type parallélogramme avec deux paires de modules linéaires motorisées en croix donnant les 4 DDL en translation et orientation nécessaires devant le périnée et un cinquième module linéaire perpendiculaire donnant le cinquième DDL pour rapprocher l'aiguille du périnée. Le module d'insertion permet de pousser l'aiguille dans le patient. La rotation de l'aiguille autour de son axe peut aller à des vitesses de 0 à 12 tr/s. Un système de débrayage mécanique est utilisé pour débrayer le moteur en cas de contact avec l'os pubien. L'embout de l'aiguille est rapidement accessible par le clinicien pour permettre de brancher le « Mick Applicateur » permettant l'insertion des grains. Il est prévu que le robot soit couvert en majorité par des housses stériles. Une sorte de manchon ou « bushing » stérile assure l'interface entre le robot non-stérile et l'aiguille stérile. Un guide-aiguille stérile est aussi utilisé à l'avant du robot pour guider l'aiguille pendant l'insertion.

La cinématique du robot est résolue par l'application de la convention Denavit-Hartenberg (DH) modifiée pour situer les repères sur les diverses articulations du robot. Le robot ayant une architecture parallèle, une solution géométrique est trouvée pour résoudre les articulations non-asservies des chaînes parallèles. Les paramètres cinématiques ont été déterminés par calibration sur le prototype en mesurant la position du robot à divers endroits partout dans son espace de travail. Un système de navigation optique, Polaris (Northern Digital Inc.), était utilisé pour ces mesures et l'erreur cinématique était minimisée en utilisant la méthode numérique Levenberg-Marquardt pour la réduire de 3.2 ± 0.94 mm (estimation initiale des paramètres) à 0.5 ± 0.20 mm (après calibration).

Le matériel d'imagerie utilisé pour guider ce système prototype consiste en une sonde échographique Ultrasonix 4DEC9-5 connectée à un échographe Ultrasonix RP. La sonde est endorectale et « end-fire », c'est-à-dire elle prend des images en éventail grâce à un capteur déplacé en rotation en bout de la sonde. Par rapport aux sondes endorectales conventionnelles qui sont 2D et « side-fire » (images prises par un capteur situé sur le côté de la sonde), cette sonde permet l'acquisition d'une image volumique de toute la prostate sans avoir à la bouger dans le rectum. De plus elle est inclinée pour permettre d'orienter les aiguilles en cas de conflit avec l'arc pubien. Par contre, le fait d'utiliser une sonde « end-fire » nécessite une reconstruction des images plus complexe pour obtenir les images sagittales telles que les cliniciens sont habitués à voir avec les sondes « side-fire » et à utiliser pour contrôler la progression des aiguilles. Malheureusement aucune sonde 3D « side-fire » n'existe sur le marché.

Le recalage des images échographiques pour le suivi des déformations de la prostate est fait par un algorithme développé au sein du laboratoire par Michael Baumann lors de sa thèse. L'algorithme était développé dans le cadre du guidage des biopsies de la prostate et est ainsi utilisé dans un produit commercialisé par la société Koelis SAS (La Tronche, France). Le recalage non rigide est entièrement automatique et basé sur une méthode iconique, multi-résolution. Il est capable de recalibrer deux images 3D prostatiques avec une précision évaluée sur patient de 0.76 ± 0.52 mm et un temps de calcul entre 6 à 8 secondes sur un PC standard.

Ce recalage est intégré dans une application dont l'interface permet de contrôler la sonde échographique et de visualiser les images 3D en trois coupes orthogonales. La reconstruction

de l'image peut être adaptée selon la vitesse du son dans le médium visualisé. Cette interface fonctionne sur l'échographe numérique et est liée au PC de contrôle du robot par un câble réseau. Le robot est contrôlé par une librairie de classes C++ qui gère la communication par un port série avec la boîte de contrôle du robot ainsi que les mouvements des moteurs.

Le but du démonstrateur développé est de pouvoir cliquer dans l'image et ainsi permettre au robot de placer l'aiguille à cet endroit en toute autonomie. Pour ceci, il faut recalibrer l'espace robot avec l'espace image. Une méthode de recalage a donc été développée. Elle utilise un bassin rempli d'eau comportant une membrane molle qui permet au robot d'insérer la pointe de l'aiguille dans l'eau. Un manchon en caoutchouc est enfilé sur le bout de l'aiguille pour diminuer les artefacts dans l'image, permettant ainsi à la pointe de l'aiguille d'être segmentée avec précision. Un nuage de positions est segmenté dans l'image et ensuite recalé avec les positions enregistrées par le robot. La transformation homogène entre les deux espaces peut ainsi être établie. Pour un nuage de 25 positions, une erreur de recalage de 0.86 ± 1.32 mm a été atteinte.

Pour tester le système, nous avons voulu simuler le bougé de la prostate réelle dans un environnement synthétique. Pour ceci un fantôme non rigide a été spécialement développé faute de solutions existantes (commerciallement ou dans la littérature). Le fantôme est fabriqué avec du PVC mou, un polymère qui peut être mélangé avec un assouplissant pour donner différentes consistances de la matière. La forme consiste en un cadre de PVC dur, rempli de PVC mou dans lequel est plongée une prostate en PVC plus ou moins dur. Un trou dans le cadre joue le rôle d'un rectum dans lequel la sonde peut être insérée. La morphologie du fantôme est visible en échographie, TDM et IRM. La vitesse du son dans le fantôme a été mesurée à 1380 m/s en moyenne. Le mouvement de la prostate a aussi été vérifié lors d'insertions d'aiguilles, montrant que la prostate pouvait bouger dans le sens de l'aiguille mais aussi en rotation autour de la tête de la sonde.

Nous avons aussi voulu tester un aspect particulier du système qui a été proposé par d'autres équipes mais pas encore validé sur patient, en ce qui concerne la rotation de l'aiguille pendant son insertion. Des tests avec des insertions dans du PVC mou nous ont clairement démontré qu'en tournant l'aiguille, on réussit à réduire la force d'insertion de l'aiguille. Nous pourrions ainsi conclure qu'avec une rotation de l'aiguille, la prostate aurait tendance à moins se déformer. Nous avons donc poursuivi nos essais sur du tissu animal in vitro ainsi que sur tissu frais cadavérique. Les deux cas ont confirmé cet avantage potentiel de la rotation. Par contre, l'effet de la rotation sur la dégradation des tissus est un aspect important à prendre en compte avant de pouvoir essayer la technique sur humain. A notre connaissance, aucune étude n'a été faite jusqu'alors sur ceci. La crainte principale serait d'accélérer la formation de l'œdème de la prostate pendant l'opération, le rendant plus difficile à gérer. Nous avons donc commencé des tests histologiques sur tissus animaux et cadavériques pour voir l'effet de la rotation sur l'intégrité des tissus. Ces tests étaient en cours lors de la rédaction de cette thèse et feront l'objet d'une future publication.

La validation du système PROSPER sur notre fantôme synthétique consistait à insérer l'aiguille vers des cibles encastrées dans la prostate et ensuite à mesurer la précision avec laquelle ces cibles ont été atteintes. Le but était de vérifier la possibilité d'utiliser le recalage couplé au robot pour automatiquement prendre en compte les bougés de la prostate. Neuf fantômes ont été réalisés avec au total 50 cibles à l'apex des prostates, et 40 cibles à leur base. Les cibles étaient des billes en verre d'un diamètre de 1 mm. La sonde était mise en place dans le rectum et une première image volumique était acquise. Le centre d'une cible était choisi à haut zoom et ses coordonnées étaient envoyées au robot, qui grâce au calibrage fait auparavant, a inséré l'aiguille jusqu'à cette position. Une deuxième image était ensuite acquise et recalée avec l'image de référence permettant ainsi de déterminer la nouvelle position de la cible par rapport au robot. Le robot a ensuite avancé l'aiguille en profondeur pour rapprocher le bout de l'aiguille de la cible mise à jour. Une fois en position finale, une bille était déposée pour marquer cet endroit. Chaque fantôme a été passé au scanner TDM à haute résolution ($0.15 \times 0.15 \times 0.33$ mm) et les cibles et billes ont été segmentées à la main. La distance entre chaque cible et sa bille

correspondante était calculée et décomposée en composantes x, y et z. A chaque insertion, la distance de réinsertion pour corriger le bougé de la cible était aussi notée.

Les résultats ont montré une erreur moyenne de 2.98 ± 1.27 mm et 1.61 ± 0.92 mm dans la direction de l'aiguille, pour des bougés moyens de la cible de 5.35 ± 2.20 mm. Ceci montre une amélioration de 75% de la précision d'atteinte de la cible dans le sens de l'aiguille. Du coup le système était bien capable de réduire l'effet de la déformation du fantôme. L'erreur finale, par contre, venait non seulement du bougé de la prostate dans le sens de l'aiguille mais aussi de la rotation de la prostate pendant l'insertion, rendant les cibles inatteignables selon la même trajectoire. Des solutions pour prendre en compte cette rotation aussi seraient : (1) de retirer l'aiguille et de la réinsérer avec un offset pour essayer de contrer cette rotation, comme ce qui est fait en pratique conventionnelle, (2) d'utiliser des aiguilles d'ancrage pour essayer de réduire la composante de rotation de la prostate, (3) d'essayer de prédire les rotations avant insertion par l'utilisation de modèles biomécaniques, ou (4) éventuellement d'utiliser du « needle steering ».

Les tests ont donc montré que le système est capable d'automatiquement améliorer le ciblage du planning dans un environnement déformable avec une amélioration potentielle de la fidélité de la distribution de la dose d'irradiation dans la prostate. En outre, sa capacité à incliner les aiguilles lui permet de contourner l'arc pubien pour accéder à des cibles impossibles à atteindre auparavant pour certains patients. La précision du système serait compatible non seulement avec les besoins de la curiethérapie mais aussi avec ceux des biopsies pour mieux localiser les cancers dans la prostate, et en parallèle permettre un traitement focal.

Chapitre 4 : LPR – Robot de ponction abdomino-thoracique guidé par scanner TDM et IRM

Le domaine d'application clinique du système LPR est la radiologie interventionnelle de l'abdomen et du thorax guidée par scanner TDM et IRM. Il a essentiellement le même objectif que le système PROSPER, c'est-à-dire de faciliter l'atteinte d'une cible avec une aiguille par voie percutanée. Du coup la méthodologie de conception et validation du LPR était similaire à celle du système PROSPER, notamment la définition de contraintes cliniques et techniques, la conception d'un protocole clinique et du manipulateur, la construction d'une maquette de validation, le calibrage robot-image et les tests de faisabilité du système.

Son but spécifique est d'améliorer la précision d'atteinte d'une cible avec plus de facilité, moins d'images, et en particulier dans des cas complexes de double-obliquité ou fortement contraintes par l'anatomie du patient (entre les côtes par exemple). L'originalité du projet est sa capacité d'atteindre une cible sous soit TDM ou IRM, ce qui élargit son champ d'utilisation. C'est aussi un robot qui est monté sur le corps du patient, et non sur le lit du scanner, lui permettant de bouger avec le patient pendant l'intervention.

Le système LPR consiste en un robot léger posé et sanglé sur le corps du patient. Ce robot tient, positionne et insère l'aiguille. Pour réduire le poids du robot et réduire le risque de produire des artéfacts dans les images, les moteurs du robot sont déportés aux pieds du patient, et contrôlent le robot par le biais de câbles et gaines (systèmes à câbles Bowden). La pneumatique est utilisée pour tenir et insérer l'aiguille. La boîte de contrôle du robot se situe en dehors de la salle d'imagerie et est contrôlée par un PC de contrôle qui peut récupérer les images provenant directement du scanner.

Le protocole clinique est similaire au protocole conventionnel, tout en simplifiant certaines étapes, les rendant plus efficaces. Le patient est mis en place sur le lit de l'imageur. Le robot est installé sur son corps. Une première image est acquise sur laquelle la cible et la trajectoire d'insertion sont choisies. Le robot positionne ensuite en autonomie l'aiguille au-dessus du patient en ligne avec la trajectoire. Une deuxième image est prise pour contrôler si l'aiguille est bien alignée avec la trajectoire désirée après quoi une séquence itérative de petites insertions et d'images de contrôle est faite jusqu'à l'atteinte de la cible. La trajectoire de l'aiguille peut être modifiée par le robot pendant l'insertion en cas de déviation.

Les principales contraintes techniques qui ont défini sa conception sont : l'incorporation de 5 DDL pour le positionnement et l'insertion de l'aiguille, la compatibilité avec les imagerie TDM et IRM, un grand espace de travail pour permettre une installation facile et un montage sur le corps du patient pour permettre de suivre les bougés du patient. La précision désirée du système dépend de la taille de la plus petite cible anatomique que le système devra viser. Des lésions d'un diamètre plus petit que 10 mm sont souvent difficiles à diagnostiquer et ne sont souvent pas considérées suffisamment importantes pour nécessiter une intervention invasive. L'objectif de précision choisi pour le robot était de la moitié, donc de moins de 5 mm.

Comme pour le système PROSPER, un prototype préclinique a été construit. Le manipulateur robotique avait une architecture similaire basée sur quatre axes de mouvements parallèles. Ces axes sont pilotés par des moteurs ultrasoniques, compatibles IRM, et permettent à l'aiguille d'être positionnée au-dessus du patient. L'insertion de l'aiguille est réalisée par deux pinces pneumatiques, l'une au-dessus de l'autre : une stationnaire pour tenir l'aiguille en place entre chaque insertion et l'autre mobile pour pousser l'aiguille pendant l'insertion. La profondeur d'insertion peut être réglée entre 0 et 30 mm par une butée ajustable et pilotée par un cinquième moteur ultrasonore. Le robot est entièrement fabriqué de matières non-magnétiques et non-conductrices pour permettre une compatibilité avec les imageurs. Deux mires sont encastrées près de l'aiguille pour permettre au robot d'être repéré dans les images. La fixation du robot sur le patient a été conçue mais n'a pas encore été développée. Elle consiste en un coussin à vide, tel qu'utilisé habituellement pour l'immobilisation radiologique, qui forme l'interface entre le robot et la peau du patient. Le tout est sanglé autour du corps du patient.

Le robot est entièrement stérilisable par stérilisation STERRAD (peroxyde d'hydrogène) et les diverses matières utilisées dans ce prototype ont été testées dans des cycles multiples pour assurer leur compatibilité. De plus, la stérilisation de l'intérieur des systèmes de gaines câbles utilisés pour actionner le robot a été testée en les imprégnant de spores de *Geobacillus Stearothermophilus*, et ensuite stérilisant et mettant en culture les systèmes complets. Aucune prolifération bactérienne n'a été observée, nous confirmant la bonne stérilisation des échantillons.

L'utilisation de câbles pour actionner le robot présente des difficultés à cause de leur élasticité qui doit être prise en compte pour assurer une bonne précision. Des câbles en Dyneema, à très basse élasticité, ont été utilisés. Néanmoins, sur la longueur de 1.5 m, une élongation de quelques millimètres était présente. Cette élongation a été prise en compte dans le logiciel de contrôle et calibrée pour chaque moteur.

Par rapport au système PROSPER, le LPR utilise des mires encastrées dans sa structure pour permettre le calibrage entre l'espace image et l'espace robot. Ceci lui permet d'être calibré automatiquement après chaque prise d'image. Une segmentation automatique a été développée à base de techniques de traitements d'images standards, tel que le seuillage et la recherche de composantes connexes. Cette procédure n'a besoin d'aucune interaction avec l'utilisateur et marche pour les deux modalités d'imagerie. Des mesures sur images TDM ont montré une précision de moins de la moitié d'un voxel.

Le logiciel de contrôle du robot a été programmé sous un logiciel libre développé dans notre laboratoire, nommé CamiTK, qui permet d'ouvrir différents types de données médicales et les faire interagir ensemble. Des composants robot, données patient, et images ont été créés. Le composant robot comprenait le modèle des mires ainsi que la position actuelle de l'aiguille. Le composant image permettait d'ouvrir les images DICOM provenant de l'imageur. Des repères étaient attachés à chaque composant, leur permettant de s'afficher l'un par rapport à l'autre dans un logiciel de visualisation. Une librairie de contrôle a été créée pour piloter le prototype et contient la cinématique du robot, ainsi que les commandes nécessaires pour communiquer avec les moteurs. L'aspect modulaire et générique du logiciel était important pendant le développement, permettant la réutilisation du code pour les futurs prototypes cliniques.

Des évaluations précliniques ont été réalisées pour 1) tester la compatibilité du prototype avec les imageurs, et 2) déterminer la précision intrinsèque du système. La compatibilité du robot a été testée sous TDM ainsi que sous séquences T1 et T2 dans l'IRM. Aucun artefact

notable n'a été trouvé dans les images TDM. Dans l'IRM, le robot a été évalué selon les normes NEMA, avec une comparaison du rapport signal-bruit entre une image avec le robot en place et une image sans robot. Aucun effet notable n'a été observé en présence du robot.

La précision du système a été évaluée en visant des cibles dans un fantôme en gélatine sous scanner TDM et IRM. La procédure suivie était de prendre une première image, choisir une cible et une trajectoire aléatoires, laisser au robot positionner et insérer l'aiguille en autonomie et ensuite prendre une image de contrôle à haute définition. Cette dernière image était utilisée pour mesurer la distance entre la position désirée de la cible et la pointe réelle de l'aiguille. Sous scanner TDM, six petites cibles d'un diamètre de 1 mm ont été visées avec des images à haute résolution ($0.67 \times 0.67 \times 0.75$ mm) ainsi que quatre cibles plus grosses d'un diamètre de 7 mm avec des images à une résolution plus réaliste en pratique clinique ($0.67 \times 0.67 \times 2$ mm). Dans l'IRM, trois insertions ont été faites pour atteindre des cibles de 7 mm, dont une insertion sous une séquence T1 ($0.73 \times 0.73 \times 5.3$ mm) et deux séquences sous une séquence T2 ($0.88 \times 0.88 \times 5.3$ mm). Deux des six petites cibles et toutes les grosses cibles ont été touchées. L'erreur de ciblage moyenne dans les images TDM était de 3.3 ± 1.7 mm avec une erreur d'orientation de l'aiguille de moins de 1° . L'erreur de ciblage dans les images IRM était de moins de 5 mm pour la pointe de l'aiguille et moins de 2° pour l'orientation.

Pendant ces essais, le prototype actuel a démontré une précision d'atteinte d'une cible de moins de 5 mm dans les deux modalités d'imagerie, ce qui correspond à la précision attendue. Avec l'utilisation d'un fantôme en gélatine très mou et facilement transpercé, les essais n'ont pas pris en compte la courbure de l'aiguille ni le déplacement de la cible. On pourrait donc s'attendre à une erreur plus grande dans de vrais tissus. Ceci dit, ces tests visaient à évaluer la capacité du robot à réaliser la procédure tout seul, sans interaction de l'utilisateur. En pratique, le clinicien ferait des images de contrôle avant chaque pas d'insertion et pourrait réajuster la trajectoire de l'aiguille pour améliorer la précision finale. Par ailleurs, des erreurs systématiques ont été repérées après coup, notamment une erreur de calibrage du modèle des mires ainsi qu'une erreur due à un artefact chimique des mires dans les images IRM, qui pourrait facilement être éliminée pour de futurs essais. Le prototype actuel a aussi des défauts de fabrication, notamment du jeu dans les articulations, qui ont aussi affecté les résultats. Le système LPR a donc un potentiel pour simplifier le ciblage de lésions sous imagerie TDM et IRM et ainsi permettre des trajectoires plus complexes.

Chapitre 5 : Conclusion

Ce chapitre met fin à la thèse en résumant le travail qui a été réalisé, les contributions qui ont été faites et en discutant les perspectives des deux projets PROSPER et LPR. Les deux systèmes ont permis de discuter des divers aspects relatifs aux robots de ponctions, en particulier : les contraintes de compatibilité d'imagerie, d'espace de travail, de degrés de liberté, de la gestion de contact avec des os, de la déformation des tissus, de la fixation du robot par rapport au patient, des méthodes de calibrage entre l'espace robot et l'espace image, de la stérilisation ainsi que de l'analyse préclinique des prototypes. Avec le système PROSPER, nous avons proposé une nouvelle approche pour réaliser les curiethérapies avec plus de précision, tout en suivant le bougé de la prostate pendant la procédure. Avec le LPR, nous avons proposé un système pour les ponctions génériques sous guidage TDM et IRM, permettant des trajectoires complexes avec double obliquité, tout en nécessitant moins d'images.

Le travail de cette thèse nous a permis d'établir les spécifications techniques détaillées ainsi que des analyses de risques, tels qu'exigés par les normes européennes, pour le développement de prototypes cliniques des deux systèmes. Ces nouveaux prototypes qui seront testés en clinique sont en cours de fabrication avec une livraison proche. Des perspectives pour le robot PROSPER sont : l'utilisation du système dans le cadre d'autres interventions prostatiques transpérinéales, tels que les biopsies ou les traitements focaux, l'intégration d'un recalage IRM-échographie développé dans le laboratoire pour permettre une segmentation

rapide et précise de la prostate en début de la procédure et le couplage avec des nouvelles méthodes de « needle steering ». Des perspectives pour le robot LPR sont : l'utilisation du système avec de l'imagerie temps-réel et le suivi de respiration pour permettre au radiologue d'insérer l'aiguille au bon moment, selon la respiration du patient, ainsi que le contrôle temps-réel du robot avec une interface haptique tel que l'Omega de Force Dimension, dans le but éventuel d'incorporer un retour d'effort pour mieux guider le radiologue.